STRUCTURAL, BIOCHEMICAL AND FUNCTIONAL ANALYSIS OF GLUTAMATE RECEPTORS AND THE AUXILIARY PROTEIN STARGAZIN

Inaugural-Dissertation

to obtain the academic degree

Doctor rerum naturalium (Dr. rer. nat.)

submitted to the Department of Biology, Chemistry and Pharmacy
of Freie Universität Berlin

by

MIRIAM CHEBLI

from Berlin, Germany

August 2016

The present work was carried out from February 2012 until February 2016 at the Leibnitz-Institut für Molekulare Pharmakologie, in Berlin-Buch, under the supervision of Dr. Andrew Plested.

1st reviewer: Dr. Andrew Plested
2nd reviewer: Prof. Dr. Markus Wahl

Date of defence: 02.12.2016

“Almost all aspects of life are engineered at the molecular level, and without understanding molecules we can only have a sketchy understanding of life itself.”
Francis Crick (1988), What Mad Pursuit: A personal View of Scientific Discovery, page 61

ACKNOWLEDGEMENTS

Foremost, I want to thank my PhD supervisor, Dr. Andrew Plested for giving me the great opportunity to work in his laboratory. Andrew has always been patient with me, he provided me with guidance, support and motivation and I am very grateful for everything I could learn in his group.

I also want to thank Prof. Dr. Markus Wahl for reviewing my PhD thesis.

Next, I want to thank all the present and past members of the Plested group for their help and especially for the unique working atmosphere. It was a pleasure for me to be part of this group. Thanks to Jelena, Héctor, Clarissa, Anna, Mette, Mila, Yuchen, Irene, Anahita and Sonja and also to Ronny, Marcus, Vale and Antje. Special thanks to Jelena and Héctor, whose hard work on the LBD project was essential to this work. I want to thank Dr. Clarissa Eibl for her help and crystallographic expertise whenever I had questions and for bearing company in the lonely ÄKTA cold room. I wish you all the best in your future career! I also want to thank Marcus, Ronny, Vale and Antje for the absolutely excellent technical assistance and work they have done. You are essential for keeping everything going in the lab.

I further want to thank the whole Daumke and Heinemann group. Incorporating us into your seminars was so helpful for me. I want to thank both groups for the fruitful and informative talks and discussions. Thanks to Manuel Hessenberger for introducing me to the liposome co-sedimentation assay and his patient help. Special thanks go to Prof. Dr. Oliver Daumke and Dr. Katja Fälber for the collaboration we had on the GluA2 LBD project. In this context, I want to thank Dr. Yvette Roske and Dr. Katja Fälber for introducing me to the BESSY synchrotron, to data collection, structure solution and refinement. Special thanks to Dr. Uwe Müller, Dr. Manfred Weiss, Dr. Sandra Pühringer and the whole MX-group at BESSY for the excellent technical support.

I want to thank Sofia for introducing me to their CD spectrometer. I want to thank Dr. Anja Schütz, Tracy and Janett for welcoming us in their laboratory and for the nice working atmosphere.

I also want to thank Philip Selenko and his whole group for the collaboration on the stargazin project, but especially I want to thank Marcel Stuiver who showed me everything in their lab, Marleen van Rossum who was always very helpful when I had questions and Dr. Stamatios Liokatis for recording the spectra with me and his help and advices in general.

Thanks to the whole mass spectrometry facility of the FMP Berlin, to Dr. Eberhard Krause, Dr. Michael Schümann, Annika Manns and especially Heike Stephanowitz for analyzing my samples.

I really appreciate the help I got from everyone. I experienced the supportive spirit on campus as really outstanding and special.

Last but not least, I would like to thank my family for their support, their belief in me and their unlimited and unconditional love. I love you all so much! Special thanks to my sister Sarah, who always had a sympathetic ear for me, especially when nothing seemed to work. You really know how to cheer me up and how to make me laugh no matter how I feel. Thank you Sari, you are the best! At last, I want to thank René for his support and for being the most patient, well-adjusted and sympathetic person I ever met.

RELATED PUBLICATIONS

Parts of this thesis have been published in the following articles:

Baranovic J*, **Chebli M***, Salazar H*, Carbone AL, Fälber K, Lau AY, Daumke O, Plested AJ

Dynamics of the Ligand Binding Domain Layer during AMPA Receptor Activation.

Biophys J. 2016 Feb 23;110(4):896-911. http://dx.doi.org/10.1016/j.bpj.2015.12.033

* These authors contributed equally to this work.

Salazar H*, Eibl C*, **Chebli M**, Plested AJ

Mechanism of partial agonism in AMPA-type glutamate receptors.

Nature Comm. 2016 (in press)

* These authors contributed equally to this work.

CONTENTS

LIST OF FIGURES

LIST OF TABLES

LIST OF EQUATIONS

ABSTRACT

Neurons communicate with each other at synapses. Neurotransmitters released from presynaptic terminals act as activators of ligand-gated ion channels at the postsynapse across the synaptic cleft and induce changes in membrane potential or activate signaling cascades. At the postsynaptic density, α-amino-3-hydroxy-5-methyl-4-isoxalzolepropionic acid (AMPA) receptors are the key mediators of fast excitatory neurotransmission in the brain through formation of excitatory postsynaptic currents (EPSCs), thus helping to propagate the electrical signal from one neuron to another. AMPARs furthermore promote formation and maturation of synapses during the early phases of synaptogenesis. The number and activity of AMPARs at the postsynapse is regulated through interaction with transmembrane AMPA receptor regulatory proteins (TARPs). The function of stargazin/type I TARPs on AMPAR trafficking itself is regulated upon TARP phosphorylation.

One aim of this thesis was to understand how fast receptor activation is achieved. We aimed to understand how ligand binding to the four ligand-binding domains of the receptor mediates opening of the ion channel, as structural information of an active AMPAR tetramer is limited. Recent full-length cryo-EM and crystal structures tried to capture the receptor in an active state, however the ion channel was either not resolved or closed. Furthermore, we also aimed to understand the cellular mechanism for regulation of AMPAR function at the synapse. AMPARs associate with TARPs at the synapse, where TARPs mediate AMPAR gating, trafficking and pharmacology. It has been shown that the 120 residue long C-terminal domain of stargazin regulates AMPAR clustering at the postsynapse in a phosphorylation-dependent manner. Nine Ser residues within the C-terminal domain of stargazin have been shown to be phosphorylated, and their phosphorylation abolishes binding of stargazin to the negatively charged bilayer mediated by a positive Arg stretch. Using biochemical, biophysical and high-resolution and real-time structural studies we aimed to gain atomic insights into stargazin phosphorylation and evaluate the dependence of the lipid interaction on phosphorylation.

By recombinantly expressing, purifying and crystallizing the isolated domain that is responsible for binding of the neurotransmitter, the isolated ligand-binding domain (sLBD), a high-resolution crystal structure of fully glutamate-bound sLBD in two different tetrameric arrangements, formed via crystal symmetry, could be obtained for the first time. We carefully analyzed the tetrameric LBD assemblies structurally, biophysically and functionally through electrophysiological recordings and computational modeling. Metal bridges at the interface between the LBD dimers and state-dependent cross-linking using zinc identified the more compact of the two LBD arrangements as being populated by full-length receptors during gating in either a fully or partially active AMPA receptor. I was furthermore also able to obtain zinc-dependent oligomers in solution as determined by static laser scattering. This study thus provides insights into the complex movements and conformational rearrangements of the LBD as a tetramer upon receptor activation.

In order to investigate the importance of stargazin phosphorylation, I recombinantly expressed and purified the complete 120 residues long intracellular and unfolded C-terminal tail of stargazin. Differently tagged protein variants were expressed and purification was optimized, so that I was able to generate the complete and untagged stargazin C-terminal tail for the first time using it for biochemical, biophysical and structural characterization.

In doing so, I could show that the C-terminal tail of stargazin electrostatically binds to negatively charged liposomes. Using mass spectrometric and NMR-spectroscopic analyses I found that stargazin C-terminal tail quantitatively gets phosphorylated by Ca^{2+}/calmodulin-dependent kinase (CaMKII) and that phosphorylation abolishes binding to the lipid bilayer with one phosphorylated Ser residue being sufficient to reduce the ability of stargazin C-terminal tail to bind to liposomes by 50%. These results suggest that stargazin as a type I TARP could provide a molecular rheostat allowing for graded changes in synaptic strength.

ZUSAMMENFASSUNG

Die Kommunikation zwischen Neuronen erfolgt an Synapsen. Neurotransmitter die an presynaptischen Terminalen freigesetzt werden, agieren als Aktivatoren von liganden-gesteuerten Ionenkanälen an der postsynaptischen Membran über den synaptischen Spalt hinaus und induzieren eine Änderung des Membranpotentials oder aktivieren Signalkaskaden. A-Amino-3-hydroxy-5-methyl-4-isoxalzolpropansäure (AMPA) Rezeptoren sind die Hauptvermittler der schnellen exzitatorischen Neurotransmission im Gehirn, verursacht durch die Bildung von exzitatorischen postsynaptischen Strömen (EPSCs) und helfen somit, das elektrische Signal von einem bis zum nächsten Neuron weiterzuleiten. AMPARs sind weiterhin für die Bildung und den Ausbau von Synapsen in den frühen Phasen der Synaptogenese verantwortlich. Die Anzahl und Aktivität von AMPA Rezeptoren an der Postsynapse wird durch ihre Interaktion mit transmembranen AMPA Rezeptor regulatorischen Proteinen (TARPs) reguliert. Die modulatorischen Eigenschaften von Typ I TARPs/Stargazin auf den synaptischen AMPAR Transport wiederum werden durch Phosphorylierung reguliert.

Eine der Zielsetzungen dieser Dissertation war es zu verstehen, wie die schnelle Aktivierung des Rezeptors realisiert werden kann und zu verstehen, wie die Liganden-Bindung an die vier Ligandenbindungsdomänen (LBDs) des Rezeptors zu einer Öffnung des Ionenkanals führt, da strukturelle Informationen über einen aktiven Rezeptor begrenzt sind. Aktuelle cryo-EM und Kristallstrukturen, mit dem Ziel, den Rezeptor in einem aktiven Zustand darzustellen, hatten entweder keinen aufgelösten Ionenkanal oder die Pore war verschlossen.

Eine weitere Zielstellung war es, den zellulären Mechanismus zu verstehen, der die Funktion von AMPA Rezeptoren an der Synapse reguliert. AMPAR assoziieren mit TARPs an der Synapse, wo TARPs Aspekte der AMPAR Aktivierung, seines Transportes und seiner Pharmakologie regulieren. Es konnte gezeigt werden, dass der 120 Reste lange C-Terminus von Stargazin die Anhäufung von AMPA Rezeptoren an der Postsynapse in einer phopshorylierungs-abhängigen Weise reguliert. Es wurde gezeigt, dass neun Serin-Reste innerhalb der C-terminalen Domäne von Stargazin phosphoryliert werden und dass die Phosphorylierung die Bindung der Stargazin C-terminalen Domäne an die negative geladene Lipid-Doppelmembran verhindert, welche durch einen Abschnitt positiv geladener Arginin-Reste vermittelt wird. Durch Verwendung biochemischer, biophysikalischer und hochauflösender, struktureller Analysen in Echtzeit wollten wir atomare Informationen über die Phosphorylierung des C-terminalen Teils von Stargazin

bekommen und die Abhängigkeit der Lipid-Interaktion von der Phosphorylierung verstehen.

Durch rekombinante Expression, Aufreinigung und Kristallisation der isolierten Domäne (sLBD), die für die Bindung des Neurotransmitters verantwortlich ist, konnte ich eine hoch-aufgelöste Kristallstruktur der Glutamat-gebundenen sLBDs in zwei durch kristallografische Symmetrie erzeugte tetramere Anordnungen erhalten. Anschließend analysierten wir die tetrameren Anordnungen genauestens strukturell, biophysikalisch und funktionell mittels elektrophysiologischer Aufnahmen und molekularer Modellierung. Metallbrücken zwischen den LBD-Dimeren und Vernetzung in Abhängigkeit des funktionalen Zustandes des Rezeptors haben es uns ermöglicht, die kompaktere der beiden tetrameren LBD Anordnungen als einen Zustand zu identifizieren, der im Zuge der Rezeptor-Aktivierung auch im volle-Länge Rezeptor eingenommen wird, entweder von partiell oder von komplett Glutamat-gebundenen LBDs. Darüber hinaus konnten mittels statischer Lichtstreuung Zink-abhängige Oligomere in Lösung erhalten werden. Diese Studie gibt damit Einblicke in die komplexen LBD Bewegungen und konformationellen Änderungen als Tetramer bei Aktivierung des Rezeptors.

Um die Bedeutung der Phosphorylierung der C-terminalen Domäne von Stargazin zu untersuchen, habe ich den kompletten 120 Reste langen und ungefalteten C-Terminus von Stargazin rekombinant exprimiert und aufgereinigt. Unterschiedlich getaggte Proteinvarianten wurden exprimiert und ihre Aufreinigung wurde optimiert, sodass zum erstmals der komplette und ungetaggte C-Terminus von Stargazin generiert werden konnte, um ihn anschließend für biochemische, biophysikalische und strukturelle Charakterisierungen zu verwenden.

Ich konnte so zeigen, dass die C-terminale Domäne von Stargazin elektrostatisch an negativ geladene Liposomen bindet. Mittels massenspektrometrischer Untersuchungen und Kernspinresonanzspektroskopie (NMR) fand ich heraus, dass der C-Terminus von Stargazin quantitativ phosphoryliert wird von der Ca^{2+}/calmodulin-abhängigen Kinase (CaMKII) und dass die Phosphorylierung die Bindung von Stargazin an die Lipid Membran zerstört, wobei ein phosphorylierter Serin-Rest ausreicht um die Fähigkeit Stargazins, an Liposomen zu binden, um 50% zu reduzieren. Diese Ergebnisse lassen uns annehmen, dass Stargazin als Typ I TARP einen verstellbaren molekularen Widerstandsregler darstellt, der eine graduelle Änderung der synaptischen Stärke erlaubt.

1 INTRODUCTION

1.1.1 The glutamate receptor superfamily

The glutamate receptor superfamily comprises the family of ionotropic glutamate receptors (iGluRs), which act as ligand-gated ion channels activated by the neurotransmitter glutamate, and of metabotropic glutamate receptors (mGluRs), which are G-protein coupled receptors. In mammals, 18 genes encode for iGluRs. Ionotropic glutamate receptors in turn can be subclassified according to their sequence similarity and their pharmacological and electrophysiological characteristics into: α-amino-3-hydroxy-5-methyl-4-isoxazole propionic acid (AMPA), kainate (KA), N-methyl-D-aspartate (NMDA) receptors and the orphan subunits δ1 and δ2 which are involved in synaptogenesis [1]. The receptors of the glutamate superfamily are named according to their specific naturally occurring or synthetic ligands (Figure 1.1). The AMPA-type iGluR family consists of four subunits (GluA1-4), the kainate receptor family contains five different subunits (GluK1-5) and the NMDA receptor family is build up by GluN1, GluN2 (GluN2A-D) and GluN3 (GluN3A and GluN3B). Consistent nomenclature for iGluRs has only recently developed and AMPA receptors were initially named both GluRA-GluRD and GluR1-GluR4, respectively. The convention today is GluA1-GluA4 for AMPARs and GluK1-GluK5 for kainate receptors [2]. Whereas AMPA and kainate receptors are pure ligand-gated channels, NMDA receptors are coincidence detectors because they require depolarization of the membrane potential in order to relieve voltage-dependent magnesium block [3, 4] as well as binding of both glutamate and glycine for activation of the receptor [5].

The first expression cloning of a glutamate receptor (GluK1) was reported in 1989 [6].

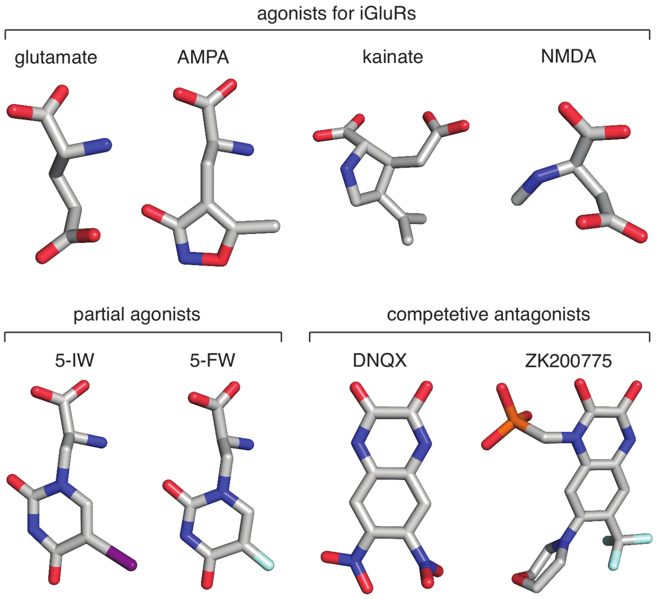

Figure 1.1: Chemical structure of glutamate receptor ligands. Stick representation of iGluR agonists (top row), partial agonists and antagonists (bottom row) that are mentioned in this thesis. AMPA and NMDA (top row) are synthetic agonists, whereas glutamate and kainate are naturally occurring neurotransmitter and agonists. Atoms are colored according to their element. AMPA - α-amino-3-hydroxy-5-methyl-4-isoxazole propionic acid, NMDA - N-methyl-D-aspartate, 5-IW – 5-iodowillardiine, 5-FW – 5-fluorowillardiine, DNQX - 6,7-dinitroquinoxaline-2,3(1H,4H)dione, ZK200775/MPQX –[[3,4-Dihydro-7-(4-morpholinyl)-2,3-dioxo-6-(trifluoromethyl)-1(2H)quinoxalinyl]-methyl] - phosphonic acid.

1.1.2 Modular structure and function of the AMPAR subfamily

1.1.2.1 Architecture, symmetry and function of iGluRs

Ionotropic glutamate receptors have a size of approximately 900 amino acids (with NMDARs being even bigger) and share a common modular domain architecture comprised of four domains: an amino-terminal domain (ATD), which is responsible for subunit assembly, a ligand-binding domain (LBD) responsible for binding of the ligand, a transmembrane domain (TMD) and a C-terminal domain (CTD) (Figure 1.2). The extracellular ATD and LBD domains account for 85% of the total receptor mass.

The ATDs of AMPARs are not necessary for receptor activation because constructs lacking the ATDs are still functional [7-9]. In AMPA-type iGluRs, the extracellular amino-terminal domain is important for protein interactions [10, 11], receptor trafficking, as well as subtype-specific assembly [12-15] and intersubunit interactions [10, 16]. In contrast, NMDAR amino-terminal domains also contribute to allosteric modulation of the receptor [17, 18], explained by the tighter connection and linkage of the NMDA ATDs to the LBDs, which is much less compact in AMPARs [19]. Accordingly, in NMDARs, the

ATDs control the open probability [20, 21] and speed of deactivation, and by binding to allosteric modulators, ion channel activity is regulated [17].

The iGluR LBD is formed by the discontinuous segments S1 and S2, which are separated by the transmembrane segments of the receptor. In the AMPAR tetramer, the LBDs form dimers in a back-to-back fashion. The LBD has a total size of ~260 amino acids. The 150 residue long S1 segment precedes the first transmembrane domain of iGluRs and the S2 segment is located between the third and the fourth transmembrane domain (Figure 1.3). The LBD is responsible for binding of the ligand and the conformational changes induced by LBD clamshell closure are transmitted to the TMD, which is thought to drive channel opening. The TMD consists of four transmembrane helices (M1-M4), with M2 acting as the central-pore like helix. The pre-M1 helix is oriented almost parallel to the membrane plane (Figure 1.3) and may serve as a docking site for non-competitive inhibitors [22] and allosteric modulators [23]. Within the transmembrane segment, the Q/R editing site is located, which determines Ca^{2+} permeability of the channel. Together, the transmembrane helices contribute to the iGluR tetrameric stability [24]. The pore of AMPARs can be blocked by intracellular polyamines including spermine and spermidine [25-27].

The CTD has been shown to be involved in AMPAR trafficking and anchoring of receptors at synapses [28-33], although deletion of the CTD still results in functional and tetrameric receptors with intact synaptic localization [34-36]. The candidate scaffolding proteins include postsynaptic density-95 (PSD-95)/disc large/zona occludens-2 (PDZ)-containing scaffolding proteins like glutamate receptor interacting protein/AMPAR binding protein (GRIP/ABP), protein interaction with C-kinase (PICK-1) and synapse-associated protein of 97 kDa (SAP-97). The C-terminal domain further interacts with cytoskeleton-interaction proteins like α-actin and spectrin and is also a substrate for protein kinases such as protein kinase A and C (PKA and PKC) and calcium-calmodulin kinase II (CaMKII) and the tyrosine kinases fyn and src [37, 38].

The extracellular ATD and LBD domains are organized as dimers-of dimers in all iGluRs. For non-NMDAR iGluRs, the interface between ATDs and LBDs is small compared to NMDAR-type iGluRs (1470 Å^2 compared to 3107 Å^2 in NMDARs) [39]. Accordingly, there is no cooperativity within the extracellular ATDs and LBDs in non-NMDARs [40, 41], whereas functional and structural data revealed allosteric coupling between the ATDs and the LBDs in NMDARs [39, 42].

A GluA2 tetramer was first proposed based on single channel recordings and the observed subconductance states [43]. Although AMPA and kainate receptors can form both homo- and heterotetramers, the majority of native AMPA and kainate receptors are heterotetramers with most of AMPARs containing GluA2 to form either GluA1/GluA2 or

GluA2/GluA3 complexes [44]. The presence of GluA2 renders the ion channel impermeable to Ca^{2+}, lowers the receptors conductance and alters its voltage dependence [28, 44-47]. Calcium-permeable GluA1/GluA4 receptors were found in Bergman glia of the cerebellum [48]. Kainate receptors can form homo- and heteromeric receptors for tetramers containing GluK1-3, however, GluK4-5 are obligate heteromers that require GluK1-3 to form functional channels [49, 50].

Surprising key features of the tetrameric glutamate receptor arrangement were unraveled with the first homomeric antagonist-bound full-length (fl) structure of the GluA2 receptor. First, a subunit swap can be observed between the extracellular ATDs and LBDs. A subunit cross-over occurs as the ATD transitions to the LBD, meaning that the extracellular domains dimerize with alternating partners in the ATD and LBD layer (Figure 1.2). In the ATD layer, subunits A and B and subunits C and D form dimers, whereas in the LBD, dimers are formed by subunits A and D and B and C, which causes a domain swapping (Figure 1.2 E). The subunit cross-over might be important to stabilize the Y-shaped non-desensitized receptor because disruption of the local dimers in the ATD and LBD layer might reduce the additional stabilization by other intersubunit contacts. Accordingly, it seems to be the domain swapping between the ATD and the LBD that is responsible for the slightly faster recovery from desensitization when the ATD is deleted [51].

Second, the extracellular domains exhibit two-fold rotational symmetry, whereas the transmembrane domain exhibits quasi four-fold symmetry, causing a symmetry mismatch between the ion channel pore and the extracellular domains (B-D). In total, the receptor resembles the letter “Y” (Figure 1.2). The domain architecture common for all iGluRs is shown in Figure 1.2.

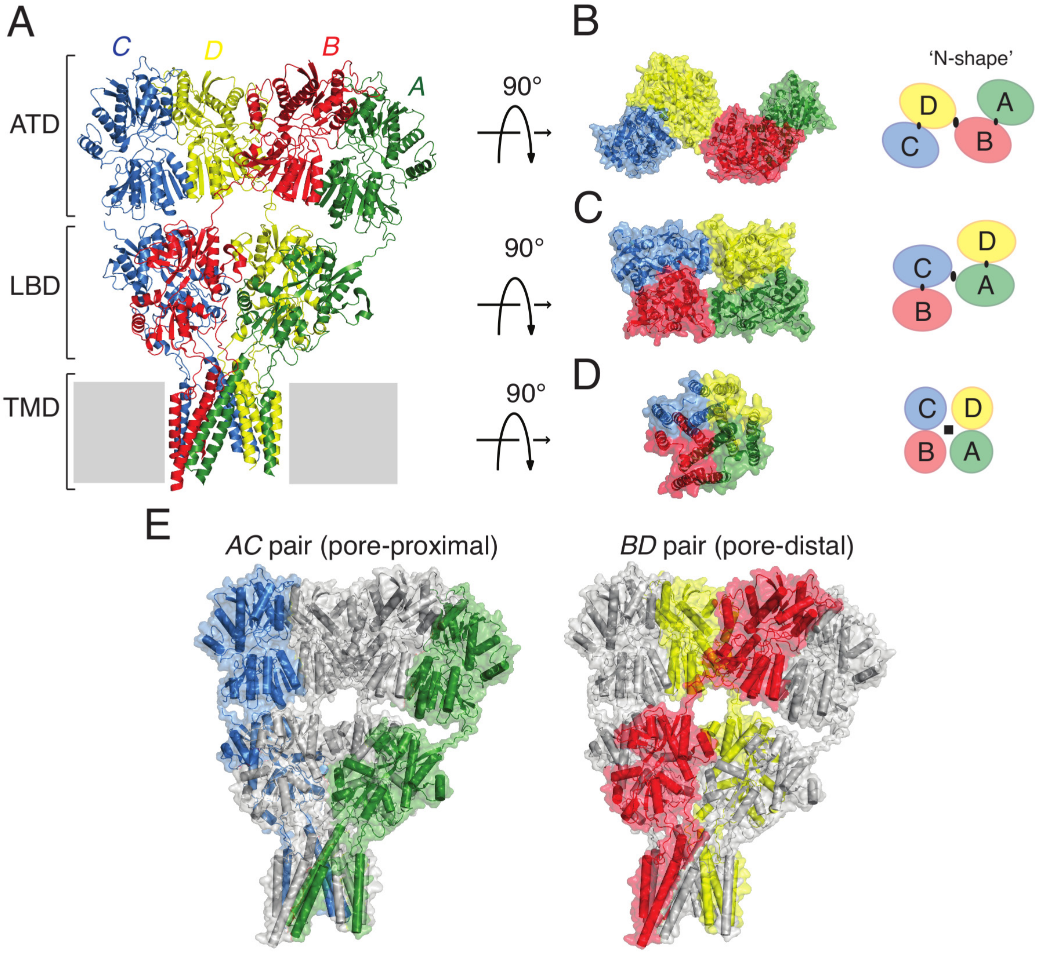

Figure 1.2: Domain architecture of the homomeric AMPA receptor GluA2 in the apo state as determined by X-ray crystallography. (A) Modular domain architecture of GluA2 tetramer [protein database identifier (PDB ID): 4U2P] consisting of an amino-terminal domain (ATD), a ligand-binding domain (LBD) and a transmembrane domain (TMD). **(B-D)** Domain layers of the receptor viewed from the top in surface representation (left panel) and schematic cartoon representation (right panel), with the same coloring as in (A). **(B)** ATD layer viewed from the top, adopting an "N shape", which is different from the "O shape" seen in GluA2/A3 NTDs as revealed from a recent heteromeric full-length, apo cryo-EM structure [19]. **(C)** LBD layer viewed from the top with domain swapping between the extracellular ATDs and LBDs. The overall two-fold axis is shown as large black ovals and the local intradimer two-fold axes of symmetry are shown as smaller black ovals. **(D)** Transmembrane domain layer with a quasi four-fold symmetry indicated by a black square. The C-terminal domain is not present in this crystal structure. **(E)** Surface representation of the ligand-free GluA2 full-length receptor showing domain swapping in the extracellular ATD and LBD. The left panel shows the pore-proximal subunits A and C, whereas the right panel shows the pore-distal subunits B and D. The extracellular domains form alternative dimer pairs at the level of the ATD and LBD (subunit crossover).

1.1.2.2 Physiological relevance of iGluRs

Glutamate is the major excitatory neurotransmitter in the mammalian central nervous system and it exerts its fast effects via ionotropic glutamate receptors [52-55]. Glutamate as a chemical neurotransmitter is released from presynaptic terminals via presynaptic vesicles and diffuses across the synaptic cleft to bind to and activate ionotropic glutamate receptors located on the postsynaptic cell. Ligand binding and clamshell closure leads to opening of the glutamate receptor ion channel pore and to transmission of the information from one neuron to another. While AMPA receptors are found mainly at postsynaptic sites, kainate receptors have regulated expression at both, pre- and postsynaptic sites [56]. NMDA receptors are coincidence receptors that open their ion channel upon membrane depolarization [3, 4], leading to Ca^{2+} influx [57]. Calcium influx itself triggers a cascade of signal transduction events that are important for synaptic plasticity [58]. The AMPA receptor density at active zones is thought to contribute to activity-dependent processes such as long-term potentiation (LTP) and long-term depression (LTD) important for learning and memory formation [32, 59]. Accordingly, blockade of NMDA receptors interferes with memory formation [60]. NMDAR encephalitis is caused by autoimmune responses to NMDA receptors and NMDAR disruption on neuronal cell surfaces [61].

Dysfunction or dysregulation of these receptors results in a number of other neurological disorders, including dementia, mood disorders, schizophrenia, depression, epilepsy and Alzheimer's disease [56, 62-68].

1.1.2.3 iGluR diversity by posttranscriptional, posttranslational control and interaction with auxiliary proteins

Further diversity of the glutamate receptor repertoire is achieved by posttranscriptional modifications such as ribonucleic acid (RNA) editing and splicing as well as posttranslational modifications such as phosphorylation and palmitoylation, leading to receptors with distinct kinetics [28]. Importantly, the functional characteristics of iGluRs are further diversified through their ability to co-assemble with auxiliary subunits.

Posttranscriptional modifications of AMPARs include splicing and RNA editing [69]. All four AMPAR subunits exist in two alternatively splice isoforms, called flip and flop. The flip/flop region is located in the LBD of the receptor and is encoded by exons 14 and 15 [70]. A single amino acid substitution in the alternatively spliced flip/flop isoform controls sensitivity of the receptor to the positive allosteric modulator cyclothiazide (CTZ) [71, 72], as well as to other allosteric modulators [71, 73, 74] and controls desensitization and deactivation [72, 75-77]. The flop isoform desensitizes much more rapidly compared to the flip isoform.

In the framework of this thesis, the flop GluA2 soluble LBD (sLBD) construct was used for structural and biophysical examination [78].

In addition to splicing, the receptor is subject to RNA-editing, with 99% of native GluA2 receptors being RNA-edited, a process involving deamination of ribonucleotides in prespliced messenger RNA (mRNA), which results in an exchange from a glutamine residue (Gln, Q) into an arginine (Arg, R) in the pore region (called Q/R site, Q607R) (also see Figure 1.3) [79, 80]. The Q/R editing affects Ca^{2+} permeability of the receptor, release from the endoplasmatic reticulum (ER) and sensitivity to voltage-dependent channel block by polyamines and Mg^{2+} [28, 44, 81].

Posttranslationally, AMPARs get phosphorylated at various residues within their intracellular C-terminus and phosphorylation at Ser821 has been shown to increase AMPAR conductance [82-84]. While AMPAR phosphorylation has been proposed to be important for the regulation of synaptic plasticity for a long time, a recent study disconfirmed the importance of AMPAR phosphorylation at these sites for regulation of AMPAR trafficking and activity. By using a more quantitative approach called Phos-tag SDS-PAGE, they showed that two major AMPAR sites implicated in regulation of synaptic plasticity, Ser831 and Ser845 are phosphorylated less than 1% and 0.1% in GluA1, respectively [85], suggesting that the functional implications of AMPAR CTD phosphorylation for synaptic plasticity must be re-evaluated.

Besides phosphorylation, the receptor gets posttranslationally modified through glycosylation when the receptor is transported through the Golgi network [30, 86].

The gating properties and kinetics of AMPARs can be further fine-tuned through their interaction with auxiliary proteins, including the transmembrane AMPA receptor regulatory proteins (TARPs) [87-90], the cornichon homologs (CNIH-2 and -3) [91], cystine-knot AMPAR modulating protein (CKAMP44) [92], GSG1L [93] and synapse differentially induced gene 1 (SynDIG1) [94].

The function of auxiliary proteins, especially of TARPs, will be discussed below (see Section 1.2.4).

1.1.3 The structure of ionotropic glutamate receptors

1.1.3.1 Isolated domains of iGluRs

Once the first glutamate receptor subunit was cloned [6], structural data along with biochemical and functional data paved the way for a better understanding of the receptor's structure function relationship.

The striking similarity of the extracellular domains of iGluRs with bacterial periplasmatic proteins such as lysine, arginine, ornithine-binding protein (LAOBP) in terms of the bi-lobed structure has been described in several publications and for both, binding of a ligand leads to closure of the two lobes [95-101]. A high-resolution structure of the periplasmatic binding protein was published in 1993 [97] and having discovered the similarity between the two proteins, by swapping portions of iGluR receptors (GluA3 and GluK2), Stern-Bach et al. found that two discontinuous segments are responsible for the receptor pharmacology, and the same was found for NMDARs at that time [102, 103].

This was the starting point for generation of sLBDs for functional and structural experiments. A water-soluble construct (termed HS1S2) containing the two extracellular segments S1 and S2, fused by a 13 amino acid (aa) long linker, was able to reproduce the ligand-binding properties of an intact receptor as revealed by [^{3}H]-AMPA binding [104-106]. Further optimization of the temperature- and protease-sensitive construct together with limited proteolysis to reveal the domain boundaries of the LBD led to generation of the HS1S2I LBD construct, that proved to be thermally stable and protected from trypsin or chymotrypsin treatment after ligand binding [107].

Purification and crystallization of the S1S2I construct resulted in the first crystal structure of GluA2 LBDs complexed with kainate, published in 1998 [108].

The S1S2I structure was further optimized and yielded the readily crystallizable S1S2J construct of the GluA2 flop LBD, harboring a shorter dipeptide linker (Gly-Thr), a trypsin site four amino acids upstream of the first resolved residue in the kainate-bound sLBD structure and deletion of the last amino acid in S1 (Pro507). The resulting S1S2J construct of the GluA2 sLBD is still used today for biochemical, biophysical and structural experiments (Figure 1.3) [78].

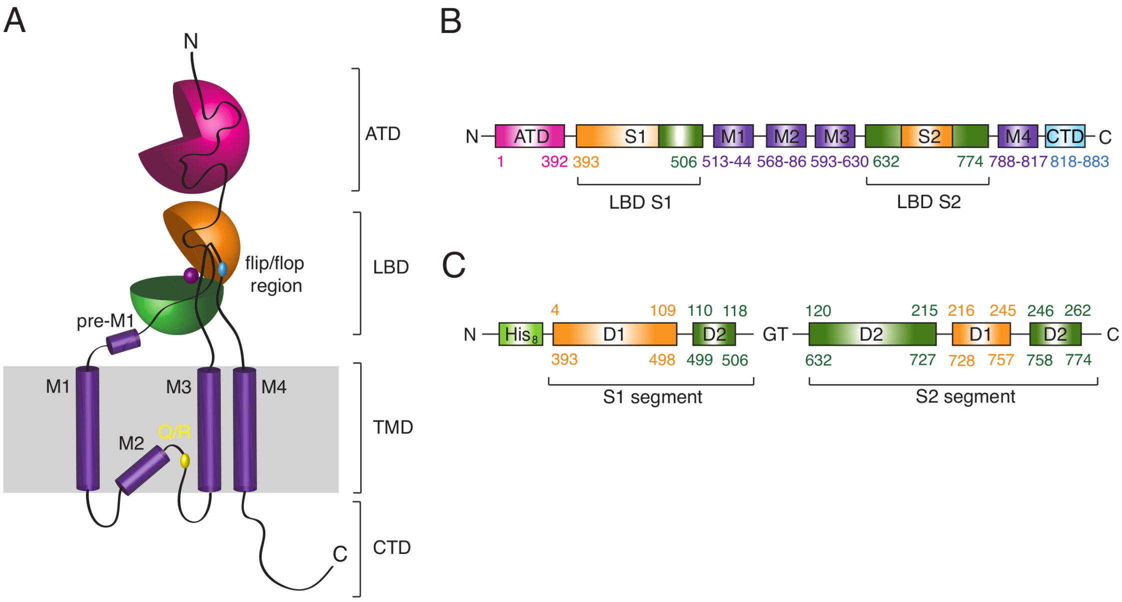

Figure 1.3: Schematic representation of the iGluR subunit topology and design of a crystallizable S1S2J construct [78]. **(A)** Cartoon representation of one glutamate receptor subunit consisting of: an extracellular ATD (shown in pink), an extracellular LBD, which is composed of an upper lobe D1 (orange) and a lower lobe D2 (green), respectively, the transmembrane domain which consists of four transmembrane helices (purple cylinders) and a C-terminal domain. The lipid bilayer is indicated in grey. Glutamate bound to the clamshell-like ligand-binding domain is shown as a magenta sphere. The flip/flop region of the receptor and the Q/R editing site are indicated with a blue and yellow oval, respectively. The domain layers are indicated on the right side. **(B)** Linear domain architecture of the full-length GluA2 structure with residue numbers of domain boundaries given below. Coloring as in (A). Segments S1 and S2 both contain parts of the upper D1 and lower D2 lobes of the LBD. **(C)** Construct design for purification and crystallization of GluA2 sLBDs that was also used in this thesis [78]. The two discontinuous segments S1 and S2 are fused together by a dipeptide linker (Gly-Thr). The construct was designed as an octahistidine (His_8) tag followed by a thrombin/trypsin cleavage site for tag removal.

Five years after the first structure of the isolated GluA2 LBD complexed with kainate, the first structure of an isolated kainate receptor domain, the GluK1 and GluK2 sLBD was published [109, 110]. To date, more than 80 high-resolution structures of kainate receptor extracellular domains and more than 120 structures of AMPAR LBDs are deposited in the Protein Data Base (PDB) with a range of different ligands, mutations and modulatory ions [15, 111-113]. Whereas sLBDs for all low-affinity kainate receptors (GluK1-3) have been crystallized, no crystal structure for the sLBDs of high-affinity kainate receptors (GluK4-5) is available to date [56].

High-resolution structures of sATDs and sLBDs of ionotropic glutamate receptors gave important insights into the dimer-dimer arrangement and important LBD contact sites, some of them were evaluated using cysteine cross-linking [41, 114-116] or histidine bridging using zinc, and made it possible to gain information on iGluR gating by comparing different partial agonist-, agonist- and antagonist-bound structures.

1.1.3.1.1 *Full-length AMPAR structures*

The first hints on the overall quaternary structure came with single-particle electron microscopy (EM) analyses at low resolution (20-40 Å) and revealed the first important structural features of iGluRs such as the internal 2-fold symmetry [117-122].

The first full-length crystal structure of an iGluR receptor was the structure of the homomeric and antagonist-bound AMPA receptor GluA2, published in 2009 [41]. The structure gave the first insights into receptor assembly as a tetramer and specific features of the receptor such as domain swapping within the extracellular domains and symmetry mismatch between the extracellular domains and the ion channel pore from two-fold symmetry into quasi four-fold symmetry [41]. From then on, a set of full-length AMPA receptor cryo-EM and crystal structures in the apo, partial agonist-bound, pre-open, desensitized and antagonist-bound states were published [40, 41, 123-126]. In all of the above-mentioned structures, the ion channel pore was either not resolved or closed.

A cryo-EM study of the GluA2 homotetramer in complex with the allosteric modulator LY451646, which blocks desensitization, suggested a novel corkscrew motion of the LBD resulting from an anticlockwise rotation of the LBDs when viewed from above combined with a D2-D2 lobe separation, and a contraction of the ATD-LBD layer by 7 Å upon receptor activation, however, the ion channel pore was not resolved in this 12 Å structure [40]. In the same study, the structure of a desensitized GluA2 receptor in complex with quisqualate [127] was described, which revealed interesting features such as variable ATD dimer separation for the different class averages and disruption of the LBD layer into four fold symmetric LBD subunits [40].

Along with the recent publication of the first cryo-EM structure of an full-length AMPA receptor GluA2/A3 heteromer, striking differences between the homomeric and heteromeric AMPA receptor assembly were revealed [19]. First, the heteromeric GluA2/A3 ATD layer assembles in a conformation different from homomeric GluA2 ATDs, which was termed "O shaped". According to their data, the ATD can transition between both, the "N-shaped" and the "O-shaped" ATD. Furthermore, the LBD layer is rotated by 30° compared to the GluA2 LBD layer (Figure 1.4 B) and the whole extracellular part of the receptor is vertically compressed by approximately 20 Å compared to GluA2 homomers, largely due to the more compact ATD/LBD layer, which is reminiscent of NMDARs. Due to the more compact arrangement of the extracellular domains, the receptor does not adopt the typical “Y“ shape.

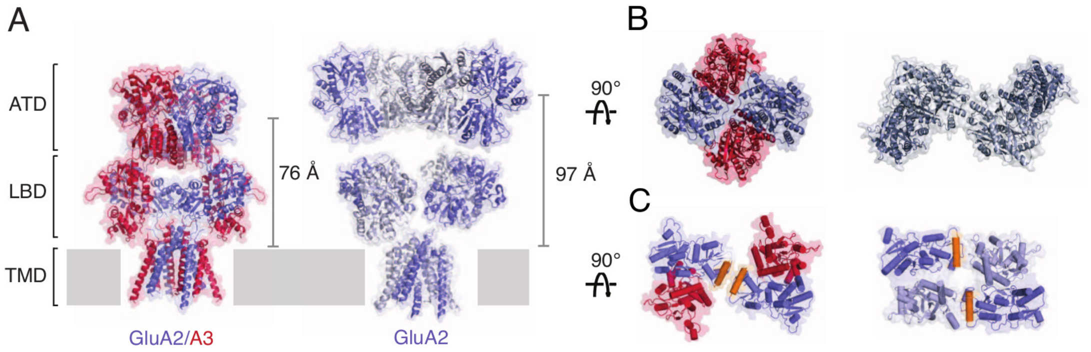

Figure 1.4: The heteromeric GluA2/A3 cryo-EM structure reveals a novel domain architecture. **(A)** Cartoon representation of the GluA2/A3 heteromer in the apo sate, representative of the resting state (PDB ID: 5IDE [40], left panel) and the agonist-bound, homomeric GluA2 cryo-EM structure (PDB ID: 4U2Q, right panel) viewed parallel to the membrane and perpendicular to the overall two-fold symmetry of the receptor. The distance between the center of mass of the ATD and Thr625 as a metric to determine vertical compression of the ATD-LBD layer was measured and is indicated by vertical bars. Individual layers of the AMPA receptors are indicated on the left. The lipid bilayer is depicted as grey bar. **(B)** Top view of the ATD layer for the GluA2/A3 (left panel) and the homomeric GluA2 (right panel) structures showing the different arrangements of the extracellular ATDs, which adopt an “O shape” in the heteromer, whereas they adopts an “N shape” in the homomer. **(C)** Top view of the LBD layer for the GluA2/A3 (left panel) and the GluA2 homomer (right panel) showing translation of the LBD canonical dimer relative to each other in the heteromer. Helix G is colored orange to emphasize the differences. Figure modified from [19].

1.1.3.1.2 *Full-length KAR structures*

Although, to date there is no crystal structure of a full-length kainate receptor, a cryo-EM full-length structure of the kainate receptor GluK2 could be obtained in the resting, antagonist-bound and in the desensitized state at 20 Å resolution [126]. The antagonist-bound GluK2 structure revealed a domain arrangement similar to the antagonist-bound homomeric GluA2 structure [41]. A more recent cryo-EM structure could be obtained from the GluK2 receptor in complex with the agonist *2S,4R*-4-methylglutamate [110] and revealed a desensitized state of the receptor characterized by a heterogenic ATD layer with different separations of ATD dimers and a transition of the LBD layer from two-fold into four-fold symmetry [40].

1.1.3.1.3 *Full-length NMDAR structures*

Several NMDAR full-length structures were published in the last years, in complex with either the allosteric inhibitor ifenprodil or Ro25-6981, partial agonists and ion channel blocker [39, 42, 128] and only in one study without any allosteric modulator [129], however, all structures revealed a closed blocked ion channel. The cryo-EM structure solved by Tajima and colleagues provide information about structural transitions from the allosterically inhibited state to the active state, although the TMD region was not resolved in their structure [129].

The first NMDA crystal structures including the membrane domain were published in 2014 [39, 42]. In the first publication, the GluN1-GluN2B heteromer was crystallized in complex with the GluN1 and GluN2B agonists glycine and L-glutamate, respectively, and the allosteric inhibitor ifenprodil that binds to the GluN2B ATD (at 4 Å resolution) [39]. The second publication reported a crystal structure of the GluN1-GluN2B heteromer in complex with the GluN2B-specific allosteric inhibitor Ro-25-6981 and the GluN2B partial agonists 1-aminocyclopropane-1-carboxylic acid (ACPC) or *trans*-1-aminocyclobutane-1,3-dicarboxylic acid (t-ACBD) and the ion channel blocker MK-801 at resolutions of 3.7 and 3.9 Å, respectively [42]. The domain architecture is comparable to AMPARs, with the overall two-fold symmetry, the layered dimer-of-dimer arrangement of the extracellular domains, the symmetry mismatch between the extracellular domains as well as the domain swapping between the ATDs and the LBDs (Figure 1.5 A-C). Key differences between non-NMDA and NMDA iGluRs concern the extracellular domains. First, the receptor's overall structure does not resemble the Y-shape of non-NMDA receptors, but rather exhibits a mushroom shape, which results from the compact packing of the extracellular domains. As a consequence, in NMDARs, the ATDs and LBDs interact much more closely with each other compared to AMPARs. This feature probably relates to the allosteric cooperation of the NMDAR ATDs and LBDs, which has been evaluated functionally and now also structurally [130-132]. In contrast, in AMPARs, there is little cooperativity between the ATDs and the LBDs. Third, the LBD layer is oriented differently in NMDARs and involves a horizontal 35° rotation compared to AMPAR LBDs that is perpendicular to the two-fold symmetry axis (Figure 1.5 C).

Recently, cryo-EM studies of the GluN1/GluN2B receptor showed the NMDAR arrangement in different states and in complex with competitive antagonists (DCKA and D-APV) [128], with agonists (glycine and L-glutamate) [128] and in complex with both agonists and the inhibitory allosteric modulator Ro25-6981 [128]. These studies revealed surprising conformational changes of the NMDAR in the antagonist-bound state that are characterized by a rupture of the LBD dimer-dimer gating ring because of a rotation of the GluN2B LBD by 110° [128], resulting in transition from two-fold into pseudo four-fold symmetry of the LBD layer accompanied by a separation of the D1-D1 LBD interface, similar to the desensitized state of non-NMDA iGluRs [40, 125, 126]. The ion channel in the heterogenic agonist-bound cryo-EM structure however, was closed. The latest NMDA GluN1/GluN2B cryo-EM structure that aimed to capture an active ion channel in presence of glycine and L-glutamate showed an active-like ATD and LBD conformation with an intact D1-D1 interface, however, the ion channel domain is not resolved in this structure [129].

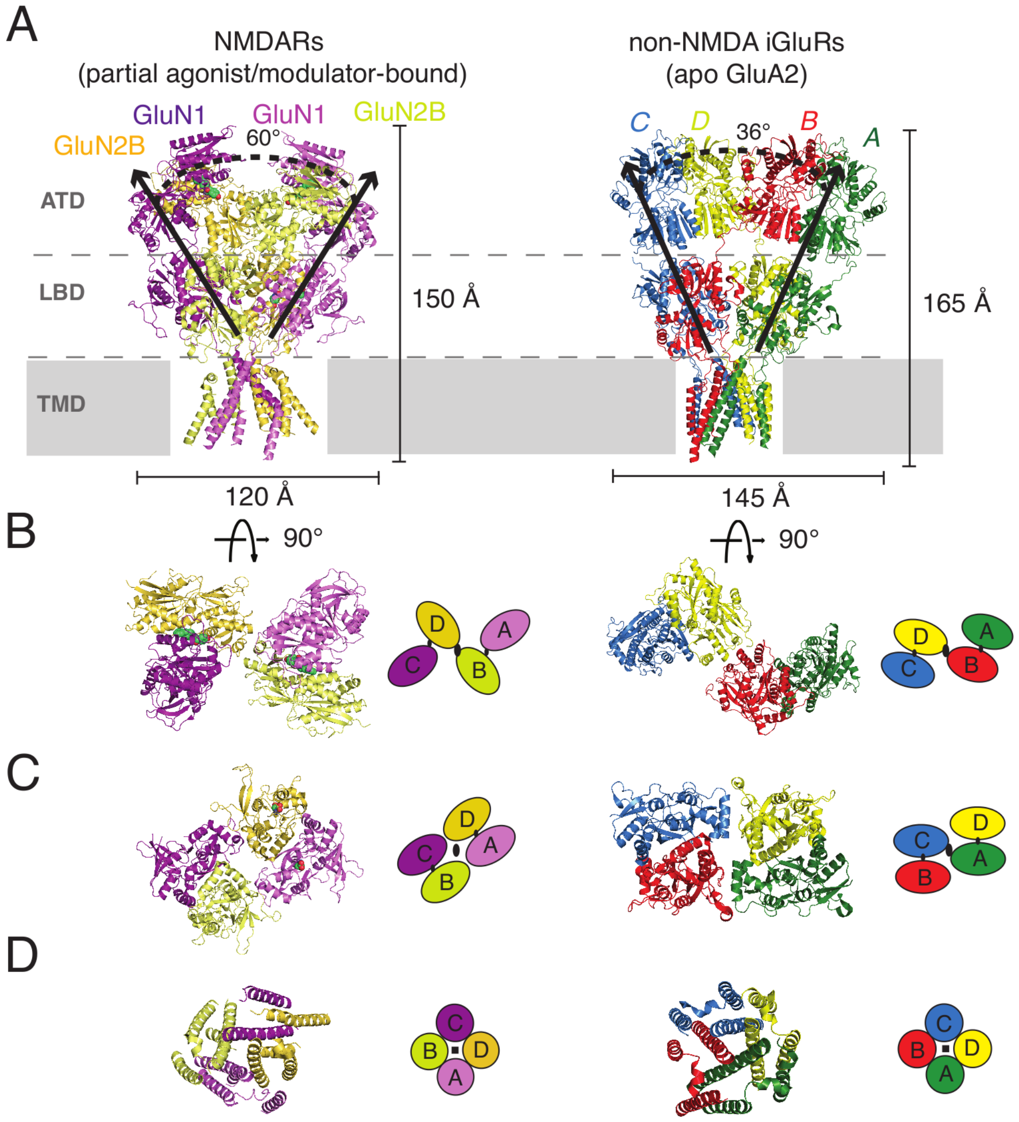

Figure 1.5: **Architecture, symmetry and domain organization of the GluN1-GluN2B NMDAR compared to non-NMDARs. (A-D)** Structural comparison between heteromeric NMDARs in complex with the partial agonists ACPC /t-ACBD, the allosteric inhibitor Ro25-6981 and the ion channel blocker MK-801 (PDB ID: 4TLL, left panel) and non-NMDAR iGluRs represented by the homomeric GluA2 receptor in the apo state (PDB ID: 4U2P, right panel) **(Figure 1.5 continued on next page)**

Figure 1.5 (continued from previous page): (A) Main differences in the overall structure between NMDARs and non-NMDA iGluRs are the vertical dimensions of the receptor and the overall shape. The horizontal and vertical dimensions of the receptor are indicated with black lines. Whereas non-NMDARs adopt the typical Y-shape, NMDARs rather resemble a mushroom because of the more compact packing of the ATDs against the LBDs. Furthermore, the LBDs are angled further off the overall two-fold axis of receptor symmetry (indicated by black arrows) in NMDARs compared to AMPARs (60° for NMDARs and 36° for AMPARs). The different layers of the receptor (amino-terminal domain –ATD, ligand-binding domain – LBD and transmembrane domain – TMD) are indicated with a grey dashed line. Subunits in the GluN1-GluN2B NMDA heteromer are colored in light/dark purple and light/dark yellow, respectively, whereas subunits in the GluA2 homomeric structure are colored as follows: A – green, B – red, C – blue, D – green. The partial agonists and the allosteric modulator are depicted as light green spheres in (A). **(B)** Top view of the ATD layer showing the arrangement of the four subunits within the LBD. Whereas the ATDs in AMPARs are arranged in "N-shape" (or "O-shape" as reported for GluA2/A3 heteromers [19]), the ATDs in the NMDAR adopt a completely different arrangement mainly affecting subunits A and C. **(C)** Top view of the LBD layer showing how NMDAR LBDs assemble in the tetramer compared to AMPAR LBDs. The NMDAR LBD exhibits a slightly different arrangement of LBD dimers relative to each other characterized by a lateral translation of the LBD dimers along the interdimer interface. The complete LBD layer is also rotated by 30° compared to the AMPAR LBD layer. **(D)** Top view of the TMD forming the ion channel pore. Both ion channel pores are similar and for both structures, the channel is closed.

1.1.4 Gating of glutamate receptors and domain movements

For iGluRs, at least three gating steps can be discriminated: active, desensitized and deactivated state. Although the same principles of receptor activation hold true for AMPA, kainate and NMDA receptors, they display very distinct kinetic profiles. AMPA and kainate receptors display fast gating kinetics, ranging in the millisecond (ms) timescale, whereas NMDARs have slower gating kinetics, with activation occurring in the 10 ms timescale [133] and deactivation in 10-1000 ms timescale [28, 134].

Accordingly, functional measurements provide most of the information about iGluR gating conformations as well as the transitions between them [135-137]. Structural data however is limited.

Ligand binding to the bi-lobed clamshell of glutamate receptors leads to clamshell closure by upward movement of the lower D2 lobes towards the D1 lobe of the LBD. Ligand binding and domain closure are supposed to occur in at least three steps [138, 139]: First, the ligand binds to the upper D1 lobe via hydrogen bonding interactions. Second, binding of the ligand induces clamshell closure with the lower D2 lobe moving upwards. The ligand can now interact with the lower D2 lobe of the LBD. And third, the cleft closed conformation of the LBD is stabilized by interlobe hydrogen interactions. While the first step is independent of the agonist, the second step seems to be largely dependent on the quality of the agonist with AMPA as full agonist being involved in stronger hydrogen bonding interactions than kainate [140, 141].

The degree of domain closure of the LBDs is different for the variety of iGluR ligands and has been calculated using DynDom [142] or a two-dimensional order parameter ($\xi1$ and $\xi2$) [143] (Figure 1.6 A and C). The degree of domain closure depends on the chemical nature of the ligand, while for the most ligands the efficacy (as measured by the current evoked by that ligand) increases with progressing degree of domain closure (Figure 1.6 C, upper panel). Glutamate as a full agonist induces the highest degree of domain closure (20°).

As the D2 lobes of the back-to-back dimers move upwards upon agonist binding, they presumably exert tension on the linker connecting them to the transmembrane domains, as measured by the dimer distance of Pro632, which is a marker atom of the S2-M3 linker. (Figure 1.6 B and Figure 1.7 A). Thus, the D2 domains convert the motion of clamshell closure into translational and rotational movements of the M3 helix and by being pulled outwards the ion channel opens (Figure 1.7 A). The M3 helix therefore has a crucial role for channel gating.

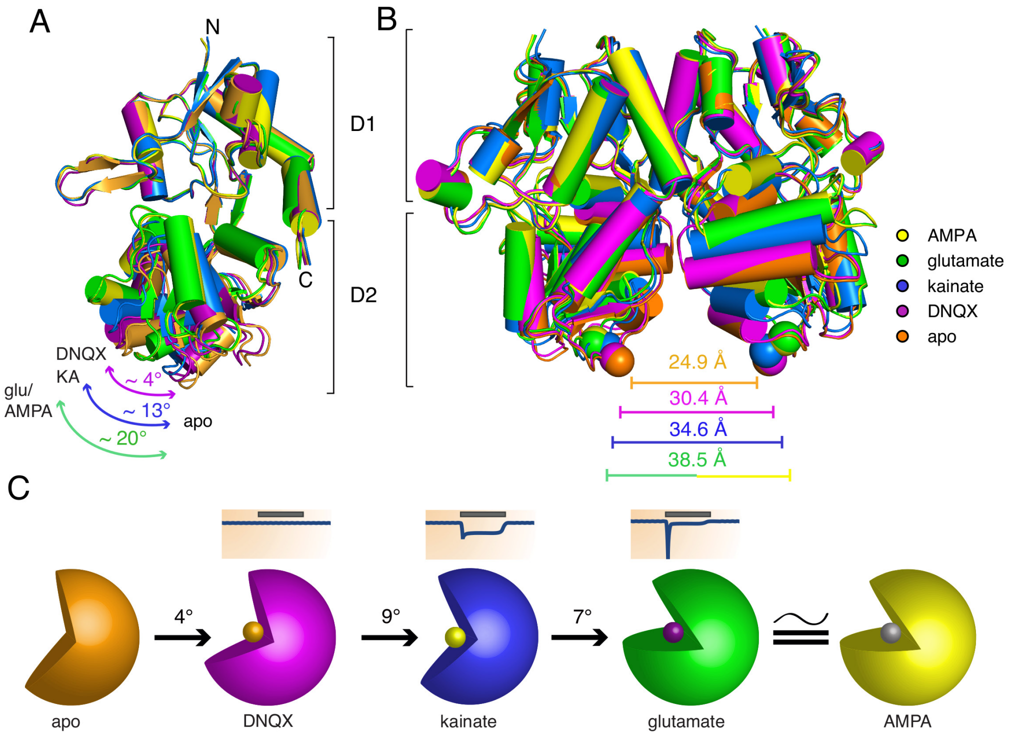

Figure 1.6: Ligands that bind within the bi-lobed ligand-binding domain of the glutamate receptor induce domain closure of the isolated domains to variable extents. (A) Superposition of sLBD monomers was performed using PyMol and the Cα atoms of the upper D1 lobe of the LBDs. The arrows below the superposed structures indicate the different extents of LBD domain closure, which is 4° for transition from the apo state (PDB ID: 1FTO) into the DNQX-bound state (PDB ID: 1FTL), 13° for transition from the apo into the kainate (KA)-bound LBD (PDB ID: 1FTK) and 20° for transition from the apo state into both the glutamate (glu)- (PDB ID: 1FTJ) and AMPA-bound (PDB ID: 1FTM) LBDs [78]. Degrees of domain closures were calculated using DynDom [142]. The color code of for sLBD structures is indicated: apo LBD – orange, DNQX-bound LBD – magenta, kainate-bound LBD – blue, glu-bound LBD – green, AMPA-bound LBD – yellow. **(B)** Cartoon representation of superposed GluA2 dimers either present in the asymmetric unit (a.u.) or generated by crystal symmetry showing how the lower D2 lobes separate with increasing agonist-driven domain closure. The dimer distance between Pro632 C-alpha (Cα) atoms was measured and is indicated below the structural superposition. Superposition was done in PyMol using the Cα atoms of the upper lobes D1 and the same PDB IDs as in (A), except for the kainate-bound sLBD structure, for which PDB ID 1FW0 was used. **(C)** Schematic cartoon showing the clamshell-like structure of the LBD with increasing domain closure, characterized by an upward movement of the lower D2 lobe of the LBD which is thought to drive opening of the pore. Ligands are shown as spheres with the following color code: DNQX – orange, kainate – yellow, glutamate – purple, AMPA – grey. Increasing domain closure is indicated in ° above the arrows. The upper panel in (C) shows schematic current traces (modified from [144]) elicited by the corresponding agonist.

However, the idea of the degree of receptor activation being dependent on the degree of domain closure was contradicted by some functional and structural data. While one ligand can produce different degrees of clamshell closure [145, 146], consistent with molecular dynamics simulations that agonist-bound LBDs can sample different conformations [143], for other ligands that have different functional effects and different affinities, an identical degree of domain closure has been reported [145, 147-152]. Thus, activation seems to be more complicated and complex than being solely explainable by domain closure [153, 154].

A key difference between activation of non-NMDA iGluRs versus NMDA receptors concerns the subunit contribution. While activation of non-NMDA iGluRs is characterized by several subconductance states and presumably independent contribution of subunits [43, 145, 152, 155-157], NMDARs and also Cys-loop receptors (CLRs) become active only when the agonist occupies all binding sites [5, 158], or to a single level, are independent of the number of ligands bound (CLRs) [159]. Moreover, in NMDARs, partial and full agonists elicit a similar degree of cleft closure as well as unitary amplitude, however the open probabilities (shorter openings and longer closing) and the efficacies decrease for partial agonists compared to full agonists [160-163]. These examples suggest that receptor activation is more complex than initially assumed and is not only a result of domain closure [153, 154].

A hallmark of most AMPA and kainate receptors is their rapid and profound desensitization in the millisecond timescale [70, 164-166] with kainate receptors displaying a 100-fold more stable desensitized state [165, 167]. In contrast, NMDA receptors slowly and incompletely desensitize [168, 169]. The importance of iGluR desensitization is emphasized by the fact that disruption of AMPAR desensitization is lethal for embryos probably because desensitization prevents neurons from being overexcited [170]. The desensitized receptor state is characterized by a ligand-bound LBD and a closed ion channel pore. This state is accompanied by major structural rearrangements in the LBD, and for kainate and AMPA receptors, desensitization has been shown to be accompanied by a LBD rupture resulting into transition from two-fold into four-fold symmetry, presumably compensating for the symmetry mismatch between the extracellular domains and the transmembrane domains (Figure 1.7) [19, 40, 126]. Furthermore, in kainate receptors, desensitization is accompanied by a 120° rotation of two LBD subunits. The findings of ATD movement upon receptor desensitization, however, are not consistent. While in some studies the conformation of the ATDs seem to be largely unaffected from desensitization [126], other desensitized structures implied variable degrees of ATD dimer separation upon receptor desensitization for GluA2 [40, 119, 125] but not for GluK2 [40]. This observation could possibly arise from the more stable GluK2 ATD dimer compared to weaker interaction within the GluA2 dimer, as revealed by analytical ultracentrifugation [171-173].

Furthermore, it has been shown that desensitization is correlated with the stability of the D1-D1 dimer interface, as desensitization is characterized by a disruption of the D1-D1 interface with the D2 domains of the dimers coming closer. Accordingly, stabilizing the D1-D1 interface of LBD dimers prevents the receptor from entering into the desensitized state. In kainate receptors, it has been shown that the D1-D1 interface is additionally modulated by ions such as Na^+, Cl^- and Zn^{2+} ions, as revealed by functional experiments and crystal structures of kainate LBDs in presence of these ions [9, 174-177]. Sodium and chloride ions are required for kainate receptor activation and in their absence, the desensitization rates increases due to the reduced dimer stability [9, 174]. Along with the finding that kainate receptor gating is affected by ions, the authors found that AMPA receptors are not [176], a criterion to distinguish AMPA from kainate receptors, because until this point it has been assumed that AMPA and KARs have similar gating properties [178].

Stabilization of the dimer interface and reduction of desensitization can be further achieved by introducing mutants at the D1-D1 interface [179, 180] and by allosteric modulators that bind within the dimer interface [181, 182], and the other way round, desensitization can be achieved or mimicked by mutations that abolish cation binding in kainate receptors [183, 184] or generally destabilize the D1 interdimer interface [114, 167]. One such positive allosteric modulator that drastically decreases the extent of desensitization is cyclothiazide (CTZ). The first crystal structure of a CTZ-bound iGluR was published in 2002 [179]. The structure shows how CTZ binds within the dimer interface and how the L483Y mutations stabilizes the D1-D1 interface through cation-π interactions with the nearby Lys752 and Leu748 of the LBD (in D1), thereby attenuating desensitization [179, 185]. Interestingly, several functional and structural studies suggest that the desensitized state is characterized by a high degree of heterogeneity, which might be due to the existence of multiple desensitized states [19, 40, 186]. According to the previous work and the recent heteromeric GluA2/A3 cryo-EM structure, a desensitized state might also be obtained even in the absence of a ligand [19, 114, 136, 187].

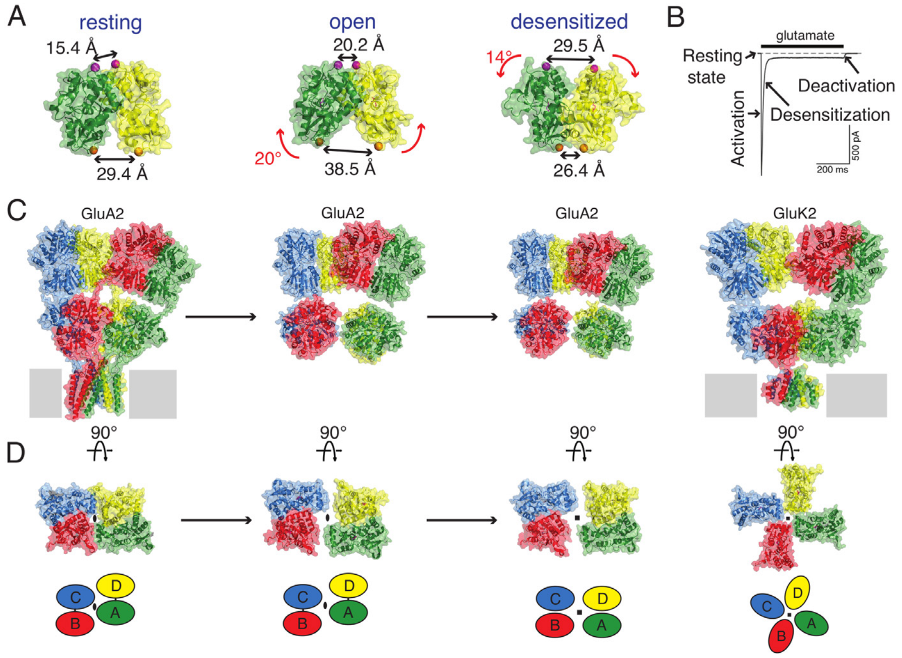

Figure 1.7: **iGluR LBD mobility during gating. (A)** Cartoon representation of canonical dimer movement from resting (PDB ID: 1FTO) to active (PDB ID: 1FTJ) to the desensitized-like state (PDB ID: 2I3W). In the resting state, the ion channel is closed. Glutamate binding to the LBD leads to LBD clamshell closure (by 20°) characterized by an upward movement of the lower D2 lobe (indicated by red arrows). This rearrangement leads to enlargement of the S2-M3 linker (black arrows) to 38.5 Å, as measured by the Cα atoms of Pro632 (orange spheres), and drives channel opening. Activation of the channel is followed by fast and profound desensitization, which itself is characterized by LBD rearrangements leading to disruption of the D1-D1 interface by a downward movement of the D1 lobes by 14°. The D1-D1 distance (measured by the Cα atoms of Ser741, magenta spheres) increases from 20.2 Å to 29.5 Å, whereas the D2 domains come closer and the Pro632 distance decreases from 38.5 to 26.4 Å. **(B)** Representative trace from whole-cell recording from human embryonic kidney (HEK) 293 cells that express rat GluA2, showing the gating steps in iGluRs. The black bar indicates the 500 ms application of glutamate. **(C)** Structural rearrangements of iGluRs in different gating steps in context of the full-length protein from the resting state (PDB ID: 4U2P) to the active, glutamate-bound state (PDB ID: 4UQ6) to the desensitized states of either GluA2 (PDB ID: 4UQK) or GluK2 (PDB ID: 4UQQ). Note that the transmembrane domains are not resolved in the open and desensitized GluA2 states. Activation leads to vertical compression of the receptor. **(D)** Top view of the LBD layer showing LBD tetramer movements upon activation. Activation leads to enlargement of the central gating ring, whereas desensitization leads to major structural rearrangements and rupture of the LBD layer with a transition from two-fold to four-fold symmetry. Desensitization in GluK2 is characterized by 120° rotation of two of the four LBDs.

1.2 GLUTAMATE RECEPTOR AUXILIARY PROTEINS

1.2.1 Transmembrane AMPA receptor Regulatory Proteins (TARPs)

AMPA receptor auxiliary proteins as components of native AMPAR macromolecular complexes were discovered based on the observation that native AMPA [188, 189] and kainate receptors [190] from isolated tissue behaved differently compared to receptors expressed in heterologous systems [74, 191, 192], suggesting that heterologously expressed AMPA and kainate receptors lack an important component [28, 88]. Rather than being alone in the postsynaptic membrane, AMPARs form supramolecular complexes with a broad range of auxiliary proteins. And the first of them that was identified in the late 1990s was the prototypical TARP member stargazin or γ-2 and named after the head-elevating behavior of the mutant mouse *stargazer* with a spontaneous mutation in the stargazin gene in both alleles resulting in a spike-wave seizure phenotype [193-195]. Stargazin was initially thought to be a calcium channel γ-subunit due to its 23% sequence homology with the γ-1 subunit of the skeletal muscle calcium channel subunit (Figure 1.8 A) [88, 194, 196]. Cerebellar granule cells (CGCs) of *stargazer* mutant mice lack functional AMPARs at the surface, indicating that stargazin might play a role in surface delivery of AMPA receptors.

A few years after the discovery of stargazin as the prototypical TARP member, Tomita et al. discovered and defined further proteins as AMPAR transmembrane auxiliary proteins based on their ability to rescue glutamate-evoked currents in *stargazer* CGCs [197]. Using immunoprecipitation and Blue-Native polyacrylamide gel electrophoresis (PAGE), TARPs were identified as binding partners of native AMPAR complexes [119, 198, 199]. Since the discovery of stargazin, the prototype of TARPs, additional AMPAR auxiliary proteins besides TARPs [87-90] have been identified: the cornichon homologs (CNIH-2 and -3) [91], cystine-knot AMPAR modulating protein (CKAMP-44) [92], synapse differentially induced gene 1 (SynDIG-1) and germ cell-specific gene 1-like protein (GSG1L) [93], which is homologous to TARPs (Figure 1.8 A and B).

There is no high-resolution structural information on TARPs yet. However, crystal structures of mouse claudin-15 and -19 revealed atomic detail about the domain architecture of claudins with a left handed bundle composed of four transmembrane helices with a long third transmembrane domain and two extracellular loops adopting a β-sheet arrangement [200, 201]. As claudins are homologous to TAPRs (Figure 1.8 A – C), these structures might reveal important structural features for TARPs as well. And indeed, a recent 7.3 Å cryo-EM structure of an AMPAR GluA2 tetramer fully occupied by TARP γ-2/stargazin [202] and cryo-EM structures of GluA2-γ-2 tandems [203] showed that TARPs adopt a similar structure to claudin-19: TARPs are non-pore forming integral membrane proteins with four transmembrane helices and a smaller extracellular loop in TARPs compared to claudin-19. The cryo-EM structure furthermore revealed and confirmed previous suggestions about interacting domains that will be discussed later (see Section 1.2.3) [202].

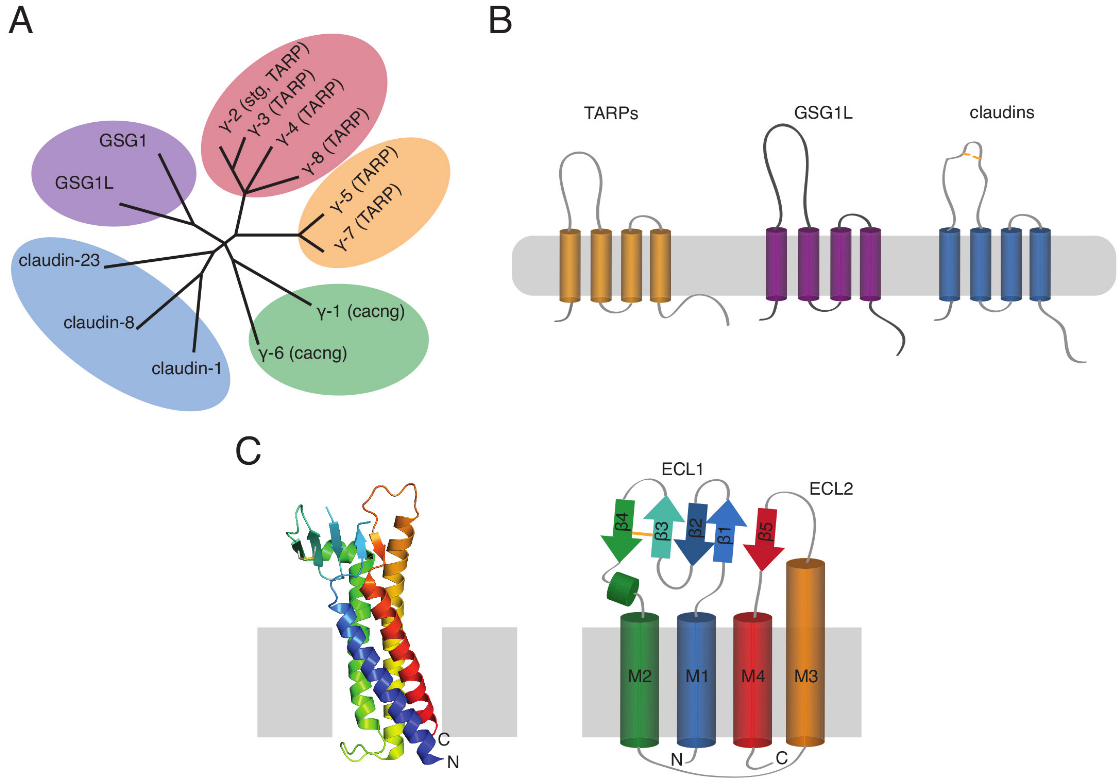

Figure 1.8: The TARP family of auxiliary proteins and their relatives. (A) Phylogenetic tree of TARP class I (γ-2, γ-3, γ-4, γ-8; red circle), TARP class II (γ-5 and γ-7; orange circle), the homologous γ-1 and γ-6 (green circle), members from the claudin family (claudin-1, -8 and -23; blue circle) and GSG1 as well as GSG1L (purple circle). **(B)** Proposed secondary structure for TARPs, GSG1L and claudins with four transmembrane helices and both N- and C-termini located intracellularly. **(C)** The recent crystal structure of mouse claudins reveal the domain architecture of claudins with a prominent extracellular β-sheet structure composed of five β-sheets (β1-β5), with a disulfide bond between β3 and β4 (Cys54 and Cys64, depicted as sticks in the helix representation and as a light orange line in the cartoon representation). Figure modified from [93, 200].

1.2.2 Different TARP isoforms

The TARP family of AMPAR regulatory proteins can be subdivided into two classes: type I TARPs and type II TARPs, based on their homology (see Figure 1.8 A) and the magnitude of effects on AMPAR gating and pharmacology. TARPs of class I contain stargazin or γ-2 as the prototypical TARP member, γ-3, γ-4 and γ-8, whereas γ-5 and γ-7 belong to type II TARPs. The homology-based classification also has functional implications with class I TARPs being able to rescue AMPAR-mediated surface currents in *stargazer* cerebellar granule neurons (CGNs), whereas class II TARPs are not [197, 204]. Type I TARPs are able to modulate AMPAR trafficking, whereas type II TARPs are not and have variable effects on gating and pharmacology. While type I TARPs all possess a conserved PDZ binding motif (-RR/KTTPV), type II TARPs have an atypical S/TSPC PDZ binding motif (Figure 1.9 A and B), resulting in much weaker interaction with PSD-95 [205].

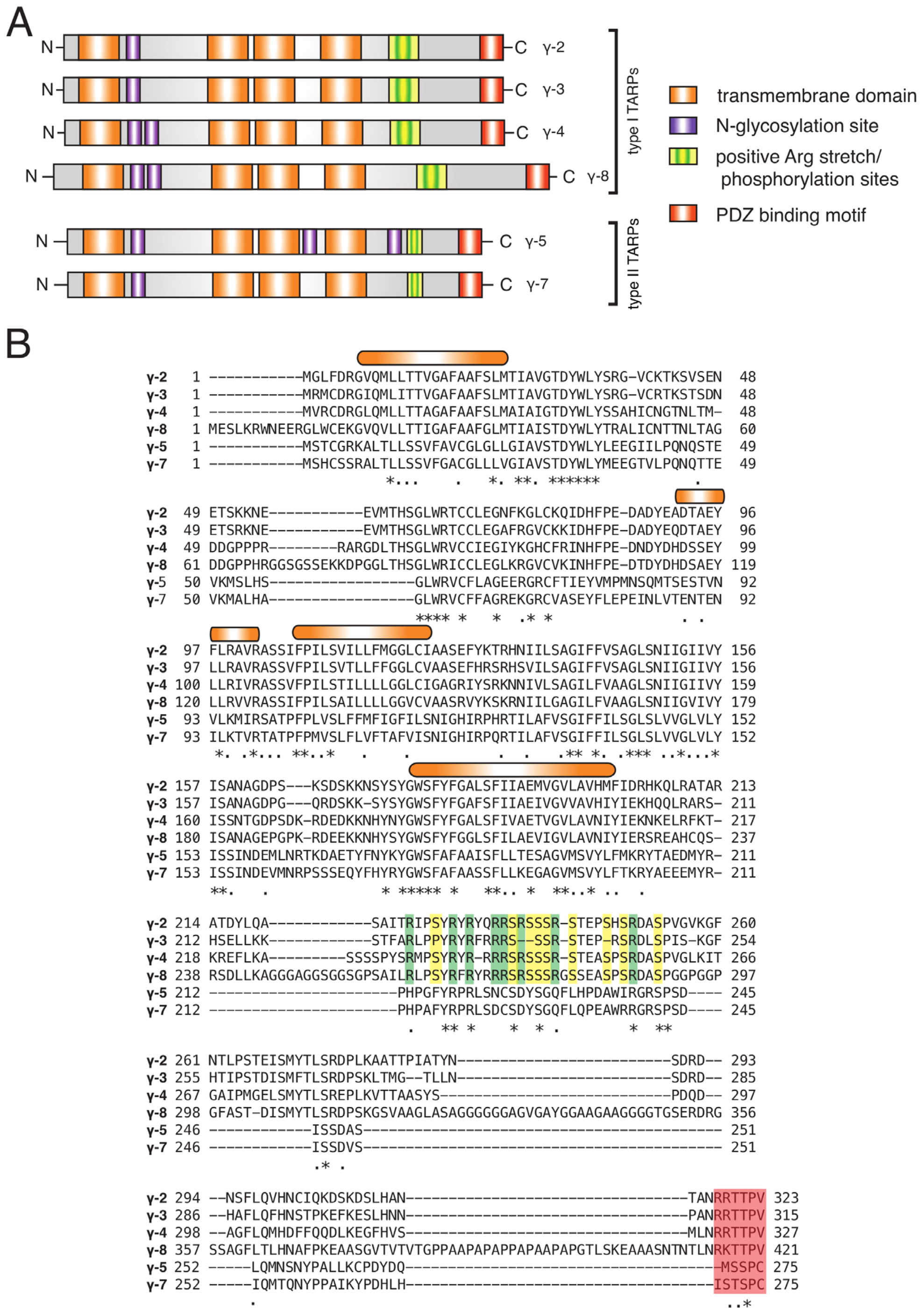

```
γ-2   1 -----------MGLFDRGVQMLLTTVGAFAAFSLMTIAVGTDYWLYSRG-VCKTKSVSEN  48
γ-3   1 -----------MRMCDRGIQMLITTVGAFAAFSLMTIAVGTDYWLYSRG-VCRTKSTSDN  48
γ-4   1 -----------MVRCDRGLQMLLTTAGAFAAFSLMAIAIGTDYWLYSSAHICNGTNLTM-  48
γ-8   1 MESLKRWNEERGLWCEKGVQVLLTTIGAFAAFGLMTIAISTDYWLYTRALICNTTNLTAG  60
γ-5   1 -----------MSTCGRKALTLLSSVFAVCGLGLLGIAVSTDYWLYLEEGIILPQNQSTE  49
γ-7   1 -----------MSHCSSRALTLLSSVFGACGLLLVGIAVSTDYWLYMEEGTVLPQNQTTE  49
                             *...    .   *. **. ******           .

γ-2  49 ETSKKNE-----------EVMTHSGLWRTCCLEGNFKGLCKQIDHFPE-DADYEADTAEY  96
γ-3  49 ETSRKNE-----------EVMTHSGLWRTCCLEGAFRGVCKKIDHFPE-DADYEQDTAEY  96
γ-4  49 DDGPPPR--------RARGDLTHSGLWRVCCIEGIYKGHCFRINHFPE-DNDYDHDSSEY  99
γ-8  61 DDGPPHRGGSGSSEKKDPGGLTHSGLWRICCLEGLKRGVCVKINHFPE-DTDYDHDSAEY 119
γ-5  50 VKMSLHS-----------------GLWRVCFLAGEERGRCFTIEYVMPMNSQMTSESTVN  92
γ-7  50 VKMALHA-----------------GLWRVCFFAGREKGRCVASEYFLEPEINLVTENTEN  92
                                **** *   *  .* *               . .

γ-2  97 FLRAVRASSIFPILSVILLFMGGLCIAASEFYKTRHNIILSAGIFFVSAGLSNIIGIIVY 156
γ-3  97 LLRAVRASSVFPILSVTLLFFGGLCVAASEFHRSRHSVILSAGIFFVSAGLSNIIGIIVY 156
γ-4 100 LLRIVRASSVFPILSTILLLLGGLCIGAGRIYSRKNNIVLSAGILFVAAGLSNIIGIIVY 159
γ-8 120 LLRVVRASSIFPILSAILLLLGGVCVAASRVYKSKRNIILGAGILFVAAGLSNIIGVIVY 179
γ-5  93 VLKMIRSATPFPLVSLFFMFIGFILSNIGHIRPHRTILAFVSGIFFILSGLSLVVGLVLY 152
γ-7  93 ILKTVRTATPFPMVSLFLVFTAFVISNIGHIRPQRTILAFVSGIFFILSGLSLVVGLVLY 152
         *. .*... **..*   .    .          .  .   .** *. .*** ..*...*

γ-2 157 ISANAGDPS---KSDSKKNSYSYGWSFYFGALSFIIAEMVGVLAVHMFIDRHKQLRATAR 213
γ-3 157 ISANAGDPG---QRDSKK-SYSYGWSFYFGAFSFIIAEIVGVVAVHIYIEKHQQLRARS- 211
γ-4 160 ISSNTGDPSDK-RDEDKKNHYNYGWSFYFGALSFIVAETVGVLAVNIYIEKNKELRFKT- 217
γ-8 180 ISANAGEPGPK-RDEEKKNHYSYGWSFYFGGLSFILAEVIGVLAVNIYIERSREAHCQS- 237
γ-5 153 ISSINDEMLNRTKDAETYFNYKYGWSFAFAAISFLLTESAGVMSVYLFMKRYTAEDMYR- 211
γ-7 153 ISSINDEVMNRPSSSEQYFHYRYGWSFAFAASSFLLKEGAGVMSVYLFTKRYAEEEMYR- 211
        **.   .             * ***** *   **.. *  **..* ..  .

γ-2 214 ATDYLQA------------SAITRIPSYRYRYQRRSRSSSR-STEPSHSRDASPVGVKGF 260
γ-3 212 HSELLKK------------STFARLPPYRYRFRRRS--SSR-STEP-RSRDLSPIS-KGF 254
γ-4 218 KREFLKA---------SSSSPYSRMPSYRYR-RRRSRSSSR-STEASPSRDASPVGLKIT 266
γ-8 238 RSDLLKAGGGAGGSGGSGPSAILRLPSYRFRYRRRSRSSSRGSSEASPSRDASPGGPGGP 297
γ-5 212 ----------------------PHPGFYRPRLSNCSDYSGQFLHPDAWIRGRSPSD---- 245
γ-7 212 ----------------------PHPAFYRPRLSDCSDYSGQFLQPEAWRRGRSPSD---- 245
                               .   ** *    *  * .        *  **

γ-2 261 NTLPSTEISMYTLSRDPLKAATTPIATYN-------------------------SDRD-- 293
γ-3 255 HTIPSTDISMFTLSRDPSKLTMG--TLLN-------------------------SDRD-- 285
γ-4 267 GAIPMGELSMYTLSREPLKVTTAASYS---------------------------PDQD-- 297
γ-8 298 GFAST-DISMYTLSRDPSKGSVAAGLASAGGGGGGAGVGAYGGAAGAAGGGGTGSERDRG 356
γ-5 246 ------------ISSDAS------------------------------------------ 251
γ-7 246 ------------ISSDVS------------------------------------------ 251
                    .* .

γ-2 294 --NSFLQVHNCIQKDSKDSLHAN---------------------------------TANRRTTPV 323
γ-3 286 --HAFLQFHNSTPKEFKESLHNN---------------------------------PANRRTTPV 315
γ-4 298 --AGFLQMHDFFQQDLKEGFHVS---------------------------------MLNRRTTPV 327
γ-8 357 SSAGFLTLHNAFPKEAASGVTVTVTGPPAAPAPAPPAPAAPAPGTLSKEAAASNTNTLNRKTTPV 421
γ-5 252 -----LQMNSNYPALLKCPDYDQ-------------------------------------MSSPC 275
γ-7 252 -----IQMTQNYPPAIKYPDHLH------------------------------------ISTSPC 275
             .                                                       ..*
```

Figure 1.9: **Alignment of TARPs and predicted domain topology. (Figure 1.9 continued on next page)**

Figure 1.9 (continued from previous page): (A) Schematic drawing of the domain architecture for type I (top) and type II (bottom) TARPs. The four transmembrane domains of TARPs are colored in orange, the N-glycosylation sites are colored in purple, the stretch containing the positive Arg residues important for lipid interaction and the phosphorylatable Ser residues are colored in yellow/green and the C-terminal PDZ binding motif is colored in red. Figure adapted from [88]. **(B)** Sequence alignment of TARPs class I and II with the asterisks below the alignment indicating fully conserved single amino acids, a colon indicating strong conservation and a period indicating weak similarities. The secondary structure prediction obtained from Psipred is shown above the alignment with orange cylinders representative of the transmembrane domains. The Arg residues in type I TARPs important for lipid interaction are highlighted in green, whereas the phosphorylatable Ser residues are highlighted in yellow. The C-terminal PDZ binding motif is highlighted in red.

TAPRs exhibit overlapping but also differential expression patterns in different regions of the brain. While most cell types express more than one TARP isoform, which allows for compensation in case of a mutation, cerebellar granule cells are the only cell types that only express one type I TARP, stargazin/γ-2 [197, 206, 207] besides type II TARP γ-7 [208]. Stargazin/γ-2 is expressed in every type of neuron but mainly found in the cerebellum [206]. TARP γ-3 is highly enriched in the cerebral cortex, γ-4 can be mainly found in the neonatal forebrain and γ-8 is abundantly expressed in the hippocampus. TARP γ-5 has been found in the CA2 region of the hippocampus [206, 209]. Some TAPRs are furthermore expressed in non-neuronal tissue. The expression pattern of type I TARPs and γ-7 is summarized in Table 1.1.

Table 1.1: Expression pattern of TARPs. Table adapted from [205].

TARP isoform	**γ-2**	**γ-3**	**γ-4**	**γ-7**	**γ-8**
Molecular weight [kDa]	36-42	32-35	36.5	35	50-55
Distribution					
Cerebellum	+++	+	+	++	-
Cerebral cortex	+++	+++	+++	+	++
Hippocampus	++	+	+++	+	+++
Midbrain	++	++	+++	-	+
Stratium	++	++	+++	+	+
Thalamus	++	+	+	+	-
Olfactory bulb	-	+	+	+	+
Heart	-	-	+	+	-
Lung	-	-	+	+	-
Testes	-	-	-	+	+
Skeletal muscle	-	-	-	+	-
References	[197, 210, 211]	[197, 210, 211]	[197, 210-212]	[212-214]	[197, 212, 215-217]

1.2.3 AMPAR-TARP stoichiometry

TARPs are thought to be associated with AMPAR tetramers only [218, 219], and therefore TARP binding to AMPARs presumably occurs at a time point between AMPAR tetramerization and the ER export of the receptor [218, 219].

Great efforts have been made in determining the stoichiometry of AMPAR-TARP complexes using different techniques such as single subunit counting and cryo-EM. A variable number of TARPs associated with AMPARs has been suggested based on a dose-dependent effect of TARPs on miniature excitatory postsynaptic currents (mEPSCs) [89] and the dose-dependent effect of TARPs on kainate efficacy [220], with one TARP molecule being sufficient to modulate AMPAR activity. These studies concluded that the number of TARPs associated with an AMPAR tetramer depends on the TARP expression level [89, 220, 221]. In contrast, another study postulated that neuronal TARPs in CGCs have a fixed stoichiometry of one [222]. Using green fluorescent protein (GFP)-tagged stargazin and a single-molecule counting technique in live cells, Hastie and colleagues showed that the maximum number of TARPs interacting with the AMPAR tetramer depends on the TARP subtype with maximally four γ-2 and γ-3 subunits per AMPAR tetramer, whereas only up to two γ-4 molecules were found to associate with the AMPAR tetramer [221].

A cooperative behavior of TARP binding was found in another study. By using chimeras of TARPs and AMPARs they found that either zero, two or four TARP molecules bind to an AMPAR [220]. The cooperative binding was contradicted by another study showing that the AMPAR-TARP stoichiometry can vary from one to four [87, 89] with cell-dependent [220] and dynamic regulation [199, 223]. A recent cryo-EM study revealed the assembly of fully occupied AMPAR-TARP complexes. By using digitonin as a detergent for purification from rat brain to ensure integrity of the AMPAR-TARP complex they were able to capture the antagonist-bound state of a homomeric GluA2 receptor bound to four TARP γ-2/stargazin molecules. In general, the AMPAR-TARP interaction is thought to be stable enough to permit biochemical co-purification and is supposed to persist for tens of seconds in live cells [218, 221]. The 7.3 Å cryo-EM structure of Zhao et al. revealed how TARPs bind to the AMPAR tetramer and showed that a stargazin molecule resides in between two AMPAR GluA2 subunits with tighter interactions between TARPs and the pore-distal GluA2 subunit pair B-D compared to the pore-proximal subunits A and C, providing evidence that the four possible binding sites for TARPs are not equal (Figure 1.11 C and D). In the same time frame, Twomey et al. published cryo-EM structures of a GluA2-stargazin tandems at resolutions of 6.4-8.7 Å with the C-terminus of GluA2 fused to the N-terminus of stargazin and they observed either zero, one or two stargazin molecules bound to the AMPAR tetramer but found no AMPAR-TARP complex with four TARP molecules [203].

1.2.4 Functional effects of TARPs

The range of TAPR effects on AMPARs is broad and they have been shown to affect AMPAR trafficking, scaffolding, stability, signaling, turnover as well as the receptor's pharmacology and gating kinetics. TARPs have been shown to interact with AMPARs early in their synthesis, but also being important for delivery of AMPAR/TAPR complexes to the plasma membrane as well as for localization of the receptor complex at the cell surface and synaptic targeting [224].

1.2.4.1 TARPs alter AMPAR gating kinetics and pharmacology

Besides the effect of TARPs on receptor trafficking and synaptic targeting (discussed in Section 1.2.4.3), the receptor's functional properties and pharmacology are also altered by TARPs with the effects being depended on the TARP subtype. Thus, type I TARPs slow desensitization and deactivation, lead to faster recovery from desensitization and enhance the amplitude of glutamate-evoked steady-state currents [225-228]. While type I TARPs increase glutamate affinity, type II TARPs either don't have an effect or decrease the affinity for glutamate. Opposite effects can also be observed for desensitization and deactivation rates with type I TARPs slowing down desensitization and deactivation rates and type II TARP γ-5 leading to faster desensitization and deactivation [197, 204, 214, 225, 226, 229, 230]. TARPs increase the efficacy of partial agonists to full agonists, they increase the mean channel conductance to the highest possible subconductance state and they diminish the effect of polyamine block on GluA2-lacking, Ca^{2+}-permeable AMPARs [25, 230, 231]. The summary of different TARP effects on gating and pharmacology are shown in Figure 1.10.

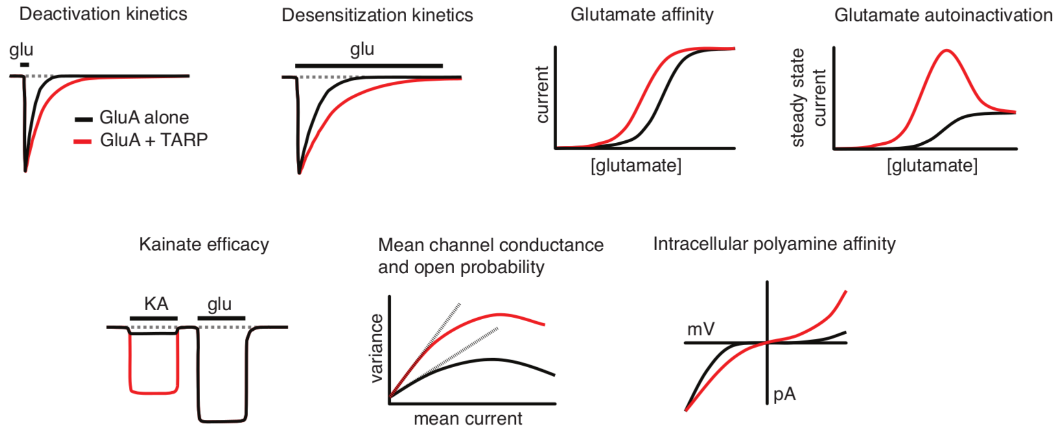

Figure 1.10: Modulatory effect of TARPs on AMPAR gating and pharmacology. Schematic representation of the variety of TARP effects on AMPAR functional aspects and pharmacology showing some aspects of TARP modulation (not all TARP effects are shown). The different effects are shown for the AMPA receptor GluA2 alone or in presence of a TARP member. Also note that the effect can be different for the distinct TARP members. Traces show the effect of TARPs on deactivation, desensitization, the increase in glutamate affinity and the reduced glutamate autoinactivation (upper panel) as well as the increased kainate efficacy in presence of TARPs, the increased open probability and channel conductance and the reduced polyamine block of GluA2-lacking AMPARs in presence of a TARP (lower panel). Figure adapted from [88].

1.2.4.2 Interacting domains between AMPARs and TARPs

Using low-resolution single-particle electron micrographs, it was shown that TARP transmembrane domains directly interact with AMPARs [119, 121] and also recent cryo-EM structures reveal membrane interaction between TARPs and GluA2, involving AMPAR transmembrane domains M1, M2 and M4 and TARP transmembrane domains M3 and M4 [202, 203]. Also, the effect of TARPs is dependent on the pore-resident Q/R site [232].

Functionally, the effects of TARPs have been attributed to distinct TARP domains by performing domain-swapping experiments with isoform-exchange of the first extracellular loop and the C-terminal domain. The first extracellular loop (ECL1) of stargazin regulates AMPAR gating but not trafficking, which can be explained by its influence on and direct interaction with the ligand-binding domain [233]. These findings are emphasized by the fact that the LBDs but not the ATDs are essential for TARP modulation of gating [234]. The C-terminal tail of type I TARPs is essential for AMPAR aspects of gating and trafficking, the latter through its interaction with scaffolding proteins such as PDZ-95, PSD-93 and SAP-102 [199, 226-228, 235, 236]. A recent cryo-EM GluA2-γ-2 structure revealed major contact points between AMPARs and TARPs with extensive non-polar and hydrophobic contacts between TARP and AMPAR transmembrane domains (Figure 1.11 A and B), and electrostatic interactions between an acidic region of the first extracellular loop and a positively charged area of the lower D2 lobe of the LBD [202]. Mutating this KGK motif in AMPARs almost completely abolishes stargazin effects on GluA2 [237]. As γ-2 adopts a structure resembling an open hand with the extracellular β-sheets representing the palm and the α1-helix representing the thumb, γ-2 is positioned underneath the LBD to modulate the degree of LBD domain closure and thus agonist efficacy (Figure 1.11 D). However in this structure the LBD was bound to an antagonist (MPQX/ZK200775), and the mentioned domains were too distant in the presented structure to form salt bridges but might come closer in the active, agonist-bound receptor-TARP complex.

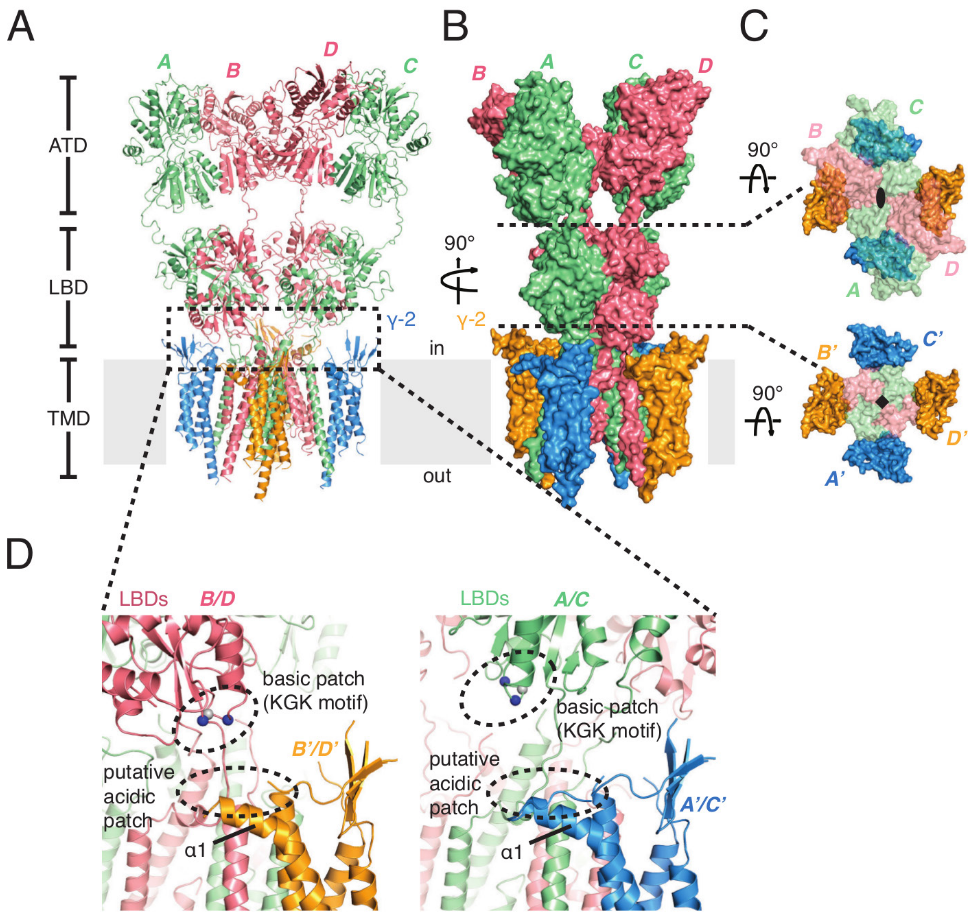

Figure 1.11: Structure of an AMPAR-TARP complex fully occupied with TARP γ-2 as determined by cryo-EM at 7.3 Å. MPQX/ZK200775-bound GluA2 homomer fully bound by TARP stargazin was received by purifying the complex in presence of digitonin. **(A)** Cartoon representation of the AMPA-TARP complex (PDB ID: 5KK2) when viewed from the front and perpendicular to the two-fold axis of symmetry. The proximal AMPAR subunits A and C are colored in pale green, whereas distal subunits B and D are colored in pale red. Stargazin molecules associating with AMPAR A/C and B/D subunits are colored in blue and gold, respectively. The lipid bilayer is indicated with a grey bar. **(B)** Side view of the AMPAR-TARP complex showing the assembly as surface representation. **(C)** Top view of the LBD layer (upper panel) and the TMD layer (lower panel) with the LBD and the TMD layer being shown in transparent surface representation for better visualization of the TARP molecules. The two-fold and four-fold axes of symmetry of the LBD and TMD layers are shown as a black oval and square, respectively. **(D)** Magnification into the extracellular interaction site between TARPs and AMPARs involving a basic "KGK" motif (aa 697-699) of the lower D2 lobe of the LBD (boxed with a black dashed line) and the TARP acidic patch of the first extracellular loop α1 helix (boxed with a black dashed line). Strikingly the TARP-AMPAR interactions are different for GluA2 proximal and distal subunits, with TARP γ-2 being more closely to the LBD in the B/D position. Figure adapted from [202].

1.2.4.3 TARPs mediate trafficking and synaptic targeting of AMPARs

TARPs have been shown to be associated with AMPAR tetramers starting at an early stage of their biogenesis as tetramers assemble from dimers in the ER (also see Figure 1.12). In *stargazer* CGNs, AMPARs exhibit immature glycosylation rendering them unable to exit the ER, which explains why *stargazer* CGNs lack surface AMPA receptors [197, 205, 238-240]. Overexpression of full-length stargazin/γ-2 in *stargazer* CGNs rescues synaptic and surface AMPAR activity, while a deletion construct missing the last four amino acids of stargazin C-terminal tail (stargazinΔC or stargazinΔTTPV) restored surface but not synaptic AMPARs [240]. This important result indicates that surface expression and synaptic targeting of AMPARs are distinctly regulated by TARPs, with synaptic targeting but not surface expression being dependent on stargazin's C-terminal PDZ binding motif (Thr-Thr-Pro-Val, TTPV).

Two possible scenarios could explain how TARPs promote the exit of AMPARs from the ER. First, by interacting with AMPARs, TARPs could mask an ER retention signal and second, TARPs themselves could harbor an ER export signal [197, 228, 238]. A recent study unraveling the importance of the TARP C-terminal domain for the ER export of AMPARs suggests that the first half of TARPs C-terminus (aa 203-269) contains an ER export signal [224]. Further proteins have been shown to assist in the surface trafficking of AMPAR-TARP complexes; one of them is the Golgi-enriched protein neuronal isoform of protein-interacting specifically with TC10 (nPIST) [241]. And also microtubule-associated protein 1, light chain 2 (MAP1 LC2) has been shown to bind to the C-terminal domain of stargazin and assisting in the trafficking of AMPAR-TARP complexes to the cell surface [242], where it can bind to scaffolding proteins like PSD-95, which is highly enriched at the electron-dense area beneath the postsynaptic site, the postsynaptic density (PSD).

Besides forward trafficking and surface delivery, TARPs also modulate the synaptic localization of AMPARs and thereby are important for regulation of the number of AMPARs at the PSD, which in turn modulates synaptic strength.

TARP I class member all contain a class I PDZ binding motif at their very C-terminus (TTPV) important for synaptic targeting of AMPARs, while type II TARPs contain an atypical S/TSPC motif.

AMPARs are characterized by a high degree of mobility and can be easily exchanged between extrasynaptic and synaptic sites by lateral diffusion [215, 243, 244]. Regulating the number of AMPAR at the synapse is an important mechanism for modulation of synaptic strength. The number of AMPARs at the PSD can be increased through immobilization and clustering of AMPARs at synaptic sites. However, AMPARs do not bind directly to PSD-93 and PSD-95, and via the type I TARP C-terminal PDZ-binding motif, the AMPAR-TARP complex is anchored and stabilized at the PSD (Figure 1.12) [240, 245, 246]. Disruption of the stargazin-PSD-95 interaction through deletion of the stargazin PDZ binding motif (stargazinΔC) abolishes the clustering of AMPAR-TARP complexes at the PSD [240, 243, 246]. Further TARP interacting proteins have been identified including PDZ-containing proteins [outer membrane protein (OMP25), multi-PDZ domain protein 1 (MUPP1), protein-interacting specifically with TC10 (PIST) and membrane-associated guanylate kinase, WW and PDZ domain containing 2 (MAGI2)] and non-PDZ-containing proteins [(light chain 2 of the microtubule-associated protein (MAP1 LC2)] as well as PDZ-95-like membrane-associated guanylate kinases (MAGUKs) [241, 242, 247, 248].

1.2.4.4 TARP phosphorylation regulates AMPAR activity at the synapse

Synaptic strength is determined by the number and channel properties of synaptic AMPA receptors. In order to regulate the number of AMPARs at the postsynapse, the modulatory function of stargazin itself needs to be regulated. The C-terminal domain of type I TARPs contain various Ser, Thr and Tyr residues with consensus sequences for protein kinases such as PKA, PKC and CaMKII [249, 250], with nine Ser residues being phosphorylated in cultured cortical neurons under basal conditions (Figure 1.9) [215, 251]. Neuronal activity increases calcium influx through NMDA receptors to activate calcium-dependent kinases like CaMKII, for which stargazin C-terminal tail is a substrate [251].

Multisite Ser phosphorylation of stargazin C-terminal tail is important for stargazin-mediated synaptic clustering of AMPARs and an increase of AMPARs at the PSD [32, 252-255]. The phosphorylatable Ser residues are surrounded by positively charged Arg residues. As replacement of the positive Arg stretch by seven Leu and one Gly residue completely abolishes the ability of stargazin to bind to lipids, this positive Arg stretch has been shown to be responsible for the electrostatic interaction between stargazin C-terminal tail and the negatively charged lipid bilayer [256]. Phosphorylation of the C-terminal tail introduces negative charges that interfere with the electrostatic binding to the lipid head groups, leading to dissociation of the C-terminal tail from the membrane and to an increase of the effective length of stargazin C-terminal tail. Stargazin now becomes more mobile and can diffuse laterally in and out of the PSD, where it can bind to scaffolding proteins such as the highly enriched PSD-95 via its C-terminal PDZ binding motif. Graded artificial lengthening of stargazin C-terminal tail has been shown to enable it to interact with deeper PDZ domains as well [257]. As the lipid interaction of stargazin C-terminal tail with the membrane renders it inaccessible for interaction with PSD-95 [256, 258], phosphorylation of stargazin intracellular C-terminal domain is required to allow interaction with PDZ domains and leads to immobilization of the AMPAR-TARP complex at the PSD.

Thus, clustering of AMPARs at the PSD is dependent on interaction of stargazin with PSD-95, which itself is regulated in a phosphorylation-dependent manner (Figure 1.12).

The effect of stargazin C-terminal tail phosphorylation has been investigated by using phosphonull (S9A) or phosphomimic mutants (S9D) [251, 256]. A stargazin mutant lacking all nine phosphorylatable Ser residues still enhances AMPAR surface expression but is incapable of anchoring them at the PSD [251]. Phosphorylation and dephosphorylation of stargazin C-terminal tail regulates synaptic transmission and AMPAR trafficking bidirectionally [251].

Interestingly, the C-terminal PDZ binding motif contains a consensus sequence for phosphorylation by PKA (RRT**T**PV, Thr321). Phosphorylation of Thr321 within the PDZ binding motif interferes with the ability of stargazin C-terminal tail to bind to PSD-95 (Figure 1.12) [259, 260]. A phosphomimic mutant (T321E or T321D) reduces AMPAR-mediated synaptic transmission due to the loss of interaction between stargazin and PSD-95 [259, 260]. The molecular basis of this interaction has been deciphered with a crystal structure of the third PDZ domain bound to its ligand and has shown that the hydroxyl oxygen of Thr321 is critical for the PDZ-ligand interaction as it forms a hydrogen bond with the N-3 nitrogen of His372. Phosphorylation of the Thr residue disrupts the interaction with His372 [261].

Thus, while phosphorylation of Ser residues within the C-terminal tail of stargazin is required to induce liposome dissociation of the C-terminal tail and allow binding to PDZ domains, phosphorylation of Thr321 within the PDZ binding motif (effect mimicked by using the phosphomimic mutant T321E) abolishes binding to PSD-95 [259, 260, 262]. Therefore, phosphorylation of stargazin C-terminal tail has different effects depending on the phosphorylated sites. Also, different kinases have been shown to phosphorylate the two functionally distinct phosphorylation sites. While the nine Ser residues within the C-terminal domain of stargazin have been shown to be phosphorylated by CaMKII, Thr321 has been shown to be phosphorylated by PKA. Phosphorylation and dephosphorylation of stargazin as mechanisms to strengthen or weaken the synaptic strength by increasing or decreasing the number of AMPARs at the synapse are important mechanisms for hippocampal long-term potentiation (LTP) and long-term depression (LTD), respectively [251]. Accordingly, expression of a phosphomimic mutant with all phosphorylatable Ser residues within stargazin cytoplasmatic C-terminal domain mutated to aspartate (S9D), leads to enhancement of AMPAR synaptic delivery and prevents LTD [251, 263]. In turn, a phosphonull stargazin mutant (S9A) prevents induction of LTP [251]. CaMKII might therefore have a key function in synaptic plasticity [264-266] and multisite phosphorylation of stargazin C-terminal tail likely provides a molecular rheostat for graded changes in synaptic plasticity, with kinases and phosphatases acting on stargazin C-terminal tail enhancing and decreasing synaptic strength, respectively (Figure 1.12).

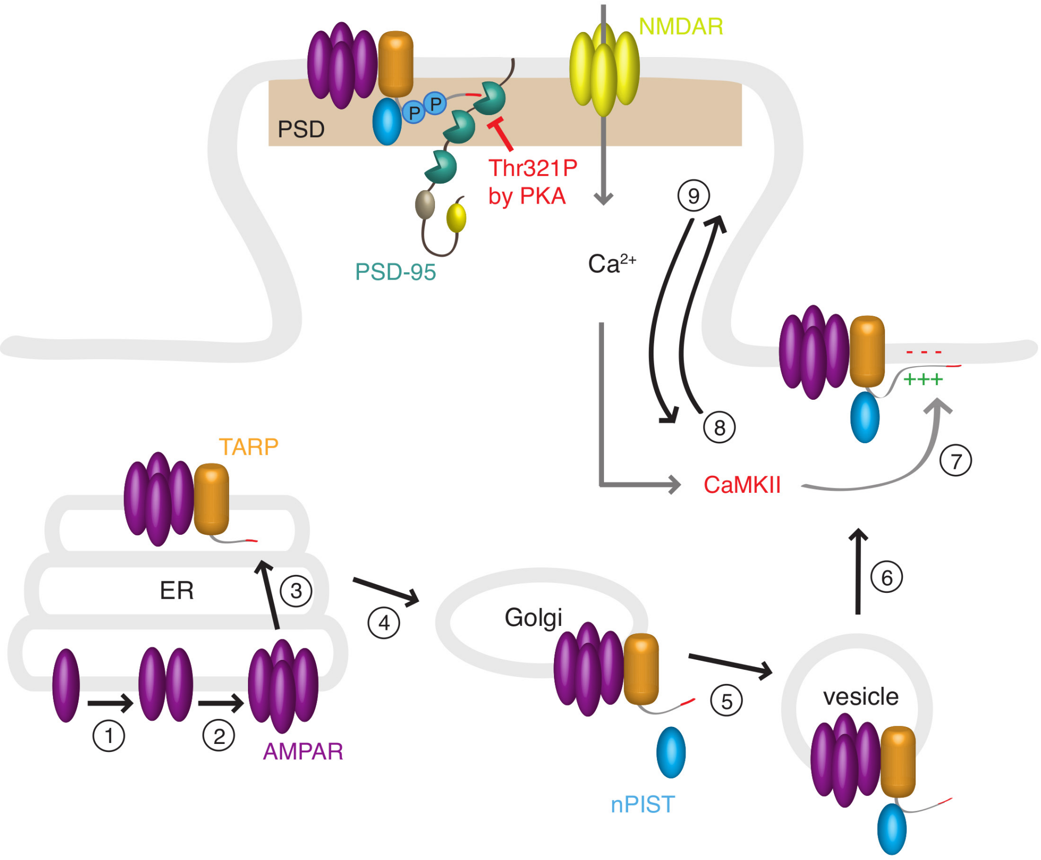

Figure 1.12: TAPR-mediated AMPAR trafficking at the synapse. In the ER, AMPAR form dimers and tetramer formation is achieved through assembly of dimers **(1 and 2)**. TARPs associate with AMPAR tetramers in the ER **(3)** and assist in trafficking from the ER to the Golgi **(4)**, where nPIST binds to the C-terminal tail of stargazin, acts as a chaperone and assists in AMPAR-TARP trafficking to the cell surface from vesicles **(5 and 6)**. Stargazin and type I TARPs electrostatically interact with the lipid bilayer via the TARP C-terminal positive Arg stretch. Neuronal activity increases Ca^{2+} influx through NMDARs, which leads to activation of calcium-dependent kinases such as CaMKII and PKC. Phosphorylation of stargazin C-terminal tail by CaMKII **(7)** abolishes binding to liposomes and leads to diffusion of AMPAR-TARP complexes to the PSD **(8).** At the PSD, phosphorylated stargazin C-terminal tail can binds to scaffolding proteins like PSD-95 via its C-terminal PDZ binding motif, which leads to anchoring and clustering of AMPAR-TARP complexes at the PSD. Dephosphorylation of stargazin C-terminal tail by phosphatases like PP1 and PP2A/B increases the mobility of AMPAR-TARP complexes again and reduces synaptic clustering of AMPAR-TARP complexes **(9)**. The PSD is highlighted in light brown. Figure modified from [196, 205, 267].

1.2.5 Neurological aspects of dysregulated AMPAR-TARP interaction

The spontaneous mutation in the stargazin gene of the *stargazer* mutant mouse leads to a specific form of epilepsy, called absence epilepsy, which is characterized by loss of consciousness in humans and abnormal rotation of the eyes as well as a tottering, lethargy and weight loss phenotype [204]. This form of epilepsy arises from abnormally synchronized cortex and thalamus activity.

Defects in iGluR-driven synaptic transmission have been implicated with a variety of neurodegenerative and psychiatric disorders such as epilepsy and schizophrenia. TARPs themselves seem to be involved in these disorders as well. Defects of a region within chromosome 22 which also encodes the stargazin gene and defects on chromosome 16 which encodes the γ-3 gene have been implicated in high frequency of epilepsy, schizophrenia and a hear loss [268-270]. Abnormal stargazin expression was also found in the dorsolateral prefrontal cortices of patients with bipolar disorders and depression [271, 272].

TARPs are of high interest for drug design in order to either potentiate or suppress AMPAR activity. AMPAkines, drugs that act as AMPAR potentiators to target diseases such as schizophrenia, Alzheimer's disease and Parkinson's disease, have the big disadvantage that they cannot be cell-specifically targeted because AMPARs are expressed ubiquitously. In contrast, as mentioned in Section 1.2.2, TARPs are expressed in different cell types and TARP isoform-specific drugs could help to address AMPARs cell-specifically [197, 206].

1.2.6 Other auxiliary proteins of iGluRs

Besides TARPs, cornichon-homologs have been identified as auxiliary proteins for AMPARs and kainate receptors and they might assist in the early steps of AMPAR biogenesis as well [91, 273, 274].

CNIH-2 and -3 were identified in 2009 as binding partners of AMPARs [87, 91] and are the vertebrate homologs of the *Drosophila* cornichon. They share some properties of TARPs such as they also enhance AMPAR surface expression and slow desensitization and deactivation [91, 275-277]. They also promote trafficking of AMPARs as measured by the receptor's glycosylation, thereby acting as an ER chaperone. In contrast to TARPs, cornichon-homologs are shorter and only possess three transmembrane domains (Figure 1.13 A and B) [87, 88].

CKAMP44 was identified as an AMPAR auxiliary protein by immunoprecipitation and mass spectrometry [92] and is a type I transmembrane domain with only one membrane-spanning helix (Figure 1.13 A and B). The name is derived from the cysteine-rich N-terminus of the 44 kilodalton (kDa) protein that might form a cysteine knot similar to other proteins [278, 279]. CKAMP44 has effects opposite to TARPs and CNIHs because they slow deactivation similar to TAPRs, however, they accelerate desensitization and slow the recovery from desensitization in contrast to TARPs and CNIHs [92, 280, 281].

SynDIG1, a type II transmembrane protein, is another AMPAR auxiliary protein and has been shown to regulate AMPAR content at developing synapses in the hippocampus and increases AMPAR mEPSCs [282-284].

Neuropilin tolloid-like 1 (NETO-1) has been identified as an NMDAR auxiliary protein [285], and was later found to interact with AMPARs as well. NETO-1 and -2 are single transmembrane-spanning proteins and contain extracellular complement C1r/C1s, Uegf, Bmp1 (CUB) domains (Figure 1.13 A and B) [286, 287]. Another NETO protein, NETO-2, was identified as a kainate receptor auxiliary protein [288], also enhances the current and increases the efficacy for kainate on GluK2 but not GluA1. Furthermore, NETO-2 has been shown to slow deactivation and desensitization and accelerates the recovery from desensitization in kainate receptor GluK2 similar to TAPR effects in AMPA receptors. Secondary structures were proposed based on predictions and are shown in Figure 1.13 A and B. The effects of the different auxiliary proteins on the AMPA receptor GluA2 are summarized in Figure 1.13 C.

GSG1L is a tetraspanning protein similar to TARPs that has recently been identified as an AMPAR but not kainate receptor (KAR) interacting protein that is related to the claudin family. Despite the overall similarity to TARPs (see Figure 1.8), the first extracellular loop of GSG1L is 50% longer than the ECL of TARPs and also the C-terminal domain is not conserved with TARPs. Reflected by these differences, GSG1L also increases surface expression of AMPARs as efficiently as TARPs, however, GSG1L slows the recovery from the desensitized state opposite to TARPs [93].

A recent high-resolution proteomic approach using multiepitope affinity purification and a blue native/mass spectrometry from adult rat and mice brain identified 21 additional auxiliary proteins of native AMPARs as well as their molecular abundancies [87]. The novel candidate interaction proteins have different domain topologies, 12 of them are transmembrane proteins, five are secreted proteins and four are cytoplasmatic proteins. Using solubilization conditions with different stringencies, they conclude that the AMPAR macromolecular complex consists of a common inner core with two pairs of asymmetric binding sites for CNIH-2/-3 or γ-2/γ-3 and GSG1L or TARPs γ-8/γ-4/γ-2/γ-3 and outer corner constituents such like PRRTs 1/2, CKAMP44, C9orf4 and Neuritin. Except for GSG1L, the functional effects of the newly identified auxiliary proteins have not been investigated so far.

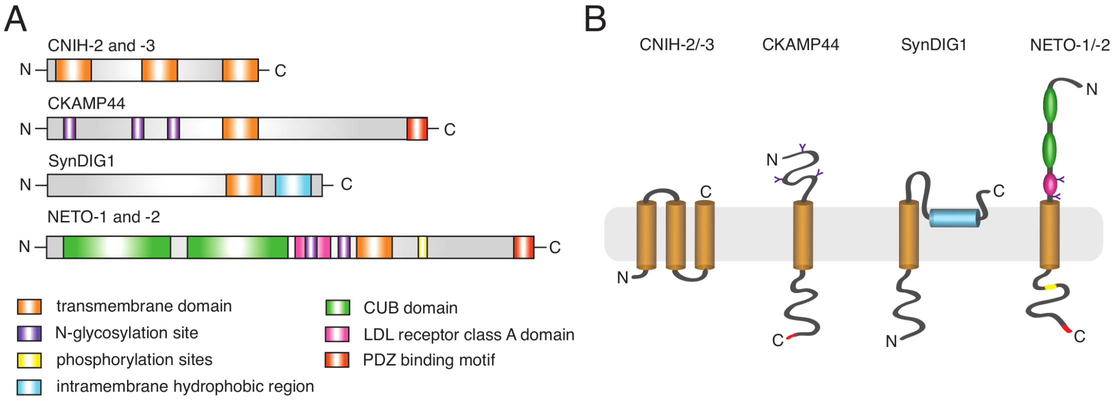

C

	TARP class I		**TARP class II**		**CNIH-2/-3**	**CKAMP44**	**SynDIG1**
	Type Ia (γ-2 & γ-3)	Type Ib (γ-4 & γ-8)	γ-5	γ-7			
Surface trafficking of AMPARs	↑	↑↑	↔	↑	↔	↓↓	unknown
AMPAR synaptic targeting	↑↑	↑↑	↔	↑	↔	unknown	↑↑
Desensitization rate	↓	↓↓	↑	↓	↔	↑	unknown
Deactivation rate	↓	↓↓	↑	↓	↔	↓	unknown
Glutamate affinity	↑↑	↑	↓	no effect	unknown	↑↑	unknown
Kainate affinity	↑↑	↑↑	no effect	↑	no effect	unknown	unknown

Figure 1.13: Variety of AMPAR-associated transmembrane auxiliary proteins. (A) Domain architecture of cornichon-homologs CNIH-2 and -3, CKAMP44, SynDIG1 and the NETO family (NETO-1 and -2). The domain coloring is indicated in the bottom panel. **(B)** Schematic protein architecture showing the proposed secondary structure of the auxiliary proteins. N and C-termini are indicated. **(C)** Summary of some effects caused by the distinct AMPAR auxiliary proteins. Green arrow – increase, red arrow – decrease, orange arrow – variable effects/conflicting reports. Table adapted from [88, 204, 280].

1.3 AIMS OF THIS PROJECT

Since the first cloning of the first glutamate receptor subunit, great efforts have been made to understand how fast signaling of AMPAR is achieved. The combination of functional and structural experiments enabled us to get important insights into receptor movements upon activation. However, despite the growing number of full-length crystal or cryo-EM structures of the glutamate receptor family, a fully active receptor could not be obtained so far, as the ion channel pore could never be trapped in an open-like conformation. Therefore, one of the overall aims of this thesis was to gather information that allow us to better understand the mechanism of fast receptor activation and how the four subunits of the receptor act together to open the ion channel pore. The specific goals were:

1. Expression and purification of isolated LBDs harboring different mutations and in complex with various ligands: antagonists, partial agonists and full agonists
2. Crystallization and crystal structure analysis of LBD arrangements obtained by crystallographic symmetry. Evaluate if distinct sLBDs/sLBD mutants in combination with different ligands produce tetrameric arrangements representative of different functional states of the receptor
3. Evaluation of the obtained tetrameric sLBD arrangement by means of electrophysiology and molecular modeling
4. Ability of mutant sLBDs to form oligomers in solution, determined by static light scattering

The second part of this thesis focuses on stargazin, the prototypical member of TARPs and how its function is regulated upon phosphorylation. While it is now well established that the C-terminal domain of stargazin is responsible for trafficking of AMPARs and that this function itself is regulated in a phosphorylation-dependent manner, the exact mechanism and time course of stargazin phosphorylation is not known. Stargazin binds to negatively charged lipid head groups via its positively charged Arg stretch. Phosphorylation of stargazin C-terminal tail at nine Ser residues introduces negative charge that abolishes binding to the lipid bilayer, thus increasing the effective length of stargazin C-terminal tail and enabling it to bind to scaffolding proteins like PSD-95 and leading to the immobilization of AMPAR-TARP complexes at the PSD. The effect of stargazin phosphorylation has been investigated using phosphomimic or phosphonull mutants and tagged stargazin C-terminal tail. An untagged protein and a kinase in order to understand the mechanism of stargazin phosphorylation more physiologically have not been used so far. Also, to date it is not known how many TARP phosphorylation sites are required for dissociation from the membrane and for the regulation of AMPAR activity. Using a combination of biophysical and structural experiments we aimed to decipher the atomic detail and mechanism of stargazin phosphorylation by CaMKII that drives stargazin C-terminal tail dissociation from lipids and leads to synaptic clustering of AMPARs. The specific goals of this second part of the thesis were:

1. Recombinant over-expression and purification of the complete, 120 aa long stargazin C-terminal tail
2. Optimization of the purification procedure to obtain untagged and pure stargazin C-terminal tail
3. Production of $^{1}H,^{15}N$-labeled and untagged stargazin cytoplasmatic C-terminal tail for structural studies
4. Biophysical characterization of stargazin intracellular C-terminal tail
5. Evaluation of the ability of the purified protein to bind to differently charged liposomes and decipher the dependence of this interaction on the electrostatics
6. Phosphorylation of stargazin C-terminal domain by CaMKII and evaluation of the phosphorylation by mass spectrometric and NMR spectroscopic means
7. Unraveling the dependence of the stargazin:lipid interaction on phosphorylation using *in vitro* CaMKII phosphorylation and liposome co-sedimentation assays

2 MATERIALS AND METHODS

2.1 MATERIALS

2.1.1 Instruments

All devices used in this work are listed in Table 2.1.

Table 2.1: Devices

Devices	Type	Manufacturer
Agarose gel chamber	Peqlab	VWR, Germany
Beamlines	14.1 14.2	Helmholtz-Zentrum Berlin, Germany
CD spectrometer	Chirascan™	Applied Photophysics, USA
Centrifuges	5810 R, Rotor A-4-81, refrigerated	Eppendorf, Germany
	Microcentrifuge 5425, non-refrigerated	Eppendorf, Germany
	J-26 XP	Beckman Coulter, Germany
Ultracentrifuge	Optima™ L-90K	Beckman Coulter, Germany
	Optima™ MAX-TP	Beckman Coulter, Germany
Chromatography columns	HisTrap HP 1 mL or 5 mL	GE Healthcare, Germany
	HiPrep Desalting column	GE Healthcare, Germany
	HiTrap Q/XL, 1 mL or 5 mL	GE Healthcare, Germany
	HiTrap SP/XL, 1 mL or 5 mL	GE Healthcare, Germany
	Superdex™ HiLoad S200 26/600 prep grade	GE Healthcare, Germany
	Superdex™ S75 10/300 GL	GE Healthcare, Germany
	Superdex™ S200 10/300 GL	GE Healthcare, Germany
	Superdex™ increase 10/300 GL	GE Healthcare, Germany
Chromatography systems (FPLC)	ÄKTA Purifier 10 (P-903)	GE Healthcare, Germany
Chromatography systems (FPLC)	DGU-20A$_{3R}$ (Degassing Unit) LC-20AD (prominence liquid chromatograph) SIL-20AC (prominence Auto Sampler) CBM-20A (communications bus module)	Shimadzu, Germany

Table 2.1 - Continued from previous page

Devices	Type	Manufacturer
	SPD-20A (prominence UV/VIS Detector	
	FR-20A (prominence fluorescence detector)	
Concentrators	Amicon Ultra	Merck Millipore, Germany
Cryoloops	Mounted Litholoops	Molecular Dimensions, UK
Crystal observation	Rock Imager (4°C, 20°C)	Formulatrix, USA
Crystallization plates	Crystal quick plate	Greiner bio-one, Germany
	Viewseal sealer, clear	Greiner bio-one, Germany
Crystallization robot	Gryphon	Art Robbins Instruments, USA
Dewar	CX100 Dry shipper	Molecular Dimensions, UK
Filtration equipment	Classic Glass Filter	Merck Millipore, Germany
Fine Screens	Formulator	Formulatrix, USA
Freezer	-20°C	Liebherr, Germany
	-80°C, New Brunswick™	Eppendorf, Germany
Fridge	Unichromat 700	Uniequip, Germany
	Unichromat 1500	Uniequip, Germany
Gel drying equipment	GelAir Drying system	Bio-Rad, Germany
Gel electrophoresis system	Mini-PROTEAN® Tetra Vertical Electrophoresis Cell	Bio-Rad, Germany
	SE250 Mighty small Mini Vertical electrophoresis unit	Hoefer, Germany
	XCell SureLock™ Mini-Cell Electrophoresis system	Thermo Fisher Scientific, Germany
	Criterion™ Vertical electrophoresis Unit	Bio-Rad, Germany
Heat block	Thermomixer comfort	Eppendorf, Germany
	Analog heatblock	VWR, Germany
Homogenizer	EmulsiFlex-C5	Avestin, Germany
Ice machine	Ice line	MIgel, Italy
Incubator	Kompaktschüttler KS15/TH-15	Edmund Bühler, Germany
	LEX bubbling system	Harbinger Biotechnology, Canada

Table 2.1 - Continued from previous page

Devices	Type	Manufacturer
Isothermal titration calorimeter	VP-ITC	Malvern, UK
MALS detector	miniDAWN TREOS	Wyatt, Germany
Microscope	HZ95 + KL1500 LCD	Leica, Germany
Microwave	R-212	Sharp, Germany
Nanodrop spectrophotometer	ND-1000	Thermo Scientific, Germany
Peristaltic pump	4-Kanal Schlauchpumpe Reglo Analog C MS-4/08-100	Ismatec, Germany
pH Meter	Radiometer PHM82 standard pH Meter	Radiometer analytical, France
Photometer	Biophotometer	Eppendorf, Germany
Pipettes	Research Plus physiocare concept	Eppendorf, Germany
Power supply (SDS PAGE)	PowerPac™ Mighty Slim SX250	Bio-Rad, Germany Hoefer, Germany
RALS system	Viscotec 270 Dual Detector Viscotec RImax	Malvern, UK
RI detector	Optilab T-rEX	Wyatt, Germany
Scales	Pioneer™ precision scale PK-352	Ohaus, Germany Denver Instruments, USA
Shaker	KS250	IKA Labortechnik, Germany
Shaker incubator	HT	Infors, Switzerland
Sonicator	Sonopuls HD 2200	Bandelin, Germany
Sonotrode	MS73 (Ø= 3 mm) TT13 (Ø= 12.7 mm)	Bandelin, Germany
Thermocycler	FlexCycler	Analytik Jena, Germany
UV lamp		Peqlab, Germany
Vacuum pump	Membrane vacuum pump	KFN, Germany
Vortex mixer	Vortex test tube mixer 7-2020	Neolab, Germany
Water purification	Millipore Synergy (SimPak®1)	Millipore, Germany

2.1.2 List of software

The software that was used in this thesis is listed in Table 2.2.

Table 2.2: Software

Software	Reference
Astra 6.1.4	Wyatt, Germany
Chirascan 10010 peptide	Applied Photophysics, USA
Collaborative Computational Project Number 4 (CCP4i) program suite	[289]
Coot	[290]
Endnote_X7.4	Michael O. McCracken
GraphPad Prism	GraphPad, USA
Gryphon 1.4.1.0	Art Robbins Instruments, USA
ImageJ	[291]
iMosflm	[292]
LabSolutions LC/GC 5.81	Shimadzu, Germany
MacVector 12.0.3	MacVector, Inc, UK
NanoDrop ND-1000 Spectrophotometer	ND-1000 V3.2.0
Phaser	[293]
Phenix Suite	[294]
Protein on plate	Formulatrix, USA
Project chemicals	Formulatrix, USA
Pymol	Schrödinger LLC, USA
Rockmaker	Formulatrix, USA
Unicorn 5.31	GE Healthcare, Germany
XDS	[295]

2.1.3 Consumables

Table 2.3 lists the items routinely used in this thesis.

Table 2.3: Consumables

Item	Type	Supplier
Bunsen burner	30% propane, 70% butane	CFH, Germany
Dialysis membranes	ZelluTrans, 3.5 kDa MWCO	Roth, Germany
	CelluSep, 10-14 kDa	Scienova, Germany
Dialysis cassettes	Slide-A-Lyzer™	Thermo Fisher Scientific, Germany
DNA marker	O'Gene Ruler™, 1 kb	Fermentas, Germany
Falcon tubes	15 mL, 50 mL	Sarstedt, Germany
Filter Unit	Millex®-GV, Low protein binding Durapore®, PVDF 0.22 µm	Merck Millipore, Germany
Garbage bag (autoclavable)	E706.1	Carl Roth, Germany
Gloves	Xceed powder free nitrile	Microflex, USA
Lysoformin® spezial		Lysoform, Germany
Nylon membrane	0.2 µm	Millipore, Germany
Parafilm	Parafilm® "M"	Sigma-Aldrich, Germany
Pipetboy	Integra pipetboy	VWR, Germany
Precast gels	Criterion^{TX}	Bio-Rad, Germany
	NuPAGE® Bis-Tris (4-12%)	Thermo Fisher Scientific, Germany
Protein Marker	PageRuler Plus Prestained protein ladder (10-250 kDa)	Thermo Fisher Scientific, Germany
	Spectra™ Multicolor low range protein ladder (1.7 – 40 kDa)	Thermo Fisher Scientific, Germany
Syringe	1 mL dispomed	A. Hartenstein, Germany
	Gastight 1700 series, 100 µL	Hamilton, USA
Test tubes (ÄKTA)	AR® Glas, starkwanding	Neolab, Germany

2.1.4 Molecular biology kits

All molecular biology kits used in this thesis are listed in Table 2.4.

Table 2.4: Commercial molecular biology kits

Kit	Supplier
Plasmid MiniPrep™ MiniKit	Zymo Research, USA
innuPREP DNA/RNA Mini Kit	Analytik Jena, Germany
innuPREP Gel Extraction Kit	Analytik Jena, Germany
Endotoxin-free Plasmid DNA purification	Macharey-Nagel, Germany
Roti®-Transform kit	Carl Roth, Germany

2.1.5 Biochemical kits

All biochemical kits used in this thesis are listed in Table 2.5.

Table 2.5: Commercial biochemical kits

Kit	Supplier
Low molecular weight (LMW) Calibration Kit	GE Healthcare, Germany
High molecular weight (LMW) Calibration Kit	GE Healthcare, Germany

2.1.6 Crystallization screens

All kits used for setting up crystallization plates are listed in Table 2.6.

Table 2.6: Commercial crystallization screens

Kit	Type	Manufacturer
Crystallization screens	Classic	Jena Bioscience, Germany
	Classic Lite Suite	Qiagen, Germany
	Classic II Suite	Qiagen, Germany
	JCSG	Jena Bioscience, Germany
	PACT	Qiagen, Germany
	PEGI	Jena Bioscience, Germany
	PEGII	Jena Bioscience, Germany

2.1.7 Chemicals

All chemicals and media used in this study (Table 2.7) were purchased from the following companies (unless stated otherwise): AppliChem (Darmstadt, Germany), Carl Roth (Karlsruhe, Germany), Jena Bioscience (Jena, Germany), Sigma Aldrich

(Taufkirchen, Germany), GE Healthcare (Germany), Tocris Biosience (UK), Ascent Scientific (UK). Chemicals were bought with the highest purity available.

Table 2.7: Chemicals used in this work

Item	Cat.-No.	Supplier
Acetic acid, 100%	6755	Carl Roth, Germany
Aceton	9375	Carl Roth, Germany
Agarose LE Seakem®	50004	Lonza, Switzerland
(S)-α-Amino-3-hydroxy-5-methylisoxazole-4-propionic acid (AMPA)	Asc-005	Ascent, UK
Ammoniumchloride ($^{15}NH_4Cl$)	299251	Sigma-Aldrich, Germany
Ammoniumperoxodisulfate (APS)	9592	Carl Roth, Germany
Antifoam 204	A6426	Sigma-Aldrich, Germany
(D+) Biotin (Vitamin H)	3822	Carl Roth, Germany
Blue Dextran	D-5751	Sigma-Aldrich, Germany
Boric acid (H_3BO_3)	100165	Merck, Germany
Bovine serum albumin (BSA)	A4503	Sigma-Aldrich, Germany
Bromphenol blue	1.11746.0005	VWR, Germany
Calciumchloride ($CaCl_2$)	CN93	Carl Roth, Germany
Cobaltchloride ($CoCl_2 \times 6\ H_2O$)	255599	Sigma-Aldrich, Germany
cOmplete Mini EDTA-free	1836170001	Sigma-Aldrich, Germany
Coomassie Brillant Blue G-250	A3480	AppliChem, Germany
Copper(II)chloride dihydrate ($CuCl_2 \times 2H_2O$)	467847	Sigma-Aldrich, Germany
Copper(II) sulfate pentahydrate ($CuSO_4 \times 5H_2O$)	C7631	Sigma-Aldrich, Germany
1,2-dioleoyl-sn-glycero-3-phosphate (monosodium salt) (DOPA)	840875P	Avanti Polar Lipids, Alabama
1,2-dioleoyl-sn-glycero-3-phosphocholine (DOPC)	850375P	Avanti Polar Lipids, Alabama

Item	Cat.-No.	Supplier
1,2-dioleoyl-sn-glycero-3-phosphoethanolamine (DOPE)	850725P	Avanti Polar Lipids, Alabama
1,2-dioleoyl-sn-glycero-3-[Phospho-rac-(1-glycerol)] (sodium salt) (DOPG)	840475P	Avanti Polar Lipids, Alabama
1,2-dioleoyl-sn-glycero-3-[phosphor-L-serine] (sodium salt) (DOPS)	840035P	Avanti Polar Lipids, Alabama
D-L-Dithiothreitol	43819	Sigma-Aldrich, Germany
DNQX disodium salt	Asc-169	Ascent, UK
dNTP		KAPA Biosystems, USA
Ethidium bromide (EtBr)	7870	Carl Roth, Germany
Ethylendiamintretraacetic acid, disodium salt (EDTA)	8040	Carl Roth, Germany
FOLCH lipids, brain extract from bovine brain, Type I, FOLCH fraction I	B1502	Sigma-Aldrich, Germany
(5)-Fluorowillardiine	Ab120036	Abcam, UK
Formaldehyde solution, 37%	4979	Carl Roth, Germany
Glucose (D+) anhydrous	X977	Carl Roth, Germany
L-glutamic acid, Kosher	10/071400	SAFC, Sigma-Aldrich, Germany
Glycerin Rotipuran, anhydrous	3783	Carl Roth, Germany
Guanidin hydrochloride	0037	Carl Roth, Germany
HEPES PUFFERAN®	HN78	Carl Roth, Germany
Hydrochloric acid (HCl), 37%	4625	Carl Roth, Germany
Imidazole	A1073	AppliChem, Germany
(S)-5-Iodowillardiine	Ab120222	Abcam, UK
IPTG	2316	Carl Roth, Germany
Iron(III) chloride hexahydrate ($FeCl_3$ x $6H_2O$)	2466466	Merck, Germany
Isopropyl alcohol (2-Propanol)	UN1219	VWR, Germany
Kainic acid	Ab120100	Abcam, UK

Item	**Cat.-No.**	**Supplier**
Magnesium chloride hexahydrate ($MgCl_2$ x $6H_2O$) CELLPURE	HN03	Carl Roth, Germany
Magnesium sulfate	M2643	Sigma-Aldrich, Germany
2-Mercaptoethanol	63689	Sigma-Aldrich, Germany
MES monohydrate	6066	Carl Roth, Germany
Methanol, extra pure	PC43	Carl Roth, Germany
L-Methionine, CELLPURE®	1702	Carl Roth, Germany
MOPS PUFFERAN®	6979	Carl Roth, Germany
Ni(II)sulfate heptahydrate ($NiSO_4$)	2038905	Sigma-Aldrich, Germany
Pefabloc® SC AEBSF	11429876001	Roche Diagnostics, Germany
1,10-Phenanthrolin	13,137	Sigma-Aldrich, Germany
Potassium dihydrogen phosphate, (KH_2PO_4)	P018	Carl Roth, Germany
Rotiphorese® Gel 30 (37.5:1)	3029	Carl Roth, Germany
Sodium acetate, anhydrous (NaAc)	106268	Fluka Chemicals, Switzerland
Sodium chloride (NaCl), CELLPURE	HN00.3	Carl Roth, Germany
Sodium dodecyl sulfate (SDS), ultrapure	2326	Carl Roth, Germany
Sodium fluoride (NaF)	215309	Sigma-Aldrich, Germany
Sodium hydrogen carbonate ($NaHCO_3$)	6885	Carl Roth, Germany
di-sodium hydrogen phosphate, (Na_2HPO_4)	A1046	AppliChem, Germany
Sodium hydroxide (NaOH)	6771	Carl Roth, Germany
1-stearoyl-2-arachidonoyl-sn-glycero-3-[phosphoinositol-4,5-bisphosphate] (tri-ammonium salt) [PI(4,5)P_2]	850165P	Avanti Polar Lipids, Alabama
Temed	2367	Carl Roth, Germany

Item	Cat.-No.	Supplier
Terrific Broth Medium	X972	Carl Roth, Germany
Thiamin hydrochloride (Vitamin B_1)	A0955	AppliChem, Germany
Trichlormethane	6340.2	Carl Roth, Germany
Tricine	T0377	Sigma-Aldrich, Germany
Tris hydrochloride	9090	Carl Roth, Germany
Tris(hydroxymethyl)aminomethane	1.08382	Merck, Germany
Urea	2317	Carl Roth, Germany
(S)-Willardiine	Ab120040	Abcam, UK
Zinc chloride ($ZnCl_2$)	320,808-6	Sigma-Aldrich, Germany

2.1.8 Antibiotics

All antibiotics used in this thesis are listed in Table 2.8.

Table 2.8: Antibiotics

Antibiotic	Cat.-No.	Supplier
Ampicillin sodium salt	K029	Carl Roth, Germany
Chloramphenicol	3886	Carl Roth, Germany
Kanamycin sulfate	T832	Carl Roth, Germany
Tetracycline hydrochloride	0237	Carl Roth, Germany

2.1.9 Synthetic genes

Synthetic genes were ordered from Life Technologies and codon-optimized for expression in *E.coli*.

2.1.10 Enzymes

All enzymes used in this thesis are listed in Table 2.9.

Table 2.9: List of enzymes

Enzyme	Supplier
Alkaline phosphatase	NEB, Germany
CaMK II	NEB, Germany
DNase I (from bovine pancreas)	Roche Diagnostics, Germany
Lysozyme	Carl Roth, Germany
Phusion polymerase	NEB, Germany
PreScission Protease (His_6-tagged)	Home-made, recombinant
Q5 High fidelity DNA polymerase	NEB; Germany
Restriction endonucleases, Fast digest	Thermo Fisher Scientific, Germany
T_4 DNA Ligase	NEB, Germany
TEV protease (His_6-tagged)	Home-made, recombinant
Thrombin, restriction grade	Novagen, Germany
Trypsin	Carl Roth, Germany

2.1.11 Bacterial strains

All bacterial strains that were used in this thesis are listed in Table 2.10.

Table 2.10: Bacterial strains

E.coli **strain**	**Genotype**	**Utilization**	**Supplier**
NovaBlue Giga Singles competent cells	endA1 hsdR17(r_{K12}- m_{K12} -) supE44 thi-1 recA1 gyrA96 relA1 lac F'[proA$^+$B$^+$ lacI^{q}ZΔM15::Tn10 (Tc^R)]	For plasmid propagation	Novagen, Germany
E.coli Origami™ B (DE3) competent cells	F- *ompT hsd*SB(rB- mB-) *gal dcm lacY1 ahpC* (DE3) *gor522*:: Tn*10* *trxB* (Kan^R, Tet^R)	For protein expression	Millipore, Germany
Rosetta™ (DE3)	F$^-$ *ompT hsd*SB(r_B^- m_B^-) *gal dcm* (DE3) pLysSRARE (Cam^R)	For protein expression	Millipore, Germany

2.1.12 Plasmids and constructs

Table 2.11 summarizes the vector systems that were used in this thesis.

Table 2.11: List of vectors

Vector	Description	Reference
pET22b	Amp^R, N-terminal octahistidine-tag and trypsin/thrombin cleavage site	Eric Gouaux, USA
pET Duet	Amp^R, N- and C-terminal hexahistidine and GB-1 tags, TEV protease and thrombin cleavage site	Phil Selenko, Germany
pRSET	Amp^R, N-terminal heptahistidine-tag, non-cleavable	Per Jemth, Sweden

Table 2.12 lists all the plasmids encoding the protein of interest for recombinant protein expression. The numbering of the amino acids is according to the full-length GluA2 receptor. All GluA2 LBD construct harbored an N-terminal octahistidine (His_8)-tag, cleavable by either trypsin or thrombin.

Table 2.12: List of constructs used in this thesis

Vector	Protein	Length	Comment	Abbreviation/ construct number
Rattus norvegicus GluA2 LBD constructs				
pET22b	GluA2 LBD	394 – 506-(GT dipeptide linker)-632 – 774	Flop isoform, WT, S1S2J	WT
pET22b	GluA2 LBD	394 – 506-(GT dipeptide linker)-632 – 774	Flop isoform, A665C	
pET22b	GluA2 LBD	394 – 506-(GT dipeptide linker)-632 – 774	Flop isoform, A665C, L483Y	

Table 2.12 – Continued from previous page

Vector	Protein	Length	Comment	Abbreviation/ construct number
pET22b	GluA2 LBD	394 – 506-(GT dipeptide linker)-632 – 774	Flop isoform, I664C	
pET22b	GluA2 LBD	394 – 506-(GT dipeptide linker)-632 – 774	Flop isoform, I664C, L483Y	
pET22b	GluA2 LBD	394 – 506-(GT dipeptide linker)-632 – 774	Flop isoform, E713T	
pET22b	GluA2 LBD	394 – 506-(GT dipeptide linker)-632 – 774	Flop isoform, E713T, Y768R	TR
pET22b	GluA2 LBD	394 – 506-(GT dipeptide linker)-632 – 774	Flop isoform, G437H, K439H, D456H	HHH
pET22b	GluA2 LBD	394 – 506-(GT dipeptide linker)-632 – 774	Flop isoform, E713T, Y768R, G437H, K439H, D456H	HHH_{TR}
pET22b	GluA2 LBD	394 – 506-(GT dipeptide linker)-632 – 774	Flop isoform, L483Y, G437H, K439H, D456H	HHH_{LY}
pET22b	GluA2 LBD	394 – 506-(GT dipeptide linker)-632 – 774	Flop isoform, G437H, K439H, D456H, H412A, H435A	HHHAA
pET22b	GluA2 LBD	394 – 506-(GT dipeptide linker)-632 – 774	Flop isoform, L483Y, G437H, K439H, D456H, H412A, H435A	$\text{HHH}_{\text{LY}}\text{AA}$
pET22b	GluA2 LBD	394 – 506-(GT dipeptide linker)-632 – 774	Flop isoform, G437H, K439H, D456H, H412A, H435A, D668A	HHHAAA

Table 2.12 – Continued from previous page

Vector	Protein	Length	Comment	Abbreviation/ construct number
pET22b	GluA2 LBD	394 – 506-(GT dipeptide linker)-632 – 774	Flop isoform, L483Y, G437H, K439H, D456H, H412A, H435A, D668A	HHH$_{LY}$AAA
Rattus norvegicus Stargazin C-terminal tail (203-323, stargazin$^{203-323}$) constructs				
pETDuet	STG	203 - 323	C302S, N- terminal His$_6$ –tag, TEV cleavage site	15-58
pETDuet	STG	203 - 323	C302S, N- terminal His$_6$ –tag, PreScission Protease cleavage site	15-59
pETDuet	STG	203 - 323	C302S, N- and C-terminal GB-1/His$_6$ -tags	15-55
pETDuet	STG	203 - 323	C302S, N-terminal His$_6$/GB-1 tag	15-54
pETDuet	STG	203 - 323	C302S, N-terminal His$_6$/GB-1 tag, GGGG-linker between GB-1 and cleavage site	15-56
pETDuet	STG	203 - 323	C302S, C-terminal His$_6$/GB-1 tag,	15-57
pETDuet	STG	203 - 323	C302S, N-terminal His$_6$/GB-1 tag, (GS)$_3$ -linker before cleavage site	15-74
pETDuet	STG	203 - 323	C302S, N-terminal His$_6$/GB-1 tag, (GS)$_3$ -linker before and (Gly)$_4$-linker after cleavage site	15-73

Table 2.12 – Continued from previous page

Vector	Protein	Length	Comment	Abbreviation/ construct number
Human PDZ-domains from PSD-95				
pRSET	PDZ1	61 – 151	WT, non-cleavable His_5-tag	
pRSET	PDZ2	155 – 249	WT, non-cleavable His_5-tag	
pRSET	PDZ3	209 – 401	WT, non-cleavable His_5-tag	

2.1.13 Media and buffers

Buffers and media were prepared with Milli-Q water and filtered (0.22 µm or 0.1 µm). The pH was adjusted with 37% HCl or 10 M or 1 M NaCl if not stated otherwise. All buffers needed for molecular biology experiments are listed in Table 2.13.

Table 2.13: Buffers used for molecular biology

Medium	Components
TAE buffer	40 mM Tris 1 mM EDTA, pH 8.0 20 mM acetic acid
DNA loading dye (6x) (Thermo Fisher)	10 mM Tris-HCl pH 7.6 0.15% orange G 0.03% Xylene cyanol FF 60% glycerol 60 mM EDTA

Table 2.14 lists all media that were used for the expression of *E.coli* in this work.

Table 2.14: Media for bacterial expression

Medium	Components	Supplier
LB (Luria-Miller)	10 g/L tryptone 5 g/L yeast extract 10 g/L NaCl pH 7.0 ± 0.2	Carl Roth, Germany
LB agar (Lennox)	10 g/L tryptone 5 g/L yeast extract 5 g/L NaCl 15 g/L agar agar pH 7.0 ± 0.2	Carl Roth, Germany
M9 minimal medium	6 g/L Na_2HPO_4 3 g/L KH_2PO_4 0.5 g/L NaCl 0.5 g/L $^{15}NH_4Cl$ 4 g/L glucose 1 mM $MgSO_4$ 1 mM $CaCl_2$ 1 mg/L Biotin 1 mg/L Thiamin 50 mg/L EDTA 8.3 mg/L $FeCl_3$ x $6H_2O$ 0.84 mg/L $ZnCl_2$ 0.13 mg/L $CuCl_2$ x $2H_2O$ 0.13 mg/L $CoCl_2$ x$6H_2O$ 10 µg/L H_3BO_3 16 µg/L $MnCl_2$ x $6H_2O$	Home-made
TB (Terrific Broth)	12 g/L caseine 24 g/L yeast extract 12.5 g/L K_2HPO_4 2.3 g/L KH_2PO_4 pH 7.2 ± 0 .2	Carl Roth, Germany

Table 2.14 - Continued from previous page

Medium	Components	Supplier
SOB medium	20 g/L tryptone 5 g/L yeast extract 0.5 g/L NaCl 2.5 mM KCl pH 6.8 – 7.0	
SOC medium	1x SOB medium 10 mM $MgCl_2$ 10 mM $MgSO_4$ 20 mM glucose	Self-made; Novagen, Germany

All buffers needed for biochemical assays are listed in Table 2.15.

Table 2.15: Buffers for biochemistry

Medium	Components
Coomassie staining solution	0.25% (w/v) Coomassie Brillant Blue 50 % (v/v) Ethanol 10 % (v/v) acetic acid
Coomassie destaining solution	20% (v/v) Ethanol 7 % (v/v) acetic acid
NuPAGE® MES SDS running buffer	50 mM MES pH 7.3 50 mM Tris Base 0.1% SDS 1 mM EDTA
MOPS running buffer	50 mM MES pH 7.3 50 mM Tris Base 0.1% SDS 1 mM EDTA

Table 2.15 - Continued from previous page

Medium	Components
SDS loading dye (4x)	250 mM Tris-HCl pH 6.8 0.4 % Bromphenol blue 40% glycerol 8% SDS 6% DTT Milli-Q ad 25 mL
Separating buffer (4x)	1.5 M Tris pH 8.8 0.4 % SDS
Stacking buffer (4x)	0.5 M Tris pH 6.8 0.4% SDS
Tris/glycine running buffer (10x)	250 mM Tris pH 8.3 1.92 M glycine 1% SDS

For discontinuous SDS-PAGE, the following recipe was used (Table 2.16):

Table 2.16: Pipetting scheme for preparation of discontinuous SDS-PAGE with different percentages

Mini gel (16 mL) %	5	7,5	8,5	10	11,5	12,5	15	18	20	Upper (stacking)
Bottom gel stock (mL)	4,0	4,0	4,0	4,0	4,0	4,0	4,0	4,0	4,0	-
Upper gel stock (mL)	-	-	-	-	-	-	-	-	-	1,25
Acrylamide stock (mL)	2,7	4,0	4,6	5,3	6,1	6,7	8,0	9,6	10,7	0,75
H2O (mL)	9,3	8,0	7,4	6,7	5,9	5,3	4,0	2,4	1,3	3,0
10% APS (µL)	80	80	80	80	80	80	80	80	80	30
TEMED (µL)	8	8	8	8	8	8	8	8	8	10

All buffers used for the purification of GluA2 LBDs are listed in Table 2.17.

Table 2.17: Buffers for purification of GluA2 LBDs

Buffer	Components
Lysis Buffer/Resuspension buffer	20 mM Tris-HCl pH 8.0 150 mM NaCl 1 mM Glu 5 mM $MgSO_4$ 5 mM Met* 1 mM PEFA* 25 µg/mL DNase I* 50 µg/mL lysozyme* (* add fresh before use)
Ni-NTA buffer A	20 mM Tris-HCl pH 8.0 150 mM NaCl 1 mM Glu 5 mM Met*
Ni-NTA buffer B (elution buffer)	20 mM Tris-HCl pH 8.0 150 mM NaCl 1 mM Glu 5 mM Met* 400 mM imidazole
Dialysis buffer post-NTA	20 mM Tris-HCl pH 7.4 200 mM NaCl 1 mM Glu 1 mM EDTA 1 mM $CaCl_2$ 5 mM Met*
Dialysis buffer post trypsin cleavage	20 mM NaAc pH 5.0 1 mM EDTA 1 mM Glu 5 mM Met*

Table 2.17 - Continued from previous page

Buffer	Components
Cation exchange buffer A	20 mM NaAc pH 6.0 1 mM EDTA 1 mM Glu 5 mM Met*
Cation exchange buffer B	20 mM NaAc pH 6.0 1 mM EDTA 1 mM Glu 5 mM Met* 1000 mM NaCl
Size exclusion buffer	10 mM HEPES pH 7.0 150 mM NaCl 10 mM Glu 1 mM EDTA
Crystallization buffer	10 mM HEPES pH 7.0 150 mM NaCl 10 mM Glu 1 mM EDTA
Ligand exchange buffer #1 (removal of glutamate)	10 mM HEPES pH 7.0 150 mM NaCl 1 mM EDTA
Ligand exchange buffer #2 (washing in of new ligand)	10 mM HEPES pH 7.0 150 mM NaCl 1 mM EDTA 10 µM ligand
Ligand exchange buffer #3	10 mM HEPES pH 7.0 150 mM NaCl 1 mM EDTA 10 mM ligand

All buffers used for the purification of the stargazin C-terminal tail are listed in Table 2.18.

Table 2.18: Buffers for purification of stargazin C-terminal tail

Buffer	Components
Lysis Buffer/Resuspension buffer	20 mM Tris-HCl pH 8.0 150 mM NaCl 1 mM PEFA* 25 µg/mL DNase I* 50 µg/mL lysozyme* (* add fresh before use)
Ni-NTA buffer A	10 mM Tris-HCl pH 8.0 150 mM NaCl
Ni-NTA buffer B	10 mM Tris-HCl pH 8.0 150 mM NaCl 500 mM imidazole
Dialysis buffer	10 mM Tris-HCl pH 8.0 150 mM NaCl
Cation exchange buffer A	10 mM Hepes pH 7.0
Cation exchange buffer B	10 mM HEPES pH 7.0 1000 mM NaCl
Size exclusion buffer	10 mM HEPES pH 7.0 150 mM NaCl
NMR buffer	10 mM HEPES pH 6.8 75-100 mM NaCl

Buffers used for biophysical measurements are listed in Table 2.19.

Table 2.19: Buffers for biophysical measurements

Buffer	Components
RALS measurement	10 mM HEPES pH 7.0 150 mM NaCl
CD spectroscopy	100 mM NaF (or $NaClO_4$) 10 mM KPO_4 (K_2HPO_4 and KH_2PO_4) pH 8.5
Liposome co-sedimentation	10 mM HEPES pH 7.0 75 mM NaCl

2.2 METHODS

2.2.1 Molecular biology methods

All molecular biology methods were performed as described in Green and Sambrook, 2012, unless stated otherwise [296]. Commercial kits were used according to the manufacturer's instructions.

2.2.1.1 Site-directed mutagenesis

2.2.1.1.1 *Preparation of mutagenesis and flanking primers*

Mutagenesis primer/mismatching primers and flanking primers were designed using the MacVector software (MacVector, Inc., Cambridge, UK). Primers were ordered from Eurofins MWG (Ebersberg, Germany). Lyophilized primers were dissolved in 1x TAE buffer (Macherey Nagel, Germany) and stored at -20°C prior to usage.

2.2.1.1.2 *Polymerase chain reaction (PCR)*

Polymerase chain reaction (PCR) is an *in vitro* method for a primer-based, enzymatic amplification of a specific deoxyribonucleic acid (DNA) region. This exponential reaction is catalyzed by a thermostable DNA-dependent DNA polymerase. Repeating steps of denaturation (generation of single-stranded DNA), annealing [annealing of primers to single-stranded DNA (ssDNA)] and extension (extension of primers from 5'→ 3' end) lead to specific amplification of a desired DNA region.

For amplification of DNA fragments either Phusion polymerase or Q5 polymerase (NEB, Germany) were used according to the manufacturer's recommendations.

2.2.1.1.3 *Site-directed mutagenesis by overlap PCR*

In order to site-specifically incorporate mutations into a gene of interest, overlap PCR was used [297]. This is a two-step PCR reaction that uses flanking primers (F1 and F2) and specific mutagenesis primers (m1 and m2) carrying the mutation to be introduced. A scheme describing the method for overlap extension PCR is shown in Figure 2.1.

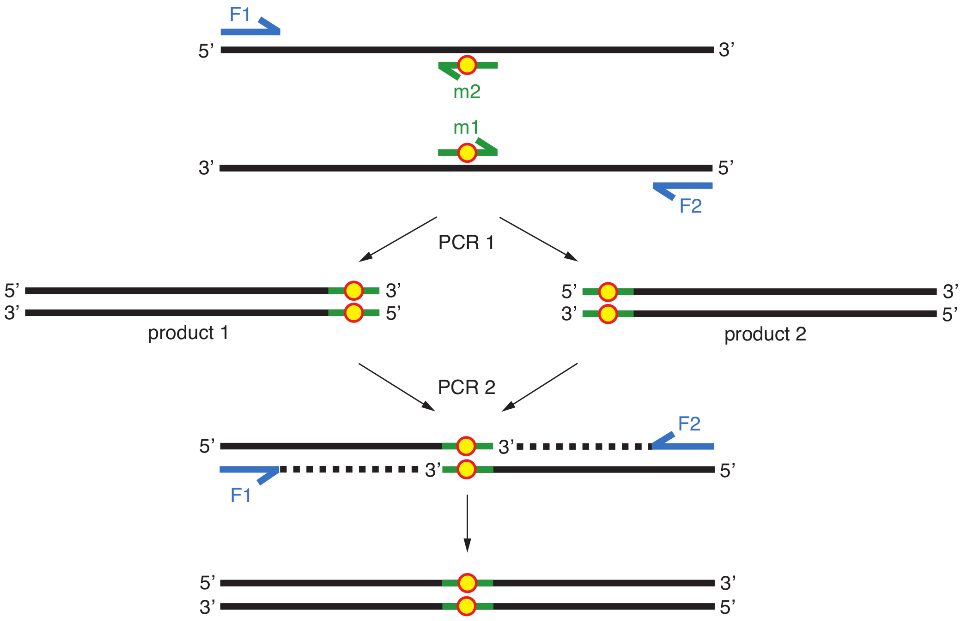

Figure 2.1: Schematic representation of an overlap PCR in order to introduce site-specific mutations. Mutagenesis primers (green) and flanking primers (blue) were used in order to specifically replace one amino acid (yellow dot). Intermediate PCR products were formed by combination of the primer pairs F1 + m2 and F2 + m1, respectively and contain an overlapping region with the introduced mutation. The two fragments were used as DNA template in a second round of PCR together with flanking primers F1 and F2. This leads to amplification of the full insert that will later be ligated into an appropriate DNA vector.

The first round of the PCR consists of two separate PCR reactions and leads to formation of two PCR intermediates (F1 and m2 generate PCR product 1 and F2 and m1 generate PCR product 2) with partial overlapping sequences. Since the overlapping parts are complementary they can anneal in the second round of PCR, thus acting as a DNA template. The polymerase fills out the missing parts and flanking primers F1 and F2 are used for amplification of both strands.

2.2.1.1.4 *PCR for overlap PCR*

A typical pipetting scheme for an overlap PCR is shown in Table 2.20.

Table 2.20: Pipetting scheme for an overlap PCR

Component	Stock concentration	Amount	Final concentration
DNA template	X ng/µL	10 ng	10 ng
5 x HF buffer	7.5 mM $MgCl_2$	10 µL	1.5 mM $MgCl_2$
dNTP mix	10 mM	1 µL	0.2 mM
Primer 1	25 µM	1 µL	0.5 µM
Primer 2	25 µM	1 µL	0.5 µM
Phusion polymerase	2 U/µL	0.5 µL	1 U
Nuclease-free H_2O (ad 50 µL)		X µL	
Total volume		50 µL	

The annealing temperature is dependent on both primer length and primer sequence and was calculated using the "Multiple primer analyzer" (Thermo Fisher Scientific, Germany). The annealing temperature was usually set 2°C above the T_M of the primer with the lower T_M. Alternatively, if one given T_M didn't yield any DNA fragment, a gradient PCR with different annealing temperatures was conducted. Table 2.21 shows typical thermocycling conditions for a PCR.

Table 2.21: Typical PCR program showing thermocycling conditions

Step	Temperature	Time	Cycles
Initial denaturation	98°C	1 min	
Denaturation	98 °C	15 sec	25-35 cycles
Annealing	T_M-3°C	10-30 sec	
Extension	72°C	20-30 sec/kb	
Final extension	72°C	5 min	
Hold	7°C	hold	

2.2.1.1.5 *Restriction-free (RF) cloning*

Restriction-free (RF) cloning is a method that is independent of restriction sites or alterations in the vector and thus also doesn't need a ligation step as needed for conventional overlap PCRs [298]. In contrast to conventional overlap PCR, this method enables incorporation of whole genes into the vector.

In this thesis, RF cloning was used for the incorporation of a synthetic gene encoding for stargazin C-terminal tail into an appropriate expression vector. In contrast to ligation-independent cloning (LIC), no special vector system is needed. RF cloning also consists of two steps similar to the conventional overlap PCR. However, only mutagenesis primers harboring the mutation or gene are required. Figure 2.2 shows a scheme for the RF cloning approach.

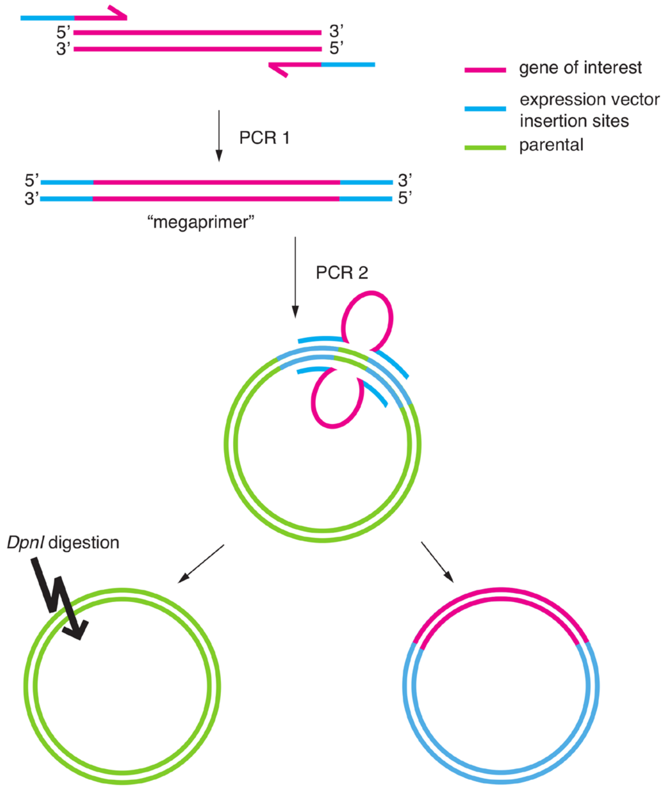

Figure 2.2: Schematic representation of restriction-free (RF) cloning. Primers are generated that overlap with both the gene of interest (magenta) and the target vector (cyan). The first PCR leads to generation of megaprimers that are complementary to the target vector on both the 5' and the 3' end. These megaprimers are used in a second PCR for a linear amplification reaction.

In the first round of PCR "megaprimers" are being generated. For this first step a set of two primers is needed as well as the synthetic gene. The forward primer has a ~24 nucleotide (nt) overlap with the vector followed by the start codon of the gene of interest and ~25 nt of the 5' end of the gene of interest. Accordingly, the reverse primer has a ~24 nt overlap with the 3' end of the point of insertion. The first PCR thus leads to generation of a "megaprimer" that will be used in the second round of PCR. Together with the DNA template the synthetic gene is than incorporated into the new expression vector. The PCR product was *DpnI* (2 µL) treated for 2 hours at 37°C in order to digest the parental methylated DNA.

2.2.1.1.6 *PCR for RF cloning*

A typical PCR program for the first step (generation of megaprimer) of the restriction-free approach is shown in Table 2.22.

Table 2.22: 1st PCR step: generation of megaprimers

Component	Stock concentration	Amount	Final concentration
DNA template	X ng/µL	1 pg-10 ng	1 pg-10 ng
Phusion HF buffer (5x)	5x	10 µL	1x
dNTPs	10 mM	1 µL	0.2 mM
Fwd primer	10 µM	2.5 µL	0.5 µM
Rev primer	10 µM	2.5 µL	0.5 µM
Nuclease-free H_2O (ad 50 µL)		X µL	
Phusion DNA polymerase	2 U/µL	0.5 µL	0.02 U/µL
Total volume		50 µL	

The thermocycling conditions for this PCR are shown in Table 2.23.

Table 2.23: PCR program for RF cloning approach

Step	Temperature	Time	cycles
Hot start	98°C	hold	
Initial denaturation	98°C	30 sec	
Denaturation	98 °C	10 sec	35 cycles
Annealing	T_M-3°C	30 sec	
Extension	72°C	20-30 sec/kb	
Final extension	72°C	8 min	
Hold	4°C	hold	

In the second PCR, the whole new vector is amplified. Therefore the elongation time is much longer. Typically 2 min per kilobase (kb) were used.

2.2.1.2 Agarose gel electrophoresis

PCR products were typically loaded on an agarose gel after each PCR step in order to separate the products from impurities or excess primers and to visualize the result of the PCR reaction.

Depending on the length of the DNA fragment a 0.8%-1.0 % agarose gel was prepared. Agarose gels were prepared and run according to standard procedures [296]. Shortly, the agarose was dissolved in 1x TAE buffer and supplemented with ethidium bromide (1:10000 of a 1% solution). DNA fragments or PCR products were supplemented with 6 x DNA loading dye and then separated by applying a voltage of 100-120 V. A DNA standard was always included.

The loading dye was chosen depending on the DNA fragment size, since the dyes themselves run differently in the gel. Xylene cyanol migrates at approximately 4 kilobases (kb), whereas bromphenol blue migrates much lower at 300 base pairs (bp) and orange G migrates at 50 bp. Separated DNA fragments were visualized using a ultraviolet (UV) lamp and excised for later gel extraction if necessary.

2.2.1.3 DNA purification

In order to have pure PCR products to proceed with and to eliminate the remaining primers, bands comprising the DNA of interest were excised with a sterile razor blade under UV light and purified according to the manufacturer’s recommendations (InnuPREP Gel Extraction Kit, Analytik Jena, Germany).

2.2.1.4 DNA restriction

In order to prepare the DNA inserts for ligation into an appropriate vector, both the vector backbone and the insert have to be treated with the same set of restriction enzymes.

The DNA was digested using restriction endonucleases from Thermo Fisher Scientific (NEB, Germany) according to the manufacturer’s protocol. Fast digest endonucleases (FD) have 100% buffer compatibility and according to the manufacturer, 1 µL of enzyme is able to digest 1 µg of DNA in 5-15 minutes at 37°C. A schematic protocol for a digestion is shown in Table 2.24.

Table 2.24: Pipetting scheme for DNA digestion

Component	Volume
XhoI FD	1.3 µL
XbaI FD	1.3 µL
DNA	1 µg
10 x FD buffer	6 µL
H_2O	ad 50 µL
Σ=	60 µL

2.2.1.5 Dephosphorylation of the vector backbone

After digestion the vector backbone was dephosphorylated using alkaline phosphatase (FastAP). Digested DNA possesses a 5' phosphate group that can re-ligate with the 3' hydroxyl group of the backbone. In order to prevent re-ligation, a dephosphorylation of the vector backbone was carried out after DNA restriction. For dephosphorylation, 3 µL of FastAP were added to 60 µL of the digested sample and incubated for 10 minutes at 37°C. The phosphatase was heat inactivated for 5 minutes at 70°C. Samples were run on an agarose gel and insert DNA and vector backbone were excised for a ligation reaction.

2.2.1.6 DNA ligation

Ligation reactions were ideally performed on the same day as the transformation to increase transformation efficiency. For ligation into the host vector the molar ratio between insert and vector was usually 3:1, but the ratio also depends on the size [299]. T4 DNA ligase (NEB, Germany) was incubated for 20 minutes at room temperature followed by heat inactivation for 5 minutes at 70°C. As a control, a ligation reaction was prepared with the dephosphorylated vector backbone but without DNA insert. The reaction batch was prepared as shown in Table 2.25.

Table 2.25: Ligation of DNA insert into host vector

Component	DNA insert and vector backbone	Control: vector backbone
T4 DNA ligase	1 µL	1 µL
T4 DNA ligase buffer (10 x)	2 µL	2 µL
DNA insert	x µL	----
DNA template	x µL (50 ng)	2-3 µL
H_2O	x µL	15 µL
Σ	20 µL	20 µL

2.2.1.7 Transformation of chemically competent E.coli cells

Depending on the downstream purpose, different bacteria strains were used. For plasmid maintenance, the *E.coli* NovaBlue Giga Singles competent cells were used (Novagen, Germany). For protein expression either *E.coli* Origami™ B (DE3) competent cells or Rosetta™ (DE3) cells were used.

20-60 µL of competent cells were thawed on ice. 2 µL of the ligation reaction was added to the competent cells and incubated for 10 min on ice. DNA uptake is achieved by a 40 sec heat shock at 42°C, which generates pores within the bacterial cell membrane and thereby allows uptake of the DNA. After the heat shock, the cells were chilled on ice for 2 min. 250 µL SOC medium was added and the tube was shaken for 1 h at 37°C and 200 rounds per minute (rpm) in order to allow the antibiotic resistance gene to be activated. Approximately 70 µL were plated out on an agar plate (LB agar) containing the appropriate antibiotics (typically 1:1000).

2.2.1.8 Preparation of chemically competent E.coli cells

Chemically competent cells were prepared from Rosetta cells using the Roti®-Transform kit (Carl Roth, Germany) and aliquots were stored at -80°C until usage.

2.2.1.9 Isolation of plasmid DNA

Isolation of plasmid DNA was carried out according to the protocol of the manufacturer (Plasmid MiniPrep™ MiniKit from Zymo research, USA or innuPREP DNA/RNA Mini Kit from Analytik Jena, Germany). For DNA isolation a 5-10 mL culture was prepared in LB and inoculated with a clone. The culture was grown at 37°C and 190 rpm overnight or for least 7-8 hours.

2.2.1.10 Determination of DNA concentration

DNA concentrations were measured using the Nanodrop ND-1000 (Thermo Scientific, Germany).

The ratio of the absorption at 260 nm and 280 nm was used to assess the purity of the DNA and should ideally lie between 1.8 and 1.9.

2.2.1.11 Preparation of E.coli cryo stocks

If not stated specifically, protein expression was carried out from a glycerol stock enabling for long-term storage of bacteria. Glycerol stocks were prepared by mixing 1 mL of an overnight culture (with OD_{600} between 0.5 and 0.7) with 0.5 mL sterile 100% glycerol. Cryo-stocks were stored at -80°C.

2.2.1.12 DNA sequencing

In order to confirm the success of mutagenesis all insertions were double-sequenced using the Source Bioscience sequencing service (Berlin, Germany). A sequencing sample was prepared by mixing 5 µL of 100 ng/µL together with 5 µL of a 3.2 µM primer.

Sequences were checked using ClustalW (v1.83) implemented in MacVector (MacVector, Inc, UK) [300].

2.2.1.13 Long-term plasmid storage in archive

For long-term storage of the plasmid DNA, 1-2 µg DNA were stored in a final concentration of 70% EtOH (non denatured) at -20°C.

2.2.1.14 Sequence alignments

DNA sequence alignments were performed using MacVector (MacVector, Inc, UK). ClustalW was used for multiple protein sequence alignments [301-303]. For secondary structure predictions JPred [304] or PsiPred were used.

2.2.2 Protein expression and purification

Purification of histidine-tagged fusion proteins consisted of the following steps:

1. Nickel nitrilotriacetic acid (Ni-NTA) affinity chromatography
2. Tag cleavage and removal by trypsin or tobacco etch virus (TEV) protease
3. Reapplication of cleaved protein to Ni-NTA column (for stargazin)
4. Cation exchange
5. Size exclusion chromatography

All purification steps were performed on an ÄKTA purifier. The purification was monitored by measuring the absorption at 280 nm and peak fractions were analyzed by SDS-PAGE (Section 2.2.4.1). All chromatographic procedures were performed at 10°C. A detailed description of the individual chromatographic steps can be found in this section (Section 2.2.2.7 until Section 2.2.2.11).

2.2.2.1 Antibiotics

Working concentrations for antibiotics in either liquid medium or agar plates used in this work are listed in Table 2.26.

Antibiotics were dissolved in the corresponding solvent and sterile-filtered through a 0.22 µm membrane.

Table 2.26: Stock concentrations and final concentrations of antibiotics

Antibiotic agent	Stock concentration	Final concentration	Dilution	Solvent
Ampicillin (Amp)	100 mg/mL	100 µg/mL	1:1000	Milli-Q
Chloramphenicol (Cam)	34 mg/mL	34 µg/mL	1:1000	100% EtOH
Kanamycin (Kan)	15 mg/mL	15 µg/mL	1:1000	Milli-Q
Tetracycline (Tet)	12.5 mg/mL	12.5 µg/mL	1:1000	Milli-Q

2.2.2.2 Protein over-expression test in E.coli

In order to test protein over-expression of the desired construct, a 5 mL overnight culture was prepared in medium [Luria Miller (LB), Terrific Broth (TB) or M9] supplemented with the respective antibiotics and grown at 37°C until the OD_{600} reached 0.8-1.0. Protein expression was induced by addition of 0.1-1 mM isopropyl-β-D-thiogalactopyranoside (IPTG), depending on the construct. Different expression temperatures were tested in order to screen for high expression rates, i.e. 18°C, 30°C or 37°C. A decreased temperature leads to slow down of cell growth and endogenous protein synthesis thereby helping to keep the over-expressed protein soluble. A 50 µL aliquot was taken before (non-induced; NI) and after induction (induced; I) and centrifuged for 5 min at 20000 x g. The pellet was resuspended in 40 µL Milli-Q and supplemented with 10 µL 4x sodium dodecylsulfate (SDS) loading dye, boiled for 5 min at 95°C and subjected to sodium dodecylsulfate polyacrylamide gel electrophoresis (SDS-PAGE).

2.2.2.3 Small scale protein solubility test

To test the solubility of a given construct, 1 L TB medium supplemented with the respective antibiotics was inoculated with 20 mL of an overnight *E.coli* culture in LB medium. Cells were grown at 37°C and 190 rpm until an OD_{600} of 0.6-0.8. The culture was cooled down to typically 18°C and protein expression was induced by addition of 0.1-1 mM IPTG and cells were grown for another 16-20 h. Bacteria were collected by centrifugation at 7,000 rpm (12,227 x g) and 4°C for 10 min in a Beckman Coulter Avanti J-26 XP centrifuge with a JLA 8.1000 rotor. Cell lysis was performed as described below. The supernatant was supplemented with 20 mM imidazole and applied on a HisTrap HP chromatography column equilibrated with 5 column volumes (CV) Ni-NTA buffer A. The column was washed extensively with Ni-NTA buffer supplemented with 20 mM imidazole until a stable baseline was reached. The sample was either eluted with a linearly increasing concentration of imidazole or a step elution. Typically, 2 mL fractions were collected during elution. Aliquots were taken at every step of the test purification for further analysis with SDS-PAGE.

2.2.2.4 Large scale protein over-expression

In order to obtain sufficient protein amounts for downstream applications like crystallography or NMR, a 12 L culture was prepared. To ensure proper air supply, buffled 4 L flasks were used and filled with 2 L of LB or TB medium supplemented with the corresponding antibiotics. For higher expression yields of stargazin C-terminal tail, bacteria were grown in TB medium, whereas LBD constructs were expressed in LB medium. The culture was inoculated 1:100 with an overnight *E.coli* culture harboring the expression construct. The cells were grown to an OD_{600} of 0.8-1.0 at 37°C and 170 rpm. Prior to induction, the cells were cooled down to 18°C and expression was induced by adding 0.1- 1 mM IPTG.

The cells were harvested by centrifugation at 7,000 rpm for 10 min at 4°C in a JLA 8.1000 rotor, pellets were scraped out and filled into a 50 mL tube. The pellet was either directly lysed for purification or flash-frozen in liquid nitrogen for storage at -80°C.

2.2.2.5 Large scale over-expression of ^{15}N -labeled protein

In order to produce ^{15}N-labeled protein for nuclear magnetic resonance (NMR) studies, all other natural nitrogen sources have to be withdrawn from the medium. Addition of a ^{15}N-salt ($^{15}NH_4Cl$) ensures incorporation of the heavy nitrogen isotope into the protein. However, the cell growth and the protein expression were very low when the starting culture was prepared in M9. Therefore the culture was prepared in TB medium for maximal cell growth and then switched to M9 minimal medium for protein expression only (also see Section 3.2.6.1). A starting culture of 10 mL was inoculated with clones from a fresh transformation of *E.coli* cells harboring the construct of interest. The starting culture was grown at 37°C and 200 rpm. 10 mL of this culture were used for inoculation of 1 L TB medium supplemented with the appropriate antibiotics. The main culture was shaken at 37°C and 190 rpm until an OD_{600} of > 2. Bacterial cells were collected carefully at 3000 x g for 10 min at 4°C using a Beckman Coulter Avanti J-26 XP centrifuge with a JLA 8.1000 rotor. Cells were washed twice with ice-cold Milli-Q and carefully centrifuged again. The washed pellet was resuspended in M9 minimal medium supplemented with the respective antibiotics and the $^{15}NH_4Cl$ salt. Typically, the pellet from 4 L in TB medium was resuspended in 1 L M9 medium to increase cell density.

Cells were shaken for 1 h at 37°C and 170 rpm to allow adaption to the new medium. After 1 h in M9, protein expression was induced by addition of 1 mM IPTG for 4 h. After 4 h, cells were harvested as described below (Section 2.2.2.6) and either lysed and purified or flash-frozen in liquid nitrogen and stored at -80°C until further usage.

2.2.2.6 E.coli cell lysis and preparation of soluble fraction

The bacterial cell pellet was thawed on ice by adding 5- 10 mL of lysis buffer per 1 g of cell pellet. The buffer was supplemented with 25 µg/mL DNase I, 50 µg/mL lysozyme and 1 mM PEFA. For cell lysis of Origami™ B (DE3) cells the suspension was passed at least twice through an ice-cooled Avestin EmulsiFlex-C5 to disrupt the cells. For efficient lysis, the pressure was set to 15,000-17,000 psi.

Rosetta™ (DE3) cells were lysed using sonication (Sonopuls HD 2200). The sample was sonicated 5-6 times for 20 seconds. Between the repetitions, the sample was chilled on ice for 1 min. One sonication pulse consists of a 0.5 sec pulse, followed by a 0.5 sec period of rest (5 cycle). The lysate was ultracentrifuged at 32,000 rpm (175,000 x g) in a Beckman Coulter Optima™ L-90K centrifuge with a Ti SW-32 rotor for 45 min at 4°C. Alternatively centrifugation was done in a Beckman Coulter Avanti J-26 XP centrifuge with a JA 22.50 rotor and a speed of 22,500 rpm (61,236 x g) for 40 min at 10°C.

The supernatant was supplemented with 50 mM imidazole and applied on an HisTrap HP chromatography column equilibrated with 5 column volumes (CV) Ni-NTA buffer A.

2.2.2.7 Ni-NTA affinity chromatography

Immobilized metal affinity chromatography (IMAC) is based on a biospecific, coordinated interaction between basic groups on a protein, in most cases histidine residues, and metal ions immobilized on a resin [305]. The columns used in this thesis are prepacked with Ni Sepharose™ and cross-linked agarose beads. Immobilized chelating groups on the surface of the beads are responsible for metal ion coordination. NTA has four chelating sites for nickel ions, which makes it a relatively strong chelator.

All chromatographic procedures were conducted at 10°C. 20 mM imidazole was added to the supernatant to decrease binding of unspecific proteins to the column and the supernatant was loaded on a 1 mL/5 mL HisTrap HP column equilibrated with 5 CV of Ni-NTA buffer A. The column was washed with Ni-NTA buffer and an imidazole concentration of 20 mM imidazole until a stable baseline was reached (typically 10 CV). The protein was eluted with a linear gradient ranging from 10 mM to 400 mM imidazole over 10 CV, collecting 1 or 2 mL fractions. The elution profile was monitored by measuring the absorption at 280 nm. Protein-containing fractions were subjected to SDS-PAGE.

2.2.2.8 Histidine-tag cleavage and dialysis

2.2.2.8.1 *Octahisitidine (His$_8$)-tag cleavage for GluA2 LBD (S1S2J) constructs*

Eluted protein from the first chromatography column was subjected to tag cleavage by a specific protease.

GluA2 LBD constructs have a thrombin cleavage site upstream of the LBD sequence. The tag can also be cleaved with trypsin. Trypsin cleaves proteins C-terminally to Arg and Lys residues [306]. Using a limited proteolysis approach for identification of the ligand-binding domain boundaries it has been shown that ligand-bound S1S2 domain is stabilized against trypsin digestion, thereby being a good candidate for easy removal of the histidine tag [107].

For buffer exchange, pooled fractions were dialyzed overnight at 4°C against dialysis buffer post-NTA using a 12-14 kDa molecular weight cutoff membrane (MWCO). Optionally, a desalting column was used for buffer exchange if purification was continued on the same day. The N-terminal histidine tag was removed by addition of 1:100 molar ratio of trypsin. Digestion was performed for 1 h at room temperature and stopped by adding 1 mM Pefabloc® SC AEBSF and incubation for 10 min on ice. Adding 1 mM EDTA for 10 minutes at room temperature stopped Pefabloc®.

2.2.2.8.2 *Hexahistidine (His$_6$)-GB-1-tag cleavage for stargazin constructs and second Ni-NTA chromatography*

For constructs harboring the cytoplasmatic tail of stargazin a tobacco etch virus (TEV) cleavage site was incorporated for removal of the tag. The tag itself comprises of a hexahistidine-tag (His$_6$) followed by a GB-1 tag, an immunoglobulin-binding domain of the B1 domain of *Streptococcal* protein G. GB-1 is commonly used to overcome problems of low expression levels, protein insolubility and instability [307-309]. TEV protease was recombinantly expressed and purified in the laboratory by a one-step Ni-NTA affinity purification and contained a non-cleavable N-terminal hexahistidine-tag for subsequent removal. It is a very specific protease with a strict seven amino acid cleavage recognition site of ENLYFQG/S, while cleavage occurs between Q and G/S. For tag removal, pooled fractions containing stargazin C-terminal tail were dialyzed overnight at 4°C into dialysis buffer with simultaneous cleavage using 1:30 (m/m) TEV protease. The efficiency of cleavage is highly dependent on the buffer choice and it has been shown that 200 mM imidazole significantly inhibits cleavage [310]. The next day the dialyzed and cleaved protein was subjected to another Ni-NTA affinity chromatography step. The tag-free stargazin cytoplasmatic domain (verified by mass spectrometry and SDS-PAGE) was still able to bind to the Ni-NTA column, albeit with less affinity. Therefore, fractions of elution contained protein of interest, whereas the tag and the hexahistidine-tagged TEV protease eluted at much higher imidazole concentrations.

2.2.2.9 Ion exchange chromatography (IEX)

Ion exchange chromatography (IEX) is based on the net surface charge of the protein. This method is supposed to be able to separate proteins differing in only one charged amino acid. The pK_a value of an amino acid side chain gives information about the ionizability of the corresponding amino acid. Below pH 8.5, positive amino acid side chains are positively charged [e.g. arginines, lysines, tyrosines and histidines below pH 7.9). Above pH 6, negative amino acid side chains like aspartate, glutamate and C-terminal carboxyl groups have a negative charge [311] [312]. All these ionizable groups can be titrated (they are amphoteric), which means that their charge can be changed with pH. Ion exchange is based on the reversible interaction between charged groups on the protein surface and an oppositely charged molecule on the resin. For cation exchange (SP/XL), a sulfite ion is placed at the end of a linker ($-CH_2CH_2CH_2SO_3^-$), whereas the anion exchange (Q/XL) resin has a trimethylamine group [$-N^+(CH_3)_3$] covalently attached to the surface of the resin.

2.2.2.10 Cation exchange

For further protein polishing, the protein was subjected to cation exchange. The cation exchange contributed greatly to purity of stargazin constructs since the GB-1-His_6 tag and stargazin C-terminal tail sequence have opposite pI values thereby are good candidates for ion exchange.

In order to prepare the protein for ion exchange, it was dialyzed into cation exchange buffer. This step brings the protein into a low salt buffer that is required to allow binding of the protein to the resin; the ionic strength should be kept below 5 mS/cm. The protein was loaded on a 1 mL or 5 mL HiTrap SP/XL equilibrated with 5 CV of cation exchange buffer A, followed by a wash step with 5 CV of buffer A. The protein was eluted with a gradient ranging from 0 to 1 M NaCl over 10 CV. Fractions that showed UV absorption in the chromatogram were checked by SDS-PAGE. For elution of stargazin C-terminal tail, the final salt concentration was increased to 1500 mM NaCl due to strong binding of the protein to the column.

2.2.2.11 Size exclusion chromatography (SEC)

Size exclusion chromatography (SEC) or gel filtration chromatography is often used as the final protein-polishing step and separates proteins based on their size. In contrast to other methods it does not depend on buffer composition, as proteins do not directly bind to the resin. The matrix is composed of dextran that is covalently bound to highly cross-linked agarose. The separation by size is based on the interaction between small molecules and the porous matrix of spherical particles. In order to ensure sufficient resolution and separation of the peaks eluting from the column, the sample volume should not exceed 2% of the column bed volume.

For test purifications or small amounts of protein (< 10 mg), an analytical Superdex column was used, e.g. a Superdex 10/300 GL. For protein amount larger than 10 mg, a preparative column was used (a Superdex 200 26/600 HiLoad prep grade).

The protein was concentrated using Amicon Ultra concentrators and passed through a 0.22 µm filter or centrifuged for 10 min at 10,000 x g.

The concentrated protein was applied on a pre-equilibrated Superdex column and a flow rate of 0.5 mL/min (for Superdex 10/300 GL) or 1-2 mL/min (for Superdex 200 26/600). Fractions were collected and samples were run on an SDS-PAGE.

2.2.2.12 Concentrating protein

Protein solutions were concentrated using Amicon Ultra centrifugal devices with an appropriate MWCO (3 kDa, 10 kDa or 30 kDa). Prior to usage the filters were washed with Milli-Q to remove remaining glycerol and pre-equilibrated with buffer.

2.2.2.13 Protein concentration determination

In order to properly determine protein concentrations, the extinction coefficients of the different protein constructs were determined using the Expasy Protparam tool (http://web.expasy.org/protparam/) according to Wilkins et al, 1999 [313]. Protein concentrations were determined using the Nanodrop 200 at a wavelength of λ= 280 nm. The linear dependence between absorption and sample concentration is explained by the Lambert-Beer law (Equation 2.1):

$$A = -\log(\frac{I}{I_0}) = \varepsilon \cdot c \cdot l$$

Equation 2.1: **Lambert-Beer law.** A – absorbance, I – intensity of light after passing the solution, I_0 – incident light intensity, ε – molar extinction coefficient in $M^{-1}cm^{-1}$, l – pathlength in cm

The extinction coefficient can also be determined empirically using Equation 2.2 [314]:

$$\varepsilon_{280} = (5500 \cdot n_{Trp}) + (1490 \cdot n_{Tyr}) + (125 \cdot n_{S-S})$$

Equation 2.2: Calculating the extinction coefficient for a folded protein. The numbers indicate the molar absorbances for Trp, Tyr and Cystine residues, ε – extinction coefficient at 280 nm, n – number of residues in the protein.

The ratio of the absorbances at λ= 260 nm and λ= 280 nm (260/280) gives information about the sample purity. A high 260/280 ratio (above 1) indicates a high degree of DNA contamination.

2.2.2.14 Ligand exchange for LBDs

Purification of GluA2 LBDs was carried out in presence of glutamate. In order to completely remove the ligand or exchange it for a different ligand, the protein was extensively dialyzed into ligand exchange buffer #1 with at least 5 buffer exchanges, followed by dialysis into ligand exchange buffer #2 with low concentration (10 µM) of new ligand. In the last step, the concentrated protein was mixed with a 1:1 (v/v) solution containing 10 mM ligand (ligand exchange buffer #3). The protein was concentrated to the desired concentration using Amicon Ultra centrifugal devices with a MWCO of 30 kDa [110].

2.2.2.15 Protein storage

Pure and concentrated protein fractions were divided into appropriate aliquots, flash-frozen in liquid nitrogen and subsequently stored at -80°C.

2.2.3 Mass spectrometric analysis of purified protein

In order to verify the protein of interest after purification, samples were analyzed by the mass spectrometry facility (AG Krause, FMP Berlin). Analysis was either done from excised gel bands or from solution.

For protein analysis in solution, 1-3 µL of a 1 mg/mL sample was prepared. Whole protein measurements were done using matrix assisted laser desorption ionization-time of flight (MALDI-TOF/TOF). For analysis of smaller peptides, the protein was digested with LysC or trypsin. Peptides were analyzed via nano-liquid chromatography mass spectrometry (LC-MS/MS).

2.2.4 Biochemical and biophysical methods

2.2.4.1 Sodium dodecyl sulfate polyacrylamide gel electrophoresis (SDS PAGE)

Protein samples were analyzed by SDS-PAGE [315]. This method separates denatured proteins according to their molecular weight [316]. The proteins have to migrate through a highly cross-linked matrix under the influence of an externally applied electric field. The migration does not only depend on the molecular weight but also on the protein's charge and the molecular radius. In order to separate all proteins according to their molecular weight only, all other influencing factors like the protein's charge and the molecular radius have to be eliminated. Therefore, SDS is added to the sample and boiled for 10 min at 95°C leading to the disruption of the protein's tertiary structure. SDS masks the protein's charged side chains by hydrophobically interacting with the protein via the hydrocarbon chains of SDS. The SDS sodium sulfate head group points to the solvent thereby leading to uniformly negatively charged protein molecules. Roughly, 1.4 g SDS binds to 1 g protein. In this work, SDS-PAGE was either performed under denaturing conditions using β-mercaptoethanol (β-MetOH) or Dithiothreitol (DTT) or under non-denaturing conditions using a gel loading dye without DTT or β-MetOH.

For discontinuous SDS-PAGE consisting of stacking and separating gel, 10-20% Tris-glycine gels were prepared and gels were run in 1 x Tris/Glycine running buffer.

For running gradient gels, protein samples were loaded on NuPAGE Novex 4-12% Bis-Tris gels with 1 x MES running buffer in the Xcell SureLock™ system at 180-200 V until the bromphenol blue dye reached the bottom of the gel.

2.2.4.2 Coomassie staining and destaining of polyacrylamide gels

For visualization of protein bands, gels were stained for 10 min with coomassie brilliant blue and destained using 20% (v/v) ethanol and 7% (v/v) acetic acid until bands became visible [317].

2.2.4.3 Right-Angle light Scattering (RALS) and Multi-Angle Light Scattering (MALS)

Static light scattering (SLS) is a biophysical technique for the volume-based determination of the absolute molecular weight of a protein. It is based on interaction of light with matter. Light can interact with particles in four different ways: diffraction, refraction, reflection and absorption. In a light scattering experiment, laser diffraction is measured as the incident light beam hits a particle. Most of the light will continue in the original direction and only a small fraction (0.1%) will be scattered in other directions than the incident beam. In a RALS experiment, the scattered light is only measured at one angle (90°), whereas MALS have multiple photodiodes for detection of the scattered light (in this thesis: three). The angle and the intensity of the scattered light depend on the particle size, which makes it an indirect method because the particle size is not directly measured. In contrast, dynamic light scattering measures the Brownian motion of particles, which directly gives information about their size. Big particles scatter light at small angles, a lot of light will be found in the center, whereas small particles scatter light at higher angles. An SLS instrument measures the light energy in dependence of the angle (detector number). As a result, one obtains a particle size distribution and the radius of gyration, R_G. In the 19th century, Rayleigh first described the mathematical explanation for the interaction of light with matter. For molecules larger than the wavelength of light, light scattering in solution can be described by the Rayleigh-Gans-Debye (RGD) theory of light scattering. For light scattering experiments, the Zimm equation was applied (Equation 2.3) [318] [319]:

$$\frac{K^*c}{R(\theta,c)} = \frac{1}{M_w P(\theta)} + 2A_2 c$$

Equation 2.3: **Zimm equation.** $R(\theta)$= excess Rayleigh ratio of the solution as a function of scattering angle θ and concentration c. c= solute concentration, M_W= weight-averaged molar mass, A_2= second virial coefficient describing the interaction between particle and solvent , $K^*= 4\pi^2(dn/dc)^2 n_0^2/N_a\lambda_0^4$, $P(\theta)$= angular dependence of the scattered light and can be related to root-mean square radius, N_a= Avogadro's constant = $6.022\cdot10^{23}$ mol^{-1}, dn/dc= refractive index increment.

The angular dependence of the scattered light to first order can also be expressed as shown in Equation 2.4, clearly illustrating that the particle size (r_g) and the angular dependence have a linear relation.

$$P(\theta) = 1 - \frac{16\pi^2 n_0^2}{3\lambda_0^2}\sin^2(\frac{\theta}{2})\langle r_s^2\rangle + ...$$

Equation 2.4: **Angular dependence.** n – refractive index of the solvent, λ – vacuum laser wavelength, r_g – rms radius

For RALS or MALS online measurements, a tandem technique of fast liquid protein chromatography (FPLC) and light scattering was used. An FPLC system equipped with UV detection and analytical gel filtration column was connected in line to a refractive index (RI) and RALS/MALS detector (Malvern and Wyatt, respectively). The flow rate was set to 0.5 mL/min. The RI was used in order to determine concentration of the sample. Data were analyzed with provided software (Astra 5 or Omnisec). For RALS experiments, 100 µL of a 3 mg/mL protein solution was injected, for MALS experiments, 60 µL of a 1 mg/mL solution was injected on a pre-equilibrated analytical gel filtration column. RALS buffer supplemented with different chemicals was used as running buffer. For Zn coordination experiments by His mutants, the running buffer as well as the protein buffer contained either 5mM EDTA or 1mM $ZnCl_2$. For lights scattering experiments with LBD cysteine mutants, the protein was either incubated in 500 µM copper phenanthroline (CuPhen) for 30 minutes at 37°C or incubated in 25 mM DTT (also present in the running buffer). Ligands were not present in the RALS running buffer. Data evaluation was done based on the Mie scattering theory.

2.2.4.4 Circular dichroism (CD) spectroscopy

Circular dichroism is a phenomenon observed when polarized light interacts with optically active (with a center of chirality) matter. A CD spectrometer uses circularly polarized light that is generated when two linearly polarized waves, one rotating clockwise, the other rotating anti-clockwise, with the same amplitude interact. Circular dichroism can be observed when the two circular polarized components, left circularly polarized light (L-CPL) and right circularly polarized light (R-CPL) are differently absorbed, which leads to elliptical polarized light. A CD spectrometer measures ellipticity (θ) as a function of wavelength [320]. The CD signal is positive when L-CPL is absorbed to a greater extent than R-CPL and it is negative when L-CPL is absorbed to a lesser extent than R-CPL (see Equation 2.5).

$$\Delta\varepsilon = \varepsilon_{L-CPL} - \varepsilon_{R-CPL} = \frac{\Delta A}{c \cdot l}$$

Equation 2.5: Extinction coefficients for left (ε_{L-CPL}) and right (ε_{R-CPL}) circularly polarized light are different. In a CD experiment, Δε is plotted against the wavelength λ [321]. c – molar concentration, ΔA – absorption, l – pathlength in cm.

The measured ellipticity θ_{meas} (in mdeg) was recalculated into mean molar ellipticity per amino acid θ_{MRW} according to Equation 2.6 [322]:

$$\theta_{MRW} = \frac{\theta_{meas} \cdot M_W}{10 \cdot c \cdot d \cdot N}$$

Equation 2.6: **Molar ellipticity.** θ_{MRW} – mean molar ellipticity per amino acid ($\deg \cdot cm / dmol$), θ_{meas} – measured ellipticity (mdeg), MW – molecular weight of the protein (g/mol), N – number of amino acids in protein, c – protein concentration (mg/mL), d – pathlength (cm).

The CD spectrum of proteins is dominated by the n → π* and π → π* transitions of amide groups and as this transition is influenced by the geometries of the polypeptide backbones it gives information about the secondary structure elements [323].

For a CD experiment, the protein was dialyzed into CD spectroscopy buffer (see Table 2.19). For one CD measurement, 200 µL of a 0.2 mg/mL protein solution was filled into a special cuvette with a pathlength of 0.1 cm (Starna Scientific Ltd.). A CD spectrum was recorded in 0.5 nm steps at 20°C ranging from 190 nm to 260 nm and a bandwidth of 1 nm. Three repeated measurements were recorded using the Chirascan™ spectrometer (Applied photophysics) and traces were averaged for data evaluation. Buffer spectra were subtracted from each protein spectrum.

The raw data were analyzed using the Chirascan 10010 peptide software (Applied Photophysics) and secondary structure estimations were done using the Dichroweb server (http://dichroweb.cryst.bbk.ac.uk/html/home.shtml) with the CDSSTR algorithm [324].

Figure 2.3 shows an exemplary CD spectrum of proteins with different major secondary structure elements.

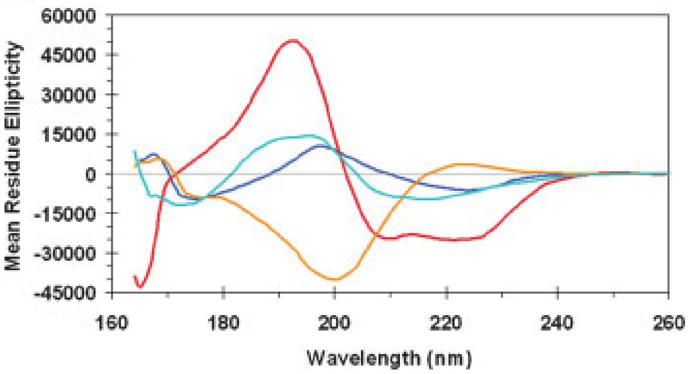

Figure 2.3: **The mean residue ellipticity is plotted against the wavelength.** The CD spectra of myoglobin (red, mostly helical), concanavalin A and β-lactoglobulin (blue and cyan, respectively, mostly β sheets) and collagen (orange, polyproline-rich) are superimposed. Figure extracted from [323].

2.2.4.5 Liposome co-sedimentation assay

For liposome co-sedimentation assays, stargazin C-terminal tail or phosphorylated stargazin cytoplasmatic tail was tested for its ability to bind to liposomes. Liposomes were prepared from different lipids (FOLCH lipids and polar lipids, respectively; Avanti Polar Lipids). Liposomes were formed using the lipid film hydration method [325]. Lipids were dissolved in a 1:3 (v/v) methanol:chloroform mixture on ice, gently dried under an argon stream and desiccated for 2 hours. For preparation of multilammelar vesicles (LMV) at a final concentration of 1 mg/mL, 0.5 mg of dried lipids were hydrated using 0.5 mL of liposome buffer (see Table 2.19). Formation of liposomes was achieved by allowing hydration at room temperature for at least 1 h with vigorous mixing and sonication for 2 x 5 sec [326]. The temperature of the hydrating medium should be above the gel-liquid transition temperature T_m [327]. The driving force for liposome formation is the hydrophobic effect [327].

10 µM protein was mixed with 1 mg/mL LMV in 50 µL liposome buffer and incubated for 10 min at RT. The mixture was separated at 70,000 rpm (213,000 x g) for 10 min at RT in a Beckman Coulter Optima™ MAX-TP Ultracentrifuge provided with a TLA100 rotor. Supernatant and pellet were analyzed by SDS-PAGE. Liposome-bound protein co-sedimented together with the liposomes, whereas unbound protein remained in the supernatant. Supernatant and pellet fractions were quantified using ImageJ [291]. As a control, a protein sample was centrifuged in the absence of lipids to find a speed where the protein alone does not precipitate.

2.2.4.6 Protein in vitro phosphorylation

For *in vitro* phosphorylation of stargazin cytoplasmatic tail, the truncated monomer (amino acid residues 1-325) of the α-subunit of Ca^{2+}/Calmodulin-dependent protein kinase II (CaMKII) from rat was used [328]. The Ser/Thr kinase has the recognition site HydXRXXS/T or HydXRNBXS/T with Hyd as a hydrophobic residue, X as any amino acid and NB as a non-basic residue [329].

In order to convert the kinase into its active form it needs to be autophosphorylated at site Thr-286 in presence of adenosine triphosphate (ATP)/Mg^{2+} and Ca^{2+} and calmodulin (CaM) [330]. After phosphorylation the enzyme is autonomous and independent of Ca^{2+}/CaM [331]. For kinase activation, CaMKII was mixed with 400 µM ATP, 1.2 µM CaM and 2 mM $CaCl_2$ in 1 x PK buffer (50 mM Tris-HCl pH 7.5 at 25°C, 10 mM $MgCl_2$, 0.1 mM EDTA, 2 mM DTT, 0.01% Brij 35) and incubated for 10 min at 30°C. For substrate phosphorylation, activated kinase was added to the protein sample and incubated at 30°C for the desired time. In general, 80 U of CaMKII were used for phosphorylation of 1 µg of purified protein sample.

Phosphorylation was either verified directly by mass spectrometry, NMR or indirectly by using the liposome co-sedimentation assay.

2.2.5 Crystallography and structure determination

2.2.5.1 Protein crystallization

For crystallization trials either fresh or frozen protein was used. Frozen protein samples were thawed on ice and either centrifuged for 10 min at 10,000 x g or filtered through a 0.22 µm membrane to remove possible impurities or precipitates.

Crystallization trials of GluA2 WT LBD and mutants thereof were set up in a 96 well format using the Gryphon robot (Art Robbins Instruments) and the sitting drop vapor diffusion method [332]. The drop consisted of 200 nL of protein and 200 nL reservoir solution. The reservoir was filled with 80 µL. Plates were set up at 4°C and 20°C but the best-diffracting crystals grew at 4°C.

Protein crystal growth was observed over three months using the Rock Imager (Formulatrix). Crystal structures of the GluA2 LBD present in the protein databank (PDB) predominantly crystallized in the presence of polyethylene glycol (PEG). Therefore, initial screens containing PEG molecules were tested, including: PEGI, PEGII, PACT, JCSG, Classic, Classic Lite Suite and Classic II Suite.

For all constructs crystals grew within 2-3 days and were of cubic-like shape. GluA2 E713T/Y768R crystals grew in 20% (w/v) PEG3350 and 200 mM $(NH_4)_2HPO_4$, whereas the best-diffracting GluA2 WT crystals grew in 20% (w/v) PEG 3350 and 200 mM KNO_3. The best-diffracting crystals for A665C/L483Y grew in 25% (w/v) PEG3350, 200 mM $(NH_4)_2SO_4$, 100 mM HEPES pH 7.0.

Good diffracting crystals for histidine mutated GluA2 LBD were obtained in 20% (w/v) PEG6000, 100 mM sodium acetate pH 6.0. 10 µM $ZnCl_2$ was included as additive (HHH mutant in WT background, kainate-bound).

2.2.5.2 Cryo protection of crystals

For cryo protection of the crystals, different cryo protectants were tested (MPD, glycerol, ethylenglycol). Crystals were transferred into the reservoir solution supplemented with 25% (v/v) glycerol as cryo protectants. All crystals were cryo-cooled by flash-freezing in liquid nitrogen.

2.2.5.3 Data collection

Diffraction images were recorded beamline 14.1, BESSY II Berlin, Germany equipped with an Rayonics MX-225 3x3 CCD detector or beamline 14.2 (equipped Mar165 CCD

detector) at a wavelength of 0.91814 Å. For all datasets the crystals were rotated with an increment of 1° at a temperature of 100 K (-173.15°C).
Initial indexing and determination of an optimal data collection strategy was done using the program iMOSFLM [292].

2.2.5.4 Protein structure solution

All datasets were integrated and scaled using the XDS program suite [295]. The structure was solved by molecular replacement (MR) using one chain of the glutamate-bound LBD (PDB accession code: 1FTJ) [78] as a search probe in Phaser [293]. Prior to MR, glutamate was removed from the PDB file. Phaser was implemented in the Collaborative Computational Project Number 4 graphical interface version 6.4.0 [289].

2.2.5.5 Atomic model building and refinement

Atomic models were built iteratively and fitted into electron density maps using the crystallographic object-oriented toolkit (COOT) program [290]. The structures were refined using the program Phenix [294]. For cross-validation, 5% of the measured X-ray intensities were set to R_{free} for the refinement [333]. Due to its high resolution, GluA2 WT and GluA2 E713T/Y768R could be refined using anisotropic B-factors.

2.2.5.6 Protein structure validation and deposition

All atomic coordinates, contacts and the geometry of the atomic models were evaluated using the MolProbity server [334, 335] and the SFCHECK program [336]. Validated models were deposited in the Protein Data Bank (http://www.rcsb.org/pdb/home/home.do) using the wwwPDB Deposition System (http://deposit.wwpdb.org/deposition/) with the following PDB-IDs: 4Z0I (GluA2 WT) and 4YU0 (GluA2 E713T/Y768R).

2.2.5.7 Figure preparation

Figures were prepared with the Pymol Molecular Graphics System, Version 1.7, Schrödinger, LLC. The size of the interfaces was calculated using the PISA server [337]. Ramachandran plots were prepared using RAMPAGE by Paul de Bakker and Simon Lovell (http://www-cryst.bioc.cam.ac.uk/rampage/) [338].
Intrinsically unstructured proteins were predicted using IUPred [339, 340].

2.2.6 NMR spectroscopy

The protein was dialyzed into an NMR-appropriate buffer. The total ionic strength should be kept as low as possible which will lead to a better radio frequency signal from the coil to the sample. The salt concentration should therefore not exceed 100 mM. The pH of the buffer also affects the quality of the spectrum. A higher pH (above 7.0) facilitates the base-catalyzed exchange of backbone amide protons which in turn can lead to worse detection of the amide group.

For one heteronuclear multiple quantum correlation (HMQC) experiment, a protein concentration of 20-150 µM and a volume of 150 µL is needed. The sample was supplemented with deuterated water (D_2O) at a final concentration of 5%. By monitoring the deuterium signal from the solvent the stability of the spectrometer is ensured.

First, a 1D spectrum was recorded, followed by 2D spectra. 2D $^1H/^{15}N$ SOFAST-HMQC experiments with 128 transients and 1.024 (^1H) x 128 (^{15}N) complex points were recorded on a 750-MHz Bruker Avance spectrometer equipped with cryogenically triple-resonance ^1H ($^{13}C/^{15}N$) probe (TCl) at 283 K. Continuous spectra were recorded at 293 K. All NMR spectra were processed with iNMR 3.3.9. Spectra were recorded together with Dr. Stamatios Liokatis as part of collaboration with the Selenko group (FMP Berlin).

2.2.7 Electrophysiology

Dr. Jelena Baranovic and Dr. Hector Salazar performed electrophysiological recordings. GluA2 WT and mutant AMPA receptors were transiently expressed in HEK-293 cells for outside-out patching. The external solution contained 150 mM NaCl, 0.1 mM $MgCl_2$, 0.1 mM $CaCl_2$ and 5 mM HEPES, titrated to pH 7.3. Different drugs were added during recordings via perfusion tools from custom-manufactured four-barrel glass (Vitrocom). The (pipette) internal solution contained: 115 mM NaCl, 1 mM $MgCl_2$, 0.5 mM $CaCl_2$, 10 mM NaF, 5 mM Na_4BAPTA, 10 mM Na_2ATP and 5 mM HEPES, also titrated to pH 7.3. For trapping experiments in presence of zinc ions, zinc was either added directly to the external solution (10 µM) or buffered with 10 mM tricine [341]. 10 µM or 2 mM EDTA were added to the external solution for zinc-free conditions. Patches were clamped at –30 to –60 mV for macroscopic recordings and at –60 to –80 mV for single-channel recordings. Currents were filtered at 1-10 kHz (–3 dB cutoff, 8-pole Bessel) and recorded using Axograph X (Axograph Scientific) via an Instrutech ITC-18 interface (HEKA) at 20 kHz sampling rate [342].

2.2.8 Molecular modeling

Molecular modeling was performed by Dr. Albert Y. Lau (Johns Hopkins University of School of Medicine, Baltimore).

Amino acids were substituted using the program SCWRL4 [343]. Initial modeling of zinc ions was performed by placing them between the coordinating histidine. Using the program CHARMM, both the histidine side chains and the chelated zinc ions were subjected to energy minimization, which included the steepest descent algorithm followed by an adopted basis Newton-Raphson method [344]. All other residues were either held fixed or restrained by an RMSD-restraining potential (applied to all non-hydrogen atoms of each LBD dimer). For each obtained model, the nitrogen atoms (Nδ or Nε) of the imidazole ring were protonated alternately for every modeled histidine. The coordination geometry after manual placing of the zinc ion was evaluated using the calcium bond-valence sum method (CBSV) [345].

3 RESULTS

3.1 TETRAMERIC STRUCTURES OF THE LIGAND-BINDING DOMAIN OF GLUA2

3.1.1 Rationale for mutant choice

In order to understand gating of the receptor at atomic level, we aimed to crystallize GluA2 LBDs in different functional states. In this thesis, sLBDs harboring different mutations were crystallized with the aim to obtain crystal structures representative of different functional states of the receptor.

The E713T/Y768R (TR) double mutant is an AMPA receptor variant that showed drastic effects on AMPA receptor kinetics. Compared to the single mutants E713T and Y768R, the combination showed a supra-additive effect on recovery from desensitization. The double mutant displays slow recovery from desensitization as residues are switched between the fast recovering GluA2 and the slow recovering GluK2 LBD [165]. Both mutations are located within the lower lobe (D2) of the LBD, at its base. E713T is in helix I, whereas Y768R is located in helix K (Figure 3.1).

The A665C/L483Y mutation has been functionally characterized and crystallized in presence of the competitive antagonist DNQX (6,7-dinitroquinoxaline-2,3(1H,4H)dione) [116]. Crystallographic studies of sLBDs revealed a disulfide cross-linked LBD tetramer. This tetramer displayed a distinct conformation of LBDs reached by a 30° rotation of the LBD dimers and was called "closed angle" (CA) arrangement. Cross-linking of LBD subunits occurred between residues A665C in subunits A and C (proximal subunits). Functional experiments using histidine mutants for metal coordination suggest that this LBD arrangement represents a partially active conformation, as trapping only occurs at intermediate concentrations of glutamate but not at fully saturating glutamate concentrations. As LBDs are monomeric in solution, the L483Y mutation was additionally introduced in order to promote dimer formation and block desensitization because it decreases the K_D for dimer formation from 6 mM for GluA2 WT sLBDs to 30 nM for L483Y sLBDs [179]. The aromatic ring of L483Y is involved in cation-π interactions with Lys752 and in hydrophobic interactions with Leu748, explaining the increased dimer stability and blocked desensitization in presence of this mutation [179].

A triple His mutant, HHH, has been investigated in the same study. The three mutated histidine residues G437H, K439H and D456H (HHH) are located at the top of the D1 domain and in functional experiments using full-length GluA2 receptors it has been shown that the cross-link occurs at intermediate glutamate concentrations [116]. Similar to the histidine cross-links designed for evaluation of the tight tetrameric arrangement,

zinc coordination in the HHH mutant is supposed to occur between opposing subunits A and B (and between subunits C and D). The HHH mutant was cloned into different S1S2J backgrounds (see Table 3.1), for example into the L483Y, shortly LY, background to promote dimerization of canonical active dimers (between A-D and B-C).
The location of the different mutations is shown in Figure 3.1.

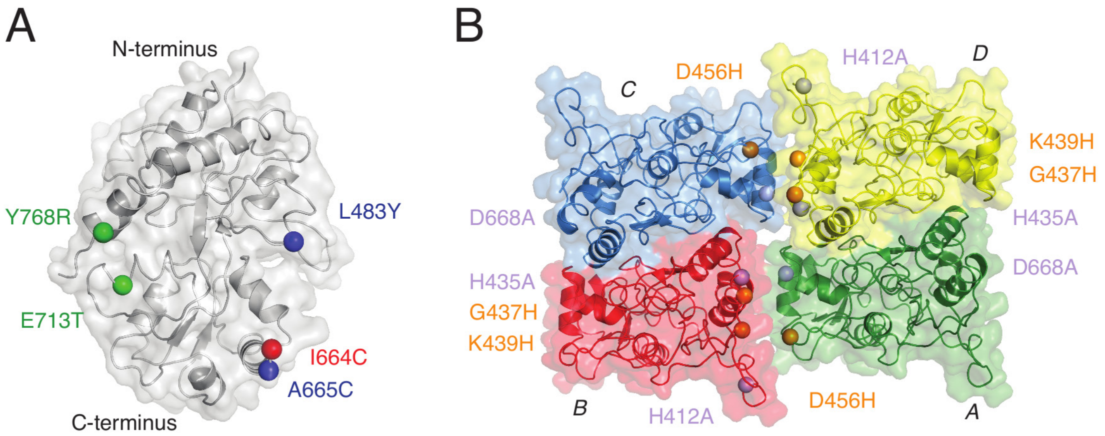

Figure 3.1: Location of LBD mutations used in this thesis. (A) Surface representation of an LBD monomer crystallized in this thesis (PDB ID: 4YU0). Mutations introduced in the LBD constructs are shown as colored spheres. **(B)** Top view of the LBD tetramer with subunits colored as followed: A – green, B – red, C - blue, D – yellow. C alpha (Cα) atoms of histidine mutants and alanine mutants are shown as orange and light purple spheres, respectively.

Table 3.1 summarizes all the GluA2 LBD constructs tested for over-expression and solubility. An overview of all cloned GluA2 LBD constructs together with their simplified abbreviation is given in Section 2.1.12 (Table 2.12).

Table 3.1: Summary of recombinant flop *rn*GluA2 protein over-expression and solubility. Amino acid mutations are indicated. n.d. – not determined.

Construct	Over-expression	Solubility	Crystallized	Final yields [mg/L culture]	
Wild-type (WT)	+/+	+/+	+	1.8	Active LBD
E713T	-	+	n.d.	0.05	
E713T/Y768R ("TR")	+/+	+/+	+	1.1	
I664C/L483Y	+	+	n.d.	0.3	Partially active LBD
A665C	+	+	+	1.1	
A665C/L483Y	+	+	+	0.25	
HHH	+	+	+	0.1	
HHH$_{TR}$ (HHH in TR background)	+	+	+	0.1	
HHH$_{LY}$ (HHH in L483Y background)	+	+	+	0.1	
HHHAA	+/-	+/-	+	0.1	
HHHAA$_{LY}$	+/-	+/-	+	0.1	
HHHAAA	-	-	-	0.06	
HHHAAA$_{LY}$	-	-	-	0.1	

3.1.2 Protein production

To obtain structural, biochemical and biophysical data of the rat GluA2 sLBD and mutants thereof, a pET22b vector containing the GluA2 WT flop LBD gene was used for expression (kindly provided by E. Gouaux). It has been shown that a construct harboring a fusion construct of the two S1 and S2 segments of the AMPA receptor LBD is necessary and sufficient for binding of the ligand and can fully reproduce the intact receptor [104]. The construct was further optimized by varying the linker lengths between S1 and S2, thereby leading to a soluble and crystallizable sLBD construct [107]. In order to introduce the mutations listed in Table 3.1, mutagenesis was performed by overlap PCR. After sequence verification, plasmids were transformed into Origami™ B (DE3) and each construct was expressed in a small-scale format as described in Section 2.2.2 to assess protein over-expression and solubility. Origami™ B (DE3) cells were used for protein expression in order to ensure disulfide formation. GluA2 LBDs contain four cysteine residues, two of them forming a disulfide bridge [41]. Mutation in the thioredoxin reductase (*trxB*) and glutathione reductase (*gor*) genes of Origami™ B (DE3) cells provide an oxidizing cytoplasmatic environment for disulfide bond formation and proper protein folding [346].

All GluA2 LBD constructs harbored an N-terminal octahistidine tag (His$_8$) removable by trypsin or thrombin. The domain architecture similar for all constructs is shown in Figure 3.2.

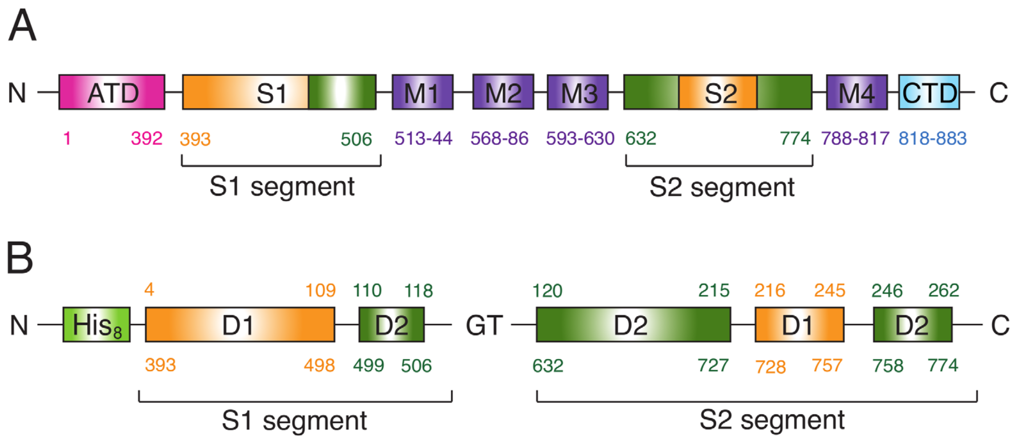

Figure 3.2: Domain architecture of *rn*GluA2 and the *rn*GluA2 LBD S1S2J fusion construct. (A) Scheme showing the domain architecture of a full-length GluA2 receptor subunit. ATD (pink), S1 – segment 1 of the extracellular LBD (orange and green), S2 – segment 2 of the extracellular LBD (orange and green), M1-M4 – transmembrane domains (red, also called TMD), CTD – cytoplasmatic domain (blue). **(B)** Domain architecture of the sLBD construct used for biophysical and structural studies. His$_8$ – octahistidine tag (purple), D1 – upper lobe of the LBD, D2 – lower lobe of the LBD, GT – dipeptide linker (glycine and threonine) fusing S1 and S2 segments together, N and C mark the N- and C-termini, respectively. Numbers on the top and bottom are domain boundaries for the LBD according to sLBD construct and full-length AMPA receptor GluA2, respectively. Note that S1 and S2 are similar but not identical to upper and lower lobes D1 and D2.

Soluble constructs were over-expressed in a large-scale format as described in Section 2.2.2. A Ni-NTA affinity chromatography was performed and following dialysis and cleavage the protein was subjected to cation exchange chromatography and SEC, yielding very pure and homogenous protein.

3.1.2.1 Protein production for WT and E713T/Y768R mutant sLBDs

Protein from either GluA2 WT or E713T/Y768R mutant sLBDs could be highly overexpressed in Origami™ and enriched using Ni-NTA, cation exchange and size exclusion chromatography (Figure 3.3).

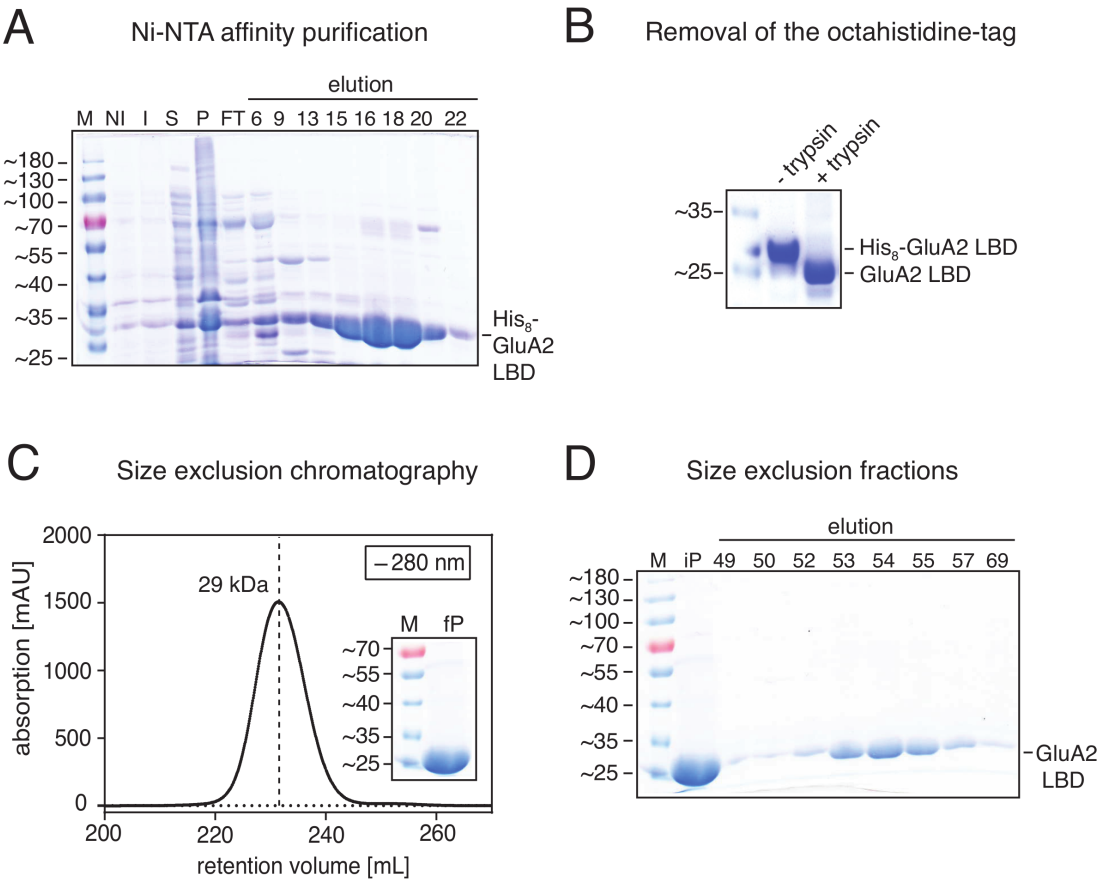

Figure 3.3: Exemplary large-scale purification of GluA2 WT LBD. (A) Coomassie-stained discontinuous 15% SDS gel showing the performance of the Ni-NTA purification. **(B)** Removal of the octahistidine-tag (His_8) by trypsin leads to a clear shift in mass on SDS-PAGE. **(C and D)** The final purification step consisted of a gel filtration using a Superdex™ HiLoad S200 26/600 prep grade column. The protein migrated as a monomer (MW_{exp}=28.5 kDa and MW_{calc}=29.2 kDa, see black dashed line). Peak fractions were subjected to SDS-PAGE. The molecular weight in kDa is shown on the left side. Small box in (C) shows purity of the final sample. M – marker, NI – non-induced/before IPTG induction, I – induced/after IPTG induction, S – supernatant after cell lysis and ultracentrifugation, P – pellet, FT – flow through, 6…22 – eluted fractions, fP – final, pure protein after SEC, AU – arbitrary unit, iP – injected protein (before SEC).

The gel filtration profile shows a distinct peak, indicating a homogenous, monodisperse protein sample as judged by the absorption at 280 nm (Figure 3.3). The calculated molecular weight from the Expasy Protparam tool (MW_{calc}) matches the experimentally determined molecular weight (MW_{exp}) from the elution volume. For GluA2 WT and E713T/Y768R LBDs, final protein yields of 1.8 mg and 1.1 mg per liter of bacterial culture could be obtained, respectively. The corresponding fractions of the gel filtration peak were pooled, concentrated and either directly used for biochemical, biophysical and structural characterization or flash-frozen in liquid nitrogen and stored at -80°C. All sLBD constructs were purified in the presence of at least 1 mM glutamate. The final purification step was performed in presence of 10 mM glutamate.

3.1.2.2 Protein production for A665C/L483Y mutant sLBDs

Cysteine mutations at the interdimer interface have been used in functional, biochemical and structural studies to understand LBD movements upon receptor activation [114, 116]. Cloning and small-scale/large-scale expression was performed as described in Section 2.2.2. Shortly, the protein was applied to Ni-NTA affinity chromatography after cell lysis (Figure 3.4 A), followed by dialysis and removal of the octahistidine tag (Figure 3.4 B). Cleaved GluA2 LBDs were subjected to either cation exchange chromatography or directly transferred to SEC (Figure 3.4 C). For preparative purposes such as crystallization, purification from 12 L bacterial culture was performed and the protein was loaded on a Superdex 200 26/600 HiLoad prep grade for the final polishing step.

Figure 3.4 shows an exemplary purification for the A665C/L483Y LBD construct. The protein eluted as a mixture of monomers, dimers and tetramers due to the engineered disulfide bridge. The single mutant A665C essentially showed the same behavior during purification except for tetramerization in solution due to the missing L483Y mutation. The yields for the double mutant A665C/L483Y decreased to 25% compared to the yields of the single A665C mutant.

Expression of A665C and A665C/L483Y LBDs was reduced compared to WT (Table 3.1), therefore protein preparation from at least 12 L but rather 24 L was needed for further structural and biophysical characterization. For A665C and A665C/L483Y, the final protein yields per 1 L of bacterial culture were 1.1 mg and 0.25 mg, respectively.

Interestingly, the protein eluted as a mixture of monomers, dimers and (for A665C/L483Y) tetramers. Furthermore, the oligomers were resistant to reducing SDS-PAGE and the reducing agent DTT present in the loading dye (Figure 3.4 D).

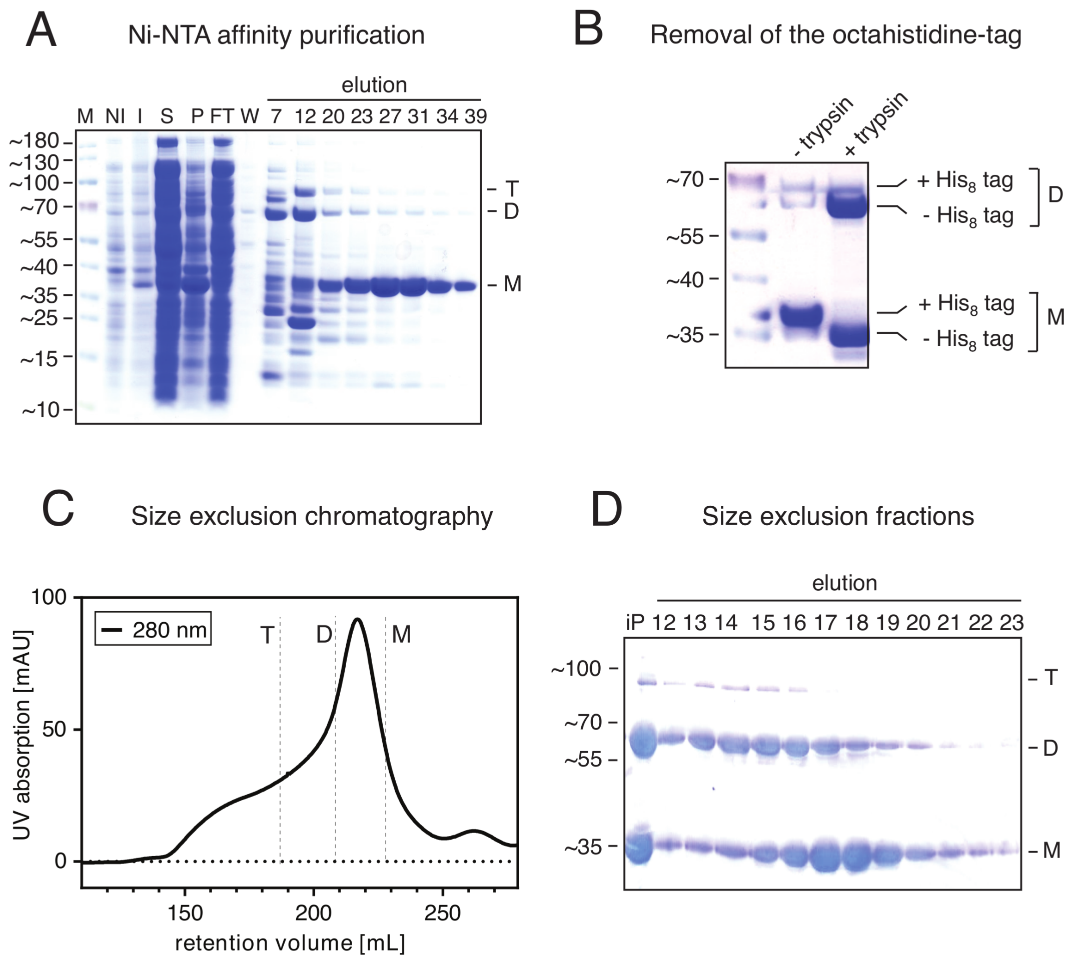

Figure 3.4: Exemplary large-scale purification of GluA2 A665C/L483Y LBD. (A) Coomassie-stained discontinuous 15% SDS gel showing loaded protein samples after every step of the purification and eluted fractions. Molecular weight (MW) of marker bands is shown on the left in kDa. **(B)** Removal of the octahistidine tag (His$_8$) leads to visible shift of the monomer and the dimer band. **(C-D)** Size exclusion chromatography was applied as the final protein purification step. **(C)** For preparative purposes, the protein was applied to a Superdex 200 26/600 HiLoad prep grade. The chromatogram shows protein absorption at 280 nm plotted against the elution volume in mL. The protein elutes in a broad peak comprising monomeric, dimeric and tetrameric protein species (see black dashed lines) **(D)** Fractions from SEC subjected to SDS-PAGE. Tetramers and dimers are stable against 6% DTT present in the SDS loading dye. M – marker, NI – non-induced/before IPTG induction, I – induced/after IPTG induction, S – supernatant after cell lysis and ultracentrifugation, P – pellet, FT – flow-through, W – wash, 7…39 – eluted fractions, M – monomer (MW= 29.2 kDa), D – dimer (MW= 58.4 kDa) , T – tetramer (MW= 116.8 kDa), AU – arbitrary unit, iP – injected protein.

3.1.2.3 Protein production for HHH mutant sLBDs

All histidine mutants (HHH) listed in Table 3.1 were designed to trap a partially active state of the receptor by coordination of zinc ions. Introduction of these mutations that are on the surface of the LBD had a big impact on protein expression and final yields were very small compared to GluA2 S1S2J WT (≤ 0.2 mg/L bacterial culture). Additional alanine mutations that were introduced in the dimer interface (HHHAA) in order to prevent undesired zinc coordination further reduced expression. An exemplary purification for the HHH mutant is shown in Figure 3.5.

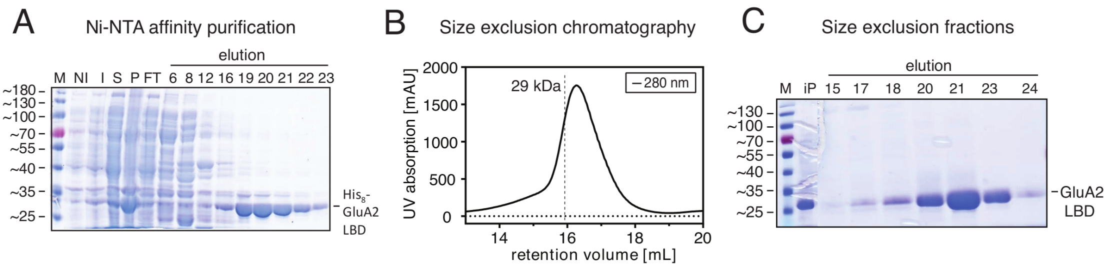

Figure 3.5: Exemplary purification of triple His mutant HHH in S1S2J WT background. (A) Coomassie-stained SDS-PAGE after Ni-NTA purification. Eluted fractions are not as pure as for WT LBDs. Protein yields decreased drastically when further mutations were introduced. His-tagged protein eluted at ~29 kDa, which corresponds to a monomer. The molecular weight of marker bands is given on the left side (in kDa). **(B)** Chromatogram from size exclusion chromatography. Since protein yields from a 12 L expression were rather low, an analytical gel filtration column was used as the final purification step (Superdex S200 10/300 GL). The protein elutes roughly as a monomer (29.2 kDa) from the column. **(C)** Coomassie-stained SDS gel loaded with protein fractions of the SEC run. M – marker, NI – non-induced/before IPTG induction, I – induced/after IPTG induction, S – supernatant after cell lysis and ultracentrifugation, P – pellet, FT – flow-through, 6…23 – eluted fractions, iP – injected protein, AU – arbitrary unit

3.1.3 Biochemical and biophysical characterization of tetrameric LBDs

3.1.3.1 Static light scattering experiments using WT and E713T/Y768R sLBDs

A monodisperse protein sample favors crystallization. Therefore the oligomeric state of WT and E713T/Y768R (TR) GluA2 LBDs was analyzed in solution using static light scattering (SLS). In solution, isolated LBDs are known to be monomeric, having a K_D in the mM (6 mM for WT) range [179]. Analytical gel filtration in combination with RALS was carried out in order to determine the oligomeric states of purified LBDs and to obtain the absolute molecular weight. LBDs were applied on a Superdex 200 10/300 GL column for optimal separation. Both constructs behaved as monomers in solution (Figure 3.6). Data obtained from RALS measurements are listed in Table 3.2.

Table 3.2: RALS data for glutamate–bound GluA2 WT and TR sLBDs

	WT	E713T/Y768R
Peak retention volume [mL]	16.9	16.9
Molecular weight [kDa]	30.4	32
Oligomeric species	Monomer (M)	Monomer (M)

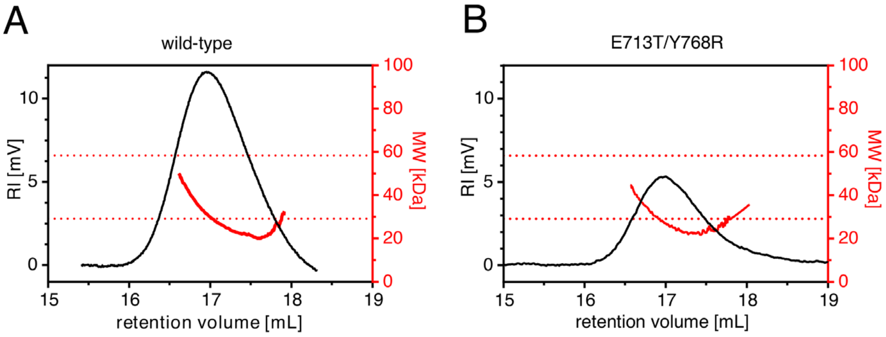

Figure 3.6: Oligomeric state of GluA2 WT and E713T/Y768R sLBDs in solution as determined by RALS. The refractive index (RI, black line) and the absolute molecular weight (in kDa, red) are plotted against the retention volume in mL for **(A)** GluA2 WT LBDs and for **(B)** GluA2 E713T/Y768R LBDs. Both proteins were monomeric in solution. M – monomer, D – dimer.

3.1.3.2 A665C and A665C/L483Y oligomer stability

A665C and A665C/L483Y oligomers (presumably generated by cysteine cross-linking) are stable and resistant to reducing SDS-PAGE (Figure 3.4 D). Under the same conditions, WT and TR GluA2 LBDs are running as monomers on the gel. To test oligomer stability, the protein was incubated with different concentrations of reducing (DTT or β-MetOH) or oxidizing agents (copper phenanthroline, CuPhen). These different conditions were also tested in RALS and MALS (see Figure 3.8). Expression in Origami cells promotes disulfide formation due to the oxidizing environment, and therefore, a monomer-dimer mixture and a monomer-dimer-tetramer mixture could be obtained for the A665C mutant and the A665C/L483Y double mutant, respectively. To test the oligomer stability, the protein was stored at 22°C and in presence of different concentrations of reducing agent, either DTT or β-MetOH. The SDS sample loading dye contained 6.6 % DTT, which wasn't able to reduce the disulfide bonds. Incubating the protein in presence of 1.5 M β-MetOH completely disrupted oligomers, however, lower β-MetOH concentrations were not able to disrupt disulfide-linked oligomers, suggesting high stability of the cross-link. The protein itself was quite stable and didn't show any degradation over days at room temperature (Figure 3.7 A). To test if the observable dimer and tetramer fraction could be further increased, purified protein (A665C/L483Y sLBDs) was treated with CuPhen for 30 minutes at 37°C and for visualization of oligomerization, the protein was loaded on a non-reducing SDS-PAGE, i.e. SDS-PAGE with detergent-free loading dye (Figure 3.7).

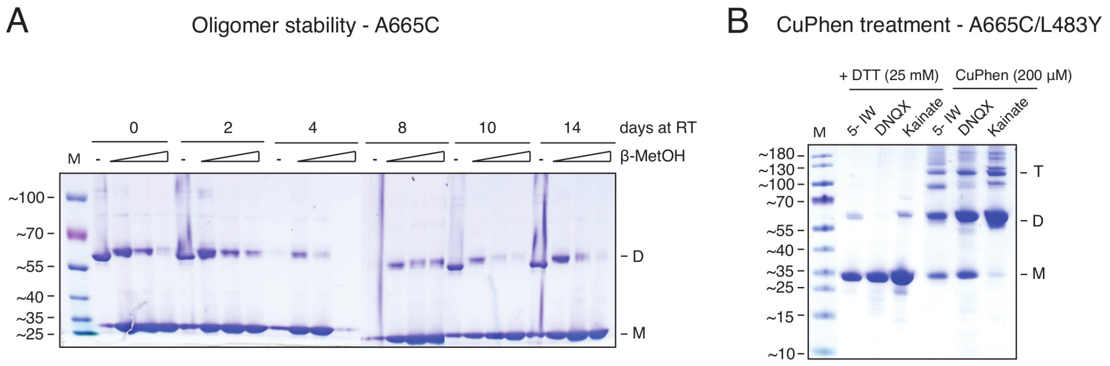

Figure 3.7: Resistance of cysteine cross-linked A665C and A665C/L483Y against reducing agents. (A) Non-reducing SDS-PAGE of GluA2 LBDs harboring the A665C single mutation to cross-link diagonal subunits A-C. The protein eluted as a monomer-dimer mixture from SEC. Dimer stability was tested against different concentrations of fresh prepared β-MetOH and against storage at 22°C for several days (0-14 days). The triangles indicate increasing β-MetOH concentrations (0.5 M, 1 M, 1.5 M). The molecular weight for the marker bands is shown on the left side (in kDa). **(B)** Non-reducing SDS-PAGE (sample buffer without DTT or β-MetOH) after CuPhen treatment of A665C/L483Y purified LBDs. M – marker, T – tetramer, D – dimer, M – monomer, RT – room temperature, DTT - D-L-Dithiothreitol, CuPhen – copper phenanthroline, 5-IW - (S)-5-Iodowillardiine, DNQX – 6,7-Dinitroquinoxaline-2,3(1H,4H)dione.

In presence of 25 mM DTT, the protein was completely reduced to monomers, whereas incubation with 0.2 mM CuPhen for 30 minutes at 37°C promoted dimer and tetramer formation (Figure 3.7 B). Taken together, these biochemical results suggest that the A665C mutant forms monomers and dimers in solution due to the engineered disulfide cross-link. The L483Y mutation is efficient in promoting dimer formation, so that the A665C/L483Y double mutant contains a fraction of tetrameric LBDs that can be further cross-linked using CuPhen.

3.1.3.3 Static light scattering experiments using A665C/L483Y sLBDs

As light scattering experiments give an idea of the oligomeric state of a given protein by calculating the absolute molecular weight, observable dimer and tetramer formation in the presence of oxidizing agents such as CuPhen was further investigated using MALS. The instrument was connected in line to an analytical gel filtration column. For analysis of cysteine mutated LBDs, a Superdex™ increase 10/300 GL column was used and 60 µL of a 1 mg/mL solution was injected on the column. The A665C/L483Y double mutant was tested in presence of different ligands in the protein buffer: either the partial agonist (5)-Fluorowillardiine (5-FW) (Figure 3.8 A) or the full agonist glutamate (glu) (Figure 3.8 B). Oligomerization was investigated in presence of either 25 mM DTT as reducing agent or 500 µM CuPhen as oxidizing agent. Since the LBDs were purified in presence of glutamate, the ligand was carefully exchanged for partial agonists by performing extensive dialysis (see Section 2.2.2.14). A similar mutant, I664C/L483Y was investigated regarding its ability to form oligomers in solution (Figure 3.8 C). The data obtained from RALS measurements are listed in Table 3.3.

Table 3.3: RALS and MALS data for GluA2 A665C/L483Y and I664C/L483Y sLBDs bound to different ligands

	A665C/L483Y (10 mM 5-FW)		**A665C/L483Y (10 mM glu)**		**I664C/L483Y (10 mM glu)**		**GluA2 WT (10 mM glu)**	
	DTT	CuPhen	DTT	CuPhen	DTT	CuPhen	DTT	CuPhen
Peak retention volume [mL]	15.2	14.8; 12.8	14.9	14.8; 12.8	15.4	15.6; 14.4	12.1	12.1
Molecular weight [kDa]	48	57; 117	57	59; 111	48	58; 116	31	33
Oligomeric species	D	D; T	D	D; T	D	D; T	M	M

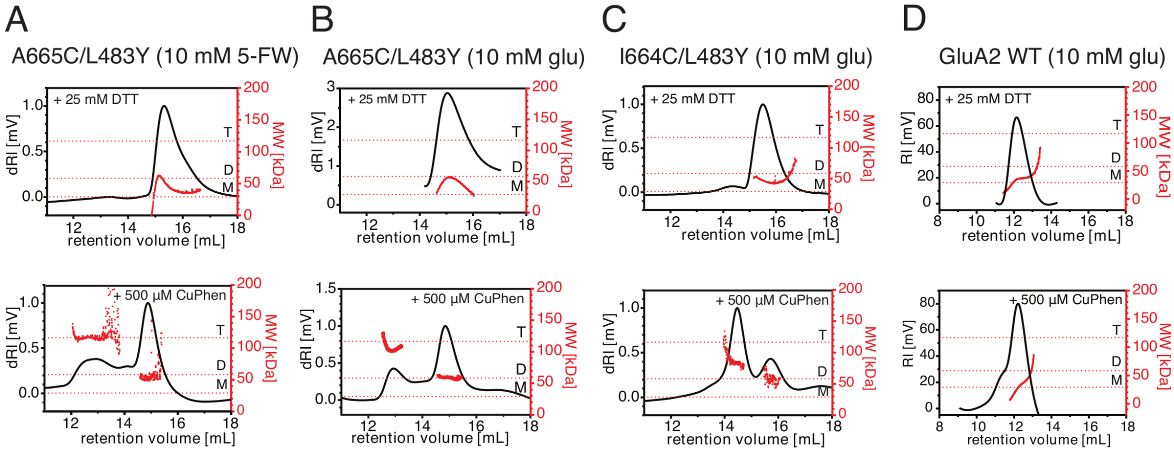

Figure 3.8: RALS and MALS analysis of A665C/L483Y or I664C/L483Y GluA2 LBDs in reducing or oxidizing conditions. (A-D) Purified GluA2 LBDs were subjected to MALS for determination of the absolute molecular weight. In the graphs, the differential refractive index for MALS (A-C) and the refractive index for RALS (D) (dRI or RI, black) and the absolute molecular weight (MW, in kDa, red dots) are plotted against the elution volume in mL. The upper panel shows behavior of the protein in presence of 25 mM DTT in both the protein buffer and the running buffer, whereas the lower panel shows the RI and the MW of the protein in presence of 500 µM CuPhen in the protein solution. Red dashed lines indicate theoretical MW for monomers, dimers and tetramers, respectively. **(A)** A665C/L483Y GluA2 LBDs bound to the partial agonist 5-Fluorowillardiine (5-FW) form dimers in absence of cross-linking agent and a dimer and tetramer mixture when being incubated in CuPhen. **(B)** A665C/L483Y GluA2 LBDs bound to glutamate behave similar to partial agonist-bound sLBDs and form dimers under reducing conditions, whereas they additionally form tetramers under oxidizing conditions **(C)** I664C/L483Y bound to glutamate also forms tetramers when being exposed to the oxidizing agent CuPhen. **(D)** GluA2 WT sLBDs as control. CuPhen or DTT didn't affect the monomeric state of the protein. The different elution volumes in (D) arise from the fact that a distinct system was used for the light scattering experiment which also consisted of a different column.

All mutants investigated here eluted as dimers from the analytical gel filtration when DTT was present. This might be partially due to some remaining DTT-resistant dimers (at least at the concentrations used here), but presumably mainly due to the L483Y mutation that stabilizes canonical LBD dimers and is not influenced by an oxidative or reductive milieu. Following incubation with 500 µM CuPhen at 37°C, all LBD constructs contained a remarkable fraction of tetramers beside the dimer fraction, irrespective of the ligand bound to the LBD.

These data show that despite the high K_D value for dimer formation, dimers and even tetramers of sLBDs can be formed in solution in the presence of mutations that promote oligomerization. The L483Y mutation does so by non-covalent cation-π interactions between canonical dimers [179, 185, 347], whereas further oligomerization to tetramers is achieved by covalent disulfide cross-linking (via the A665C or I664C mutation) between diagonal subunits. Functional data suggests that the disulfide cross-link forms when the receptor is not fully active, however in the MALS experiments, tetramers could be observed for glutamate-bound LBDs as well (Figure 3.8 B), mainly due to the fact, that the LBDs don't have any constraints in solution, they can freely diffuse. And so it seems that the free mobility of the LBDs in solution compensates for different domain closures in presence of different ligands that would normally account for the ability of subunits A and C to cross-link in the presence of the A665C/I664C mutation.

3.1.3.4 Static light scattering experiments using His mutant sLBDs

As described earlier, the triple His mutant HHH was shown to coordinate zinc ions in functional experiments. Trapping was only observed at intermediate concentrations of glutamate, but not at saturating glutamate concentrations, indicating that a partially active receptor was captured. The histidine residues are located at the tip of the LBD, and their distance is way too far in the closed or active LBD structure.

In biophysical experiments using MALS, oligomerization of the triple His mutants in solution was investigated by either running the protein in zinc-free conditions (5 mM EDTA, upper panel in Figure 3.9 A-C) or in zinc-containing conditions (1 mM $ZnCl_2$, lower panels in Figure 3.9 A-C). The ligand was present in the protein buffer only (10 mM). The elution volumes of the protein peaks as well as the calculated absolute molecular weights from RALS/MALS data are given in Table 3.4. Zinc-free conditions resulted in monomeric protein species for both tested HHH mutants (in WT or TR background), irrespective of the ligand bound to the LBDs. Presence of 1 mM $ZnCl_2$ in the protein and running buffer resulted in dimer formation for the HHH and the HHH_{TR} mutants, however in this experiment, the HHH mutant bound to 5-FW still contained some monomeric species (Figure 3.9 A, lower panel). The GluA2 WT LBD is insensitive to zinc, and the protein eluted equally in presence of 5 mM EDTA and 0.5 mM $ZnCl_2$.

Table 3.4: RALS data for GluA2 sLBD HHH mutants bound to different ligands

	HHH (10 mM 5-FW)		**HHH$_{TR}$ (10 mM glu)**		**WT (10 mM glu)**	
	EDTA	$ZnCl_2$	EDTA	$ZnCl_2$	EDTA	$ZnCl_2$
Peak retention volume [mL]	16.3	16.3; 14.2	16.9	17.1	16.9	16.8
Molecular weight [kDa]	29	30 65	30	47	17	31
Oligomeric species	M	M; D	M	D	M	M

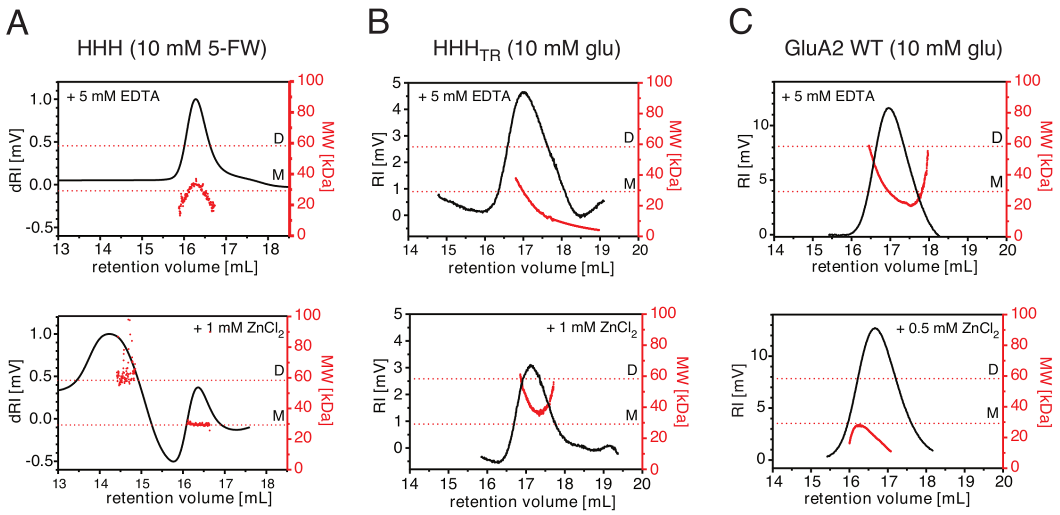

Figure 3.9: RALS and MALS analysis of HHH mutants in presence or absence of $ZnCl_2$. (A) MALS data were recorded for GluA2 HHH LBDs complexed with 10 mM of the partial agonist (5)-S-Fluorowillardiine (5-FW). The differential refractive index (dRI, in mV, black) and the absolute molecular weight (MW, in kDa, red dots) are plotted against the retention volume in mL. **(B-C)** RALS data were recorded for **(B)** HHH$_{TR}$ GluA2 LBDs complexed with glutamate and **(C)** GluA2 WT LBDs bound to glutamate as a control run**.** The refractive index (RI, in mV, black line) and the absolute molecular weight (MW, in kDa, red dots) are plotted against the retention volume in mL. Red dashed lines indicate the theoretical molecular weight for monomeric and dimeric species. M – monomer, D – dimer.

To conclude, these experiments suggest that isolated LBDs of the HHH mutant can form dimers in solution and in presence of zinc, similar to functional experiments and biochemical data in full-length GluA2 receptors. However, using isolated LBDs, the proteins are not restrained in solution. Their free mobility enables them to form dimers also in fully saturating conditions that should fully activate the receptor (10 mM glutamate). This free mobility again might explain oligomerization also in fully activating conditions, which are conditions that did not allow metal trapping in full-length receptors because they still have the conformational restrictions due to the connection to the ATDs and the TMDs

3.1.4 Structural analysis of tetrameric LBDs

3.1.4.1 Crystallization and structure determination of glutamate-bound GluA2 WT and E713T/Y768R LBDs

Initial crystallization trials were carried out using purified GluA2 LBDs from either WT or E713T/Y768R at 10 mg/mL and 4°C or 20°C. LBDs already deposited in the protein data bank (PDB) favoured crystallization in polyethylene glycol (PEG)-containing conditions, therefore various commercial screens containing PEGs were tested first (PEGI, PEGII, PACT, JCSG, Classic, Classic Lite Suite and Classic II Suite). Freezing of the protein prior to crystallization did not affect crystallization. Crystals formed quickly within 2-3 days and were of cubic-like shape (Figure 3.10). They reached their final size after approximately 3-4 days.

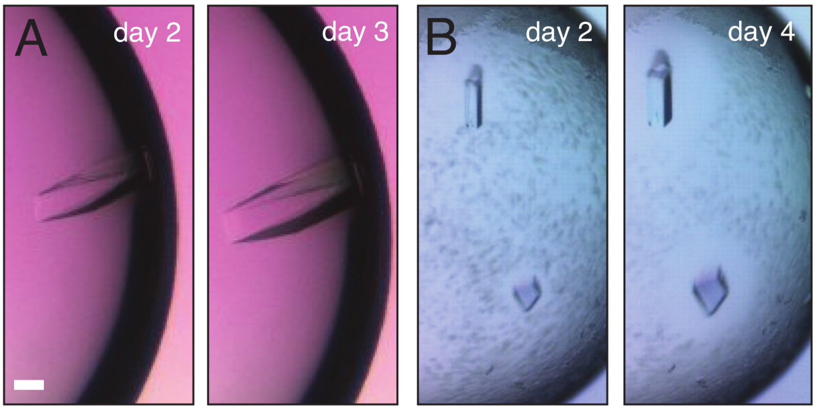

Figure 3.10: Crystals of GluA2 WT and E713T/Y768R LBDs complexed with glutamate. **(A)** The best-diffracting GluA2 WT LBD crystal grew in 200 mM $(NH_4)_2HPO_4$ and 20% (w/v) PEG 3350 (JBS-PEG). **(B)** The best-diffracting GluA2 E713T/Y768R LBD crystals grew in 200 mM KNO_3 and 20% (w/v) PEG 3350 (JBS-PEG). Pictures show crystal growth after 2-4 days. The scale bar corresponds to 100 µm.

The best-diffracting crystals grew at 4°C. X-ray data were collected as described in Section 2.2.5.3. The GluA2 WT LBD crystal grew to a final size of 400 x 120 x 80 µm, diffracted to a maximum resolution of 1.45 Å and belongs to the monoclinic space group P2 with cell dimensions (in Å): a= 47.2, b= 47.3, c= 116.8 and angles of α= 90°, β= 93.6° and γ= 90°.

The E713T/Y768R GluA2 LBD crystal at the bottom of Figure 3.10 B had final dimensions of 120 x 100 x 80 µm. The crystal diffracted to a maximum resolution of 1.26 Å and belongs to the monoclinic space group P2 with cell dimensions (in Å): a= 47.1, b= 47.4, c= 116.9 and angles of α= 90°, β= 93.6° and γ= 90°.

Data collection statistics are shown in Table 3.5. Values in parentheses indicate values for the highest-resolution shell.

Table 3.5: Data collection statistics for glutamate-bound GluA2 WT and E713T/Y768R sLBDs

Data Collection Statistics	**Wild-type** **PDB ID: 4Z0I**	**E713T/Y768R** **PDB ID: 4YU0**
Space group	P2	P2
Cell dimensions		
a, b, c (Å)	47.2, 47.3, 116.8	47.1, 47.4, 116.9
α, β, γ (°)	90, 93.6, 90	90, 93.6, 90
Wavelength (Å)	0.918	0.918
Resolution (Å)	50-1.45 (1.49-1.45)	50-1.26 (1.29-1.26)
Crystal mosaicity (°)	0.19	0.14
R_{sym} (%)	7.5 (55.7)	5.0 (42.8)
R_{meas} (%) [a]	8.7 (64.1)	5.5 (54.0)
Total reflections	368,109 (26,352)	538,950 (24,607)
Unique reflections	90,541 (6,622)	138,023 (9,367)
I/σI	11.7 (2.6)	14.3 (2.4)
Completeness (%)	99.0 (98.3)	99.1 (92.0)
Redundancy	4.1 (4.0)	3.9 (2.6)

[a] R_{meas}, intensity of the i-th measurement of reflection hkl; $\langle I(hkl)\rangle$ – average value of the intensity of reflection hkl for all I measurements, n – redundancy.

$$R_{meas} = \left(\frac{n}{n-1}\right)^{1/2} \frac{\sum_{hkl}\sum_{i}\left[\left|I_i(hkl) - \langle I(hkl)\rangle\right|\right]}{\sum_{hkl}\sum_{i} I_i(hkl)}$$

The phase problem was solved by MR using the rat GluA2 soluble LBD structure as search probe (PDB-ID: 1FTJ) [78]. The complexed glutamate was omitted from the PDB file for MR in order to prevent biases in the electron density. Two LBD molecules were found in the a.u. with a Matthews coefficient of 2.3 Å^3/Da, indicating a solvent content of approximately 45% [348]. The final model was refined to R_{work}/R_{free} of 17.7%/20.8% and 12.9%/15.7% for WT and E713T/Y768R, respectively. The refinement statistics are shown in Table 3.6.

Table 3.6: Refinement statistics for glutamate-bound GluA2 WT and E713T/Y768R sLBDs

Refinement Statistics	**Wild-type** **PDB ID: 4Z0I**	**E713T/Y768R** **PDB ID: 4YU0**
Resolution	47.27-1.45 (1.47-1.45)	47.05-1.26 (1.27-1.26)
Reflections	90,525 (2,834)	138,019 (3,877)
R_{work} (%)^b	17.7 (22.5)	12.9 (20.9)
R_{free} (%)^b	20.8 (24.6)	15.7 (23.5)
No. of protein molecules per a.u.	2	2
No. of protein atoms	4,276	4,290
No. of water molecules	850	822
Average B factors (Å^2)		
Overall	16.3	16.4
Protein	14.4	13.7
Solvent	25.2	29.6
Root mean square deviation from ideality		
Rmsd bonds (Å) ^{c}	0.0081	0.014
Rmsd angles (°) ^{c}	1.2	1.5
Ramachandran statistics		
Ramachandran favoured (%)	98.7	98.7
Ramachandran outliers (%)	0	0
Rotamer outliers (%)	0.43	0.43

^{b} R-factors: $R_{work} = \frac{\sum_{hkl}\left[\left\|F_{obs}\right| - k\left|F_{calc}\right\|\right]}{\sum_{hkl}\left|F_{obs}\right|}$ and $R_{free} = \frac{\sum_{hklTS}\left[\left\|F_{obs}\right| - k\left|F_{calc}\right\|\right]}{\sum_{hklTS}\left|F_{obs}\right|}$; hklTS – test set, F_{obs} and F_{calc} – observed and calculated (from the model) structure factor amplitudes.

^{c} Rmsd – root mean squared deviation

Values in parentheses indicate values for the highest-resolution shell. Both WT and E713T/Y768R GluA2 LBD structures were deposited in the PDB with IDs 4Z0I and 4YU0, respectively.

The Ramachandran plot shows that for both structures, more than 98% of all residues are in the favoured regions of φ and ψ angles, with no residues in disallowed regions (Figure 3.11).

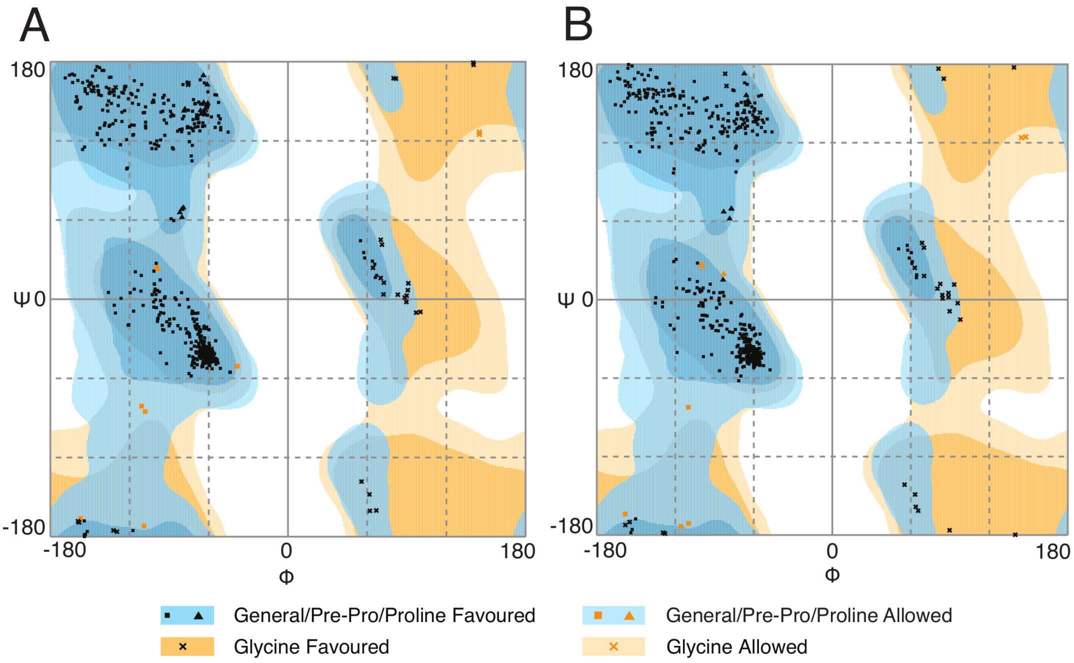

Figure 3.11: Ramachandran plots of (A) GluA2 WT and (B) GluA2 E713T/Y768R sLBDs. The Ramachandran plot shows torsion angles for all peptide bonds. Squares and triangles represent general and proline residues, whereas crosses represent glycine residues. **(A)** 98.3% of all residues of the GluA2 WT LBD structure are in the favoured region (dark blue and dark orange), whereas 1.7% of the residues are in the allowed region (light blue and light orange). No residue has phi-psi combinations in the disallowed region. **(B)** 98.2% of all residues of the GluA2 TR LBD structure are in the favoured region and 1.8% of all residues are in the allowed region with no residue being in the disallowed region. Ramachandran plots were prepared using RAMPAGE by Paul de Bakker and Simon Lovell (http://www-cryst.bioc.cam.ac.uk/rampage/) [338].

3.1.4.2 Crystallization and structure determination of glutamate-bound GluA2 A665C/L483Y sLBD

Initial crystallization trials of GluA2 A665C/L483Y were carried out using purified protein at a concentration of 10 mg/mL and 4°C, since WT and E713T/Y768R sLBDs preferentially crystallized at 4°C. Again, focusing on PEG-containing crystallization conditions seemed the most promising, since a majority of sLBDs deposited in the PDB were crystallized in presence of PEG molecules. Compared to GluA2 WT LBDs, crystals were much smaller (Figure 3.12), but still gave very good diffraction pattern. Purified protein was also dialyzed extensively against different partial agonists including kainate and different willardiines. However, although A665C/L483Y LBDs could be crystallized when bound to partial agonists, crystal packing did not produce tetrameric LBD arrangements.

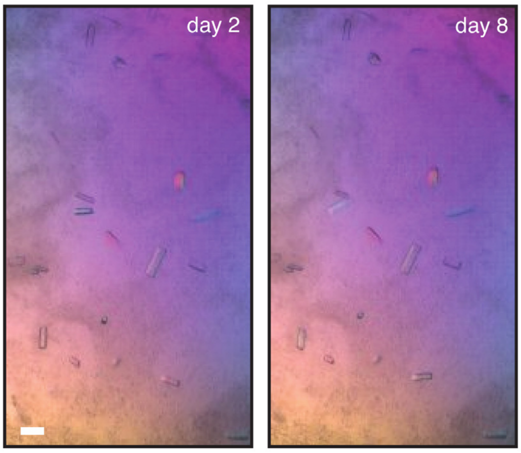

Figure 3.12: Crystals of GluA2 A665C/L483Y LBDs complexed with glutamate. The best-diffracting crystal grew in 200 mM $(NH_4)_2SO_4$, 100 mM HEPES pH 7.0 and 25% (w/v) PEG 3350 (ClassicII_Suite). The pictures show crystal growth after 2 and 8 days. The scale bar corresponds to 100 µm.

Crystals of GluA2 A665C/L483Y LDB (complexed with glutamate) also grew in PEG-containing conditions, appeared after 2 days and didn't grow any further (Figure 3.12). They varied in size but the biggest crystals grew to final dimensions of 30 x 100 x 10 µm. The crystal diffracted to a maximum resolution of 2.01 Å and belongs to the monoclinic space group P2 with cell dimensions (in Å): a= 47.4, b= 47.2, c= 117.3 and angles of α= 90°, β= 92.8° and γ= 90°. Data were collected using the rotation method with a φ increment of 1° at a temperature of 100 K. Data collection statistics are summarized in Table 3.7. Values in parentheses are for the highest-resolution shell.

Table 3.7: Data collection statistics for the glutamate-bound GluA2 A665C/L483Y sLBD

Data Collection Statistics	**A665C/L483Y**
Space group	P2
Cell dimensions	
a, b, c (Å)	47.4, 47.2, 117.3
α, β, γ (°)	90, 92.8, 90
Wavelength (Å)	0.918
Resolution (Å)	50-2.01 (2.06-2.01)
Crystal mosaicity (°)	0.27
R_{sym} (%)	12.3 (73.5)
R_{meas} (%) [a]	14.4 (88.3)
Total reflections	129,977 (8,223)
Unique reflections	34,762 (2,503)
I/σI	10.56 (1.9)
Completeness (%)	99.5 (96.7)
Redundancy	3.7 (3.3)

[a] R_{meas}, intensity of the i-th measurement of reflection hkl; $\langle I(hkl)\rangle$ – average value of the intensity of reflection hkl for all I measurements, n – redundancy.

$$R_{meas} = \left(\frac{n}{n-1}\right)^{1/2} \frac{\sum_{hkl}\sum_i\left[\left|I_i(hkl)-\langle I(hkl)\rangle\right|\right]}{\sum_{hkl}\sum_i I_i(hkl)}$$

The phase problem was solved by MR using the rat soluble GluA2 LBD structure (PDB-ID: 1FTJ) [78]. The complexed glutamate was omitted from the PDB file for MR in order to prevent biases in the electron density. Two LBD molecules were found in the asymmetric unit with a Matthews coefficient of 2.26 Å^3/Da, indicating a solvent content of approximately 45% [348]. The final model was refined to R_{work}/R_{free} of 18.9%/24.3%. Refinement statistics are shown in Table 3.8. Values in parentheses indicate values for the highest-resolution shell.

Table 3.8: Refinement statistics for the A665C/L483Y GluA2 sLBD complexed with glutamate

Refinement Statistics	**Wild-type**
Resolution	36.78-2.01 (2.06-2.01)
Reflections	34,757 (2,451)
R_{work} (%)[b]	18.9 (26.2)
R_{free} (%)[b]	24.3 (33.6)
No. of protein molecules per a.u.	2
No. of protein atoms	4,107
No. of water molecules	362
Average B factors (Å^2)	
Overall	26.9
Protein	26.4
Solvent	31.6
Root mean square deviation from ideality	
Rmsd bonds (Å) [c]	0.002
Rmsd angles (°) [c]	0.680
Ramachandran statistics	
Ramachandran favoured (%)	98.5
Ramachandran outliers (%)	0
Rotamer outliers (%)	0.45

[b] R-factors: $R_{work} = \frac{\sum_{hkl}\left[\left\|F_{obs}\right|-k\left|F_{calc}\right\|\right]}{\sum_{hkl}\left|F_{obs}\right|}$ and $R_{free} = \frac{\sum_{hklTS}\left[\left\|F_{obs}\right|-k\left|F_{calc}\right\|\right]}{\sum_{hklTS}\left|F_{obs}\right|}$; hklTS – test set, F_{obs} and F_{calc} – observed and calculated (from the model) structure factor amplitudes.

[c] Rmsd – root mean squared deviation

The Ramachandran plot shows the quality of refinement. No residues are located in disallowed regions and 98.2% of all residues are in the favoured regions of ψ and φ angles (Figure 3.13).

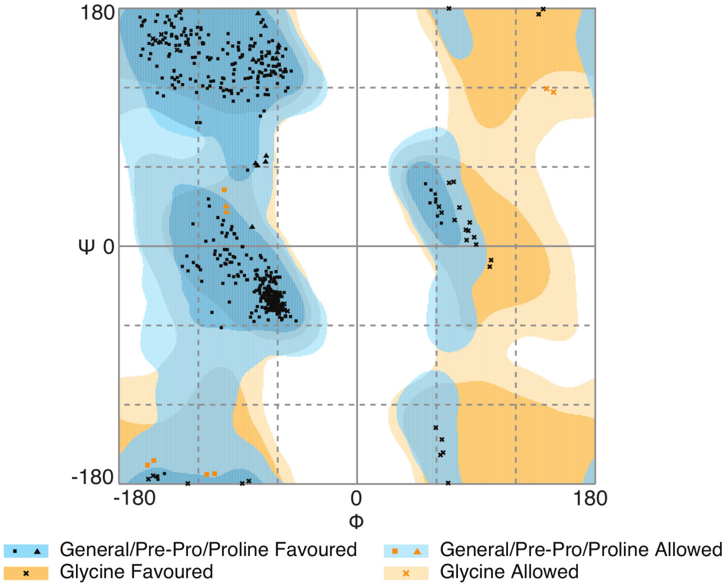

Figure 3.13: Ramachandran plot of the GluA2 A665C/L483Y sLBD. The Ramachandran plot shows torsion angles for all peptide bonds. Squares and triangles represent general and proline residues, crosses represent glycine residues (also see legend). 98.2% of all residues are in the favoured region, 1.8% of all residues are in the allowed region and no residue is located in the disallowed region/outlier region. The Ramachandran plot was prepared using RAMPAGE by Paul de Bakker and Simon Lovell (http://www-cryst.bioc.cam.ac.uk/rampage/) [338].

3.1.4.3 Overall structure

The two molecules within the a.u. of the three solved sLBD structures are almost identical and they can be superimposed with a root mean squared deviation (rmsd) of 0.1 Å. The monomers in the asymmetric unit of the WT, TR and A665C/L483Y structure are also almost identical, they can be superimposed with an rmsd of 0.06 Å-0.2 Å (depending on which molecule in the asymmetric unit is used).

The double mutant E713T/Y768R does not participate in crystal contacts and despite the dramatic effect in functional experiments, it doesn't have any effect on the LBD conformation. Since both, the WT and the TR structures are almost identical, this suggests that the arrangement adopted by the TR crystal is not a consequence of the initial mutations. And very interestingly, albeit the fact that GluA2 E713T/Y768R was crystallized in conditions favoring desensitization, the D1-D1 interface appears intact rather than ruptured [115].

Since both crystal structures (WT and E713T/Y768R) are nearly identical, further structural analysis will be performed based on the higher resolution structure of the E713T/Y768R LBD.

The overall structure of the LBD is given in Figure 3.14, while the location of the double mutant is shown in Figure 3.1. The LBD adopts the typical and well-described clamshell-like structure with the upper lobe D1 and the lower lobe D2 [78, 108]. The LBD adopts a folding consisting of 13 β-strands and 11 α-helices. The ligand binds between the two lobes D1 (orange) and D2 (green).

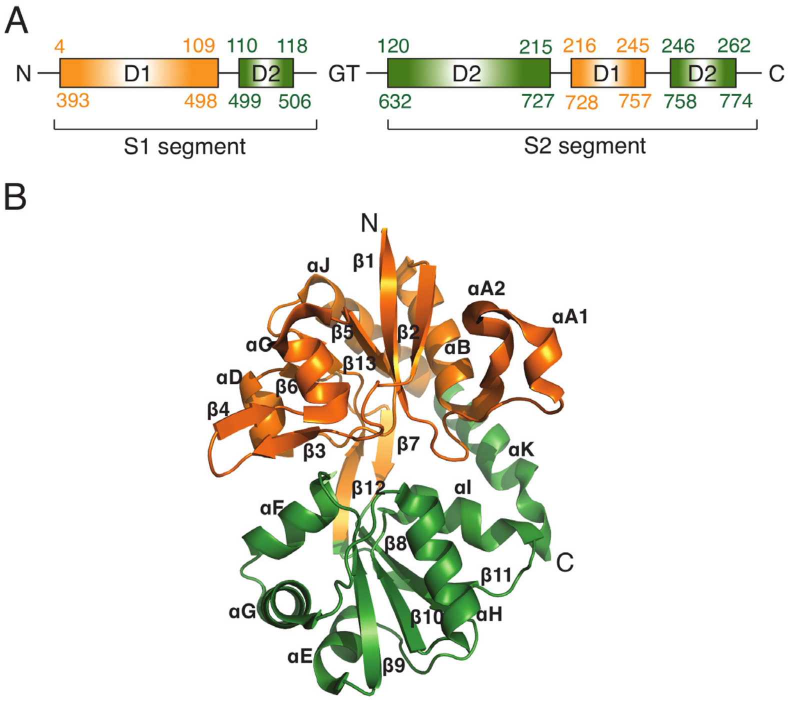

Figure 3.14: Cartoon representation of the GluA2 sLBD complexed with glutamate as determined by X-ray crystallography. (A) Schematic representation of the domain architecture of GluA2 LBD formed by segments S1 and S2, fused together via a GT dipeptide linker. Both segments contribute to the upper lobe D1 (orange) and the lower lobe D2 (green) of the LBD. **(B)** Numbering of secondary structure elements for GluA2 LBD crystal structure. Alpha helices were labeled from αA-αK and beta sheets were labeled from β1-β13. Numbering is according to previously published GluA2 LBD structures [179]. The N- and C-termini are indicated.

Due to the high resolution of the WT and TR structure, it was not only possible to clearly model glutamate as the ligand, but it was also possible to build phosphate ions as well as PEG molecules into the density, both being present in the crystallization buffer (Figure 3.15 A). Glutamate in the ligand-binding pocket is hydrogen-bonded to residues in D1 and D2 as previously described [78]. Due to the high resolution of the crystal structure, several water molecules could be built into the density (in total 822 water molecules for the TR structure), three of them are hydrogen-bonded to the γ-carboxylic group of glutamate (Figure 3.15 B).

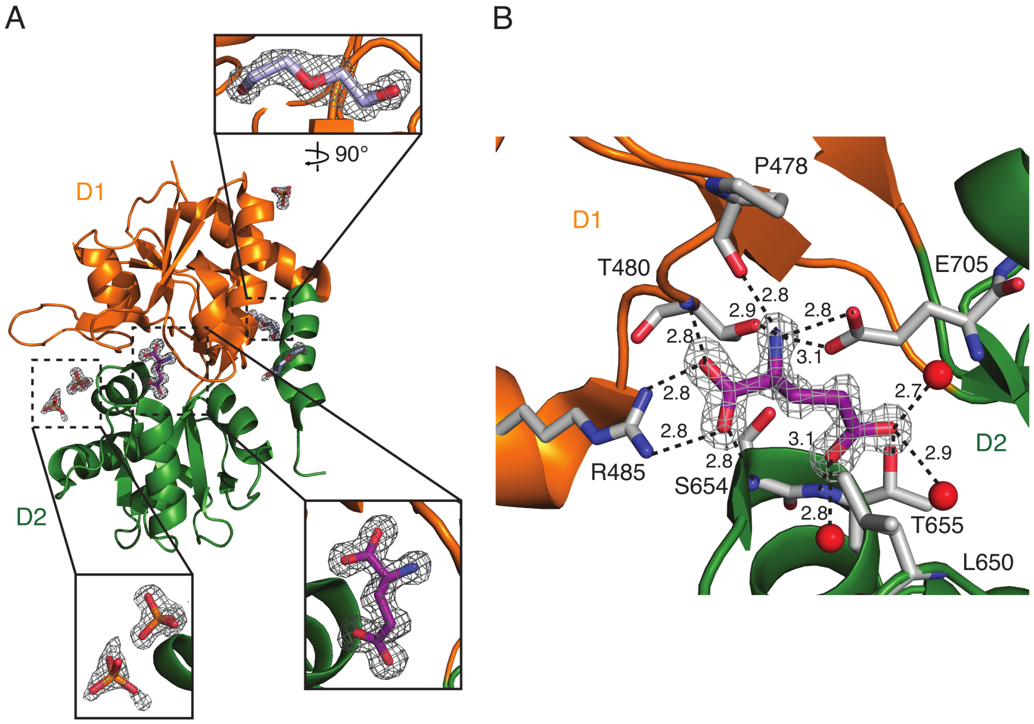

Figure 3.15: Electron density for the high-resolution glutamate-bound GluA2 LBD structure. **(A)** Cartoon representation of one glutamate-bound LBD monomer with insets showing the electron density for the ligand, for a PEG molecule and for two phosphate ions, shown in stick representation. Magnifications show (from top): electron density for PEG (light blue), glutamate (magenta) and phosphate ions, PO_4^{3-} (orange). The electron density is contoured at 1 σ and shown as grey meshes. **(B)** Magnification into the ligand-binding pocket of the GluA2 LBD showing how glutamate is hydrogen-bonded to the upper and lower lobes of the LBD. Glutamate is contoured at 1 σ. Water molecules are depicted as red spheres. Black dashed lines indicate hydrogen bonds.

In crystal structures complexed with higher affinity agonists such as AMPA or quisqualate, water molecules no longer participate in hydrogen-bonding the agonist [127]. For glutamate, the lower affinity allows for fast signaling because the ligand can unbind faster compared to higher affinity agonists.

Mutations of residues that form interlobe hydrogen bonds (between Thr686 in D2 and Glu402 in D1, not shown in Figure 3.15) have been shown to reduce efficacy of the ligand because of missing hydrogen bonds rather than altered domain closure [136, 349].

3.1.4.4 Domain closure in full-length receptors versus soluble LBDs

Binding of a ligand to the binding pocket of iGluRs leads to closure of the clamshell-like LBD and these conformational changes are transmitted to the transmembrane domains, finally leading to opening of the ion channel pore. Therefore it is crucial to understand how ligand binding leads to channel activation. It has already been proposed that the ligand efficacy is directly correlated with the degree of cleft closure [78, 145, 152, 350]. This seems to be true for most cases. Partial agonists may occupy the fully closed state albeit with less probability [147]. In order to measure the extent of domain closure for different full-length GluA2 and sLBD structures two distances, ξ1 and ξ2, were measured that span the upper D1 and the lower D2 lobes of the LBD (Figure 3.16) [143].

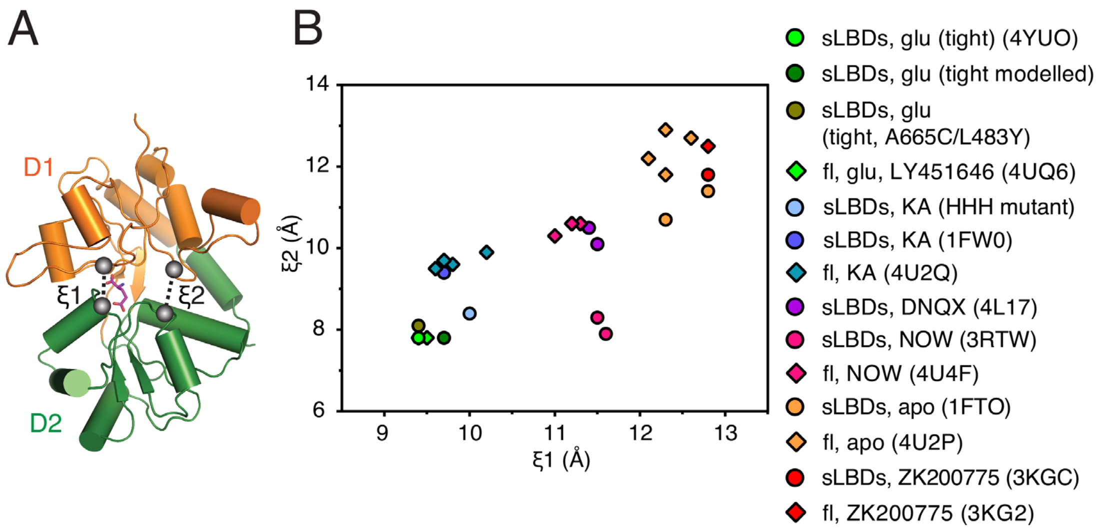

Figure 3.16: LBD clamshell closure for full-length versus sLBD structures. (A) A soluble LBD structure (4YUO) bound to glutamate (purple sticks), showing the two distances ξ1 and ξ2 (black dashed lines) used to describe clamshell closure. ξ1 is the distance between the centers of mass (COM, grey sphere) of residues 479-481 in lobe D1 and residues 654-655 in lobe D2. ξ2 describes the distance between the COMs of residues 401-403 in D1 and 686-687 in D2. Upper lobe D1 and lower lobe D2 are colored in orange and green, respectively. Centers of mass were calculated using Pymol and are displayed as grey spheres. **(B)** Plot of ξ2 against ξ1 distances for different fl and sLBD structures in Å. sLBD structures bound to different ligands are marked as circles, full-length structures have a diamond symbol with respective coloring of sLBD structure. PDB IDs are given in parentheses, if available. Glu – glutamate, KA – kainate, NOW – (S)-5-Nitrowillardiine, DNQX – 6,7-Dinitroquinoxaline-2,3(1H,4H)-dione. Note that the full-length glutamate-bound structure (4UQ6) is an EM structure. Domain closure was identical for PDB ID 4YU0 and 4Z0I, therefore only the ξ1/ξ2 distances for the TR mutant are displayed.

Different full-length and soluble LBD structures were analyzed in context of their domain closure. What could be observed is that domain closure increases with increasing ligand efficacy. The higher the ligand affinity, the higher the degree of clamshell closure. This hypothesis holds true for most cases [152], however there are a few exceptions [148, 154, 351]. The ξ1 and ξ2 distances for full-length structures as well as for soluble LBD structures decrease as follows: ZK > apo > NOW > KA > glu. In most cases, the domain closure for full-length structures as well as for soluble LBDs is similar. For two of the isolated LBD structures (NOW, apo), the two distances ξ1 and ξ2 are strikingly different from the distances in the corresponding full-length structures [124].

For our glutamate-bound structure (4YU0) as well as the modeled structure (see Section 2.2.8), ξ1 and ξ2 are very much in accordance with the glutamate-bound full-length structure, suggesting that crystal structures of isolated LBDs can be used to describe clamshell motions of an intact receptor, albeit lacking the connection to the ATDs and the TMDs. The same degree of domain closure could be measured for the A665C/L483Y LBDs. The ligand-binding pockets in the WT and E713T/Y768R sLBDs are fully bound to glutamate and have the ability to close completely as LBDs from intact receptors do. If the degree of domain closure correlates with channel opening, this should be measureable and accordingly, with increasing domain closure, the receptor should become more active. A marker position that has been used previously in order to describe this movement is the Cα atom of Pro632 (see Section 3.1.4.7) [41].

3.1.4.5 Crystal packing

As described in Section 3.1.4.3, monomers from the GluA2 WT, TR and A665C/L483Y LBD structures are very similar. Not only the monomers are nearly identical to previously published glutamate-bound LBDs but also the canonical dimers; they can be superimposed based on their Cα atoms with an rmsd of 0.3, 0.4 and 0.5 Å for the TR, the WT and the A665C/L483Y structure, respectively (reference structure: glutamate-bound sLBDs with PDB ID: 1FTJ). In the present structure, canonical dimers are formed by crystallographic two-fold symmetry, whereas in 1FTJ the dimer is formed within the asymmetric unit. Two molecules from chain A form a canonical dimer by crystallographic symmetry and the same is true for molecules from chain B. Furthermore, both protomers form two distinct tetramers by crystallographic symmetry. Monomers from chain A form a very loose tetramer via crystallographic symmetry, termed “loose tetramer” in this work, whereas monomers from chain B form a tighter arrangement of four subunits, thereby being named “tight tetramer”. Since the canonical dimers are identical, the main difference between the two tetrameric forms is the lateral displacement between dimers. In the loose tetramer, the two dimers forming the tetramer are laterally moved in the x-direction (Figure 3.17). The tetrameric arrangements are very similar for WT, E713T/Y768R and A665C/L483Y LBD structures, with small differences that are discussed later. Due to same space groups and the same principal crystal packing of the WT and TR structure, in Figure 3.17, crystal packing and resulting tetrameric LBDs is displayed for the E713T/Y768R sLBD structure.

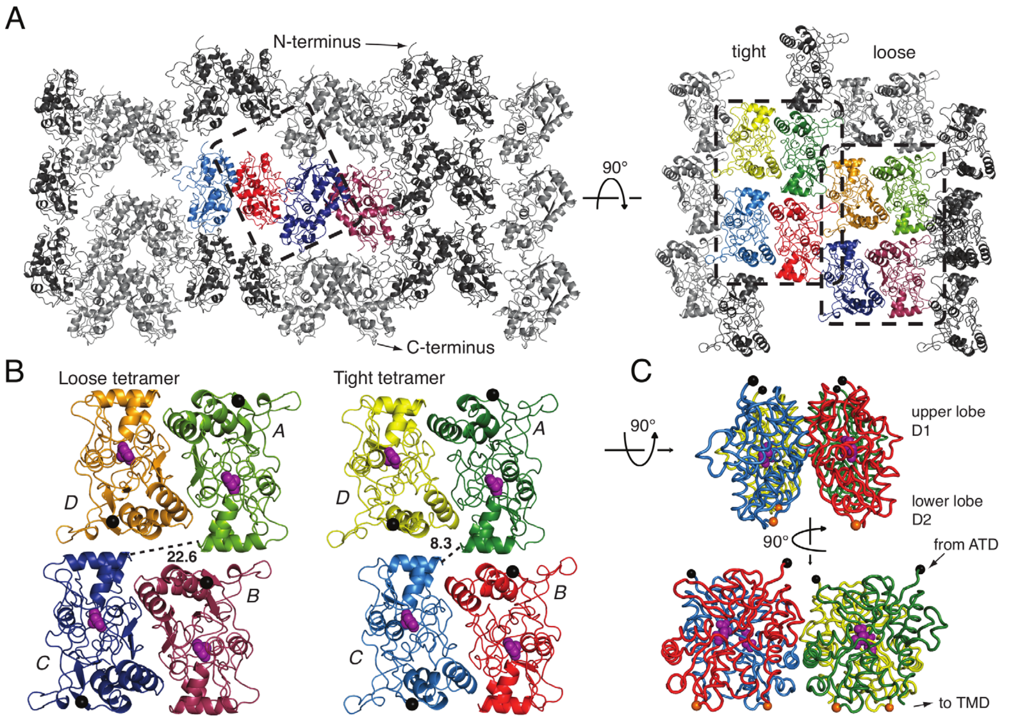

Figure 3.17: Crystal packing of GluA2 WT/TR LBD structure reveals two different tetrameric arrangements, a loose and a tight tetramer with different lateral placements. **(A)** The left panel shows one layer of LBD molecules perpendicular to the a-c plane. Subunits are labeled according to the full-length receptor (subunit coloring A – green, B – red, C – blue and D – yellow, those in the loose tetramer are shown in darker colors). The two molecules in the a.u. are boxed in black dashed lines. Symmetry-related molecules from chain A and B are colored in light and dark grey, respectively. The right panel shows one layer of LBD molecules perpendicular to the b-c plane with the "tight" and the "loose" tetramer being boxed. **(B)** The crystal packing with two molecules in the a.u. (chain A and B) produces two different tetramers containing identical LBD active dimers. The distance between the Ala665 Cα atoms in the distal subunits is 8.3 Å in the tight tetramer whereas the same Cα atoms are 22.6 Å apart in the loose tetramer of the TR mutant (dashed lines). The tight and loose tetramers are built by four molecules of chain B and A, respectively. Glutamate is shown as magenta spheres. The resolved N-termini (Cα of Asn3) are shown as black spheres. **(C)** The crystal packing of both tetramers leads to a physiologically plausible tetramer arrangement (here shown for the tight tetramer) with all four ATD linkers (black spheres) facing to one side and the four TMD linkers (Pro632, orange spheres) facing to the other side. D1 interfaces are intact. Figure modified from Baranovic et al, 2016 [342].

Both tetramers have their subunits in a physiologically relevant arrangement, their N-termini (linker to the ATD) are pointing to one direction, whereas their C-termini (linker to the TMD) are pointing to the opposite side. This was not necessarily the case for all GluA2 sLBD structures we obtained (see Section 3.1.4.9). Superimposing the tetramer from the sLBD structure on AMPA receptor full-length structures clearly shows that the tetrameric arrangement adopted in our crystal structure might be physiologically relevant. The main difference between different tetrameric LBD structures either from soluble LBDs or from full-length GluA2 receptors is the lateral displacement of the canonical dimers relative to each other (see Figure 3.18 B-E). The tight tetramer from the TR double mutant (Figure 3.18 B, upper panel) has a distance of 8.3 Å between Cα atoms of A665 in subunits A and C, whereas the same distance increases to 22.6 Å in the TR loose tetrameric arrangement (Figure 3.18 B, lower panel).

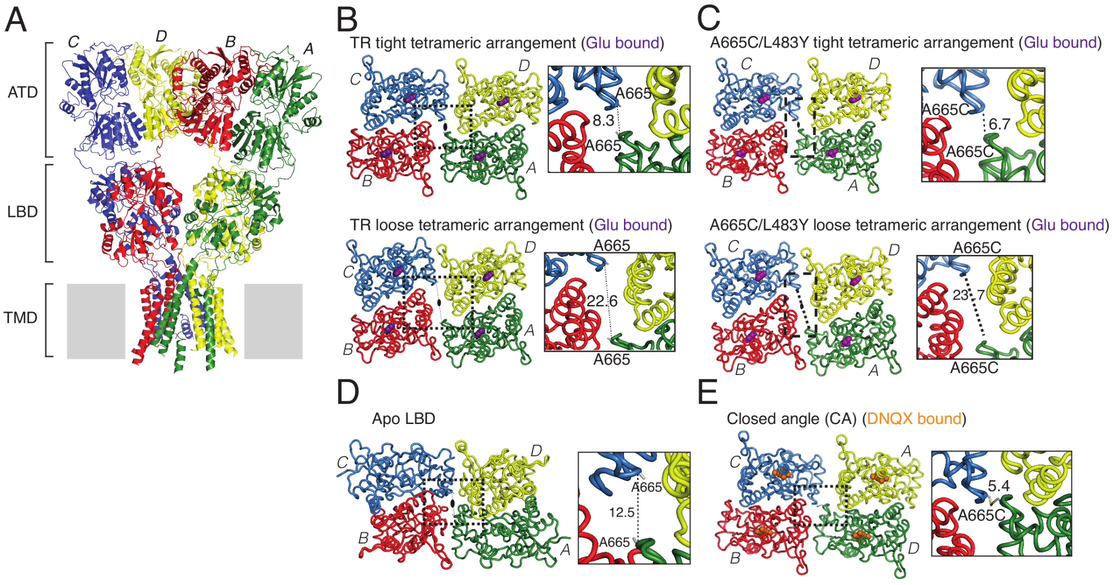

Figure 3.18: Crystal structures of tetrameric LBDs from sLBDs or full-length structures. Full-length crystal structure of GluA2 bound to the competitive antagonist ZK200775 (PDB ID: 3KG2) [41], consisting of the amino-terminal domain (ATD), the ligand-binding domain (LBD) and the transmembrane domain (TMD). The four subunits are colored as followed: A – green, B – red, C – blue, D – green. The lipid bilayer is indicated with grey bars. **(B-E)** Top view of LBDs with distances between Cα atoms of A665 of subunits A and C. Insets on the right side shows a magnified picture of the dotted box. Distances are plotted in Å. The overall two-fold symmetry axes between dimers are shown as black ovals, subunits are colored as indicated in (A). **(B)** LBD tetramer from sLBDs in tight arrangement, fully bound by glutamate (magenta spheres). **(C)** The A665C/L483Y mutant exists in two different tetrameric arrangements similar to the TR and WT tetrameric arrangements. However the lateral placement is slightly different. **(D)** Tetrameric LBD arrangement from full-length apo structure (PDB ID: 4U2P). **(E)** sLBD tetramer bound to DNQX (orange sphere) with an engineered cross-link in the A-C interface caused by the A665C and L483Y mutations. Figure modified from [342].

The same distances are slightly different in the A665C/L483Y tetramer (Figure 3.18 C) with the tight tetrameric LBD arrangement displaying a tighter interface between subunits A-C (6.7 Å as measured by the distance of A665C Cα atoms) and the loose tetrameric LBD arrangement displaying an even less compact (23.7 Å) interface compared to the distances in the TR and WT tetramer. In the ligand-free full-length structure of GluA2 (Figure 3.18 D), the A665 Cα atom distance between subunits A and C increases by about 4Å compared to the tight arrangement. Soluble LBDs have been previously trapped in a tetrameric arrangement by an engineered cysteine cross-link between A665C of subunit A and C. The overall arrangement of this tetramer (CA, closed angle) is similar to the tetrameric arrangement seen in the tight structures. However, the covalent cross-link forces the LBDs to adopt a more compact interface, the distance between A665C Cα atoms in subunits A and C decreases to 5.4 Å (Figure 3.18 E).

3.1.4.6 Analysis of the LBD interdimer interfaces

3.1.4.6.1 *Analysis of the A-C interdimer interface*

Crystal structures from sLBDs mostly yielded monomers or dimers, but - except for the CA structure - no tetramers. However, interdimer interfaces can only be described in context of tetramers. In the last years, crystal structures and EM structures of full-length GluA2 receptors and NMDA receptors were published, aiming to capture the receptor in an open, active state. However, they all had a closed ion channel pore or were of low resolution in case of the glutamate-bound EM structure [39, 40, 42, 123-125].

Therefore, analysis of the interdimer interfaces in fully glutamate-bound sLBDs that could potentially represent an active state of the receptor is very interesting and important for the understanding of subunits structural rearrangements upon activation. The interface between diagonal subunits A and C (termed A-C interface) is rather small and the loop between helices F and G (FG loop) mainly contributes to this interdimer interface (Figure 3.19 A and Figure 3.20). The lateral A-C interface is completely absent in the apo structure due to larger separation of subunits A and C. The most compact interface could be observed in the engineered disulfide cross-linked and DNQX-bound A665C/L483Y sLBD tetramer, with the only interaction between subunits A and C being the engineered disulfide bridge (Figure 3.19 D). In comparison, the A-C interface in the TR tight tetrameric arrangement is less compact (also measured by the A665 Cα distance) and contains two water-mediated hydrogen bonds, the first between the carbonyl oxygen of Lys663 and a water molecule that is located on the two-fold symmetry axis and the second one between two water molecules W1 and W1’ (which are symmetry equivalent) and the main chain NH of Ala665 (Figure 3.19 B). The interdimer interface between subunits A and C in the A665C/L483Y glutamate-bound tetramer is less compact than the interface in the disulfide cross-linked sLBD tetramer but more compact than the A-C interface in the TR tight structure, albeit lacking the disulfide bridge (Figure 3.19 C). In presence of the cysteine mutant and a full agonist no electron density for a disulfide cross-link could be observed in contrast to the DNQX-bound GluA2 LBDs.

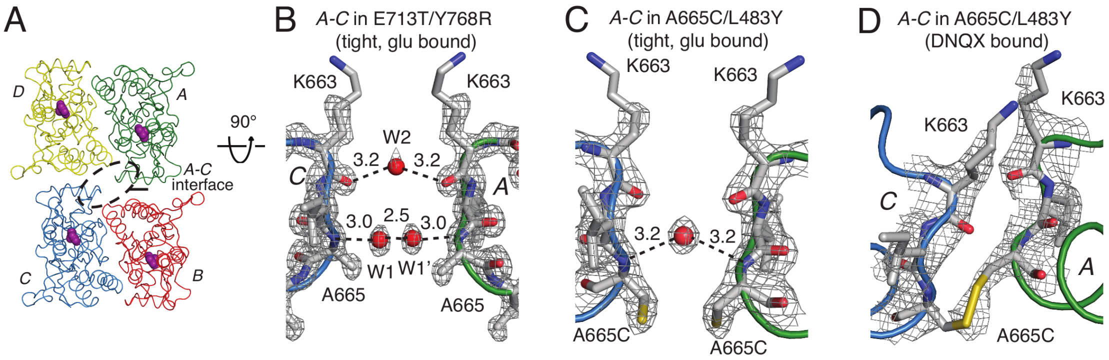

Figure 3.19: Analysis of the A-C interdimer interfaces. (A) Top view of the GluA2 sLBDs from the extracellular side. Glutamate bound in the ligand-binding pocket is colored as magenta spheres. Subunits are labeled with oblique letters (*A-D*). A black dashed line boxes the analyzed interface. **(B-D)** Comparison of the A-C interface in the **(B)** tight tetrameric arrangement observed in the TR crystal structure (PDB ID: 4YU0), **(C)** glutamate-bound A665C/L483Y tight tetrameric arrangement and **(D)** CA arrangement (PDB ID: 4L17). Interfaces are shown from the side. The $2F_o$ - F_c density is contoured at 1 σ and displayed as grey meshes. Note that water molecule W1' (in B) is generated through crystal symmetry from water molecule W1.

As already previously mentioned, the interface between diagonal subunits A and C (termed A-C interface) is rather small and the loop between helices F and G (FG loop) mainly contributes to this interdimer interface (Figure 3.20 A). Cysteine cross-linking experiments revealed that cross-links in this interface could form in all gating states: resting, active and the desensitized state. This suggests a high mobility of LBDs and fluctuating conformations during gating [114, 138, 140, 143, 145, 146, 352-355].

The FG loops from subunits A and C are closer together in the tight tetrameric arrangement compared to full-length structures bound to different ligands (Figure 3.20 A-E). The distance between Cα atoms of Ile664 in subunits A and C expands from 8.3 Å in the tight tetrameric arrangement to 13 Å in the unbound structure. In the loose tetrameric LBD arrangement the A-C interface is completely absent due to the high separation of diagonal subunits. For example, the Cα atoms from Ile664 are 19.9 Å apart from each other (between A and C), as compared to 8 Å in the tight arrangement of LBDs (Figure 3.20 E). Although the Cα atoms from position 665 are much closer in the tight arrangement compared to the CA structure, the distance of Ile664 Cα atoms expands from 8.3 Å to 8.6 Å in the CA structure. In the full-length glutamate-bound GluA2 receptor, the distance between diagonal FG loops increases to 20.2 Å (Figure 3.20 B), while the same distance is only 8.3 Å in sLBDs.

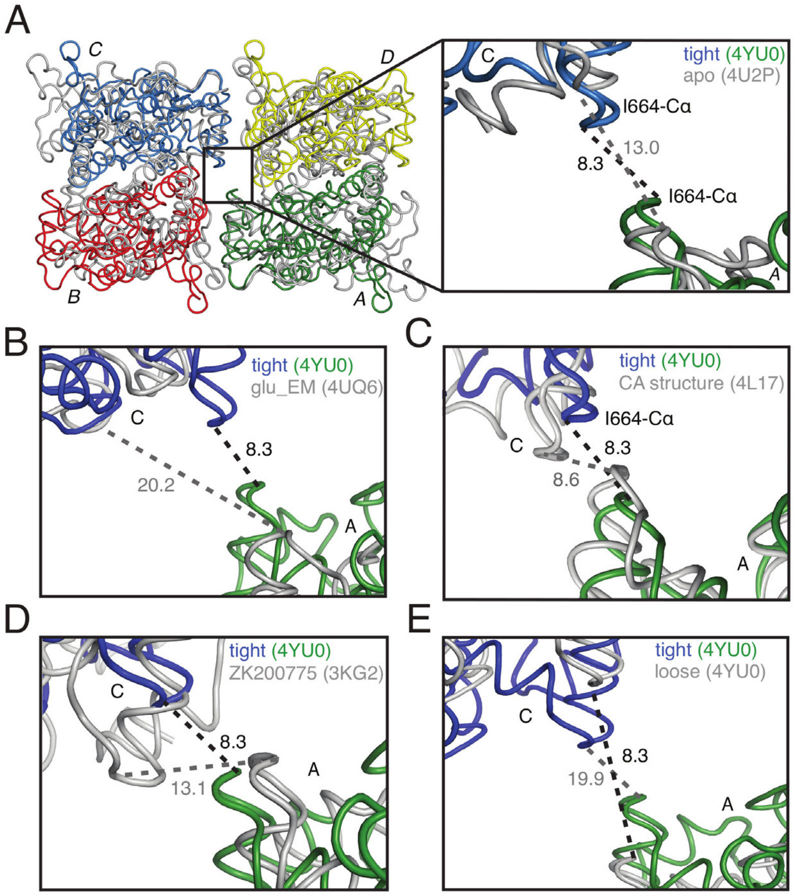

Figure 3.20: Comparison of FG loops in different sLBD and full-length structures. Distances (in Å) are measured between I664 Cα atoms of diagonal subunits A and C, indicated by dashed lines. Subunits A and C from the TR tight tetrameric arrangement are always colored in green and blue, respectively. Superimposed structures are colored in grey. Superposition was done using only the upper lobe D1. Right panel in (A) and (B-E) show magnification of the FG loop at position 664. **(A)** Left Panel shows top view of superimposed LBD structures with the FG loop being boxed. Right panel shows magnification of the FG loop with superposition of the tight tetrameric structure (PDB ID: 4YU0) and ligand-free full-length crystal structure (PDB ID: 4U2P), superposition of **(B)** TR tight tetramer and glutamate-bound LBDs from electron microscopy (PDB ID: 4UQ6), **(C)** TR tight tetramer and partially active sLBDs bound to DNQX (PDB ID: 4L17), **(D)** TR tight tetramer and antagonist-bound LBD (PDB ID: 3KG2) and **(E)** superposition of the TR tight and loose tetrameric arrangements (4YU0).

These observations agree with observations of a dynamic FG loop that can be cross-linked at various positions between residues 663 to 665 [41, 114]. For a precise superposition, the program SUPERPOSE within the CCP4i program suite was used. LBDs were overlaid using the complete D1 domain (amino acid residues 393-498 and 758-774). The CA structure (PDB ID: 4L17) and the tight tetrameric LBD arrangement (PDB ID: 4YU0) could be superimposed with an rmsd of 1.3 Å, whereas superposition of the antagonist-bound closed LBD (PDB ID: 3KG2) yielded an rmsd value of 7.2 Å. The ligand-free LBD (PDB ID: 4U2P) could be superimposed on the tight tetrameric arrangement with an rmsd of 6.7 Å.

3.1.4.6.2 *Analysis of the A-B and C-D interdimer interfaces*

Another feature that can only be described in context of LBD tetramers is the interface between subunits A and B (termed A-B interface) as well as the interface between subunits C and D (termed C-D interface). Activation of the receptor leads to tightening of the interface as shown by a bigger dimer interface area. The interface covers 281 Å^2 in the CA structure and 309 Å^2 in the tight structure (Figure 3.21). Interestingly, the TR tight interface differs from the interface of full-length GluA2 bound to glutamate and the positive allosteric modulator LY451646, where the interface is practically completely absent, albeit being bound to the same agonist. LY451646 is an allosteric modulator that blocks desensitization [40, 356]. Like other allosteric modulators, it sits at the dimer interfaces between canonical dimers (i.e. A-D and B-C). The transmembrane domain is not resolved in this EM structure, making it difficult to find explanations for why the tetrameric arrangement of the LBDs differs so much from other active-like LBD structures.

The dimer interface of the TR loose tetramer has a 1.6-fold larger interface compared to the tight tetrameric arrangement. This shows that the large distance between A665 Cα atoms is due to shifting of the canonical B-C and A-D dimer pair relative to each other rather than due to an increase in dimer separation that would correlate with receptor activation. The interface for the sLBD structure representing an intermediate state of receptor activation (PDB ID: 4L17) has a dimer interface area almost as large as for the fully glutamate-bound sLBD structure. The large interface can be mostly attributed to the engineered disulfide cross-link between A665C atoms of proximal subunits A and C, bringing the two subunits in very close proximity (see Figure 3.18 E). The tight and loose tetrameric arrangements seen in the A665C/L483Y double mutated sLBD display a larger interdimer interface area compared to the same interfaces in the TR structure, which might be due to the double mutant introduced into the protein.

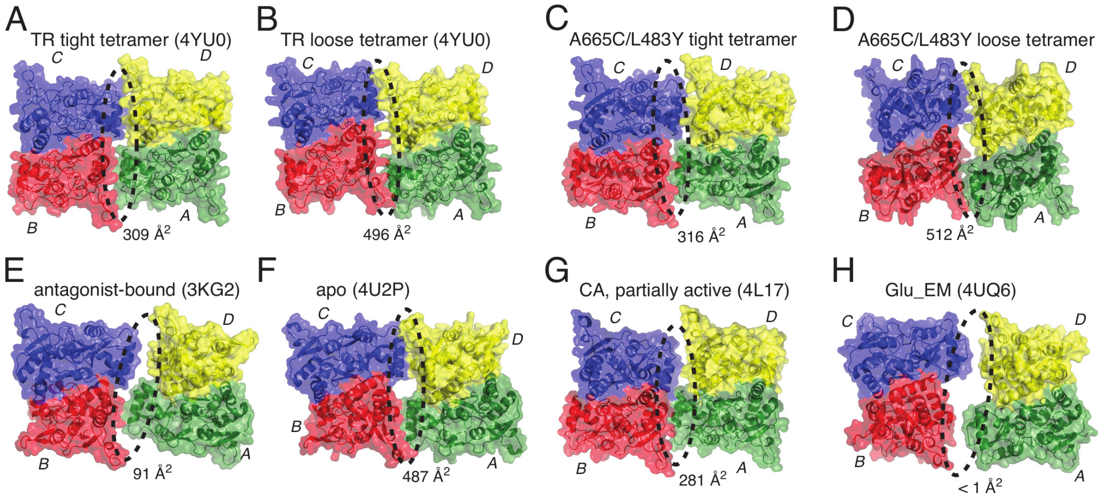

Figure 3.21: LBD layer interdimer surface. **(A-H)** Top view of the LBD layer. Structures are shown as a molecular surface. LBD dimer-dimer interface (between subunits A-B, C-D and A-C) is boxed with a dashed oval. The interdimer interface is given below each structure (in Å²). Subunit numbering (A-D) is indicated with italic letters. The interfaces were calculated using the PISA server [337]. The PDB ID is given in parentheses if available.

Looking at the interdimer interfaces reveals different degrees of hydrogen bonding networks depending on the proximity of these subunits and the solvent network. It should be noted, that the A-B interface is equivalent to the C-D interface for the tight structure as well as for the A665C/L48Y structure because the four monomers in the tight arrangement are formed by crystallographic symmetry. The same holds true for the CA conformation, where two molecules (Mol1 and Mol2) in the a.u. form a canonical dimer within the tetramer. Therefore, the A-B and C-D interfaces are identical as well.

The tight tetrameric arrangement displays a more compact interdimer interface compared to the CA structure. As an example, the distance between the Cα atoms of Lys765 in subunit D and Thr672 in subunit C is 8 Å compared to 12 Å in the CA structure. The relatively large interdimer distances in the tight structure precludes for salt bridges but subunits C and D (or A and B) are connected via a multitude of water-mediated hydrogen bonds. Furthermore, two phosphate ions from the crystallization buffer interact with alternative conformations of Arg675 and Arg660. In contrast, in the CA structure, only a single water-mediated hydrogen bond could be resolved between Ser676 in subunit C and Lys765 in subunit D. This might be partially due to the weaker interdimer interface but also due to the lower resolution of the crystallographic data (2.8 Å) (Figure 3.22 B and F).

The rather tight interdimer interface of the apo LBD full-length structure shows six hydrogen bonds and salt bridges, with no water modeled (which presumably is due to the resolution) (Figure 3.22 G and H). In general, the opposing subunits are much closer which enables them for direct electrostatic interaction. Still, despite the proximity of the subunits, the interdimer interactions are very sparse which is consistent with the lateral placement of the dimers measured by Arg660 Cα and Gln756 Cα distance in subunits A and C, respectively (Figure 3.23). For example, in the apo structure the Cα atoms of Lys765 in subunit D and Thr672 in subunit C are separated by 11 Å. Hydrogen bonding and salt bridges occur between the ε-amino group of Lys770 in subunit B (or D) and the oxygen of the γ-carboxyl group of Asp668 in subunit A (or C), and also between the ε-amino group of Lys669 in subunit A (or C) and the carbonyl oxygen of Gly771 in subunit B (or D). These interactions are the same in both interdimer interfaces (A-B and C-D) but differ slightly in distances (Figure 3.22 G and H).

The loose tetrameric arrangement that results from crystallographic symmetry of the sLBDs fully bound by glutamate (PDB ID: 4YU0) has an even tighter interdimer interface compared to the tight tetrameric arrangement. Similar to the tight tetrameric arrangement it is characterized by a very complex water-mediated hydrogen-bonding network (Figure 3.22 C), however in contrast to the tight arrangement, also direct hydrogen bonds could be resolved. The carbonyl oxygen of Lys410 in subunit D is hydrogen-bonded to both amine groups of the Arg675 guanidinium group in subunit C (distances are 2.9 and 3.2 Å). The second hydrogen bond with a distance of 3.2 Å involves the side chain amide group of Asn411 and the hydroxyl group of Ser676. The main difference between the loose and the tight tetrameric arrangement becomes very clear when looking at these interdimer interfaces. For example, the side chain of Arg675 is hydrogen-bonded to Lys765, Asp427, Glu422 and Asn418 in the tight tetrameric arrangement, whereas the same residue is hydrogen-bonded to Lys410 in the loose tetrameric arrangement. The distance between Cα atoms of R675 in subunit C and Lys765 in subunit D in the tight and loose tetrameric arrangement is 13.5 Å and 23 Å, respectively. As a result, the main difference between the two different tetrameric arrangements is the lateral shift of the B-C dimer relative to the A-D dimer, resulting in a distinct interface. Consistent with its importance for the interdimer interface, the R675S mutation speeds deactivation of GluA2 [165]. The double mutant R675S/K761M displayed a deactivation that was three-fold faster than WT GluA2 receptors (4000 ± 550 s^{-1}, n=6; recorded by Dr. Anna L. Carbone) [165]. The C-D interface in the tight tetrameric structure of the A665C/L483Y mutant is characterized by a weaker hydrogen bonding network compared to the C-D interface in the TR tight tetrameric arrangement, however the same set of residues is involved in hydrogen bonding.

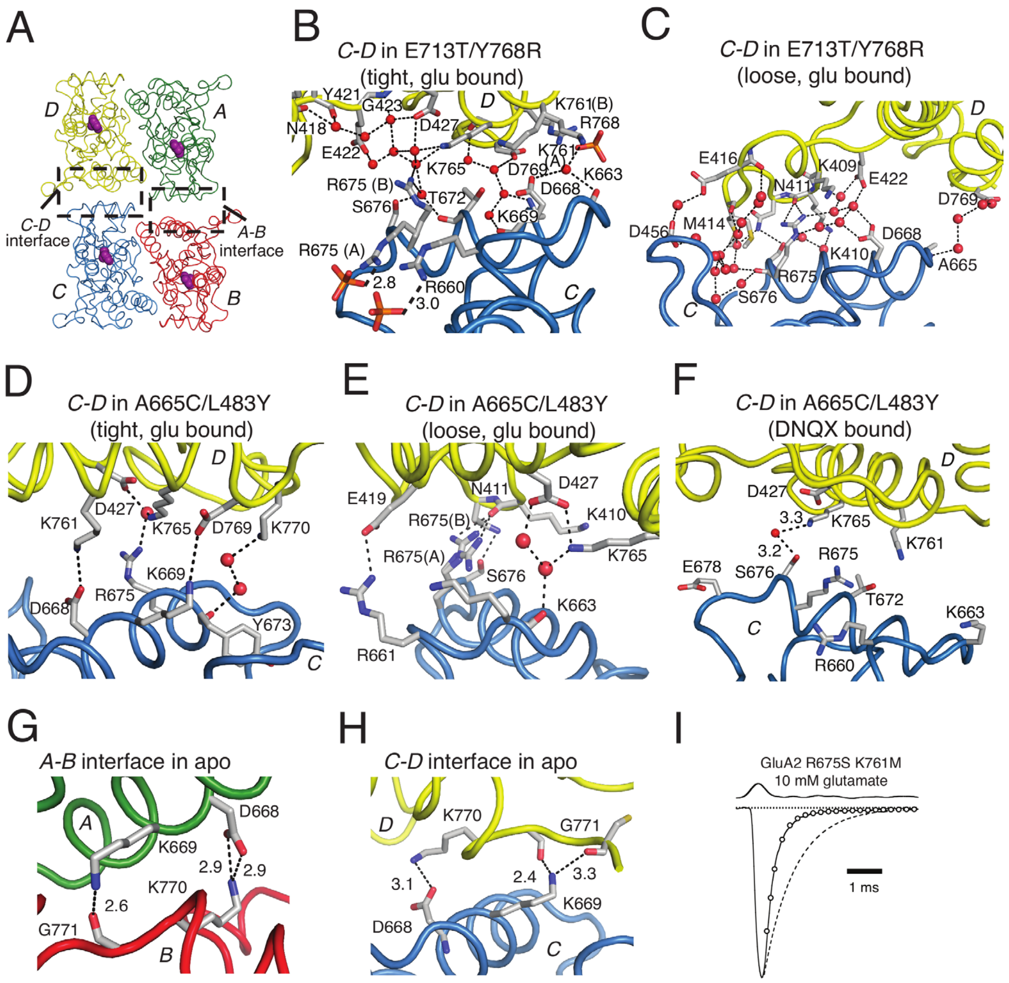

Figure 3.22: Analysis of the A-B and C-D interdimer interfaces. (A) Top view of the GluA2 sLBDs from the extracellular side. Glutamate bound in the ligand-binding pocket is colored as magenta spheres. A black dashed line boxes analyzed interfaces, which are named according to the LBD subunits that are involved. **(B-F)** Comparison of the C-D interfaces in the **(B)** tight tetrameric arrangement observed in the TR crystal structure (PDB ID: 4YU0), **(C)** loose tetrameric arrangement observed in the TR crystal structure (PDB ID: 4YU0), **(D)** tight tetrameric LBD conformation in the glutamate-bound A665C/L483Y crystal structure, **(E)** loose tetrameric LBD conformation in the glutamate-bound A665C/L483Y crystal structure and **(F)** tetrameric arrangement in the CA structure (PDB ID: 4L17). **(G-H)** A-B and C-D interface in the ligand-free full-length GluA2 crystal structure (PDB ID: 4U2P). **(I)** Patch clamp recording of the R675S K761 double mutant (open circles). For comparison, a WT recording is shown in the same trace with dashed line. Upper trace shows solution exchange for the 1 ms glutamate pulse. The GluA2 R675S/K761M double mutant has a faster deactivation compared to WT (deactivation time constant from exponential fit is 3300 s^{-1}. Dr. Carbone performed recordings. Figure modified from [342].

For example, in both tetrameric arrangements, the carboxyl group of Asp769 (in subunit D) is involved in a hydrogen bond with the nitrogen of the ε-amino of Lys669 (in subunit

C), however due to the different interface areas (Figure 3.21 and Figure 3.22), the residues are directly hydrogen-bonded in the A665C/L483Y structure, whereas a water mediates the hydrogen bond between the above described residues in the TR tight tetramer. The same holds true for hydrogen bonds formed between Lys765 in subunit D and Arg675 in subunit B, or for the hydrogen bond involving Lys761 in subunit D and Asp668 in subunit C (Figure 3.22 B and D). Different from that, the loose tetrameric arrangements in the TR and the A665C/L483Y structures involve different sets of hydrogen bonds; they only have a hydrogen bond between Asn411 and Ser676 in common (Figure 3.22 C and E).

3.1.4.7 LBD movements upon receptor activation

Evaluation of different tetrameric sLBD as well as full-length structures might help to get insights into how ligand binding leads to opening of the ion channel opening and to determine the LBD movements crucial for receptor activation. In this section, tetrameric LBD structures were evaluated regarding different aspects that might be important for activation of the receptor.

3.1.4.7.1 *Lateral placement of LBD subunits*

The lateral placement and diagonal subunit separation of the four subunits in different functional states can also be displayed by measurement of the distance between Cα atoms of residue Arg660 in subunits A and C and the Cα atom distance between residues Gln756 in subunits B and D [125]. Arg660 is located at the end of helix F in the lower lobe D2 and Gln756 is located at the tip of helix J in the upper lobe D1 (Figure 3.23 A and B). Both residues are close to the central opening of the gating ring that leads to the ion channel pore in full-length receptors. In Figure 3.23 C, marker distances are compared between tetrameric structures from sLBDs and full-length structures. Transition from a partially active state (PDB ID: 4L17) to a fully glutamate-bound state (PDB ID: 4YU0) leads to an increase in the A-C distance by about 5 Å. Interestingly the B-D distance slightly increases from partially occupied LBDs to fully occupied LBDs by about 2 Å. This change in the lateral placement could be due to the artificial cross-link between subunits. For LBDs from full-length structures, an increase of the diagonal dimers separation can be observed as the receptor gets fully activated. Both, the B-D and the A-C marker distances increase as follows: apo < KA < glutamate. Both, structures from sLBDs and from full-length structures suggest that the central opening enlarges upon activation of the receptor.

Interestingly, for all structures investigated in Figure 3.23, the A-C Arg660 pair distances are always larger compared to the changes in the B-D Gln756 pair. This is also in contrast to the Pro632 Cα distances measured between diagonal subunits. From the Pro632 distances, one could conclude that the distal subunit pair B and D plays a more important role in ion channel opening because of the bigger distances compared to the A-C pair. For the Arg660 and the Gln756 distances the opposite effect could be observed. In the investigated tetrameric structures, the change of A-C pair Arg660 distances is bigger than the change of the B-D pair Gln756 distances. Gln756 is located in the upper lobe D1, whereas Arg660 is located in the lower lobe D2 at the outer tip of the clamshell. As D2 moves upwards towards D1 upon ligand binding, the diagonal Arg660 distance between subunits A and C increases upon activation, explaining why A-C Arg660 distances are larger than B-D pair Gln756 distances. The Arg660 distance therefore might slightly be affected by clamshell closure.

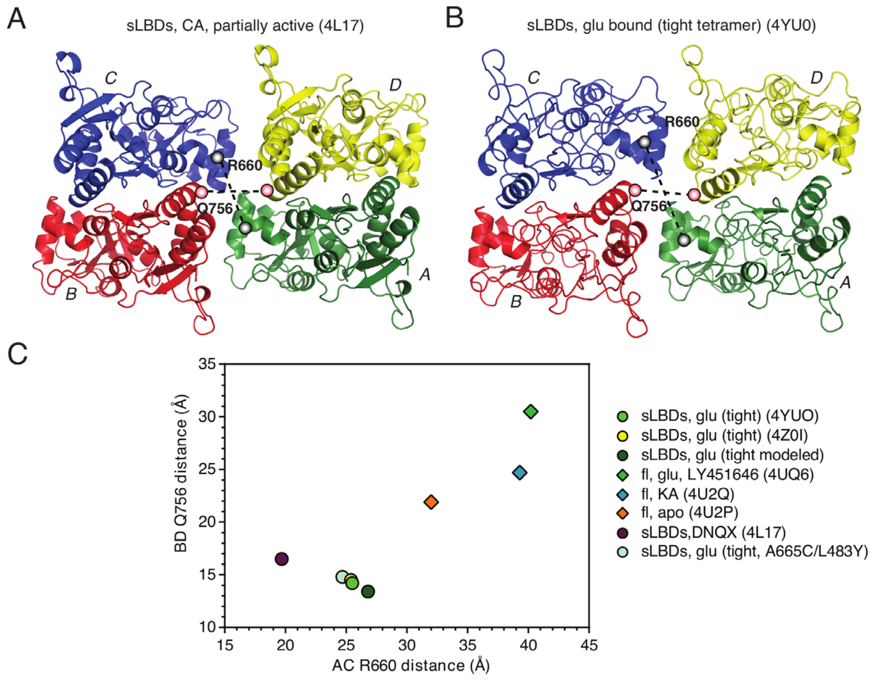

Figure 3.23: Diagonal separation of the A-C and B-D dimers of the GluA2 LBD tetramer. (A-B) Top view of the LBD from the extracellular side. Marker atoms for measurement of the subunit separation, the Cα atoms of R660 and Q756, are shown as grey and red spheres, respectively. Diagonal distance is indicated by a black dashed line **(A)** Diagonal separation of A-C and B-D dimers for tetrameric sLBD structure bound to DNQX and trapped by an engineered disulfide bridge (4L17), representing an intermediate in receptor activation [116]. **(B)** Intersubunit distances for subunits A-C and B-D for the tight tetrameric sLBD arrangement with all four subunits fully bound by glutamate (4YU0). **(C)** The B-D pair Q756 distance is plotted against the A-C R660 distance**.** Distances are shown in Å. The dark green circle shows interdimer separation for a structure obtained from molecular modeling of the TR tight crystal structure and will be referred to as “tight modeled” in this work. Molecular modeling results are shown in Section 3.1.6.

Evaluating changes in the A-C and B-D marker positions for different functional states of sLBD structures is not possible due to the lack of sLBD crystal structures in different functional states. The marker atom distance for the tight tetrameric arrangement of the A665C/L483Y structure is almost the same as for the TR tight tetrameric arrangement, again supporting the assumption that we did not capture a partially active state with the A665C/L483Y LBD structure.

3.1.4.7.2 *Domain linker movements upon receptor activation*

LBD clamshell closure leads to rearrangements of the LBD dimers as described above. These rearrangements within the LBD layer are supposed to drive opening of the ion channel pore. In order to understand how LBD conformational changes correlate with ion channel opening, distances of Pro632 Cα atoms were measured between diagonal subunits A-C and B-D. Pro632 is located at the bottom of the LBD S2 segment as the LBD passes over into the third transmembrane helix, therefore referred to as M3-S2 linker. The M3 helix bundle coats the inner membrane pore, and upon activation the M3 helices must be pulled apart at the bundle crossing (Figure 3.24 C). Pro632 has been previously used as a reference in order to describe channel opening [41]. As the D2 domains of the LBD move upwards upon activation, the distances of the M3-S2 linker also change upon activation. In Figure 3.24, diagonal Pro632 (A-C and B-D) distances were measured for different structures, representing distinct functional states of the receptor. According to Figure 3.24 B, resting or desensitized states (apo and NOW, respectively) have the smallest diagonal separation of proline residues at positions 632. This is consistent with a closed ion channel in both the resting unbound state and the ligand-bound desensitized state. As the receptor starts to bind glutamate and enters a partially active state (PDB ID: 4L17 with subunits B and D modeled as glutamate-bound LBD from PDB ID: 1FTJ), their diagonal subunits undergo the largest movements. Subunits A and C separate by ~9 Å, whereas subunits B and D undergo a much larger movement of ~29 Å. Transition from the partially active state to an LBD structure with all four subunits bound to glutamate (tight, PDB ID: 4YU0) leads to further increase of the B-D Pro632 Cα distance by 3.8 Å with slightly decreasing A-C distance (< 1 Å). Transition from the tight crystal structure to the tight rigid body modeled structure further increases the A-C distance by 1.5 Å, whereas the BD distance decreases (2 Å).

These comparisons suggest that receptor activation and ion channel opening requires clamshell closure and LBD rearrangements and that the four subunits of the receptor contribute differently to channel opening. Concluding from the Pro632 displacements, the diagonal B-D subunit pair mostly contributes to diagonal separation of the LBDs, whereas subunits A and C separate to much lesser extent. Going further, one could assume that distal subunits B and D are more important for ion channel gating than proximal subunits A and C.

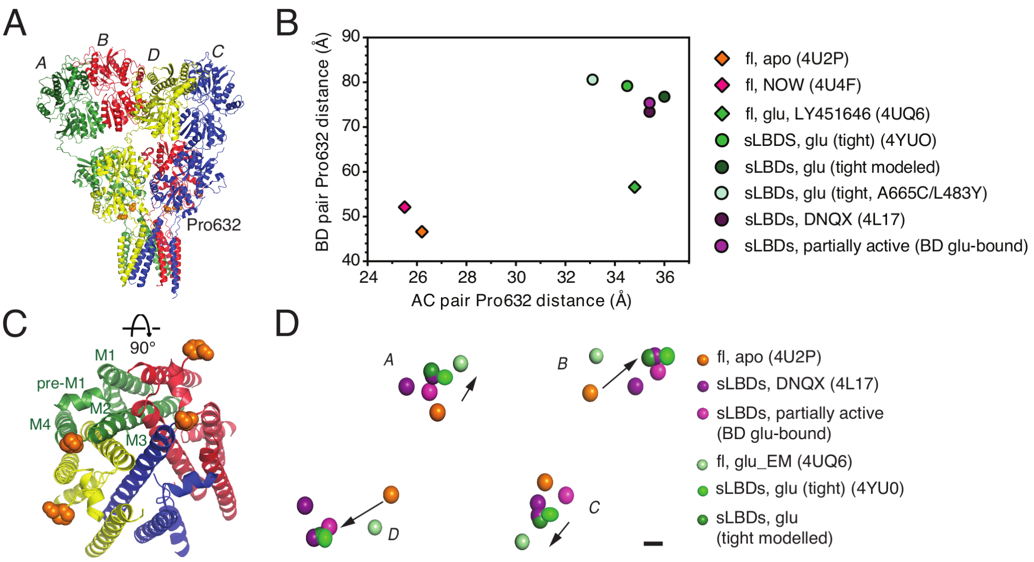

Figure 3.24: Lateral positions of Pro632 atoms as a marker for channel opening. (A) Full-length GluA2 apo structure (PDB ID: 4U2P) showing the position of Pro632 as orange spheres. **(B)** Displacement of diagonal Pro632 Cα atoms between subunits B-D and A-C for apo full-length structure (PDB ID: 4U2P, orange), full-length GluA2 complexed with (5)-Nitrowillardiine (NOW) (PDB ID: 4U4F, pink), EM structure of GluA2 bound to glutamate and LY451646 (positive allosteric modulator, green) (PDB ID: 4UQ6), and structures of soluble LBDs: tight (PDB ID: 4YU0, green), tight after rigid body movement (dark green), sLBDs bound to DNQX (PDB ID: 4L17, purple) and the CA structure with subunits B and D modeled as glutamate-bound LBDs (from 1FTJ) (magenta). Full-length structures have a diamond symbol, soluble LBDs a filled circle. **(C)** View of the TMD of GluA2 (PDB-ID: 3KG2) from the extracellular side of the membrane down the overall 2-fold symmetry axis showing the four transmembrane helices with same coloring as in (A). Helices (M1-M4) are labeled for subunit A (green). Pro632 residues are shown as orange spheres. **(D)** Displacement of Pro632 atoms. View from the top. Pro632 Cα atoms are displayed as spheres. Coloring is according to (B). Arrows indicate movement of Pro632 residues. The scale bar corresponds to 10 Å.

Comparing domain closures for different structures as well as Pro632 distances as a marker for channel opening supports the idea that the major contribution to receptor activation and channel opening results from the domain closure and the resulting conformational changes. The extent of domain closure directly correlates with the separation of D2 domains measured by Pro632 and therefore correlates with channel opening. This suggests that the LBD is the driving force for TMD movements.

To understand how clamshell closure leads to movement of the LBD tetramer and how this is related to receptor activation, in Figure 3.25, movement of linkers connected to the LBD were measured. Change of linker positions were measured for the S1-M1 linker (measured through the Cα of Lys505), the M3-S2 linker (measured through the Cα atoms of Glu634, similar to Pro632), the S2-M4 linker (measured through the Cα atoms of Gly771) and the linker connecting the ATD and the S1 segment of the LBD (measured through the Cα atoms of Val395).

For the linker connecting the S1 segment and the M1 transmembrane helix, a large outward movement by 12Å of the distal subunits B and D can be observed upon activation, whereas the proximal subunits A and C move by ~4 Å. This observation is consistent with larger movements of distal B-D subunits upon receptor activation as measured through the M3-S2 marker Pro632 (also see Figure 3.25 B). The Lys505 atoms don’t move much out of plane. The M3-S2 linker, measured through Glu634 is very similar to the changes of the Pro632 distances. Also here, distal subunits B and D move 3 times as much as the proximal A-C subunits (Figure 3.25 B). The S2-M4 linker is undergoing vertical movements (upper panel in Figure 3.25 C) rather than horizontal movements. Transition from the ligand-free to the active receptor leads to flapping down of marker atoms from subunits B and D, resembling transition from a half-closed book to an open book. The ATD linker seems to undergo inward movement upon receptor activation (Figure 3.25, upper panel). Taken together, these results show how closure of the LBD is connected to movement of the LBD tetramer and linked to receptor activation.

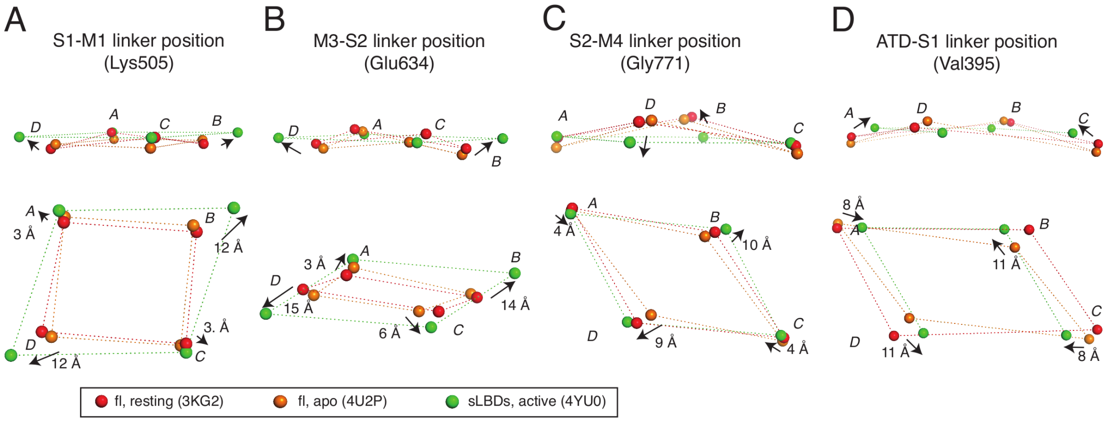

Figure 3.25: Structural changes within the LBD tetramer accompanying receptor activation, measured via linker marker atoms. (A-D) Upper panel shows movement of linker atoms viewed parallel from the membrane and lower panel shows the same movement viewed from the top. Distances were measured from Cα atoms (displayed as spheres). Arrows show the direction of movement from the resting, antagonist-bound state (ZK200775, red spheres) to the ligand-free state (apo, orange spheres) and to the active state (glutamate, green spheres). Distances for the transitions from resting to active state are displayed in Å. Movements are shown for the S1-M1 linker **(A)**, the M3-M2 linker **(B)**, the S2-M4 linker **(C)** and the linker from the ATD to the S1 segment of the LBD **(D)**.

3.1.4.7.3 *Intradimer LBD separation upon activation*

As the ligand binds within the ligand-binding pocket of the LBD, the lower lobes D2 move upwards towards D1, leading to closure of the clamshell. The D2 domains thereby separate upon receptor activation. The upward movement of the lower lobe exerts force on the linkers to the transmembrane domain, thereby pulling the transmembrane helices apart. Analysis of the Pro632 Cα distances of diagonal subunits and domain closure showed that both are intertwined. In Figure 3.26, intradimer separation is measured between the Cα atoms of Ser741 within canonical dimers (i.e. between subunits A and D or between subunits B and C). Ser741 is located at the beginning of helix J in D1 and serves as a marker atom for intradimer LBD separation upon receptor activation. For all measured structures (except the desensitized structure), the D1 interface remains intact. The Ser741 distances don't change dramatically and only vary by 2-3 Å, because all crystal structures have an intact D1-D1 interface and represent non-desensitized structures (except for PDB-ID: 2I3W which represents a desensitized structure). As already described above, the Pro632 atoms of diagonal subunits separate upon receptor activation and distal subunits B and D separate by 30 Å, whereas proximal subunits A and B always separate to lesser extent. For the sLBD structure carrying the S729C mutation (PDB ID: 2I3W), there is a drastic increase in the S741 dimer separation and the D1 interface is not intact anymore. Disruption of the D1-D1 interface is a key feature of desensitization [115]. The D1-D1 interface cannot only be disrupted by the S729C or G729C mutation [114], but also by disrupting the Glu486/Lys493 salt bridge [8, 115].

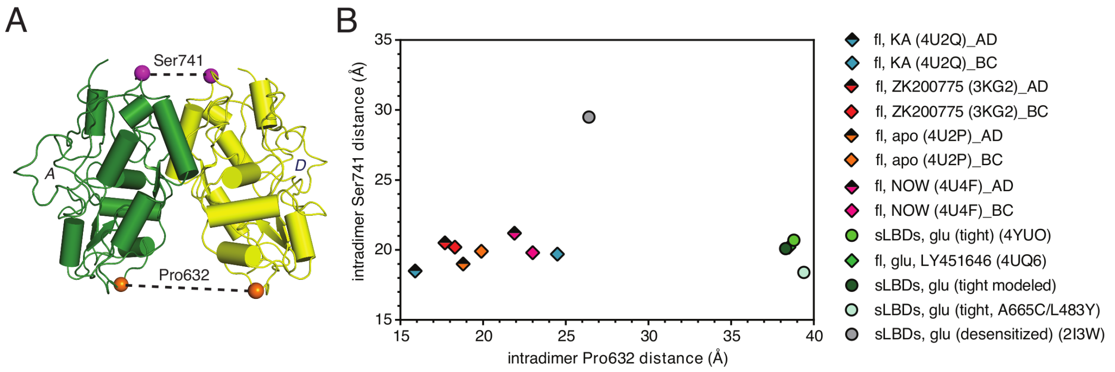

Figure 3.26: Intradimer LBD separation upon activation. (A) Side view of canonical LBD dimers pair A-D. Marker atoms for dimer separation, the Cα atoms for Ser741 in D1 and for Pro632 in D2, are shown as magenta and orange spheres, respectively. Distances are indicated with black dashed lines. The A-B dimer is omitted for clarity. **(B)** Plot of Ser741 pair versus Pro632 pair distances for different structures. Pair distances were measured for canonical dimers, i.e. between subunits A and D (or B and C, if the structure was tetrameric). PDB IDs are given in parentheses. Values for full-length structures have a diamond symbol, whereas sLBD structures have a colored circle. Distances for A-D dimers have a half-filled symbol and distances for B-C dimers have a fully open symbol. If the structure does not contain any tetramer, as it is the case for some sLBD structures, only one canonical dimer distance could be measured.

3.1.4.7.4 *Relative dimer orientation*

The canonical dimers between different structures are very similar. For example, the active A-D dimer from the CA structure (PDB ID: 4L17) can be superimposed on the active dimer from the tight LBD arrangement (PDB ID: 4YU0) with an rmsd of 0.5 Å, with Cα atoms of the upper lobe D1 used for the alignment. All structures shown in Figure 3.27 could be superimposed with an rmsd of < 0.6 Å, indicating that the canonical dimers are very similar, except for different domain closures. The respective overlay using all Cα atoms of the LBDs yields higher rmsd values. Superposition of the tight tetrameric arrangement and the CA structure based on all Cα atoms yields an rmsd value of 1.4 Å.

The relative orientation of the two canonical dimers in the tetramer has previously been described by an interdimer angle. This angle is measured between the two vectors spanned by the Cα atom of Leu748 in subunits A and C and the center of mass (COM) of the Cα atoms of Ala665 in subunits A and C [116].

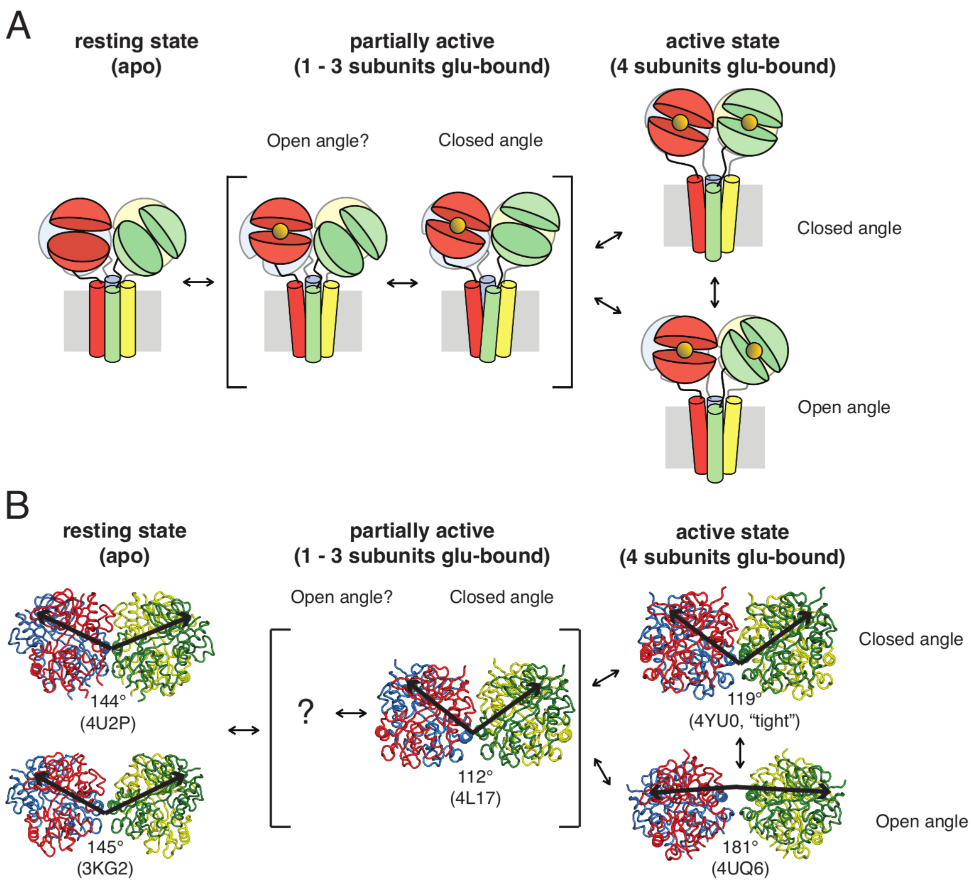

Figure 3.27: Possible conformational transitions upon GluA2 receptor activation. (A) Cartoon of possible LBD dimer movements upon receptor activation. ATDs and CTDs are omitted for clarity. In the ligand-free resting state the LBDs are in an open angle (OA) conformation. Agonist binding to subunits B and D (orange spheres) leads to decrease in the interdimer angle by ~22°. Ligand binding in all four subunits leads to full activation of the receptor with LBDs either adopting an OA or a CA dimer configuration. **(B)** Relative dimer orientation for full-length or sLBD crystal structures. The relative dimer angle was determined using two vectors originating at the A665 Cα COM of subunits A and C to the Cα atoms of Leu748 in subunits A and C. COMs and angles were determined using Pymol. Arrows indicate vectors determined in order to calculate the angle between dimer pair A-D and B-C. The relative dimer angle is given below each structure (in °) and the PDB ID is displayed in parentheses. Figure modified from [342].

Transition from the ligand-free resting state to a partially active state (with 1-3 subunits bound to glutamate) leads to a decrease in the relative dimer angle by 22°. The NOW- and KA-bound LBDs from the full-length GluA2 structure (PDB IDs 4U4F and 4U2Q, respectively) adopt a dimer angle of 157° and 164°, respectively (not shown). Assuming that these partial agonist-bound structures represent an intermediate in receptor activation, the partial active state could also include an OA conformation (marked with a question mark in Figure 3.27). Binding of glutamate to all four subunits of the receptor leads to full activation of the receptor and according to different crystal structures the active receptor can either adopt a closed angle conformation (CA) or an open angle conformation (OA). The interdimer angle in the tight tetrameric arrangement of the A665C/L483Y structure is 122° and 121° in the loose tetrameric arrangement, being very different from the disulfide cross-linked structure harboring the same mutations. Again, the glutamate-bound A665C/L483Y tetramer has a dimer angle representative of an active state.

3.1.4.8 Analysis of the LBD intradimer interface

Canonical dimers of the AMPA receptor were analyzed and described even before the first full-length structure of the GluA2 receptor was published. Structures of isolated LBDs often yielded canonical dimer arrangement that gave first important insights in how ligand binding might lead to channel opening [78, 179, 337, 357, 358]. The dimer interface between canonical active dimers, i.e. between subunits A and D (or between subunits B and C) has therefore been described earlier. Crystal structures of isolated LBDs having at least a canonical dimer in the a.u. or formed by crystal symmetry, gave first insights into the importance of the dimer-dimer interface for channel gating.

Regardless of the construct (full-length or sLBDs), the active dimer interface obtained from crystal structures remained almost always unchanged. The interdimer interface comprises ~1700-1900 Å^2, depending on the structure (Figure 3.28 B-G) and is characterized by two symmetric salt bridges (comprising the same residues in subunits A and D) and eight hydrogen bonds. The interactions are symmetric because identical residues are involved in both subunits. Despite the different interface areas, the hydrogen bonds and salt bridges involved in the interface are conserved. For all structures described below, the interaction network remains unchanged, irrespective of the ligand. Hydrogen bonds for the tight tetrameric structure are shown in Figure 3.28 A. Interestingly, the ligand-free LBDs from full-length GluA2 receptor shows the largest LBD intradimer interface, however, the hydrogen-bonding network remains unchanged (Figure 3.28 G). The dimers are arranged in a back-to-back fashion with contacts through upper lobes D1 only. Intrasubunit contacts are made by helix J and helix D.

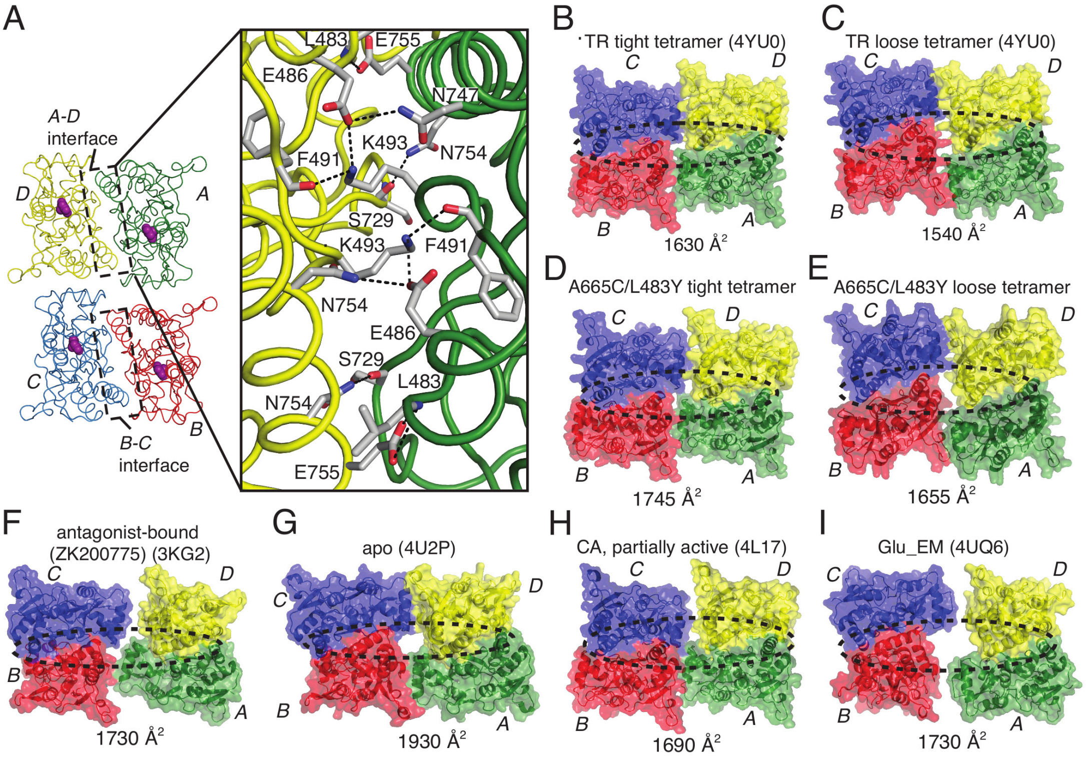

Figure 3.28: The LBD intradimer interface is conserved across full-length and sLBD structures. **(A)** Left panel: top view of LBDs with all four subunits bound to glutamate (purple spheres). The LBD intradimer interfaces (between subunits A-D and B-D) are boxed (dashed line). Right Panel: Magnification of the tight tetrameric A-D interface. Since both sLBD tetramers bound to glutamate are composed of symmetry molecules from the same chain, the A-D and the B-C interfaces are identical and only the A-D interface is displayed for the tight tetrameric structure. **(B-I)** Surface representation of LBDs viewed from the top showing the intradimer area in Å^2 for **(B-C)** the TR tight and the loose tetrameric arrangement with all four subunits bound to glutamate, respectively, **(D-E)** the tight and loose tetrameric arrangement observed in the glutamate-bound A665C/L483Y sLBD crystal structure, respectively, **(F)** DNQX-bound LBDs from full-length GluA2, **(G)** ligand-free LBDs from a full-length crystal structure, **(H)** DNQX-bound sLBDs representing a closed-angle (CA) conformation and a partially active receptor and **(I)** GluA2 LBDs bound to glutamate obtained from a cryo-EM structure. The PDB IDs are given in parentheses. Subunits are labeled with italic letters. Note, that interfaces also contain water molecules for the three solved structures (TR, WT and A665C/L483Y), which are not shown in (A). Interface surfaces were calculated using the PISA server [337].

Being characterized by a disruption of the D1-D1 interface, a desensitized tetramer lacks the D1-D1 electrostatic interactions. The dimer interface comprises a hydrophobic cluster with Leu483 being involved, which is known to block desensitization when mutated to a tyrosine. This example shows how stability of the D1-D1 interface relates to desensitization [179, 359]. In the L483Y mutation, Lys483 makes cation-π interactions with Lys752 and hydrophobic contacts with Leu748.

In Figure 3.28 A, Lys483 symmetrically contacts Glu755, resulting in two hydrogen bonds. Glu486 forms a symmetric salt bridge with Lys493 and is furthermore hydrogen-bonded to Asn747. Leu483 together with Glu486 are conserved in all non-NMDA iGluRs, underlining their importance for interface stability and receptor activation. Lys493 is symmetrically hydrogen-bonded to the backbone carbonyl oxygen of Phe491. The backbone carbonyl oxygen of Ser729 is hydrogen-bonded to the nitrogen atom of the Asn754 carboxamide group. Asn754 is known to be critical for CTZ sensitivity [72]. Ser729 has been investigated in different functional studies, showing that intermolecular disulfide cross-links inhibit the receptor, with the cross-link being state-dependent (trapping in the desensitized state) [114, 115, 360].

3.1.4.9 Crystallization attempts for HHH mutants and derivatives thereof

3.1.4.9.1 *Crystallization and structure of the HHH mutant bound to kainate*

Data from static light scattering (Section 3.1.3.4) suggested that LBDs of the HHH mutant are able to form oligomers by coordination of metal ions. In crystallographic studies using zinc ions for coordination, we attempted to obtain a tetrameric LBD structure with coordinated zinc that would represent a distinct subunit arrangement compared to the TR and WT tetrameric LBD arrangement and thereby a different functional state. By crystallizing the protein in presence of different ligands like partial agonists, we aimed to obtain a crystal structure of tetrameric LBDs that would represent a partially active state of the receptor, as functional studies suggest [116].

Initial crystallization experiments were carried out with the HHH mutant in different backgrounds, for example in S1S2J WT, the L483Y or the TR background. Out of the different partial agonists that were tested – HW, FW, IW and kainate – a dimeric LBD arrangement with coordinated zinc ions could be obtained for the HHH mutant complexed with the partial agonist kainate. Different from the other three solved sLBD structures, the triple His mutant crystallized in the orthorhombic space group 18 ($P2_12_12$). Crystallization plates were set up with zinc as additive. Crystals were of cubic-like shape, grew within 2-3 days at 4°C and had final dimensions of 140 x 120 x 80 µm (Figure 3.29).

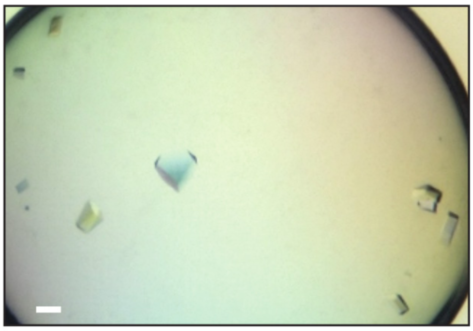

Figure 3.29: Crystals of GluA2 HHH mutant LBD complexed with kainate. The best-diffracting GluA2 HHH LBD crystal grew in 100 mM NaAc pH 6.0, 20% (w/v) PEG 6000 and 10 mM $ZnCl_2$ (finescreen). The scale bar corresponds to 100 µm.

As mentioned already, the crystal belongs to the space group $P2_12_12$ with cell dimensions (in Å): a= 63.0, b= 88.9, c= 48.1 and angles of α= β= γ= 90°. Table 3.9 lists the data collection statistics. Values in parentheses indicate values for the highest resolution shell.

Table 3.9: Data collection statistics for the kainate-bound GluA2 HHH sLBD mutant

Data Collection Statistics	**G437H, K439H, D456H + kainate**
Space group	$P\ 2_1\ 2_1\ 2$
Cell dimensions	
a, b, c (Å)	63.0, 88.9, 48.1
α, β, γ (°)	90, 90, 90
Wavelength (Å)	0.918
Resolution (Å)	50-1.4 (1.45-1.41)
Crystal mosaicity (°)	0.093
R_{sym} (%)	4.7 (62.4)
R_{meas} (%) [a]	5.4 (72.3)
Total reflections	209,835 (14,777)
Unique reflections	52,486 (3,796)
I/σI	15.07 (2.05)
Completeness (%)	99.3 (99.5)
Redundancy	4.0 (3.9)

[a] R_{meas}, intensity of the i-th measurement of reflection hkl; $\langle I(hkl)\rangle$ – average value of the intensity of reflection hkl for all I measurements, n – redundancy.

$$R_{meas} = \left(\frac{n}{n-1}\right)^{1/2} \frac{\sum_{hkl}\sum_i\left[\left|I_i(hkl)-\langle I(hkl)\rangle\right|\right]}{\sum_{hkl}\sum_i I_i(hkl)}$$

The phase problem was solved by molecular replacement. One LBD molecule was found in the a.u. with a Matthews coefficient of 2.32 $Å^3$/Da, indicating a solvent content of approx. 47% [348]. The preliminary final model was refined to R_{work}/R_{free} of 17.9%/20.6%. The refinement statistics are shown in Table 3.10. Values in parentheses indicate values for the highest-resolution shell.

Table 3.10: Refinement statistics for the kainate-bound GluA2 HHH sLBD

Refinement Statistics	**HHH + kainate**
Resolution	48.13-1.41 (1.44-1.41)
Reflections	52,486 (2,579)
R_{work} (%)[b]	17.90 (27.85)
R_{free} (%)[b]	20.58 (31.11)
No. of protein molecules per a.u.	1
No. of protein atoms	2,092
No. of water molecules	362
Average B factors (Å^2)	
Overall	21.10
Protein	19.60
Solvent	29.97
Root mean square deviation from ideality	
Rmsd bonds (Å) [c]	0.009
Rmsd angles (°) [c]	1.3
Ramachandran statistics	
Ramachandran favoured (%)	99.62
Ramachandran outliers (%)	0
Rotamer outliers (%)	0.45

[b] R-factors: $R_{work} = \frac{\sum_{hkl}\left[\left\|F_{obs}\right| - k\left|F_{calc}\right\|\right]}{\sum_{hkl}\left|F_{obs}\right|}$ and $R_{free} = \frac{\sum_{hklTS}\left[\left\|F_{obs}\right| - k\left|F_{calc}\right\|\right]}{\sum_{hklTS}\left|F_{obs}\right|}$; hklTS – test set, F_{obs} and F_{calc} – observed and calculated (from the model) structure factor amplitudes.

[c] Rmsd – root mean squared deviation

The Ramachandran plot shows that more than 99% of all residues are in the favoured regions of φ and ψ angles, with no residues in disallowed regions (Figure 3.30).

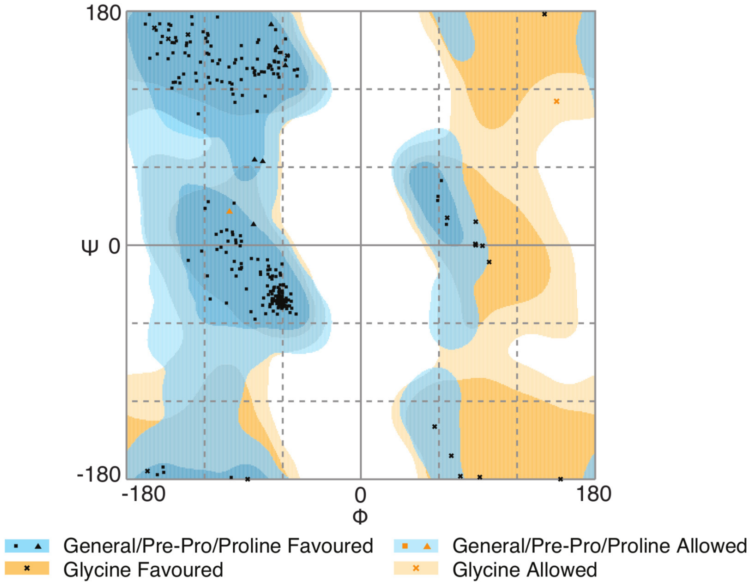

Figure 3.30: Ramachandran plot of the GluA2 HHH mutant sLBD bound to kainate. The Ramachandran plot shows torsion angles for all peptide bonds. Squares and triangles represent general and proline residues, whereas crosses represent glycine residues. 99.2% of all residues are in the favoured region (dark blue and dark orange), whereas 0.8% of the residues are in the allowed region (light blue and light orange). No residue has phi-psi combinations in the disallowed region. The Ramachandran plot was prepared using RAMPAGE by Paul de Bakker and Simon Lovell (http://www-cryst.bioc.cam.ac.uk/rampage/) [338].

The monomer in the a.u. has kainate bound in its ligand-binding pocket. The protein was purified in presence of glutamate, so that extensive dialysis into a ligand-free buffer followed by dialysis into a buffer containing the new partial agonist was necessary (see Section 2.2.2.14). As shown in Figure 3.31, glutamate was replaced by the weaker agonist kainate. The binding mode of the partial agonist within the ligand-binding pocket was described in 1998, which was at the same time the first structure of isolated LBDs of the glutamate receptor [108]. Kainate has a similar binding mode as the full agonist glutamate. For both ligands, the α-carboxylic group of the ligand is stabilized at its position through hydrogen bonds with both amino groups of the guanidinium side chain of Arg485. Different from kainate, the α-carboxylic group is furthermore hydrogen-bonded to the main chain NH group of Thr480. The amide nitrogen atom of both ligands (in kainate it is located within the pyrrolidine ring) is hydrogen-bonded to the carbonyl oxygen of Pro478, to the hydroxyl group of Thr480 and to one and two side chain carboxyl group of Glu705 for kainate and glutamate, respectively. Also the γ-carboxylic group of both ligands is hydrogen-bonded to the main chain NH of Thr655 (magnification in Figure 3.31). The different degrees of domain closure position some residues of the lower lobe D2 slightly different, accounting for the fact that the main chain NH of Ser654 interacts with the γ-carboxylic group of kainate, whereas the same residue forms a hydrogen bond with the α-carboxylic group in glutamate. The domains are more open compared to glutamate-bound LBDs.

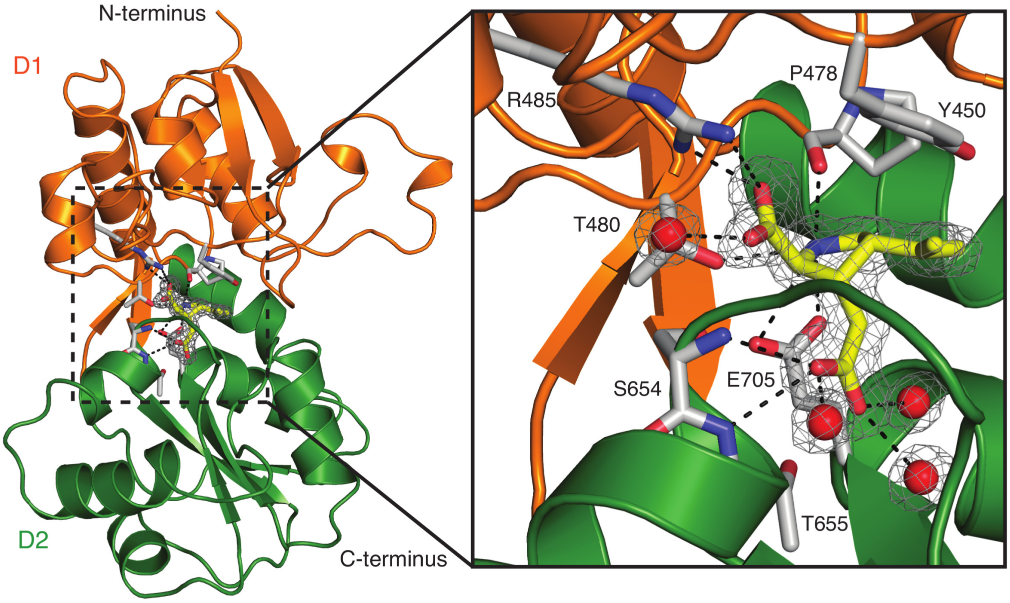

Figure 3.31: Crystal structure of the HHH mutant complexed with kainate. Upper and lower lobes of the GluA2 LBD are colored in orange and green, respectively. Residues that interact with the ligand are shown as grey sticks. Kainate is shown in stick representation (yellow) with the $2F_o - F_c$ electron density contoured at 1 σ. N- and C-termini of the GluA2 LBD are indicated. Right panel shows close-up of the ligand-binding pocket of the crystallized HHH mutant bound to kainate. Distances are indicated by black dashed lines.

The ξ1 and ξ2 distances expand to 10.0 and 8.4 Å in the kainate-bound sLBD, respectively, whereas the same distances are 9.4 and 7.8 Å in the glutamate-bound LBD, respectively. As a result of the smaller degree of cleft closure, the distances for marker positions for channel opening are also different. The distance between Ser741 as a marker position for the D1 distance between canonical dimers remains unchanged with 20.7 Å in the kainate-bound LBD (the same distance is 20.7 Å for the TR tight tetrameric arrangement), and because of the smaller degree of domain closure, the Pro632 distance as a S2-M3 marker position decreases from 38.0 Å in the glutamate-bound TR structure to 36.2 Å in the kainate-bound triple His mutant.

In other kainate-bound sLBD dimers with approx. the same degree of domain closure (ξ1= 9.7 Å and ξ2= 9.4 Å), the Pro632 Cα and the Ser741 Cα distances between dimers are 34.6 and 18.8 Å, respectively (PDB ID: 1FW0), which is slightly different but comparable to our kainate-bound LBD dimer. As the D2 domain moves upwards upon ligand binding with the D1 domain remaining largely unchanged, the S741 distance is the same for glutamate and kainate binding, whereas the D2 distance differs because kainate induces less domain closure compared to glutamate.

Canonical LBD dimers can be generated by crystallographic symmetry of the HHH crystal structure. The resulting dimers can be superimposed on the dimer pair from the TR mutant with an rmsd of 0.45 Å based on the Cα atoms of the upper lobes D1. No physiologically relevant tetramer can be obtained by crystallographic symmetry as the N- and C-termini of each dimer pair that could potentially form a tetramer, are pointing into opposite directions. Furthermore, the canonical dimer pair is distorted with one dimer pair being shifted and tilted towards the second dimer pair (Figure 3.32 A and B).

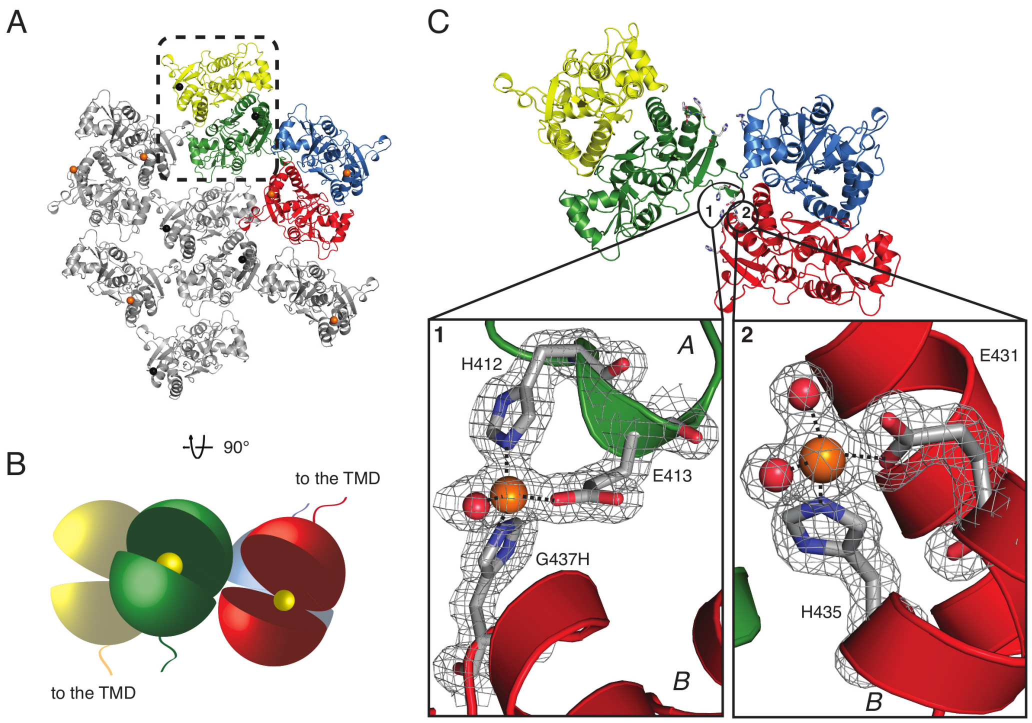

Figure 3.32: Crystal packing of the HHH mutant bound to kainate revealed by the space group P2₁2₁2. (A) By applying crystal symmetry, canonical dimers of the GluA2 LBD are formed; one is boxed with black dashed lines. A distorted tetramer is formed with one canonical dimer being translated and tilted relative to the other dimer. The N- and C-termini of two neighboring dimers are facing opposite sites (depicted as black and orange spheres, respectively). **(B)** 3D representation of the LBDs with the same coloring as in (A) and (C). Every LBD subunits is represented as a pacman with kainate bound as yellow spheres. Linkers to the TMD, which are facing to different sites for the two dimers, are indicated. **(C)** Upper panel shows a cartoon representation of the distorted tetramer with the two zinc coordination sites being boxed. Residues that are involved in zinc coordination are shown as grey sticks. Lower panel shows magnification of the metal coordination sites (box 1 and box 2). The electron density is shown as grey meshes and contoured at 1 σ. Zinc and water molecules are shown as orange and red spheres, respectively. Black dashed lines indicate the metal coordination.

Zinc that was present in the crystallization conditions, is coordinated by side chain residues of the LBD, however, only one of the mutated His residues of the HHH mutant, G437H, participates in the Zn coordination, while the other two His residues, K439H and D456H, no not participate in the metal bridge. In total, two zinc coordination sites could be observed (boxes 1 and 2 in Figure 3.32 C). Although zinc is bridging subunits in the sLBD crystal structure, this geometry could not form in the full-length receptor because of the translation of dimers relative to each other. His437 from one monomer coordinates zinc together with the native residues His412 and Glu413 from a symmetry related molecule (box 1 in Figure 3.32 C). A water molecule is involved in metal coordination to achieve a tetrahedral geometry. The second zinc ion is coordinated by Glu431 and His435 within one LBD molecule, together with two water molecules in a tetrahedral geometry (box 2 in Figure 3.32 C).

As the first attempt to obtain a crystal structure of the HHH mutant with coordinated zinc in the dimer interfaces failed due to participation of native LBD residues at the interface, respective residues were mutated to alanines, resulting in the HHHAA mutant (G437H, K439H, D456H, H412A, H435A).

3.1.4.9.2 *Crystallization and structure of the HHHAA mutant*

As the HHH mutant failed to yield the desired LBD conformation and zinc coordination, residues His412 and His435 that were involved in a zinc bridge were mutated to Ala residues (G437H, K439H, D456H, H412A, H435A, named “HHHAA” mutant). The resulting HHHAA mutant was either expressed in GluA2 S1S2J WT or in the L483Y background, again with different ligands (glutamate, kainate). Data could be collected for glutamate-bound GluA2 HHHAA mutant LBDs. Crystals of glutamate-bound were of plate-like shape and grew within 3-4 days. The biggest crystals had maximal final dimensions of 120 x 400 x 40 µm (Figure 3.33). Data could be collected for all three crystals in Figure 3.33 and they belonged to the monoclinic space group C2 (Figure 3.33 B and C) or the hexagonal space group $P6_322$ (Figure 3.33 A). However, zinc coordination could only be observed in one of the solved structures (crystal in Figure 3.33 C). Data collection statistics are given in Table 3.11. Values in parentheses indicate values for the highest resolution shell.

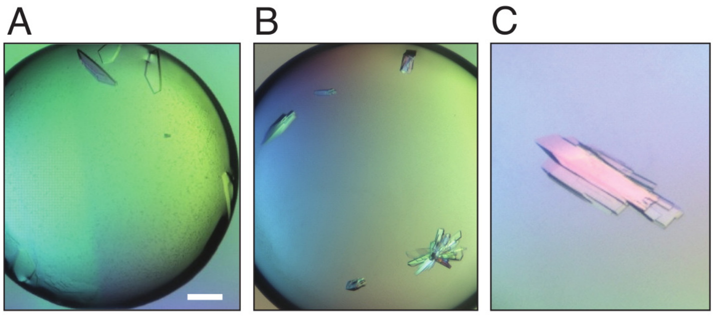

Figure 3.33: Crystals of GluA2 HHHAA mutant LBD complexed with glutamate. The best-diffracting GluA2 HHHAA LBD crystals grew in **(A)** 25% (w/v) PEG 1500, 100 mM $ZnCl_2$, 100 mM PCB buffer pH 6, **(B)** 200 mM NaAc pH 5.5, 20% PEG 3350, 10 mM $ZnCl_2$ and **(C)** 100 mM Tris pH 7.0, 20% PEG 6000, 10 mM $ZnCl_2$. The scale bar corresponds to 200 µm.

Table 3.11: Data collection statistics for the glutamate-bound GluA2 HHHAA sLBD mutant

Data Collection Statistics	**HHHAA + glutamate crystal in (C)**
Space group	C2
Cell dimensions	
a, b, c (Å)	96.8, 47.3, 127.9
α, β, γ (°)	90, 105.8, 90
Wavelength (Å)	0.918
Resolution (Å)	50-1.64 (1.74-1.64)
Crystal mosaicity (°)	0.148
R_{sym} (%)	8.7 (78.2)
R_{meas} (%) [a]	10.1 (91.8)
Total reflections	265,820 (17,857)
Unique reflections	67,327 (4,926)
I/σI	12.71 (1.99)
Completeness (%)	99.7 (98.5)
Redundancy	3.9 (3.7)

[a] R_{meas}, intensity of the i-th measurement of reflection hkl; $\langle I(hkl)\rangle$ – average value of the intensity of reflection hkl for all I measurements, n – redundancy.

$$R_{meas} = \left(\frac{n}{n-1}\right)^{1/2} \frac{\sum_{hkl}\sum_{i}\left[\left|I_i(hkl) - \langle I(hkl)\rangle\right|\right]}{\sum_{hkl}\sum_{i} I_i(hkl)}$$

The phase problem was solved by molecular replacement. Two LBD molecules were found in the a.u. with a Matthews coefficient of 2.43 Å^3/Da, indicating a solvent content of approx. 49%. The preliminary model was refined to R_{work}/R_{free} of 18.7%/22.6%. Refinement statistics are shown in Table 3.12. Values in parentheses indicate values for the highest-resolution shell.

Table 3.12: Refinement statistics for the HHHAA mutant GluA2 sLBD bound to glutamate

Refinement Statistics	HHHAA + glutamate
Resolution	46.56–1.64 (1.66-1.64)
Reflections	68,483 (2,381)
R_{work} (%)[b]	18.71 (30.7)
R_{free} (%)[b]	22.62 (35.6)
No. of protein molecules per a.u.	2
No. of protein atoms	4,069
No. of water molecules	542
Average B factors (Å^2)	
Overall	21.29
Protein	20.29
Solvent	26.21
Root mean square deviation from ideality	
Rmsd bonds (Å) [c]	0.008
Rmsd angles (°) [c]	1.2
Ramachandran statistics	
Ramachandran favoured (%)	98.46
Ramachandran outliers (%)	0
Rotamer outliers (%)	1.83

[b] R-factors: $R_{work} = \frac{\sum_{hkl}\left[\left\|F_{obs}\right|-k\left|F_{calc}\right\|\right]}{\sum_{hkl}\left|F_{obs}\right|}$ and $R_{free} = \frac{\sum_{hklTS}\left[\left\|F_{obs}\right|-k\left|F_{calc}\right\|\right]}{\sum_{hklTS}\left|F_{obs}\right|}$; hklTS – test set, F_{obs} and F_{calc} – observed and calculated (from the model) structure factor amplitudes.

[c] Rmsd – root mean squared deviation

The Ramachandran plot shows that 97.3% (different from the values in Table 3.12, obtained from the xds file) of all residues are in the favoured regions of φ and ψ angles, with no residues in disallowed regions (Figure 3.34).

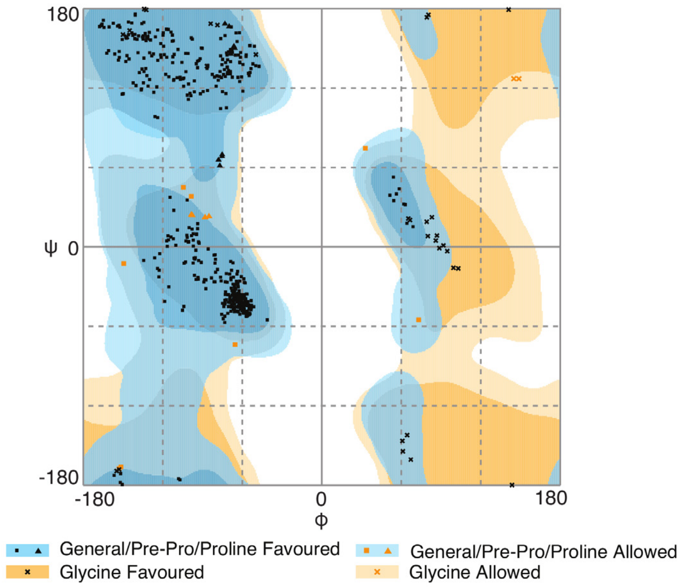

Figure 3.34: Ramachandran plot of the GluA2 HHHAA sLBD bound to glutamate. The Ramachandran plot shows torsion angles of all peptide bonds. Squares and triangles represent general and proline residues, whereas crosses represent glycine residues. 97.3% of all residues are in the favoured region (dark blue and dark orange), whereas 2.7% of the residues are in the allowed region (light blue and light orange). No residue has phi-psi combinations in the disallowed region The Ramachandran plot was prepared using RAMPAGE by Paul de Bakker and Simon Lovell (http://www-cryst.bioc.cam.ac.uk/rampage/) [338].

Via crystallographic symmetry, the two LBD molecules in the a.u. assemble in two different tetrameric arrangements. Tetramer 1 resembles the loose tetramer we already obtained for the WT/TR GluA2 LBD as well as for the A665C/L483Y LBD and tetramer 2 is characterized by distorted LBD packing. Both tetramers have a unique LBD orientation with the ATD linkers facing one site and the TMD linkers facing the opposite site (Figure 3.35 A). The canonical active dimers of both LBD arrangements can be superimposed on the TR active dimers with an rmsd of 0.28 Å (using D1 Cα atoms), indicating that the canonical dimers are similar. In tetramer 1, the two back-to-back dimers pack against each other to form an LBD tetramer with dimer pairs shifted outwards the overall axis of two-fold symmetry (Figure 3.35 B). Thus, the distance between A665-Cα atoms in subunits A and C expands to 28.7 Å, whereas the distance is 22.6 Å in the TR loose tetrameric arrangement. Due to the outward shift of one dimer pair in tetramer 1, the interdimer angle observed in this HHHAA tetramer increases to 125° compared to 118° observed for the relative dimer orientation in the TR loose tetramer.

As crystallization trials were performed in presence of 10 mM zinc, density for zinc could be observed in the interdimer interfaces of both tetramers (Figure 3.35 B and C).

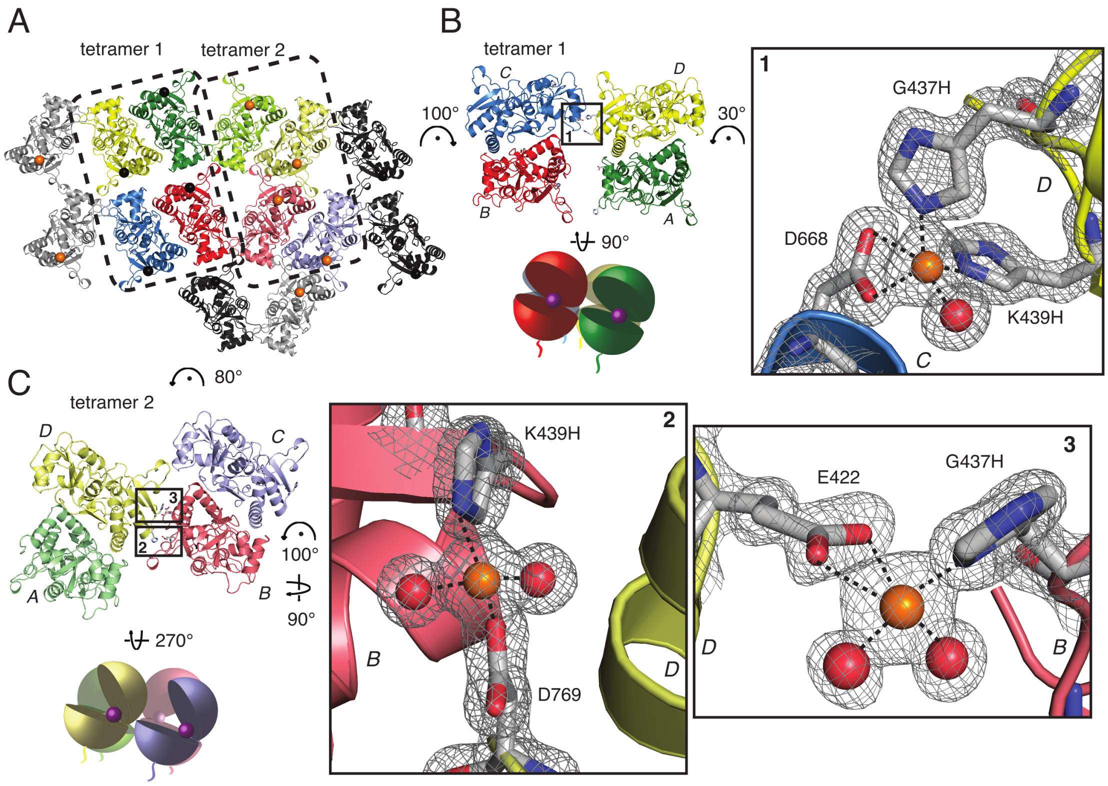

Figure 3.35: The glutamate-bound HHHAA mutant produces two different tetramers by crystallographic symmetry; both of them are coordinating zinc in the interdimer interface. Three metal coordination sites could be found between dimers (boxes 1-3). **(A)** Crystal packing reveals canonical dimer formation and two different types of tetramers, a loose-like tetramer (tetramer 1) and a tetramer with shifted subunits (tetramer 2), both being boxed with black dashed lines. Molecules from chain A assemble as tetramer 1 (light grey), whereas molecules from chain B form tetramer 2 (dark grey). Linkers to the ATD and TMD are shown as black and orange spheres, respectively. **(B)** The left panel shows zinc coordination in the loose-like tetramer (tetramer 1) with residues involved in metal coordination being boxed (box 1). The lower left panel shows 3D cartoon of the LBD conformation in this tetramer with the connection to the TMD shown as colored lines. Glutamate is shown as purple spheres and subunits are colored as in (A). The right panel shows magnification of zinc coordination by G437H, K439H and D668. **(C)** The left panel shows cartoon representation of the LBD arrangement viewed from the bottom (upper left panel) with residues involved in Zn coordination being boxed (box 2 and 3) and 3D cartoon (lower left panel) of the LBD arrangement. Middle panel in (C) shows electron density for Zn coordination by K439H and D769 (box 2) and the right panel in (C) shows electron density for the Zn coordination site between G437H and E422. Zinc ions and water molecules are shown as orange and red spheres, respectively. Electron density is contoured at 1.5 σ and shown as grey mesh. Metal binding sites were evaluated using the Metal Binding Site Validation Server (CMM) [361].

In total, three zinc binding sites could be identified (Figure 3.35 B and C), one in tetramer 1 and two metal coordination events in tetramer 2. Tetramer 1 has a zinc ion coordinated between G437H and K439H in subunit D and Asp668 in subunit C together with one water molecule to achieve a square-based pyramidal metal coordination (Figure 3.35 B, right panel).

In tetramer 2, two zinc ions are coordinated by residues in subunits B and D (Figure 3.35 C). One of the zinc ions is coordinated by K439H, Asp769 and two water molecules to achieve a tetrahedral coordination, whereas the second zinc ion is coordinated by Glu422 in subunits D, G437H in subunit B and two water molecules to obtain a square-based pyramidal metal coordination (Figure 3.35 C, right panel).

In further mutagenesis attempts, Asp668 was mutated to Ala (D668A) however introduction of a third Ala residue (HHHAAA) resulted in drastic reduction of expression in a way, that a purification from 12 L bacterial suspension yielded very little protein amounts. Unfortunately, with the experiments described above, we were not able to capture the triple His mutated LBDs in a partially active state with coordinated zinc ions.

3.1.5 Electrophysiological recordings to evaluate the TR tight structure

3.1.5.1 Histidine mutant design

Electrophysiological recordings were performed by Dr. Jelena Baranovic and Dr. Hector Salazar.

To test if the two different tetrameric arrangement that could be observed in the WT and E713T/Y768R structures are of biological importance and represent a functional state in the full-length GluA2 receptor during any step of activation, histidine bridges were designed that should be able to form in the presence of zinc ions in either the tight or the loose tetrameric arrangement. Histidine mutations were preferred over cysteine mutations since cysteine mutations express very badly and behave poorly in functional experiments [116]. Zinc can be coordinated by a variety of amino acid residues, the most common ones being cysteines, histidines, glutamates and aspartates [362-364]. It has been reported that in over 97% of deposited zinc-containing X-ray structures coordination occurs by cysteine and histidine residues [362]. In case of zinc coordination by histidines, either nitrogen (N^{δ} or N^{ε}) of the imidazole group is able to chelate the metal. The chelating group either has a formal negative charge (as it is the case for the carboxylate group of glutamate and aspartate) or no formal charge but a free electron pair. Rarely, zinc ions are coordinated by two or three ligands, however, the most stable coordination is a tetrahedral coordination with four ligands in order to satisfy the 18 electron rule. The Zn-His distance observed for crystal structures ranges from 2 to 3 Å (depending on the resolution, mean distance is 2.03 Å) [362, 363]. In order to evaluate the two different tetrameric arrangements resulting from the crystal packing, triple histidine mutations were designed in the interdimer interface (e.g. between subunits A and B and between subunits C and D, or in one exception between B and D) that should either only form in the tight or the loose tetrameric arrangement, thereby enabling us to distinguish between the two arrangements. Figure 3.36 gives an overview of the designed histidine mutants and their distances. The crystal structure from the E713T/Y768R double mutant was used as a template for mutant design into the full-length GluA2 receptor. If the His residues are in close proximity as predicted by the crystal structure, zinc coordination should occur and be measurable in patch clamping experiment after application of glutamate.

Four of the created mutants were predicted to form Zinc bridges in the tight but not the loose tetrameric arrangement, T1-T4 (T1 – D668H, T672H, K761H, T2 – D668H, T672H, K765H, T3 – D668H, K761H, K765H). These bridges were supposed to form between subunits A and B and C and D (Figure 3.36). It was more difficult to find suitable His bridges for the loose tetrameric LBD arrangement as the four subunits are displaced and have a bigger interdimer separation. One triple histidine mutant that, according to the crystal structure, should be able form a zinc bridge is L1 (E422H, D668H, T672H); this bridge is predicted to form between subunits A and B and between subunits C and D. Another single mutation, K434H, has a neighboring native histidine residue (H435) to form a zinc bridge (L2) with the same residues in the opposing subunit (between distal subunits B and D). As a control, individual single and double mutants were included. Successful metal ion coordination by the sLBDs resulted in a reduced peak current compared to the same WT patch. Metal trapping (except for one case, see later) is inhibitory. One possible explanation could be that the metal bridge puts restraints on the LBDs thereby leading to the current reduction. The LBDs seem to get trapped in a conformation that is less active than the receptor without any restraints and metal bridges.

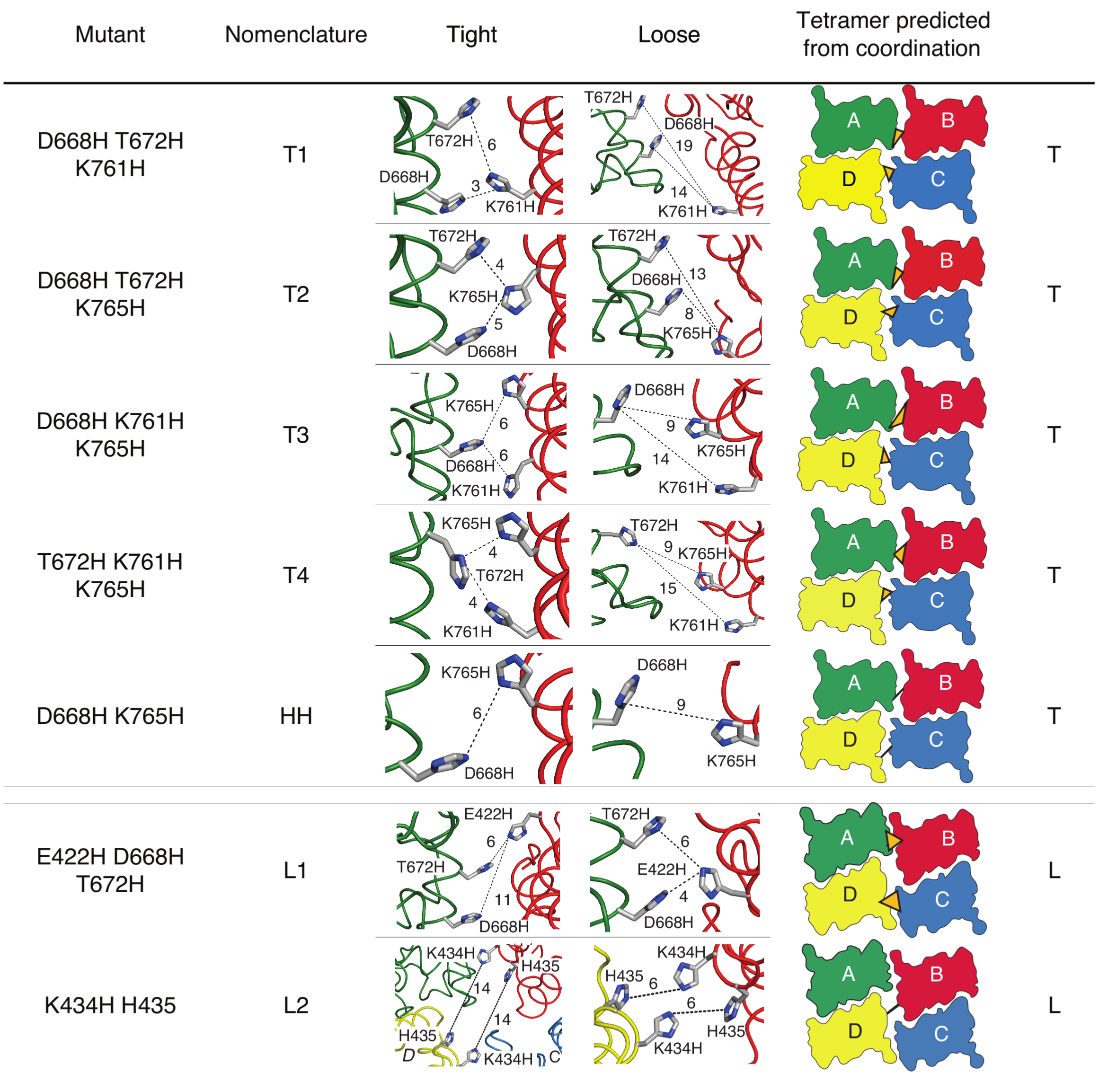

Figure 3.36: His mutations designed for evaluation of the tight and the loose tetrameric arrangement. The first column from the left describes the histidine mutations introduced into the LBD, the second column gives the nomenclature that will be used in the rest of the work for the respective mutation (T – tight tetrameric arrangement, L – loose tetrameric arrangement). The third and the fourth column show a cartoon representation of the histidine mutations (shown as sticks) modeled into the tight and the loose tetrameric arrangement, respectively. Subunits are colored as in the subsequent column (A – green, B – red, C – blue and D – yellow). Dashed lines show distances between His mutants and values are in Å. The fifth column shows a schematic cartoon of the LBD viewed from the top. Orange triangles or black lines indicate location of the histidine mutations and how the metal coordination is expected to occur. The sixth and last column shows where the bridge is expected to form based on the sLBD structure, either in the loose tetrameric arrangement (L) or in the tight tetrameric arrangement (T). Figure was taken from [342].

3.1.5.2 His mutant screening

The designed metal ion bridges were tested in full-length GluA2 receptors (Figure 3.37). Therefore, WT and AMPA receptor mutants were transiently expressed in HEK-293 cells for outside-out patching. For metal bridging experiments, zinc was added to the patches. As a control for zinc-free conditions, 2 mM EDTA was added.

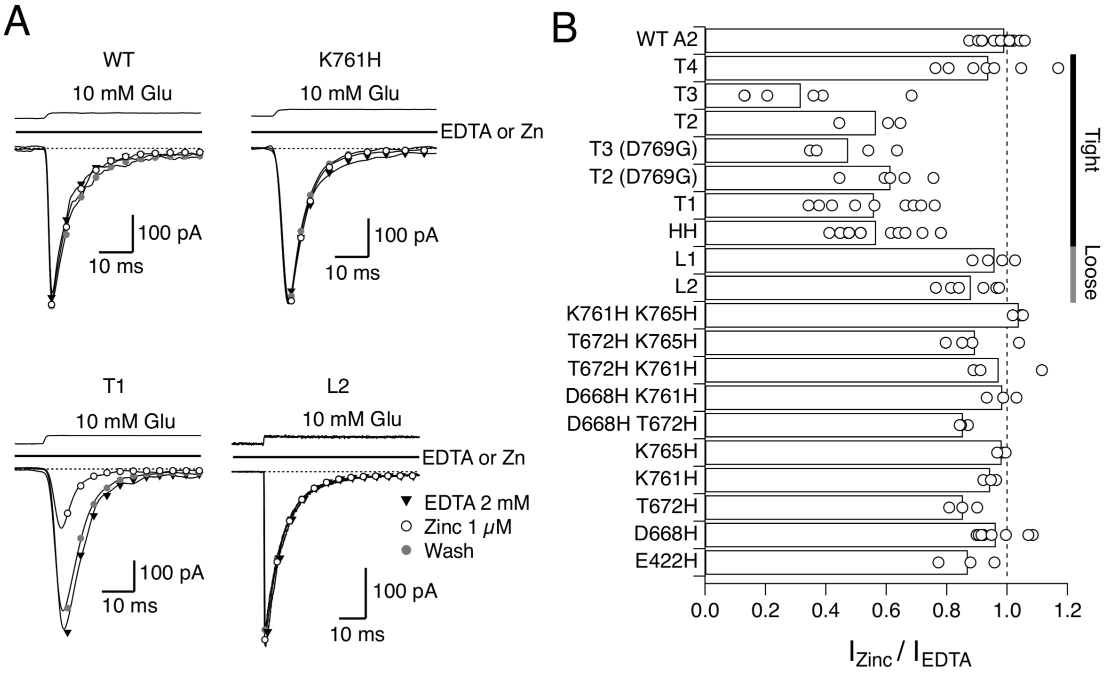

Figure 3.37: Functional metal ion trapping experiments of glutamate-bound full-length GluA2 receptors expressed in HEK-293 cells. (A) Representative traces of WT and mutant GluA2 receptors that should help to evaluate the tight and the loose tetrameric arrangement. All patches were first exposed to EDTA (triangles), followed by 1 µM zinc for metal coordination (open circles) and afterwards, the patches were washed into EDTA again (for zinc-free solution). WT GluA2 patches and one of the control single mutant K761H were insensitive to zinc. The T1 mutant (D668H, T672H, K761H) that was predicted to form in the tight tetrameric arrangement, showed a current reduction when exposed to zinc, whereas the L2 mutant didn't show any effect. **(B)** Summary of tested His mutants that are predicted to form in the tight (black line on the right) or the loose tetrameric arrangement (grey line). T1 mutant had a peak current of 56 ± 5% of that in EDTA (n=9), for T2 it is 56 ± 6% (n=3) and for T3 it is 32 ± 9% (n=6) ($p < 0.0001$). L1 peak current in Zn is 96 ± 3% (n=4). Other mutants (double and single) are control mutants to show specificity of the triple or quadruple mutants. Circles are I_{Zinc}/I_{EDTA} values for individual patches, whereas the bar shows the mean peak current from all measurements. Figure extracted from [342].

All possible mutations were tested, and indeed, the T1, T2 and T3 mutants showed a current reduction after 1 µM zinc exposure by about 50%, whereas the control double and single mutations didn't show any or just little inhibition in zinc (Figure 3.37). This suggests that bridges T1-T3 that were predicted to form from the soluble LBD crystal structure can form in the full-length AMPA receptor GluA2 during activation. A summary of the performed metal trapping experiments in given in Figure 3.37.
Although the T4 mutant (T672H, K761H, K765H) was predicted to form in the tight tetrameric arrangement, it was insensitive to zinc, the peak current was 94 ±5% of the peak current in EDTA (n=7, p=0.1).

Interestingly, another mutant gave unexpected results. The double mutant D668H, K765H (HH) showed a current reduction after exposure to zinc by 33 % ± 3% (n=17, $p < 0.0001$ compared to WT). As this double mutation is part of the T2 and T3 triple His mutants, it was first questionable if the peak current reduction seen in these triple His mutant is only a result of the HH mutant alone without the third T2 or T3 mutation. In the next paragraph, D769 is identified as a native coordination partner in the HH mutant. To test if the T2 and T3 mutants are dependent on the native D769 residue, a D769G mutation was included in the T2 and T3 background (T2 D769G or T3 D769G). The resulting quadruple mutants were still able to coordinate the zinc as seen by the current reduction (Figure 3.38 B). This suggests that the triple mutants T2 and T3 are not dependent on D769.

3.1.5.3 The HH mutant involves the native D769 residue in Zn coordination

The HH mutant showed a strong inhibition in presence of zinc, similar to that seen in the T1 mutant, albeit lacking a third His mutant. Although zinc bridges are possible with two ligands, it is not very common [363]. Also, the number of ligands involved in the metal bridge determines the affinity of the bridge. For two residues involved, the affinity is about 10^{-5} M and increases by two orders of magnitude when three residues are involved and by another two orders of magnitude (nM range) when four ligands form the metal bridge [365]. As the bridge has an IC_{50} value of 370 nM (Figure 3.38 A) this rather indicates the presence of three ligands rather than two. A native His D769 residue could be found 8 Å apart from the D668H mutant, which is usually too far apart for a metal bridge to form. Carboxylate groups can coordinate metals in a monodentate or bidentate fashion. Since D769 is too far apart from the two His residues, the LBD arrangement attained by the HH cross-link could indicate a tetrameric LBD arrangement different from the TR tight tetrameric arrangement that could be achieved by structural rearrangements of the LBD during activation.

In order to verify the hypothesis that D769 could be involved in the HH metal bridge, the residue was mutated to glycine (D769G), to lysine (D769K), to histidine (D769H) or to glutamate (D769E) and designed in the HH background (D688H, K756H) in order to obtain a set of different triple His mutants. The HH mutant shows a peak current reduction by 43%, however when mutating the putative involved native residue D769 to glutamate, the inhibition is similar to that seen in the HH mutant (p= 0.06 compared to HH, n=7) (Figure 3.38 C). The D769H mutant even further strengthened the metal coordination as the peak current reduction was ~90% (p< 0.0001 compared to HH, n=5). In turn, the D769G or the D769K mutants had only a very weak effect in zinc (for D769K: p = 0.0003 compared to HH, n = 8, and for D769K: p < 0.0001 compared to HH, n=12). These results suggest that the HH mutant needs the native D769 residue for effective zinc coordination. However, since this residue is too far apart in the tight tetrameric arrangement, the zinc bridge forming in the HH mutant (with native D769) must resemble a receptor state during activation that is different from the TR tight tetrameric arrangement.

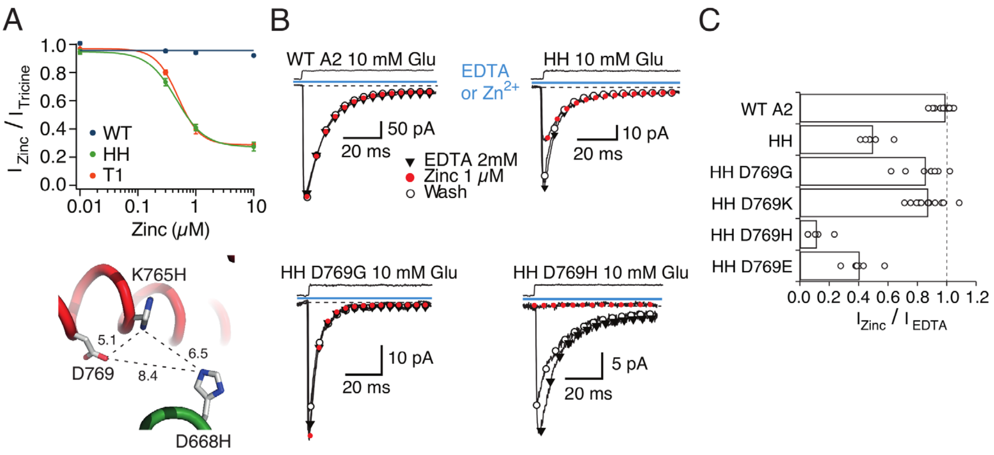

Figure 3.38: The HH mutation involves a third and native residue of the GluA2 LBD, D769. **(A)** Upper panel shows half-maximal inhibition of currents after glutamate application and zinc. Both mutants, T1 and HH had a similar IC50 value of 380 ± 10 nM and 370 ± 20 nM, respectively (n=3 each). Lower panel shows ribbon representation of subunits Subunit A (green) and B (red) with D769 and modeled K765H and D668H mutants (into the tight arrangement). Distances are in Å. **(B)** Representative current traces for WT, the HH mutant and the HH mutant with D769G and D769H mutations, respectively. After exposure to EDTA (zinc-free solution, black triangles), zinc (red circles) was applied together with the agonist glutamate. For comparison, traces were overlaid for EDTA (2 mM), zinc (1 µM) and wash (in 2 mM EDTA; open circles). **(C)** Overview of tested WT and HH mutants after application of 1 µM zinc. Open circles indicate individual measurements. Figure modified from [342].

Taken together, these results suggest that the tetrameric LBD arrangement obtained from the TR crystal structure is populated in full-length GluA2 receptors.
Trapping of the T1 mutant could be shown in functional experiments despite the relatively big distances of His residues, which suggests a certain degree of mobility of the LBDs in the resting state.

Investigating the state-dependency of the zinc trapping revealed trapping in the resting and active state. Trapping in the apo state presumably results from dynamic and mobile ligand-free LBDs as the distances between His residues in the T1 mutant are not ideal (10 and 15 Å between modeled His residues into the apo full-length structure). Trapping in presence of glutamate was observable at 100 µM glutamate and persisted at fully saturating concentrations of glutamate, however no trapping could be observed at very low glutamate concentrations (10 µM), suggesting that trapping occurs with partially or fully bound by glutamate.

The HH mutant showed peak current reduction when the patch was exposed to zinc, however the distances between D769 and D668H derived from the TR crystal structure

(8Å) would be too big for a metal chelation, suggesting that the zinc bridge produced by the HH mutant represents an LBD arrangement that is different from the TR tetrameric arrangement and results from structural rearrangements. Zinc trapping experiments of the HH mutant in presence of CTZ (blocker of desensitization) [366, 367] and quisqualate, a more potent agonist than glutamate, showed no inhibitory effect, suggesting that the HH bridge does not modulate receptors when they are fully bound by agonist.

All other metal bridges described above showed an inhibitory effect, presumably because the metal bridge restraints the LBDs from being mobile and trapping the receptor in a less active state it would be without the bridges. Therefore, functional data suggest that the crystal structure obtained from the TR LBD mutant does not represent a fully active state.

Another triple His mutant (G437H, K439H, D456H, termed "HHH" in this thesis), which was used in the CA structure to simulate an intermediate state of receptor activation [116], didn't show any effect. The triple CA-HHH mutations are located at the top of the LBD in D1 and were designed to show trapping in the presence of zinc at intermediate concentrations of zinc. In order for this bridge to form, the interdimer angle would have to decrease dramatically.

3.1.6 Molecular modeling of zinc mutants

To understand how the different geometries for the distinct mutants relate to the tetrameric LBD conformation of the crystal structure, molecular models of the respective mutants were generated. Zinc ions were modeled between the mutated His residues as described in the methods section. After placement of the zinc ion, the coordination geometry was optimized by either allowing rigid-body movement of the canonical LBD dimers or by allowing movement of only the mutated His residues. The metal ion assignment was than evaluated using the calcium bond-valence sum (CBVS) [345]. This method is supposed to be reliable for X-ray structures with resolutions better than 1.5 Å. The CBVS is based on Linus Pauling's studies and investigations on ionic crystals. He showed that the cation anion distance correlates with the sum of ion radii, the coordination number and the ratio of the radii. And so, the CBVS metric estimates the quality of the zinc coordination based on the zinc valence and the coordination distances. For octahedral coordinated zinc (Zn coordinated by six oxygen atoms) the optimal CBVS is 4.07 [345].

The CBVS wasn't ideal for any of the modeled mutants into the tight tetrameric LBD background, probably due to the lack of water molecules or other ligands to further coordinate zinc (Figure 3.39).

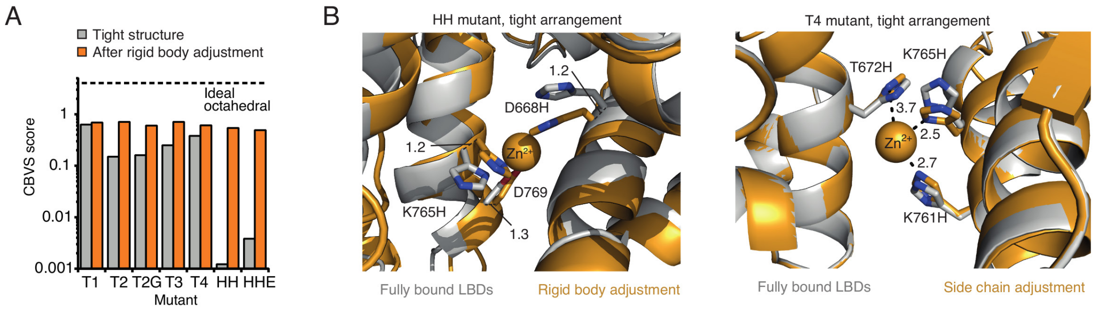

Figure 3.39: Molecular modeling results for different mutants. (A) CBVS scores for zinc coordination by mutants T1, T2, T2G, T3, T4, HH and HHE that were modeled into the tight tetrameric LBD arrangement (grey bars). After rigid body adjustment of the active dimers, a higher CBVS score could be obtained showing conformations different from the crystallographic tetramer (orange bars). **(B)** Comparison between the tetrameric LBD arrangement obtained from the crystal structure (grey cartoon) and the structure obtained after side chain or rigid body adjustment (orange cartoon). Left panel shows superposition of the HH mutant modeled into the tight tetramer and the HH mutant after rigid body adjustment of the dimers in order to optimize metal coordination (orange sphere). Right panel shows overlay of T4 mutant modeled in the tight tetrameric arrangement (grey) and the T4 mutant after side chain adjustment. Modeling reveals a steric clash between T672H and K765H, giving a possible explanation for why T4 didn't show any effect in functional experiments.

Out of the tested His mutants, the T1 mutant displayed the best CBVS value and thereby the best zinc coordination that couldn't be further improved by rigid-body movement. The HH mutant displayed the worst zinc coordination, however following a rigid-body movement of canonical dimers by 1.2 Å, the CBVS value got as good as for the T1 mutant, supporting the assumption that the HH mutant is trapped in a slightly different conformation than the tight LBD conformation. Zinc coordination together with modeling enables the identification of slightly different geometries of the tetramer.

The T4 mutant didn't show any effect in functional experiments. Of course it could be possible that metal coordination still occurs without functional effects, however, computational modeling suggests that cross-link in the T4 mutant cannot occur due to steric clashes between T672H and K765H (Figure 3.39).

3.2 STARGAZIN CYTOPLASMATIC C-TERMINAL DOMAIN (STARGAZIN$^{203-323}$)

3.2.1 Construct design and screening for soluble protein

The C-terminus of stargazin has an extremely important role for regulation of AMPAR mobility. Stargazin cytoplasmatic domain is important for AMPA receptor immobilization at the PSD. Three key features render stargazin C-terminal tail important for the AMPAR immobilization mediated by the AMPAR-TARP interaction:

1. Stargazin cytoplasmatic tail interacts with the lipid bilayer through electrostatic interactions
2. Kinases like CaMKII and PKC can phosphorylate the C-terminus of stargazin at several Ser and one Thr site which leads to dissociation of stargazin C-terminal tail from the lipids
3. Phosphorylated and dissociated stargazin cytoplasmatic domain binds to PDZ domains of scaffolding proteins like PSD-95 via its PDZ binding motif (TTPV), thereby leading to immobilization of AMPARs at the PSD

In order to investigate the interplay of these key features, we aimed to recombinantly over-express and purify the C-terminal domain of rat stargazin.

Because sufficient protein amounts are indispensable for biophysical and structural studies, a set of stargazin C-terminal tail constructs were tested for solubility and protein over-expression. The codon-optimized gene for the C-terminus of rat stargazin (stargazin$^{203-323}$) carrying a single mutation C302S to reduce unspecific disulfide bridging was cloned into a pETDuet vector using the restriction free cloning approach. The vector backbone was kindly provided by Philipp Selenko.

A summary of all tested stargazin$^{203-323}$ constructs is given in Table 3.13.

Table 3.13: Summary of stargazin recombinant protein over-expression and solubility. The table summarizes all stargazin$^{203\text{-}323}$ constructs with tag location, tag cleavage site and protein over-expression as well as solubility. Final protein yields in mg per liter of bacterial suspension are given in the last column. His$_6$ – hexahistidine tag, TEV – tobacco etch virus, PSP – PreScission protease, (Gly)$_4$ – tetraglycine linker, (GS)$_3$ – glycine/serine linker, n.d. – not determined.

Construct no.	Construct	Over-expression	Solubility	Tag removal	Final yields [mg/L culture]
15-58		-	n.d.	n.d.	n.d.
15-59		-	n.d.	n.d.	n.d.
15-55		+/+	+/+	+/-	n.d.
15-54		+	+	-	n.d.
15-56		+	+	-	n.d.
15-73 (N_GB-1)		+	+	+/+	0.3
15-57 (C_GB-1)		+/+	+/+	+/+	3.7

The C-terminus of stargazin is predicted to be unfolded (Figure 3.40 B) and the unfolded nature of the protein accounts for the fact that a construct harboring an N-terminal hexahistidine (His$_6$)-tag alone did not yield any over-expressed protein (Table 3.13 and Figure 3.40 A).

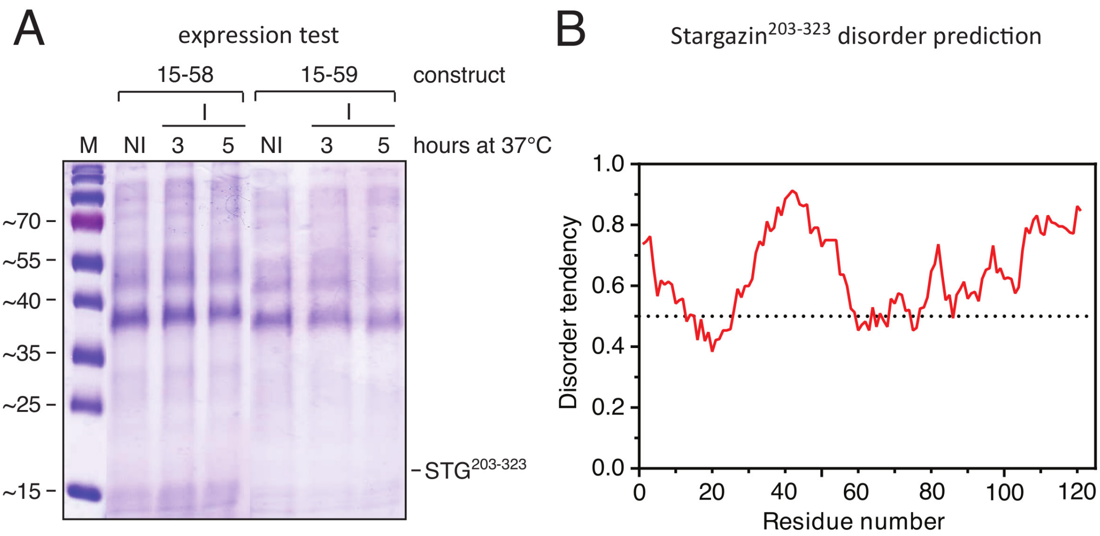

Figure 3.40: Stargazin C-terminal tail is disordered. (A) Coomassie-stained SDS-gel showing an expression test for N-terminally His$_6$-tagged stargazin$^{203-323}$ harboring a TEV protease (construct number 15-58) and a PSP protease cleavage site (construct number 15-59) for tag removal, respectively. No over-expressed protein is visible in the gel. The molecular weight of marker bands is given on the left (in kDa). M – marker, NI – non-induced/before IPTG induction, I – induced/after IPTG induction. (B) Plot of disorder tendency for the cytoplasmatic domain of stargazin. The C-terminal tail is predicted to be unstructured. Disorder tendencies were predicted using the IUPred server [339, 340].

3.2.2 Protein production

Using an N-terminal hexahistidine tag alone failed to yield any over-expressed protein, thus additional tags were introduced to obtain sufficient protein amounts. Stargazin$^{203-323}$ (C302S) was cloned into a pETDuet vector harboring N- and C-terminal His$_6$ and GB-1 tags. GB-1, the 56-residue B1 domain of the streptococcal protein G, is an immunoglobulin-binding (IgG) protein, has a size of 6.1 kDa and an acidic pI value of 4.5. GB-1 has been previously used in order to increase the expression and solubility level of proteins; it has been structurally investigated due to its extremely high thermal stability [309, 368-370]. Crystal structures as well as NMR structures of GB-1 revealed a very compact packing of a four-stranded β sheet with a large α-helix as a lid [371-373].

Purification of a construct with N- and C-terminal GB-1 and His_6 tag (construct 15-55) yielded soluble protein, however cleavage was never complete under various tested conditions.

A deletion construct omitting the C-terminal His_6/GB-1 tag did not yield any cleaved product, presumably due to steric hindrance (construct 15-54) caused by the folded GB-1 domain at the N-terminal tag. The bad accessibility of the N-terminal cleavage site accounts for the partial cleavage in the N- and C-terminally tagged construct. Insertion of a glycine linker $(Gly)_4$ behind the TEV protease cleavage site (construct 15-56) failed to increase the cleavability. Unfolding of the GB-1 tag by using urea as denaturing agent prior to cleavage led to increased accessibility of the cleavage site for the N-terminally tagged stargazin$^{203\text{-}323}$ construct (15-56).

Cleavage of the tag by TEV protease could be further improved by inserting another linker $(Gly\text{-}Ser)_3$ preceding the construct cleavage site. Rosetta cells carrying this N-terminally tagged construct (15-73) produced over-expressed protein with a removable tag.

However, since final protein yields were not satisfying and expression in minimal medium proved to be difficult, a C-terminally tagged stargazin$^{203\text{-}323}$ construct was tested and proved to give higher protein yields.

Further experiments were done with the N-terminally tagged stargazin$^{203\text{-}323}$ (construct 15-73) construct as well as with the C-terminally tagged stargazin$^{203\text{-}323}$ construct (construct 15-57). Thus, in the next section, purification of both constructs is shown.

3.2.2.1 Production of N-terminally tagged stargazin$^{203\text{-}323}$ (C302S) (N_GB-1)

Initially, purifying stargazin$^{203\text{-}323}$ from N-terminally tagged protein was favoured over C-terminally tagged protein because of the resulting free C-terminus of stargazin cytoplasmatic tail. The C-terminus of stargazin comprises a PDZ-binding motif (amino acid residues Thr-Thr-Pro-Val, short “TTPV”) important for interaction with the scaffolding protein PSD-95 and therefore is indispensable for TARP-mediated immobilization of AMPARs at the PSD. The binding mode of PDZ domains to PDZ binding motifs has been intensively studied and is well known. The C-terminal carboxylate group of the interaction partner binds to the conserved PDZ carboxylate-binding loop [374-376]. Having the C-terminus of stargazin available would enable us to perform interaction studies with lipids and PDZ domains at the same time under the influence of CaMKII.

Stargazin cytoplasmatic C-terminal tail with C-terminal GB-1 (termed C_GB-1) could be over-expressed in Rosetta cells and enriched using Ni-NTA, cation exchange and size exclusion chromatography (Figure 3.41). However, the highly positive pI and unfolded nature of the protein impeded the purification procedure. A second Ni-NTA purification step after tag cleavage emerged not to be useful, since stargazin C-terminal domain alone sticked to the Ni-NTA resin. The opposite pI values of GB-1 (pI= 4.5) and stargazin$^{203\text{-}323}$ (pI= 10.5) allowed for ion exchange (cation exchange) for tag removal instead.

Unfolded N-terminally tagged stargazin$^{203\text{-}323}$ could be over-expressed, as seen in Figure 3.41, however the level of impurities co-eluting with the protein is rather high. Additional purification steps were tested, e.g. denaturation of impurities using urea and heat purification as intrinsically disordered proteins (IDPs) are prone to be thermally stable. These attempts however did not increase protein purity. Tag cleavage leads to visible shift as observed on Coomassie-stained SDS-PAGE (right panel in Figure 3.41 B) with a ~15 kDa and a ~12 kDa band appearing after cleavage.

Peak fractions containing stargazin C-terminal tail were pooled and concentrated using Amicon Ultra centrifugal devices with an MWCO of 3 kDa. 10 kDa MWCO filters were not able to retain all of the unfolded stargazin protein. Pure stargazin$^{203\text{-}323}$ was concentrated to ~3 mg/mL; higher concentrations led to precipitation of the protein. Slightly increased solubility during protein concentration could be obtained by adding 2.5-5 % 1-3-propandiole to the protein prior to concentration.

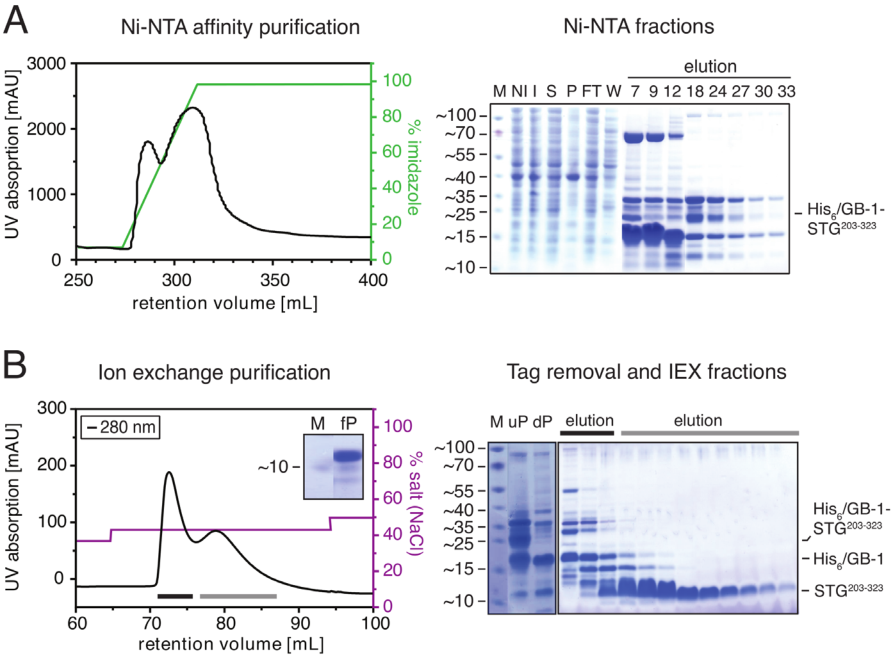

Figure 3.41: Exemplary large-scale purification of stargazin$^{203\text{-}323}$ (C302S) containing an N-terminal His$_6$-GB-1 tag (N_GB-1). (A) The first purification step consisted of a Ni-NTA purification using a linear imidazole gradient (final concentration 500 mM, green line) for elution. Elution of the protein as monitored at 280 nm. The right panel in (A) shows peak fractions of the Ni-NTA purification subjected to continuous SDS-PAGE (4-12%); the protein migrates at a molecular weight of ~25 kDa. **(B)** Following cleavage of the tag by TEV protease and dialysis, the tag was removed by cation exchange. The left panel shows the protein absorption at 280 nm as it elutes from the column by application of high salt concentration in a step-wise manner (final concentration 1 M, purple line). The right panel in (B) shows the Coomassie-stained SDS-PAGE gel of digested and undigested protein samples as well as of peak fractions eluting from the cation exchange column. Grey and black bars in (B) correspond to the two eluting peaks. The small box in (B) shows purity of the final protein sample. For SDS-PAGE, the molecular weight (MW) for marker bands is shown on the left in kDa. M – marker, NI – non-induced/before IPTG induction, I – induced/after IPTG induction, S – supernatant after cell lysis and ultracentrifugation, P – pellet, FT – flow through, W – wash step, 7…33 – eluted fractions, His$_6$ – hexahistidine tag, STG$^{203\text{-}323}$ – stargazin C-terminal domain (aa 203-323, C302S), uP – undigested protein (before adding TEV protease), dP – digested protein (after TEV protease digestion), fP – final, pure protein after SEC, AU – arbitrary unit, iP – injected protein (before SEC).

The His$_6$-GB-1 tag has a size of ~9 kDa but migrates at much higher protein molecular weight and fractions containing stargazin C-terminal tail run at much smaller molecular weights than expected (Figure 3.41 B). The protein was therefore send to the mass spectrometry facility. MALDI TOF/TOF analysis of the protein in solution revealed two major peaks, one being detected at m/z = 9592 and the second one being detected at m/z= 19191. A third small peak could be detected at m/z= 14400 (Figure 3.42).

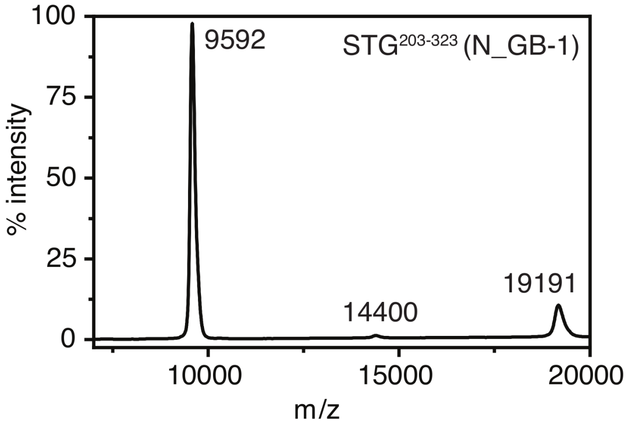

Figure 3.42: MALDI TOF/TOF analysis of purified stargazin$^{203\text{-}323}$ from the N-terminally tagged stargazin$^{203\text{-}323}$ construct (N_GB-1). The protein was diluted to 1 mg/mL for MALDI analysis. The intensity in % is plotted against the mass/charge (m/z) ratio. The three peaks of this measurement with their mass/charge ratio are indicated.

Trypsin digestion of the protein followed by Nano-LC MS/MS analysis and Mascot search of the resulting fragments revealed that the protein presumably is getting degraded from the C-terminus, because C-terminal fragments could not be detected with high ion scores.

3.2.2.2 Production of C-terminally tagged stargazin$^{203\text{-}323}$ (C302S) (C_GB-1)

Stargazin cytoplasmatic domain was also expressed as a C-terminal His$_6$-GB-1 fusion construct, mainly for two reasons: First, we aimed for higher expression yields as over-expression of N-terminally tagged stargazin$^{203\text{-}323}$ was not very high and second, mass spectrometric analysis revealed C-terminal protein degradation which might be inhibited or at least slowed by expressing the protein with a C-terminal tag.

Different expression strategies were tested aiming for maximal over-expression of the protein and expression at 37°C after addition of 1 mM IPTG led to the highest degree of over-expressed and soluble protein. A large-scale purification for C-terminally tagged stargazin$^{203\text{-}323}$ (construct 15-57) is shown in Figure 3.43.

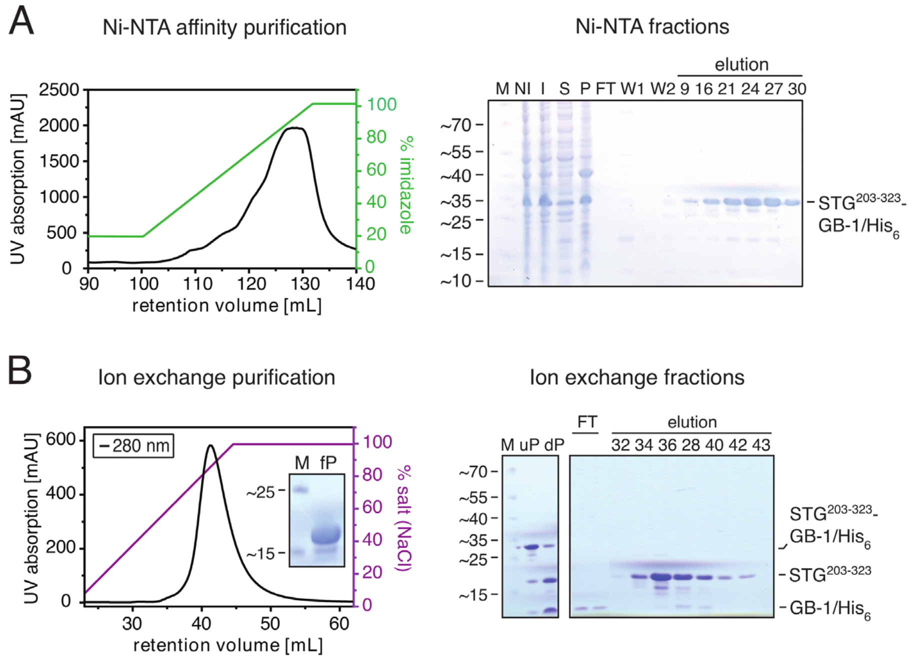

Figure 3.43: Exemplary large-scale purification of C-terminally tagged stargazin$^{203\text{-}323}$ (C_GB-1) carrying the C302S mutation. (A) Ni-NTA purification: The left panel shows the elution profile of the Ni-NTA purification with protein elution being monitored by its absorbance at 280 nm (black line). A linear imidazole gradient (final concentration 500 mM, green line) was applied for protein elution. The right panel shows protein samples from the purification procedure loaded on a continuous SDS-gel. C-terminally tagged stargazin$^{203\text{-}323}$ migrates as a monomer (MW= 22 kDa). **(B)** Following overnight dialysis and TEV protease treatment of the Ni-NTA pool, the protein was loaded on a HiTrap SP/XL cation exchange column for removal of the tag. Elution of the protein from the column was achieved by increasing salt concentration (final concentration 1.5 M, purple line). Samples from undigested and digested protein as well as from peak fractions were subjected to SDS-PAGE (right panel). For SDS-PAGE, the molecular weight of marker bands in kDa is shown on the left. AU – arbitrary unit, M – marker, NI – non-induced/before IPTG induction, I – induced/after IPTG induction, S – supernatant after cell lysis and ultracentrifugation, P – pellet, FT – flow through, W – wash step, 9…30 – eluted fractions, His$_6$ – hexahistidine tag, STG$^{203\text{-}323}$ – stargazin C-terminal domain (aa 203-323, C302S), uP – undigested protein (before adding TEV protease), dP – digested protein (after TEV protease digestion), fP – final, pure protein after SEC.

Protein expression and purification of C-terminally tagged protein was more successful than the expression of N-terminally tagged stargazin$^{203\text{-}323}$ in terms of over-expression and purity of the sample. Final protein yields were 3.7 mg per liter of bacterial culture.

3.2.3 Biophysical characterization

If not stated specifically, all subsequent experiments were performed using purified untagged stargazin$^{203\text{-}323}$ (C302S) protein from the C-terminally tagged construct (C_GB-1).

3.2.3.1 CD spectroscopy

In order to investigate the protein's secondary structure, CD spectrometric measurements were performed. The protein was dialyzed into a buffer compatible with CD spectrometric measurements (see Table 2.19). Spectra were recorded at 20° (Figure 3.44). Secondary structure estimations from the CD spectrum revealed that the majority of stargazin C-terminal tail is unfolded (Table 3.14).

Table 3.14: Secondary structure analysis of stargazin$^{203\text{-}323}$ (C302S) (C_GB-1) as determined by CD spectroscopy. Secondary structure estimations were done using the Dichroweb server and the CDSSTR algorithm [324].

Construct	α-helix (%)	β-sheet (%)	β-turn (%)	Random coil (%)	Sum (%)
STG$^{203\text{-}323}$	4	10	8	76	98

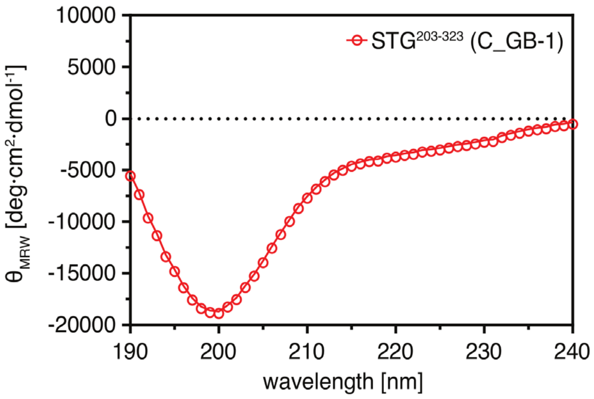

Figure 3.44: CD spectroscopic analysis of stargazin C-terminal tail (C302S). Spectra were recorded at 20°C in a 0.1 cm pathlength cuvette using 0.2 mg/mL protein in 10 mM sodium phosphate buffer (pH 7.4) and 100 mM NaF. Three individual traces were averaged and the background absorption from air and buffer was subtracted.

3.2.3.2 Static light scattering

In order to determine the absolute molecular weight of stargazin C-terminal tail, static light scattering experiments were performed. Pure protein was loaded on a Superdex 75 10/300 GL analytical gel filtration column pre-equilibrated with RALS buffer. The data are given in Table 3.15 and Figure 3.45.

Table 3.15: RALS data of stargazin$^{203\text{-}323}$ (C_GB-1)

	WT
Peak retention volume [mL]	13.2
Molecular weight [kDa]	14.6
Oligomeric species	Monomer (M)

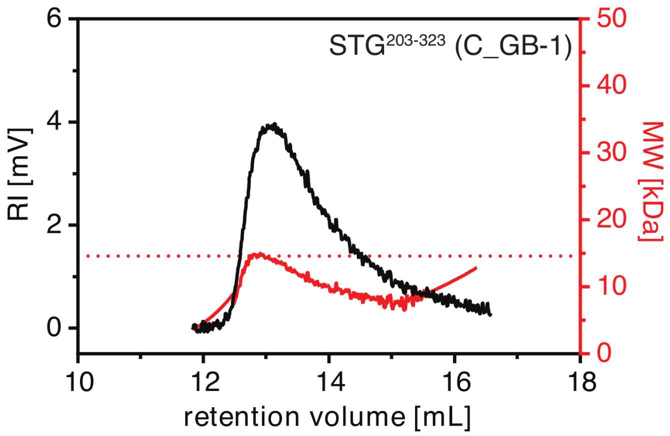

Figure 3.45: Determination of the absolute molecular weight of stargazin C-terminal tail as determined by RALS measurement. For RALS measurements, an analytical gel filtration column (Superdex S75 10/300 GL) was connected in line with an RI and RALS detector. For one RALS experiment, 100 µL of a 3 mg/mL protein solution (untagged stargazin$^{203\text{-}323}$ prepared from C-terminally tagged protein, C_GB-1) was injected onto the column pre-equilibrated with buffer and under a constant flow rate of 0.5 mL/min. The refractive index (in mV, black line) and the absolute molecular weight (in kDa, red line) are plotted against the retention volume in mL. The MW for monomeric protein is indicated with a dotted red line.

Stargazin C-terminal tail exists as monomer in solution (Figure 3.45), despite its unfolded nature (Figure 3.40 B). The absolute molecular weight determined from RALS measurements (MW_{exp}=14.6 kDa) matches the theoretical molecular weight (MW_{calc}=14.6 kDa).

RALS data together with mass spectrometric analyses revealed the correct protein size and excluded the possibility of degradation.

3.2.4 Binding of stargazin$^{203\text{-}323}$ to liposomes

The high abundance of Arg residues within the C-terminus of stargazin leads to the positive charge, which is in turn important for the interaction between stargazin and PDZ domains [240, 246, 256]. The C-terminus of stargazin contains 15 Arg residues in total. Mobile AMPARs are clustered at the PSD through interaction with TARPs, which are bound to scaffolding proteins like PSD-95. It has been shown that the interaction between stargazin and PSD-95 is regulated in a phosphorylation-dependent manner [251, 256, 377]. Stargazin cytoplasmatic domain electrostatically binds to the negatively charged lipid bilayer. Phosphorylation of stargazin C-terminal tail by kinases leads to introduction of negative charges and therefore abolishes the binding of stargazin C-terminal tail to negatively charged lipids, rendering the C-terminal domain available for interaction with PDZ domains at the PSD.

A scheme of stargazin C-terminal tail with phosphorylation sites and Arg residues is shown in Figure 3.46 (for comparison also see TARP alignment of C-terminal tails, Figure 1.9).

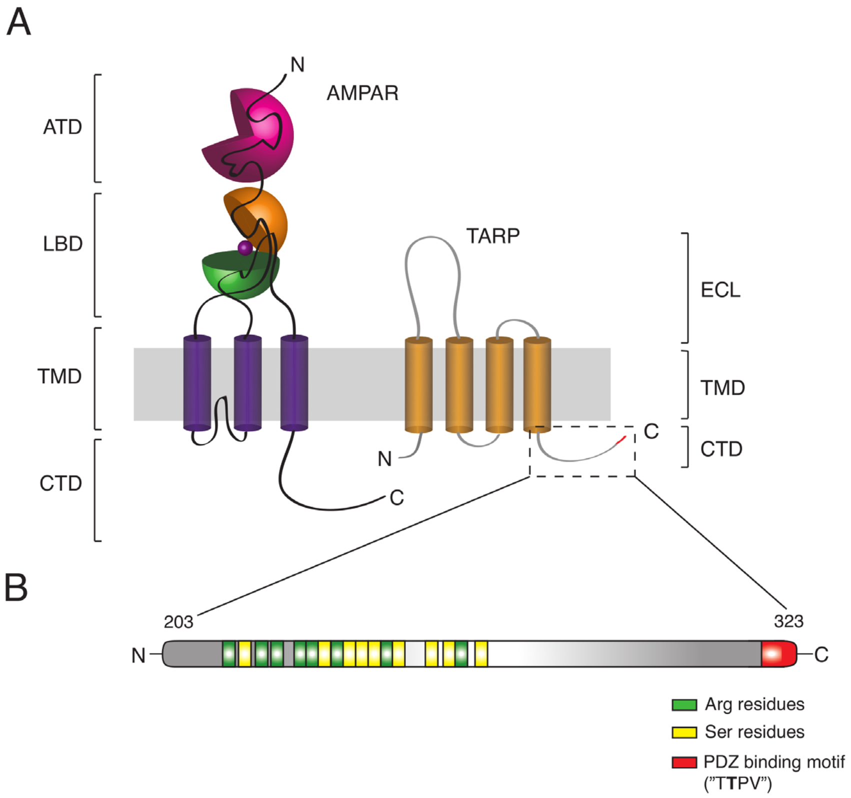

Figure 3.46: TARP stargazin interacts with membranes in a phosphorylation-dependent manner. (A) Cartoon representation of AMPAR (left side) and TARP (right side) domain architecture. Individual domains for AMPARs and TARPs are indicated on the left and right sides, respectively. The C-terminal cytoplasmatic domain of stargazin is boxed. The N- and C-termini are indicated. **(B)** Magnification of the C-terminal domain of stargazin. Stargazin cytoplasmatic domain comprises 19 Ser residues; nine of them (yellow boxes) have shown to be phosphorylated by the kinase CaMKII. Eight Arg residues (green boxes) can be found in close proximity of these nine Ser residues and are important for the ability of stargazin C-terminal tail to bind to negatively charged liposomes. The C-terminus comprises the PDZ binding motif ("TTPV", red box) important for binding to PDZ domains. The second Thr residue (Thr321) within the TTPV motif is a phosphorylation site for PKC. ATD – aminoterminal domain, LBD – ligand-binding domain, TMD – transmembrane domain, ECL – extracellular loop.

In order to investigate lipid binding of the purified stargazin$^{203\text{-}323}$ construct, liposome co-sedimentation assays were performed using FOLCH liposomes, which are composed of cow brain lipids and with polar lipids that have been used previously [256].

First, the binding ability of stargazin$^{203\text{-}323}$ was tested to a lipid mixture. Therefore, FOLCH lipids were used, which were extracted from cow brain and contain a mixture of the most abundant lipids like phosphatidylinositol and phosphatidylserine [378]. The lipid film hydration method was applied for liposome formation and yielded multilammelar vesicles (MLVs) [325]. The assay was performed as described in methods. Shortly, 10 µM protein were incubated with 1 mg/mL fresh prepared liposomes and incubated for 10-15 minutes at 20°C to allow liposome binding of the protein. Liposome-bound protein was separated from liposome-unbound protein by ultracentrifugation. The supernatant and pellet were than subjected to SDS-PAGE.

In order to exclude the possibility that the purified protein precipitates at high centrifugal speeds, a protein control was always included in absence of liposomes (Figure 3.47 A). The liposome co-sedimentation assay using FOLCH liposomes revealed that in our assay, more than 90% of the protein binds to liposomes (Figure 3.47 B). This result shows that the over-expressed and purified stargazin C-terminal tail construct is able to bind to liposomes and can be used for lipid binding studies.

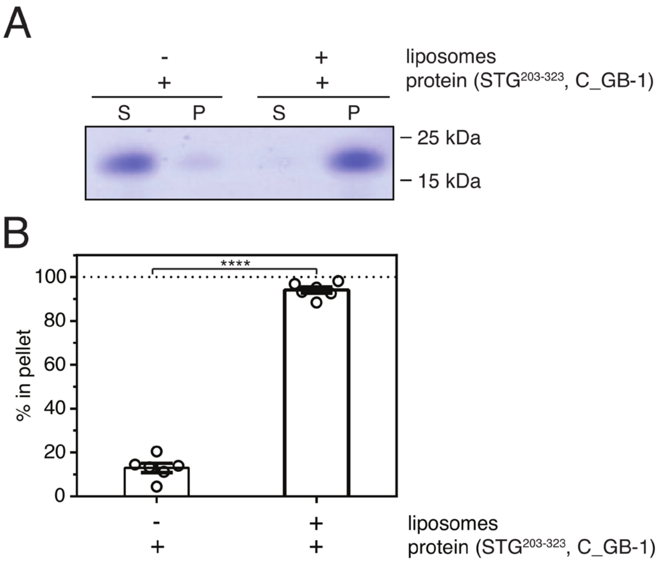

Figure 3.47: Stargazin C-terminal tail binds to FOLCH liposomes. Liposome co-sedimentation was carried at 20°C using 10 µM protein (prepared from C-terminally tagged protein, C_GB-1) and fresh prepared FOLCH MLVs in liposome buffer at a concentration of 1 mg/mL. The mixture was incubated for 15 minutes at 20°C. Liposome-bound and liposome-unbound fractions were separated by ultracentrifugation for 10 minutes at 213.600 x g. **(A)** Supernatant (S) and pellet (P) were subjected to SDS-PAGE. **(B)** Quantification of gel band intensities using ImageJ [291] (n=6 for each experiment, error bars represent the SEM). **** $p < 0.0001$.

Having established binding of stargazin C-terminal tail to FOLCH liposomes, a mixture of cow brain lipids, in a next step, the lipid preference for binding of stargazin C-terminal tail was investigated (Figure 3.48 A and B). Therefore, binding of stargazin C-terminal tail was tested for a set of different polar lipids.

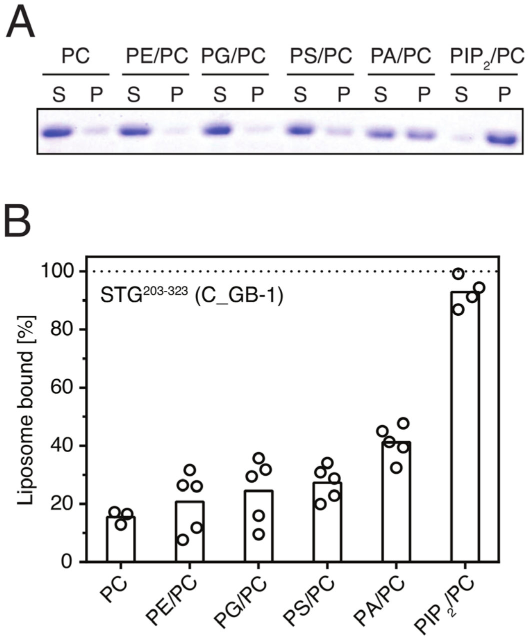

Figure 3.48: Stargazin C-terminal tail binds to negatively charged liposomes. Liposome co-sedimentation was performed using liposomes containing polar lipids (Avanti polar lipids). The ability of stargazin C-terminal tail (prepared from C-terminally tagged protein, C_GB-1) to bind to lipids was tested for differently charged liposomes: neutrally charged liposomes (PC and PE), polar liposomes (PG and PS) and negatively charged liposomes (PA and PIP_2) Lipid mixtures were prepared from phosphatidyl choline (PC) and various neutral or polar lipids (9:1). 10 µM protein were incubated with 1mg/mL fresh prepared liposomes for 10 minutes at 20°C to allow binding of stargazin$^{203\text{-}323}$ to the liposomes. The mixture was subjected to ultracentrifugation (213,600 x g) for 10 minutes at 20°C to separate liposome-bound from liposome-unbound protein. Supernatants (S) and pellets (P) were subjected to SDS-PAGE **(A)** and gel band intensities were quantified using ImageJ [291] **(B)**. PC – phosphatidyl choline, PE – phosphatidylethanolamine, PG – phosphatidylglycerol, PS – phosphatidylserine, PA – phosphatidic acid, PIP_2 – phosphatidyl-4,5-biphosphate.

In the literature it has been described that stargazin interacts with negatively charged lipids through its positively charged Arg residues and mutagenesis of the Arg residues abolishes binding of stargazin C-terminal tail to liposomes [256]. In liposome co-sedimentation assays with different lipids stargazin C-terminal tail showed a clear preference for negatively charged liposomes (PA/PC and PIP_2/PC) over polar liposomes (PG/PC and PS/PC) and neutral liposomes (PC and PE/PC). The C-terminus of stargazin interacts with negatively charged lipids via its positively charged Arg residues; it has 15 Arg residues in total. Mutation of eight of them abolishes binding of stargazin cytoplasmatic domain to liposomes [256]. In their assay, they used green fluorescent protein (GFP)-tagged or thioredoxin (Trx)-tagged stargazin C-terminal domain, presumably in order to increase protein stability and solubility. In our assay, we used untagged stargazin cytoplasmatic domain, which has not been used before. The liposome co-sedimentation assay showed that untagged stargazin C-terminal domain also binds to negatively charged liposomes (PA/PC and PIP_2/PC), and this binding is stronger than binding to polar liposomes (PG/PC and PS/PC). The weakest binding could be observed for neutral liposomes (PC and PE/PC) (Figure 3.48 A and B).

3.2.5 Phosphorylation of stargazin$^{203-323}$

3.2.5.1 Mass spectrometric analysis of stargazin$^{203-323}$ phosphorylation

Having established the ability of stargazin C-terminal tail to bind to lipids, we aimed to investigate *in vitro* phosphorylation of stargazin cytoplasmatic domain by CaMKII. As described in several reviews, CaMKII is an important key player for synaptic plasticity and LTP [377]. One of the CaMKII substrates is stargazin. Phosphorylation of stargazin is important for synaptic scaling because it induces clustering of AMPARs at the PSD [251, 260, 379]. In order to investigate the ability of stargazin C-terminal tail to get phosphorylated, the purified protein was incubated with purchased CaMKII as described in Section 2.2.4.6. Phosphorylation was carried out at 30°C and phosphorylated protein was analyzed with MALDI TOF/TOF.

The detectability of a protein or fragment depends a lot on the fragment size and charge. Multiple phosphorylations in close proximity reduce the signal sensitivity, leading to the disadvantage that not all fragments can be detected equally well.

Therefore, mass spectrometric analyses do not give 100% quantitative information because of the above-mentioned circumstances but rather give an average value of phosphorylation.

However, by comparing the mass differences between non-phosphorylated and phosphorylated sample, a semi-quantitative estimation can be made. Stargazin C-terminal tail was incubated with activated kinase CaMKII for different periods and the change in protein mass resulting from the covalent incorporation of phosphate groups was measured using MALDI TOF/TOF and electrospray ionization (ESI)-MS/MS for the intact protein and protein fragments, respectively. In Figure 3.49 A, the mass shifts for undigested stargazin C-terminal tail and for differently phosphorylated stargazin$^{203\text{-}323}$ is shown. As already mentioned, these masses are average masses because the distinct Ser residues do not necessarily get equally phosphorylated. However, from MALDI results one can roughly conclude that the first phosphorylation occurs within the first 2 minutes, with the concentration of CaMKII used in this assay. After 30 minutes, 2-3 phosphate groups are added and after 2 hours, one or two more Ser residues get phosphorylated. Complete phosphorylation of stargazin C-terminal tail (i.e. all nine Ser residues are phosphorylated) can be observed after 16 h (Figure 3.49 B).

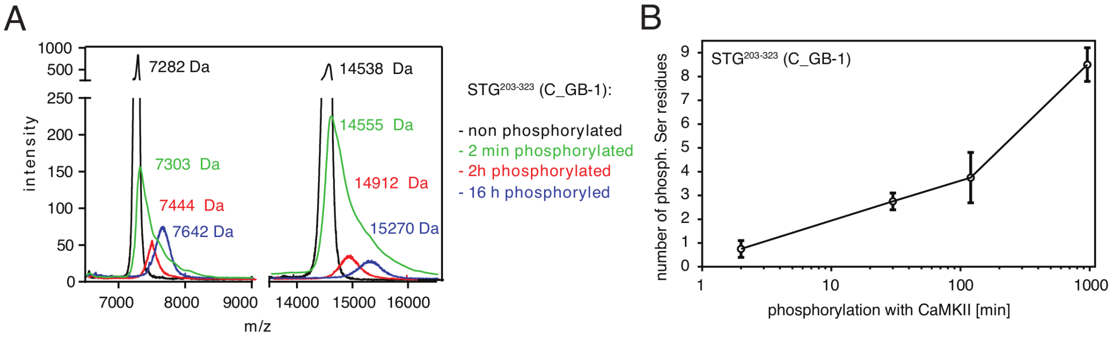

Figure 3.49: Phosphorylation of stargazin C-terminal tail was monitored using MALDI TOF/TOF and ESI MS/MS. (A) Stargazin C-terminal tail (purified from C-terminally tagged construct, C_GB-1) was phosphorylated using CaMKII for the period indicated in (A) and phosphorylation of the protein in solution was evaluated using MALDI. After measurement of the intact protein, it was fragmented using the proteases LysC or AspN. The intensity of detected protein is plotted against the mass/charge ratio (m/z). **(B)** Evaluation of (A) showing how many phosphate groups (MW= 80 Da) are added after every time point. The approximate number of phosphorylated Ser residues is plotted against the time of CaMKII incubation in minutes.

Due to the fact that the Ser residues are in very close proximity to each other (Figure 3.46), a real quantitative mass spectrometric measurement proved to be difficult. In order to investigate phosphorylation of every Ser residue on its own, a protease would be needed that cleaves in between each phosphorylation site. Stargazin C-terminal tail has three Ser residues in a row, making it almost impossible to separate them.

As the mass spectrometric measurements do not give quantitative results, we aimed to perform NMR experiments with isotope-labeled stargazin C-terminal tail in order to get a time resolved image of stargazin$^{203\text{-}323}$ phosphorylation by CaMKII.

3.2.5.2 Stargazin$^{203\text{-}323}$ phosphorylation abolishes binding to liposomes

Stargazin C-terminal tail binding to liposomes is based on the electrostatic nature of both the protein and the liposomes. When I increased the salt concentration in the liposome co-sedimentation assay from 100 mM NaCl to 150 mM NaCl, binding of stargazin C-terminal tail to liposomes is completely abolished (data not shown).

Interaction of stargazin cytoplasmatic domain with liposomes occurs via its positively charged Arg residues, eight of them are located around the stargazin Ser phosphorylation sites (Figure 3.46). Replacing these Arg residues with Gly or Leu also abolishes binding of the C-terminal tail to liposomes. Mutating the phosphorylatable Ser residues within stargazin$^{203\text{-}323}$ to Ala (S9A) does not influence binding to liposomes, however, mutating them to Asp (S9D, phosphomimic mutant) completely abolishes binding of stargazin$^{203\text{-}323}$ to liposomes [256]. Both deletion of the positive charge within the C-terminal tail of stargazin and mimicking phosphorylation of stargazin$^{203\text{-}323}$ abolishes binding to liposomes.

Since experiments were only done with a phosphomimic mutant, binding of stargazing C-terminal tail to liposomes was investigated upon phosphorylation with CaMKII in this work. Phosphorylation of stargazin$^{203\text{-}323}$ was carried out at 20°C for 2 min up to 16 h. Non-phosphorylated stargazin$^{203\text{-}323}$ binds to liposomes with an efficiency of 100%. Incubating the protein with CaMKII for 2 minutes reduces the liposome binding affinity by 50% (Figure 3.50 A). According to the mass spectrometric measurements (Figure 3.49 and Figure 3.50), approx. one phosphate group is being added after 2 minutes of incubation with CaMKII. Further phosphorylation continuously decreased liposome binding of stargazin cytoplasmatic domain. Stargazin$^{203\text{-}323}$ phosphorylation for 30 min, which (according to the mass spectrometric measurements) leads to phosphorylation of 2-3 Ser residues, reduced the liposome binding by $\geq$ 75%, showing how sensitive the electrostatic binding of stargazin C-terminal tail to liposomes is.

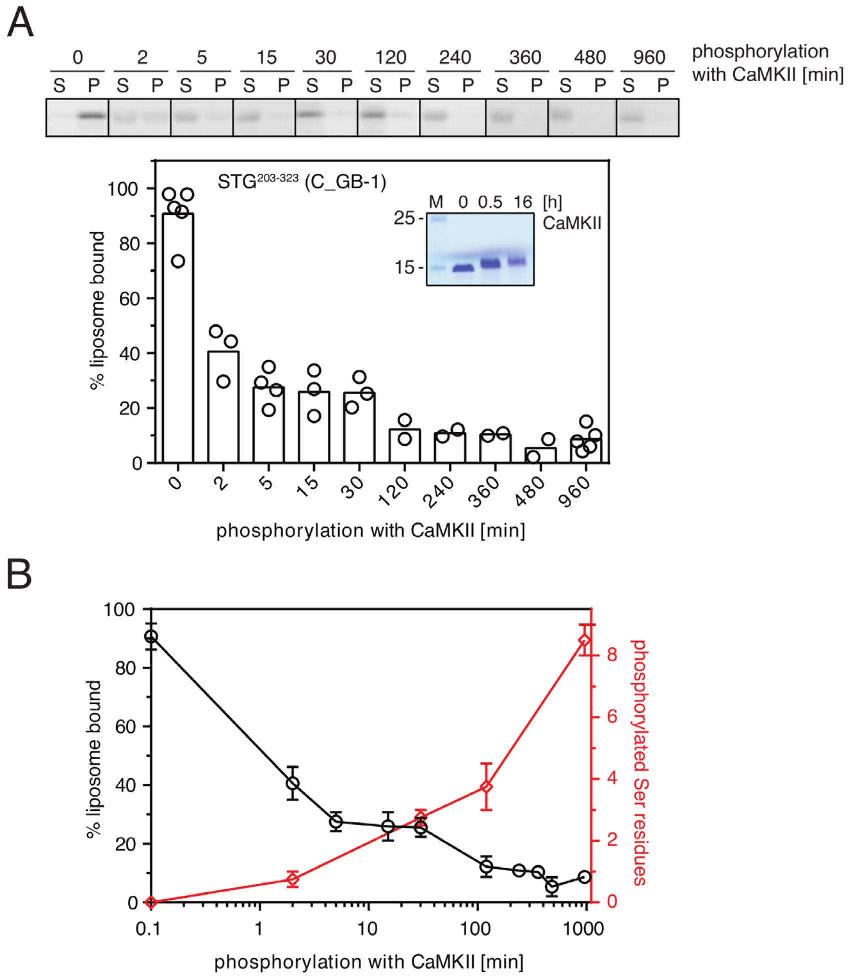

Figure 3.50: Phosphorylation of stargazin$^{203\text{-}323}$ (C302S) abolishes its ability to bind to liposomes. Purified stargazin$^{203\text{-}323}$ (prepared from C-terminally tagged construct, C_GB-1) was incubated with CaMKII and phosphorylated stargazin$^{203\text{-}323}$ protein was used for liposome co-sedimentation assay using 10 µM protein and 1 mg/mL FOLCH liposomes. As a control, non-phosphorylated stargazin$^{203\text{-}323}$ was incubated in the CaMKII buffer (without the kinase). Following incubation for 10 min at 20°C, liposome-bound protein was separated from liposome-unbound protein by ultracentrifugation at 213,600 x g for 10 min at 20°C. The same amount of CaMKII was used as for mass spectrometric measurements. **(A)** Supernatant (S) and pellet (P) from liposome co-sedimentation assay were subjected to SDS-PAGE (upper panel) and gel band intensities were quantified using ImageJ (lower panel) [291]. Phosphorylation of stargazin$^{203\text{-}323}$ reduces binding to FOLCH liposomes due to the introduction of negative charge. ($n \geq 2$). Small inset in (A) shows visible shift of gel bands that can be observed on the SDS gel upon phosphorylation of stargazin C-terminal tail. **(B)** Phosphorylation of stargazing C-terminal tail negatively regulates its ability to bind to liposomes.

8

3.2.6 Investigating phosphorylation of stargazin$^{203\text{-}323}$ using NMR

As previous results show, we were able to quantitatively phosphorylate stargazin$^{203\text{-}323}$ and monitor phosphorylation directly by mass spectrometric measurements and indirectly by performing a liposome co-sedimentation assay as phosphorylation interferes with the liposome binding ability of stargazin$^{203\text{-}323}$.

However, in order to gain precise and time-resolved insights into the phosphorylation procedure of the cytoplasmatic domain of stargazin, we aimed to perform NMR experiments using isotope-labeled stargazin$^{203\text{-}323}$.

In doing so, we would be able to watch phosphorylation over time and get a time-resolved image of stargazin$^{203\text{-}323}$ phosphorylation as well as kinetic parameters of phosphorylation. The precise mechanism of the multiple phosphorylation of stargazin C-terminal tail is unknown to date.

In the following section, production of isotope-labeled protein by using ^{15}N-NH_4Cl as the sole nitrogen source is described.

3.2.6.1 Production of ^{15}N-labeled protein

3.2.6.1.1 *Production of ^{15}N-labeled N-terminally tagged stargazin$^{203\text{-}323}$ (N_GB-1)*

Expression of unlabeled stargazin C-terminal tail in LB medium did not yield enough protein. Switching to TB allowed further cell growth and thereby led to increased protein yields (Figure 3.51).

Accordingly, the expression of stargazin$^{203\text{-}323}$ in presence of $^{15}NH_4Cl$ in minimal medium was not successful as the cells did not grow to OD_{600} values that would give sufficient protein amounts. Expression at different temperatures (overnight at 19°C, overnight at 30°C, 4 hours at 37°C or 30°C) did not change the over-expression in M9. Therefore, bacteria were grown in LB and TB medium for the preculture and the mainculture, respectively and the medium was replaced for M9 minimal medium supplemented with $^{15}NH_4Cl$ for expression of the protein (4 hours at 37°C, also see Section 2.2.2.5). To achieve high cell densities, typically a 4 L culture was prepared in TB medium to get 1 L of M9 culture. The purification procedure turned out to be a bit more complicated in terms of purity. N-terminally tagged stargazin$^{203\text{-}323}$ co-eluted with a set of impurities when expressed in M9 medium that were not present in TB medium. A slightly different purification approach was therefore applied for ^{15}N-labeled protein. After Ni-NTA purification (Figure 3.51 A), dialysis/ tag cleavage and cation exchange (Figure 3.51 B), a size exclusion chromatography was performed as this purification step further increased the protein purity slightly (Figure 3.51 C). Other approaches such as heat purification failed to increase protein purity. Thus, suitable protein purity could be achieved (inset in Figure 3.51 C, left panel).

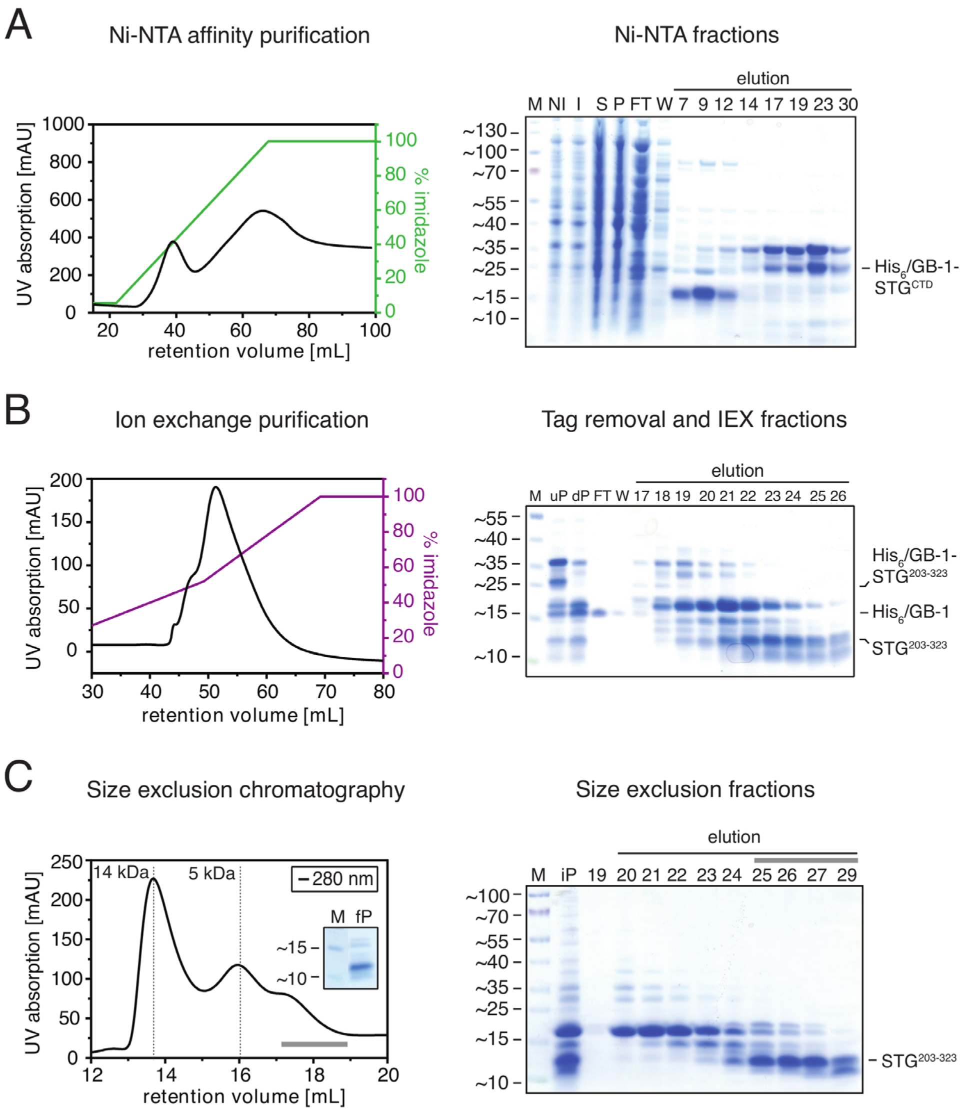

Figure 3.51: Exemplary purification for ^{15}N-labeled N-terminally tagged stargazin$^{203\text{-}323}$ (N_GB-1). (A) Left panel: Ni-NTA purification leads to enrichment of His$_6$-GB-1-tagged stargazin$^{203\text{-}323}$**(Figure 3.51 continued on next page)**

Figure 3.51 (continued from previous page): The protein was eluted using a linear imidazole gradient (final concentration 500 mM, green line) and the protein absorption was monitored by its absorbance at 280 nm (black line). Right panel: coomassie-stained continuous SDS gel showing the performance of the Ni-NTA purification. **(B)** Left panel: Cation exchange chromatography was used in order to remove the tag after cleavage. Stargazin$^{203\text{-}323}$ binds to the column, whereas the tag does not and can be found in the FT (right panel). The protein was eluted from the column using high salt (final concentration 1.5 M, purple line). Samples from peak fractions of the IEX were subjected to SDS-PAGE (right panel). **(C)** Size exclusion chromatography using a Superdex™ 75 10/300 GL was performed as final polishing step (left panel). The small inset shows purity of the final protein. The right panel shows size exclusion peak fractions subjected to SDS-PAGE with the pooled fractions indicated by a grey bar. For SDS-PAGE, the molecular weight of marker bands is shown on the left side in kDa. AU – arbitrary unit, M – marker, NI – non-induced/before IPTG induction, I – induced/after IPTG induction, S – supernatant after cell lysis and ultracentrifugation, P – pellet, FT – flow through, W – wash, 9…30 – eluted fractions, His_6 – hexahistidine tag, STG$^{203\text{-}323}$ – stargazin C-terminal domain (aa 203-323, C302S), uP – undigested protein, dP – digested protein, IEX – ion exchange chromatography, fP – final, pure protein after SEC, iP – injected protein (before SEC).

As for the ^{14}N-labeled protein, determination of the protein mass again revealed that N-terminally tagged stargazin$^{203\text{-}323}$ presumably gets C-terminally degraded as the detected masses are smaller than the expected protein size (Figure 3.52). Two broad peaks with shoulders could be detected by MALDI-TOF/TOF at mass/charge ratios of 10848, 11200, 16269 and 16578.

Phosphorylation of the purified stargazin$^{203\text{-}323}$ protein for 16 h at 30°C using CaMKII barely changed the mass spectrometric profile of the protein, indicating that phosphorylation largely failed (red trace in Figure 3.52).

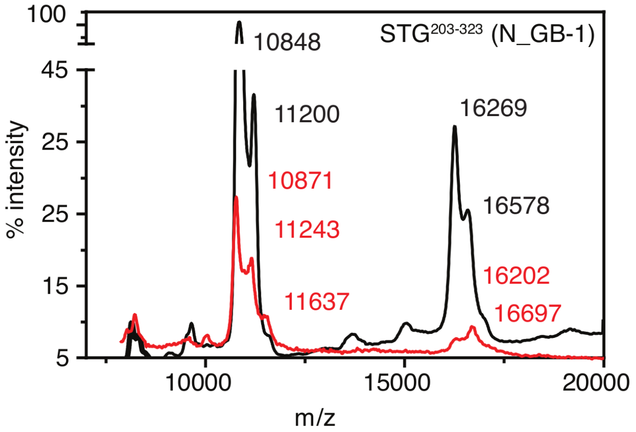

Figure 3.52: MALDI TOF/TOF analysis of stargazin$^{203\text{-}323}$ from N-terminally tagged stargazin construct (N_GB-1) after incubation with CamKII. The intensity in % is plotted against the mass/charge ratio (m/z). Following phosphorylation of the protein for 16 h at 30°C using CaMKII, the protein was again analyzed via MALDI for comparison (red trace).

3.2.6.1.2 *Production of ^{15}N-labeled C-terminally tagged stargazin$^{203\text{-}323}$ (C_GB-1)*

Purified stargazin$^{203\text{-}323}$ originating from N-terminally tagged stargazin$^{203\text{-}323}$ construct very likely got C-terminally degraded. Furthermore, due to protein degradation it gave a bad NMR spectrum. MALDI analysis of the protein before and after phosphorylation did not show any shift in mass and therefore, presumably, no phosphorylation occurred (see Figure 3.52 and Figure 3.57).

As expression and purification of unlabeled C-terminally tagged stargazin$^{203\text{-}323}$ yielded pure protein of the right size that could be phosphorylated and was able to bind to liposomes in a phosphorylation-regulated manner, this construct was also tested for expression in isotope-rich medium.

However, also for C-terminally tagged stargazin$^{203\text{-}323}$, the degree of impurities is increased in comparison to purification of unlabeled protein (Figure 3.53). In order to increase purity of the protein, a urea denaturation step was included before subjecting the protein to ion exchange (Figure 3.53).

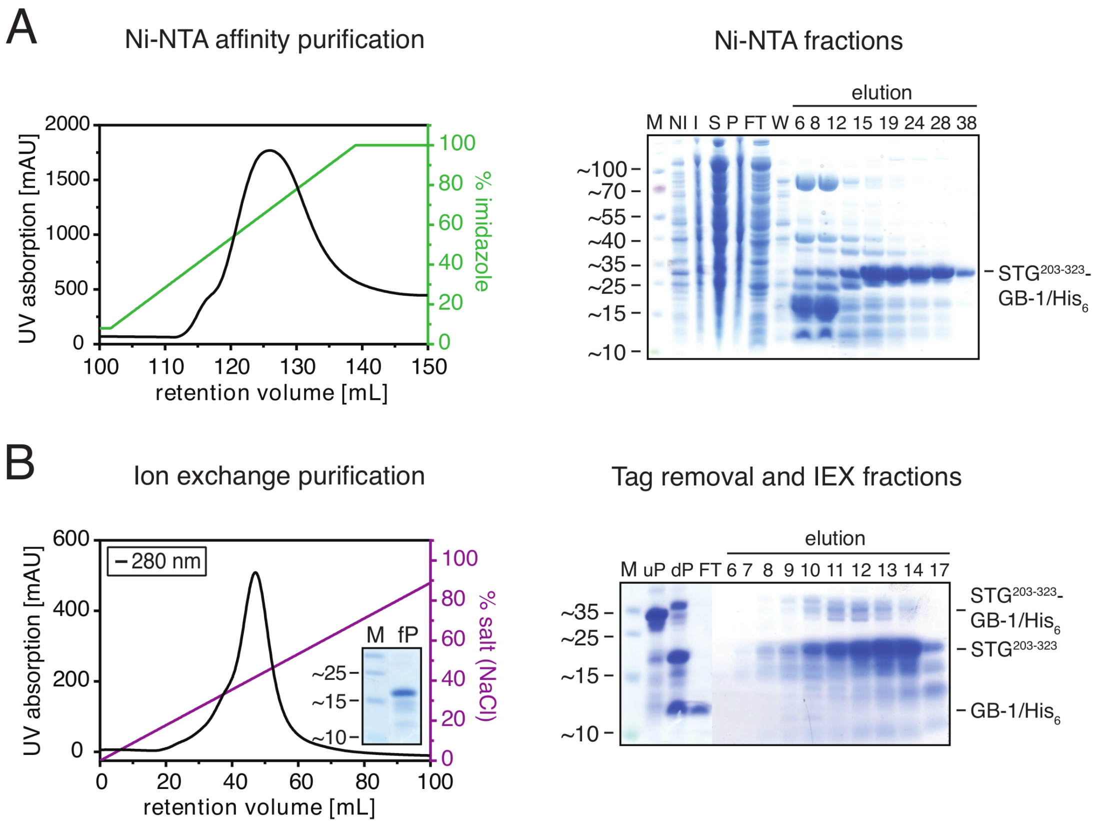

Figure 3.53: Exemplary purification of ^{15}N-labeled C-terminally tagged stargazin$^{203\text{-}323}$ (C302S) (C_GB-1). (A) Ni-NTA purification was performed to enrich His$_6$-GB-1-tagged stargazin$^{203\text{-}323}$. Bound protein was eluted using a linear imidazole gradient (final concentration 500 mM, green line) and protein elution was monitored by its absorbance at 280 nm (black line). The right panel shows purification samples loaded on a continuous SDS gel after Coomassie staining. **(B)** After dialysis and tag cleavage using TEV protease, the protein pool was denatured using urea to decrease impurity of the sample and loaded on a cation exchange column pre-equilibrated with IEX buffer supplemented with 2 M urea. Bound protein was eluted using a very slow linear salt gradient (final concentration 1.5 M NaCl, purple line). Protein elution was monitored at 280 nm (black line). The small inset shows the purity of the final protein sample. The right panel shows a Coomassie-stained SDS gel with samples of digestion (uP and dP) as well as samples of IEX peak fractions subjected to SDS PAGE. For SDS-PAGE, the molecular weight of marker bands is shown on the left side in kDa. AU – arbitrary unit, M – marker, NI – non-induced/before IPTG induction, I – induced/after IPTG induction, S – supernatant after cell lysis and ultracentrifugation, P – pellet, FT – flow through, W – wash, 6…38 – eluted fractions, His$_6$ – hexahistidine tag, STG$^{203\text{-}323}$ – stargazin C-terminal domain (aa 203-323, C302S), IEX – ion exchange chromatography, fP – final, pure protein after SEC, uP – undigested protein, dP – digested protein.

MALDI analysis of the protein in solution revealed the correct protein size. Cleaved C-terminally tagged stargazin C-terminal domain has a size of 14.6 kDa and MALDI revealed a m/z ratio of 14585 (Figure 3.54 A).

As the cells grew in isotope-free medium before expression was initiated in $^{15}NH_4Cl$ containing medium, a mixture of unlabeled, partially labeled and fully ^{15}N-labeled stargazin$^{203\text{-}323}$ could be detected (Figure 3.54 B) in a Gaussian-like distribution with partially ^{15}N-labeled protein as the majority. Incomplete isotope incorporation is, however, not relevant for NMR experiments as only ^{15}N-labeled protein will be detected in 2D-NMR experiments. Accordingly, a correction for the “effective NMR concentration” can be made for later NMR experiments.

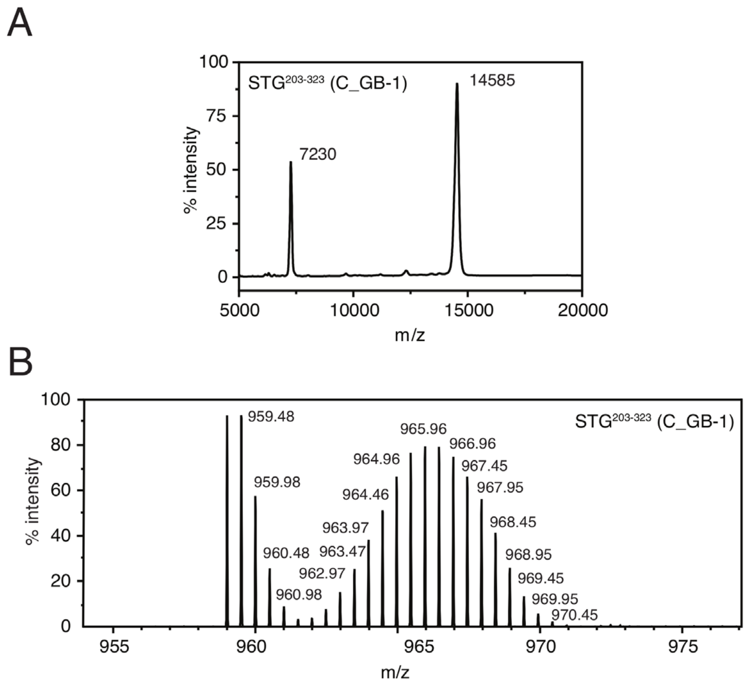

Figure 3.54: MALDI TOF/TOF and ESI analysis of ^{15}N-labeled stargazin$^{203\text{-}323}$ purified from the C-terminally tagged stargazin construct (C_GB-1). (A) MALDI TOF/TOF analysis of the protein in solution. For MALDI measurements, the protein was diluted to 1 mg/mL. Two major peaks could be detected, one at a mass/charge ratio of 7230 and the second one at 14585. **(B)** In order to determine the labeling efficiency, ESI measurement in solution of the protein fragment “^{259}GFNTLPSTEISMYTLSR^{275}” (formed after trypsin digestion) was performed. The unlabeled double positively charged fragment (100% ^{14}N) has a mass/charge ratio (m/z) of 958.97, whereas the completely ^{15}N-labeled stargazin$^{203\text{-}323}$ fragment has an m/z ratio of 969.46. The masses between 958.97 and 969.46 are partially labeled protein.

3.2.6.2 Biochemical and biophysical characterization of ^{15}N-stargazin

Having established that ^{15}N-labeled stargazin C-terminal tail (from C-terminally tagged stargazin$^{203\text{-}323}$) is the best candidate for labeled expression and that protein purity and yields were sufficient, the ^{15}N-labeled protein was biophysically and biochemically further characterized using MALS and liposome co-sedimentation. Determination of the absolute molecular mass with MALS revealed a slightly higher molecular weight (MW$_{calc}$=14.6 kDa and MW$_{exp}$= 21 kDa), possibly due to the unfolded and therefore extended conformation of the protein which might result in slightly varying elution times. Data obtained from MALS are summarized in Table 3.16 and Figure 3.55.

Table 3.16: RALS data for ^{15}N-labeled stargazin$^{203\text{-}323}$ (C_GB-1)

	WT
Peak retention volume [mL]	17.7
Molecular weight [kDa]	21
Oligomeric species	Monomer (M)

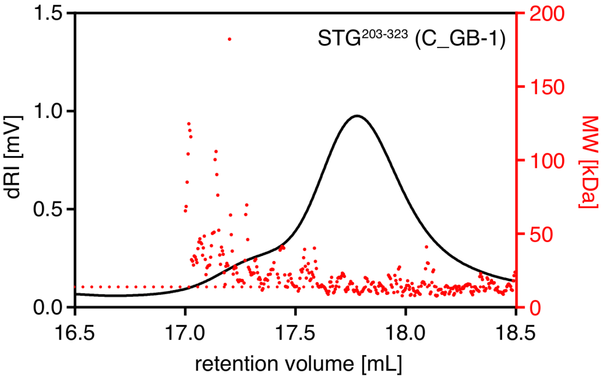

Figure 3.55: Determination of the absolute molecular weight of ^{15}N-labeled stargazin$^{203\text{-}323}$ as determined by MALS. For MALS measurement, 60 µL of a 1 mg/mL of purified protein (prepared from C-terminally tagged construct, C_GB-1) was injected on a Superdex™ 200 increase 10/300 column pre-equilibrated with RALS buffer and in a constant flow rate of 0.5 mL/min. Raw data were evaluated using Astra 6.1.5.22. The differential refractive index (dRI) and the molecular weight (MW) in kDa are plotted against the retention volume in mL. A dotted red line indicates the molecular weight for a monomer.

Before starting to investigate protein phosphorylation with NMR, ^{15}N-labeled stargazin$^{203\text{-}323}$ purified from C-terminally tagged stargazin (C_GB-1) was tested for its ability to bind to liposomes. Furthermore, the dependence of liposome-binding on stargazin$^{203\text{-}323}$ phosphorylation was investigated. Liposome co-sedimentation revealed that ^{15}N-labeled stargazin$^{203\text{-}323}$ is able to bind to FOLCH and PA/PC liposomes and that this interaction (as for ^{14}N-labeled stargazin$^{203\text{-}323}$) can be abolished upon phosphorylation of stargazin C-terminal tail (Figure 3.56), indicating that the purified isotope-labeled protein can be used for downstream applications.

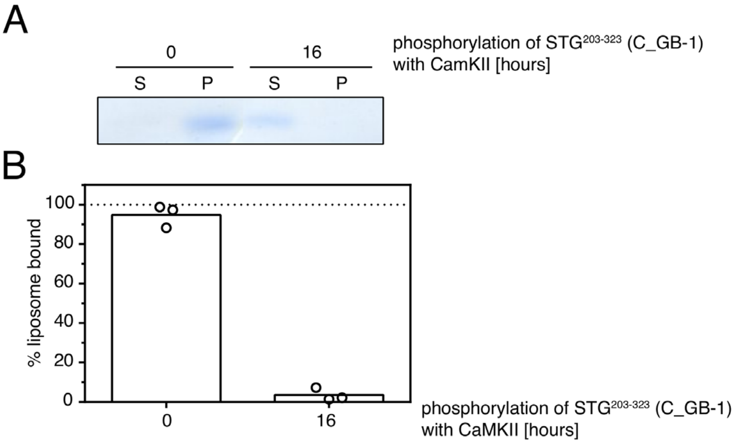

Figure 3.56: Liposome co-sedimentation assay using ^{15}N-labeled stargazin$^{203\text{-}323}$ (C302S, C_GB-1) and FOLCH as well as PA/PC polar liposomes (1:9). (A) For phosphorylation, 10 µM stargazin$^{203\text{-}323}$ prepared from C-terminally tagged protein (C_GB-1) were incubated with activated CaMKII for 16 h at 30°C. As a control, 10 µM stargazin$^{203\text{-}323}$ was incubated in the CaMKII buffer (without kinase). Protein samples were incubated with 1 mg/mL liposomes for 10 min at 20°C. Ultracentrifugation (213,600 x g) at 20°C was performed to separate liposome-bound from liposome-unbound protein. Supernatant (S) and pellet (P) after ultracentrifugation were subjected to SDS-PAGE. **(B)** Quantification of liposome-bound fractions (in %) for non-phosphorylated and 16 h phosphorylated stargazin$^{203\text{-}323}$ sample. Gel band intensities were quantified using ImageJ [291] (n= 2 for binding to FOLCH liposomes and n=1 for binding to PA/PC liposomes).

3.2.6.3 ^{1}H-^{15}N HMQC of stargazin$^{203\text{-}323}$

In order to decipher why stargazin$^{203\text{-}323}$ protein purified from N-terminally tagged stargazin C-terminal tail yielded protein that migrates at too low molecular weights on SDS-PAGE, gave inconsistent masses on MALDI measurements and did not show any mass shifts upon phosphorylation, 1D and 2D NMR spectra were recorded of the sample. The sample was also phosphorylated using CaMKII following the same phosphorylation protocol that was used for liposome co-sedimentation. In order to record ^{1}H-^{15}N HMQC spectra, a protein concentration of $\geq$ 20 µM was needed. Addition of a phosphate group to the hydroxyl moiety of a Ser residue locally alters the chemical environment of neighboring atomic nuclei, giving rise to a different chemical shift compared to the unmodified residue. These different chemical shifts can be used in order to determine protein phosphorylation sites. In order to achieve high signal quality of the NMR spectrum, the protein was dialyzed into a buffer with salt concentration below 100 mM and a pH of ~6.8. 5 % D_2O were added to the protein prior to recording the spectra. The spectra of purified stargazin$^{203\text{-}323}$ from N-terminally tagged stargazin$^{203\text{-}323}$ before and after incubation with CamKII are shown in Figure 3.57.

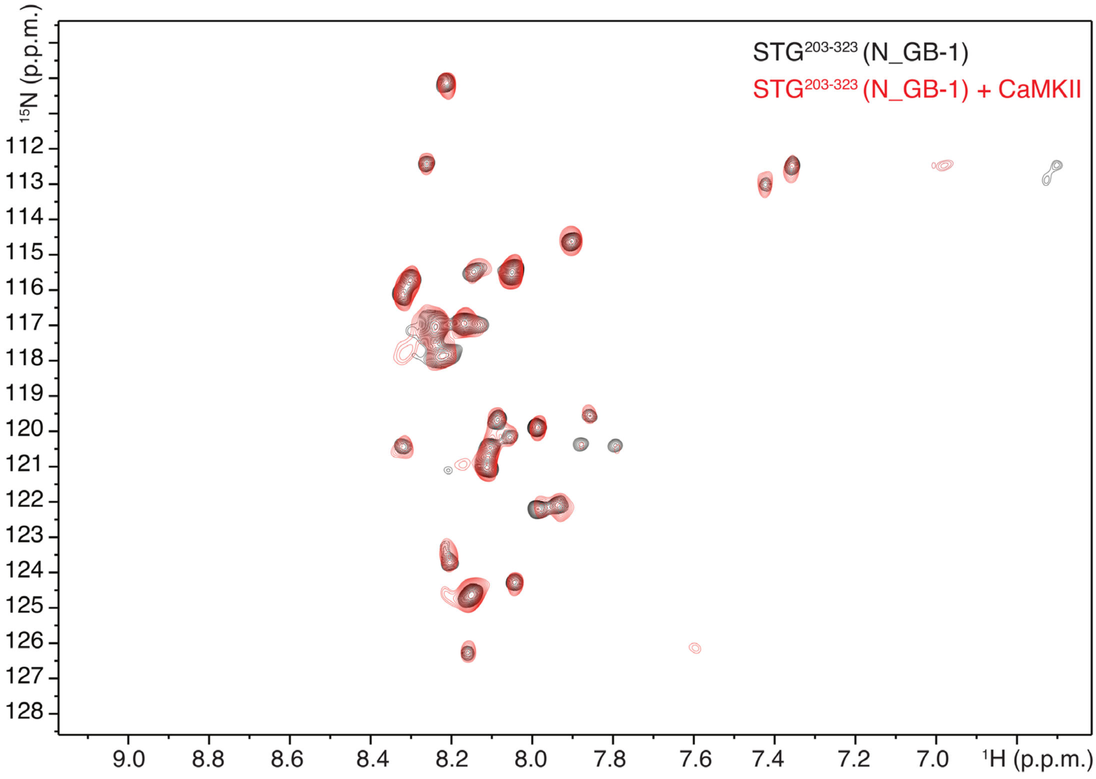

Figure 3.57: 2D ^{1}H-^{15}N HMQC spectra of stargazin$^{203\text{-}323}$ purified from N-terminally tagged stargazin$^{203\text{-}323}$ (C302S) construct (N_GB-1). ^{1}H-^{15}N amide NMR spectra of unmodified stargazin$^{203\text{-}323}$ (aa 203-323, C302S, black) and of stargazin$^{203\text{-}323}$ incubated with CaMKII for 16 h at 30°C (aa 203-323, C302S, red) are overlaid. Spectra were recorded at 283 K. No phosphorylation-induced changes are visible.

The spectrum of stargazin$^{203\text{-}323}$ in Figure 3.57 clearly shows the presence of an unfolded protein as the signals are condensed in the area between 7.8 and 8.4 p.p.m.. As NMR is nondestructive, the same sample was used and incubated with activated CaMKII for ~16 h at 30°C to initiate phosphorylation of stargazin$^{203\text{-}323}$. After incubation with CaMKII, another spectrum was recorded using the same settings. However, no chemical shifts could be observed after CaMKII treatment of this protein sample, indicating that no

phosphorylation occurred. This is in accordance with the MALDI TOF/TOF measurement, where no mass changes could be observed after incubation of the protein with CaMKII (Figure 3.52). Another feature of the protein is that it does generate fewer signals than expected. Accounting for residues that don't give a signal in 2D spectra like proline (stargazin$^{203\text{-}323}$ has seven Pro residues) and N-terminal residues (due to the solvent exchange of the NH_3^+ group), one could possibly count 40-50 signals. The protein is presumably not aggregated (this would also account for a loss of signals in the spectrum) as aggregated proteins give signals at the bottom of the spectrum.
Taking all these results together, purified stargazin$^{203\text{-}323}$ from N-terminally tagged protein does not only degrade C-terminally but also is not able to get phosphorylated, excluding it as a candidate for further studies.

Next, NMR spectra were recorded for stargazin C-terminal tail that was purified from C-terminally tagged protein. The protein preparation was similar: stargazin$^{203\text{-}323}$ was dialyzed into NMR buffer. The protein concentration was 100 µM. Because phosphorylation of stargazin$^{203\text{-}323}$ purified from C-terminally tagged protein could be directly and indirectly verified using MALDI-TOF/TOF and liposome co-sedimentation, respectively, a continuous 2D ^1H-^{15}N spectrum was recorded for stargazin$^{203\text{-}323}$ after addition of CaMKII (at 20°C) in order to continuously watch phosphorylation and to get an idea of the phosphorylation kinetics and the mechanism of stargazin C-terminal tail multiple phosphorylation. To find a compromise between kinase activity (CaMKII has its maximum activity at 30°C) and signal quality and intensity (the lower the temperature, the higher the signal intensity), continuous 2D spectra were recorded at 293 K (20°C). Overlaid spectra of unmodified stargazin C-terminal tail (black signals in Figure 3.58) purified from C-terminally tagged stargazin construct and from phosphorylated stargazin C-terminal tail (red signals in Figure 3.58) are shown in Figure 3.58.

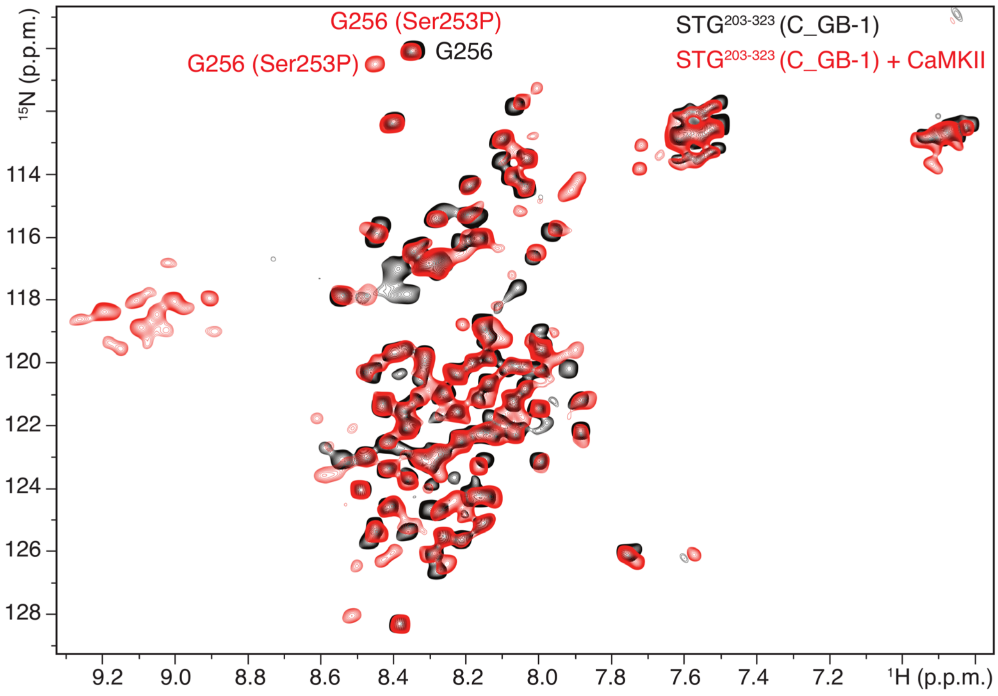

Figure 3.58: 2D ^{1}H-^{15}N HMQC spectra of stargazin$^{203\text{-}323}$ purified from C-terminally tagged stargazin$^{203\text{-}323}$ (C302S) construct (C_GB-1). ^{1}H-^{15}N amide NMR spectra of unmodified stargazin$^{203\text{-}323}$ (aa 203-323, C302S, black) and of stargazin$^{203\text{-}323}$ in presence of CaMKII (aa 203-323, C302S, red) are overlaid. Spectra were recorded at 293 K.

Comparing this spectrum to the spectrum obtained from N-terminally tagged construct, the number of signals is increased, indicative of an intact protein. Again, the signals of the unmodified protein are concentrated in the area between 7.9 and 8.6 p.p.m. indicating that the protein is unfolded. The signals at 7.6 and 6.8 p.p.m. correspond to Asn and Gln residues and originate from their side chain amide group.

Spectra were recorded continuously and the spectrum of phosphorylated stargazin C-terminal tail in Figure 3.58 (red signals) was the first spectrum recorded. With the settings used for these NMR measurements, recording one NMR spectrum took 45 minutes. After 45 minutes, however, phosphorylation already reached the maximum. Subsequent spectra did not show any additional signals appearing, concluding that the endpoint phosphorylation was already reached after 45 minutes (data not shown). Using a lower CaMKII concentration for NMR experiments in future experiments will give better resolution of the different phosphorylation events.

For comparison, phosphorylation was also performed at 30°C (as for liposome-binding and mass spectrometric experiments) and after 16 h, a ^{1}H-^{15}N HMQC was recorded, showing the same signal pattern as the spectrum continuously recorded at 20°C, indicating that CaMKII works equally well at 20°C and 30°C (spectrum not shown).

Importantly, CaMKII treatment of the protein leads to appearance of new signals in the area around 8.4-9.2 p.p.m. distinctive of phosphorylated side chain residues.

The number of appearing phosphate signals exceeds the number of phosphorylatable Ser residues within the C-terminal tail of stargazin, indicating that a mixture of different phosphorylation degrees is present that causes distinct chemical environments and leads to multiple phosphate signals for one residue.

From the overlaid spectra, one can furthermore conclude that phosphorylation does not lead to structural rearrangements because the signal positions remain unchanged (apart from the phosphorylation sites).

Exact side chain assignment is not possible because the sample was only double labeled (^{1}H and ^{15}N). In order to assign the position of every single amino acid in the spectrum, a set of NMR experiments is needed together with triple labeled stargazin$^{203\text{-}323}$ protein (^{1}H, ^{15}N, ^{13}C), which we will be doing in further experiments.

Additional information that can be gained from the ^{1}H-^{15}N amide correlation spectrum is that some Ser residues get fully phosphorylated, which can be seen from the completely disappearing Ser signals at 8.4 p.p.m..

The position of Gly256 can be assigned already with certainty as this Gly residue is the only Gly residue in proximity of phosphorylatable Ser residues. Following phosphorylation, a new Gly256 peak appears close to the Gly256 peak of unmodified stargazin$^{203\text{-}323}$. A signal at the position of unmodified Gly256 is still present, albeit with less intensity, which indicates that Ser253 does not get 100% phosphorylated.

Taken together, using a codon-optimized gene for the cytoplasmatic domain of stargazin (C302S) cloned into a vector to get a C-terminally tagged stargazin$^{203\text{-}323}$ construct yielded pure and homogenous protein for both, expression of unlabeled and of ^{15}N-labeled stargazin$^{203\text{-}323}$.

For the first time, untagged protein was used in biophysical and biochemical assays to show that recombinantly over-expressed stargazin$^{203\text{-}323}$ is able to bind to liposomes and that the protein can get phosphorylated by CaMKII, which interferes with its ability to bind to liposomes. Further experiments will give mechanistic insights into the phosphorylation of stargazin cytoplasmatic domain.

4 DISCUSSION

4.1 TETRAMERIC STRUCTURES OF THE LIGAND-BINDING DOMAIN OF GLUA2

Since the discovery of NMDA, kainate and AMPA receptors [380], scientists were eager to decipher the gating mechanisms of glutamate receptors and the structure-function relationship. Despite the immense efforts in obtaining structural information of an active AMPA receptor either by using full-length structures or isolated LBDs, the receptor could not be captured in an active state so far and LBD movements upon receptor activation are largely unknown. A high intrinsic mobility of LBDs may account for the fact of heterogeneity observed in different structures [123-125]. In the only glutamate-bound full-length AMPA receptor, the transmembrane domain is not resolved and the structure is not supported by functional experiments, making it difficult to judge about the open state of the pore [40].

In this thesis we were able to obtain five iGluR crystal structures in total with different dimer-dimer arrangements revealed from crystallographic symmetry. Three of them, glutamate-bound WT, TR and A665C/L483Y sLBDs, revealed two tetrameric arrangements by crystallographic symmetry, termed tight and loose tetrameric LBD conformation. Performing computational modeling as well as functional experiments with a battery of metal bridges enabled us to show that the tight arrangement seen in the crystal structure is indeed populated by the LBDs during gating. The results presented in this thesis give further insights into LBD tetramer movement upon activation of the receptor.

The other two crystal structures of His-mutated GluA2 LBDs revealed a distinct dimer-dimer arrangement with zinc being coordinated between them, as also evaluated by light scattering experiments using sLBDs in solution.

Motivated by the intermediate state of receptor activation trapped in the disulfide cross-linked DNQX-bound A665C/L483Y structure [116], we aimed to crystallize the corresponding His-mutated GluA2 LBD that was used in their functional experiments to ideally obtain a zinc-bridged tetramer representative of a receptor activation intermediate. Lau et al. used metal bridging experiments instead of Cys mutations to evaluate the activation intermediate in functional experiments [116].

The structures of zinc-bound His mutated LBDs could be solved and we could observe zinc coordination between canonical dimers, however, the wrong sites were involved.

Additionally, we crystallized the A665C/L483Y mutant in complex with glutamate. As already mentioned, the biological assembly obtained from crystallographic symmetry is almost identical to the tight tetrameric arrangement seen in the WT and TR crystal structure. Furthermore, no density for the disulfide bridge was visible.

In the next sections, the results obtained from the different tetrameric arrangements obtained in this thesis will be discussed in context of existing structures and compared to results obtained from full-length structures.

4.1.1 GluA2 sLBD tetrameric arrangements formed by crystallographic symmetry operations

A series of full-length AMPAR [19, 41, 123-125] and NMDAR structures [39, 42, 128, 129] were published recently and in the past years. However, none of them revealed an open ion channel pore despite using a variety of different molecules that should help to capture the receptor in an open state.

An explanation for why it might be so difficult to get structural information of an active, pore-open channel is that the receptor has a high degree of conformational flexibility in the resting, active and desensitized state, indicated by the heterogeneity of conformations obtained from cryo-EM [40, 114, 116, 119, 352]. Furthermore, the receptor undergoes very fast and almost complete desensitization in the continued presence of agonist, making it difficult to capture the receptor in an active state by means of X-ray crystallography. The authors themselves declared that it might be due to the crystallization conditions, the absence of a natural lipid bilayer, the presence of a partial agonist not sufficiently populating the open gate conformation or due to the crystallization construct that may favor a closed-state [123].

Since crystallization of a full-length GluA2 receptor in an active state seems to be very challenging and production of well-ordered and diffracting crystals of fl structures is still the bottleneck of crystallography [381-384], using isolated LBDs instead for crystallization has been shown to be valuable in a previous work, where isolated LBDs form a dimeric [78] and a tetrameric arrangement [116] upon application of crystal symmetry operations, respectively. In a second study, the flip-like N754S mutant GluA2 LBD bound to glutamate and the allosteric modulator NS5217 revealed a tetrameric arrangement similar to the tight and loose tetrameric arrangement seen in the WT and TR structure, however the authors did not mention any physiological relevance arising from the tetrameric LBD conformation [385]. Due to the similarity, the tight tetrameric LBD

arrangement obtained from this structure can be superimposed on the tight tetrameric arrangement seen in the TR structure with an rmsd of 0.91 Å (based on Cα atoms in D1). In the same paper, the same mutant was crystallized with glutamate and the allosteric modulator NS1493 at 1.95 Å resolution and this structure, per crystallographic symmetry, generated a distorted tetramer, which looks similar to the shifted tetramer obtained in the HHH structure complexed with kainate. So it seems that the distorted tetramer arrangement we obtained in this thesis is favoured through crystal contacts that are independent of the introduced His mutants.
GluA2 sLBDs have been crystallized bearing different mutations and complexed with a variety of ligands. As pointed out, some of them produced physiologically plausible tetramers by applying symmetry operators. Also isolated kainate receptor ATDs have been found to form tetrameric arrangements by crystal packing that were strikingly similar to the first (antagonist-bound) GluA2 full-length structure [386].

Oligomers obtained from crystal structures need to be evaluated in order to verify their occurrence in biological systems and to exclude the possibility of crystallographic artefacts. The usage of isolated domains does have limitations as sLBDs lack the context of the whole protein and the connection to the ATD and the TMD and therefore they don’t have the geometric constraints imposed by other domains. If LBD conformational rearrangements are affected by the ATDs for example, we would not be able to extract this information from crystallized isolated LBDs. Also, without evaluation of the sLBD assembly formed through crystal packing in functional and or biochemical experiments, a crystal structure is of low value. And although the isolated LBDs are not predicted to form quaternary assemblies in solution (as predicted by the PISA server [387]) (which is known from analytical ultracentrifugation studies) and explainable by the weak interactions between the individual LBDs, dimerization and tetramerization in solution can be promoted by using stabilizing mutations or modulators. In doing so, we were able to detect dimers of the L483Y LBD mutant and tetramers harboring the A665C/L483Y mutation.

Because it is still a fundamental problem in structural biology to distinguish biologically relevant assemblies derived by symmetry operations from crystal packing contacts/artifacts of crystallization [337, 388-391], we aimed to carefully evaluate the tetrameric arrangement obtained by the crystal packing by means of biophysical experiments and electrophysiology and we were able to show that the tight tetrameric arrangements obtained from glutamate-bound GluA2 WT, TR and A665C/L483Y sLBDs are sampled during receptor activation. And although it has been described that crystal packing contacts have smaller interfaces than biological interfaces, both the interdimer and the intradimer interfaces are comparable to those obtained from full-length structures (see Figure 3.21, Figure 3.22, and Figure 3.28).

In the framework of this thesis, we also obtained distinct and -most likely-physiologically irrelevant tetrameric arrangements for the HHH and HHHAA mutant with zinc resolved between dimers. These tetramers are characterized by a shift of canonical dimers relative to each other.
As the HHH mutant showed zinc-induced dimer formation in solution in light scattering experiments, by combining the His mutant with the L483Y mutation we aimed to capture a zinc-coordinated tetrameric GluA2 LBD arrangement. However, the HHH in combination with the L483Y mutation did not yield any crystals, and only the HHH mutant bound to kainate gave nice diffracting crystals with zinc visible in the electron density. Zinc could be observed at the interdimer interface (two zinc coordination sites are observable); however, the metal bridge was different from the desired bridge and also involved native zinc-coordinating residues (H412, E413, E431). Possibly due to this zinc bridge, the canonical dimers were shifted relative to each other. (Figure 3.32).

Crystallographic symmetry operations have been applied for a broad range of proteins in order to obtain the biological assembly of proteins [337]. A popular example is the structure of hemoglobin. Biologically functional hemoglobin consists of four chains (two α and two β subunits). Hemoglobin has been crystallized in a tetragonal space group ($P4_12_12$) with the asymmetric unit representing a portion of the biological assembly (PDB ID: 1HHO) [392] and interestingly it has also been crystallized in such a way that the a.u. corresponds to the biological unit (PDB ID: 2HHB and 1GZX) [393, 394]. A tetrameric sLBD structure has not been obtained were the a.u. matches the biological unit, however by applying crystallographic symmetry operators on one of the molecules in the a.u. (translation and 180° rotation) we were also able to obtain the biological unit of a tetrameric LBD assembly. Biological assemblies generated from the a.u. by applying matrices that represent the helical rotation and translation are also important when it comes to filamentous structures; one example is the bacteriophage Pf1 (PDB ID: 1QL2) [395]. Also for NMDARs, it has been reported that the biological tetrameric unit of the GluN1/GluN2B receptor has been obtained by application of crystallographic symmetry operators, as the a.u. only contains two halves of the full-length receptor [42].

4.1.2 Light angle light scattering was performed to determine the oligomeric state of sLBDs in solution

Macromolecular biological assemblies are characterized by weak and non-covalent interactions compared to direct protein-protein interaction [337, 396] and this is especially true for sLBDs that do not have their connections to the ATD, TMD or CTD anymore, which also explains why the protein is monomeric in solution, as determined by static light scattering (Figure 3.6). Light scattering together with analytical ultracentrifugation experiments have been proven helpful for investigating the oligomeric state of LBDs in solution [397] and revealed monomeric iGluR LBDs in solution with dimer and tetramer K_D values in the high mM range [179, 180, 398, 399].

However, it has been shown that the monomeric state of sLBDs in solution can be shifted towards a dimeric arrangement by using allosteric modulators such as CTZ or mutations that stabilize the dimeric [400] or even the tetrameric form of AMPAR LBDs [116, 342]. In the framework of this thesis, dimeric GluA2 sLBDs in solution could be obtained by introducing His mutants at the interdimer interface (Figure 3.9) and tetrameric sLBDs in solution could be obtained by combining the canonical dimer-stabilizing mutant L483Y and the intradimer cross-linking mutant A665C (Figure 3.8).

The significance of the tetrameric glutamate-bound sLBD arrangement seen in the crystal structure of the WT and TR GluA2 sLBDs has been evaluated using light scattering experiments, computational modeling and electrophysiology, providing evidence for the usefulness of tetrameric sLBDs to study the mechanism of AMPAR gating.

Interestingly, a tetramer and dimer mixture of CuPhen cross-linked A665C/L483Y sLBDs complexed with glutamate could be detected in solution using SLS (Figure 3.8). A dimer-tetramer mixture could also be obtained on non-denaturating SDS-PAGE after CuPhen cross-linking (Figure 3.4 and Figure 3.7). Without treating the GluA2 A665C/L483Y sLBDs with CuPhen, they did not form a Cys cross-link in the crystal structure, although DNQX-bound sLBDs harboring the same mutation could be cross-linked (Figure 3.19). Using either a different ligand or incubating the protein with CuPhen prior to crystallization could help to get a cross-linked tetrameric structure of A665C/L483Y sLBDs.

Light scattering data of the HHH mutant complexed with different ligands showed zinc-dependent dimer formation that could not be observed in the presence of EDTA (Figure 3.9), suggesting that by introducing His mutations at the interdimer interface we were able to obtain and stabilize dimer formation in solution in the presence of zinc.

Introduction of the L483Y mutation, which stabilizes canonical dimers, should lead to tetramerization of the HHH mutant in solution in presence of zinc.

In the crystal structure of the HHH mutant, zinc could be observed at the interdimer interface; however, the metal bridge was different from the desired bridge and also involved native zinc-coordinating residues (H412, E413, E431). Possibly due to this zinc bridge, the canonical dimers were shifted relative to each other in the tetramer obtained by crystallographic symmetry (Figure 3.32).

The same holds true for the HHHAA crystal structure, where zinc could be resolved between dimers but again, native LBD residues were involved in the metal bridge as well as histidines that we introduced (Figure 3.35). Because in the crystal, zinc bridges are favoured between residues different from the designed triple His mutant (G437H, K439H and D456H) this raises the possibility that the dimers observed in static light scattering (although they are bound to the full agonist glutamate) could result from zinc-bridging in this distorted, shifted interaction of subunits and would therefore also be different from the arrangement that has been postulated from functional experiments (resembling a functional intermediate of receptor activation) [116]. So far and with all tested ligands bound to GluA2 sLBDs harboring the triple His mutations, a biologically relevant tetrameric arrangement with zinc being bound between dimers could not be obtained in a crystal.

In presence of 1 mM zinc, the HHH mutant can form dimers in presence of either full agonist glutamate or partial agonist fluorowillardiine (Table 3.4 and Figure 3.9). Functional experiments revealed trapping of the GluA2 HHH-mutated receptor only at intermediate concentrations of glutamate, indicative of trapping the receptor in a partially active state. However, using light scattering, we were able to detect a monomer-dimer mixture not only in the presence of partial agonist, but also in presence of full agonist. Using sLBDs, the steric hindrance of full-length proteins is not given anymore, making the bridge possible to form.

Before the first AMPAR full-length structure was published in 2009 that brought light into dark of how the domains are arranged in the tetramer, Jin et al speculated about possible dimer-dimer interactions based on crystal packing and found a loose-like tetramer as well as several arrangements with zinc being coordinated between dimers [401]. The zinc coordination in their tetramer is mediated by residues Glu678, His436 and Glu431 and has shifted dimer pairs, similar to the dimer-dimer orientation seen in the HHH structure complexed with kainate, however, Glu431, His435 and two water molecules were involved in our zinc-containing structure and a second zinc coordination site involved the native Glu413 and His412 as well as the introduced mutant His437 (Figure 3.32).

4.1.3 Functional experiments based on the tetrameric sLBD structure revealed physiological relevance of the tight tetrameric arrangement

Using a combination of patch clamp experiments and molecular modeling, we aimed to evaluate the two tetrameric arrangements obtained from the TR and WT tetrameric LBD arrangements. Generation of His mutants based on the structural information of the tight tetrameric LBD arrangement showed that three out of four predicted metal bridges (T1, T2 and T3) formed readily in full-length receptors, as revealed by zinc trapping experiments and only one bridge, T4 failed to show any effect upon zinc application.

All bridges showed a current reduction following exposure to 1 µM zinc. The inhibitory effect of zinc bridges was described earlier [116]. As described in Section 3.1.5, the inhibitory effect of forming metal bridges could arise from restricting the receptor in a specific conformation without allowing the mobility that has been ascribed to LBDs. Presumably the metal bridge traps the receptor in a less active state. One exception, the double mutant D668H, K765H (HH), showed no current inhibition in presence of CTZ and quisqualate, which suggests that the bridge formed by the HH mutant does not modulate the receptor and this bridge is fully active or that the bridge does not form in this state. The suggestion that the HH mutant traps an LBD conformation different from the tight tetrameric arrangement is emphasized by the molecular modeling results, indicating that a small rigid body movement by 1 Å of the TR tetrameric arrangement will results in optimal zinc coordination of the HH mutant.

Investigating the state dependency of the bridges revealed trapping of receptors harboring the T1 bridge in the resting, ligand-free and in the active state as trapping could be observed at intermediate (100 µM glutamate) and saturating concentrations of glutamate but not at low glutamate concentrations [342]. This results suggests that at low glutamate concentrations, when only the minority of LBDs are ligand-bound, trapping of the apo state will be prevented, suggesting a high degree of mobility of apo LBDs. Highly mobile LBDs in the ligand-free state were currently also revealed by cryo-EM studies of the full-length heteromeric GluA2/A3 structure [19].

The electrophysiological recordings together with the computational modeling suggest that the tight tetrameric arrangement is populated by full-length receptors during gating that are either partially or fully bound to glutamate, however, it does not represent a fully active state of the receptor because peak current is reduced when the bridge is formed compared to the same patch in EDTA. In contrast, the HH mutant even showed potentiation when exposed to CTZ and quisqualate, suggesting that the LBD conformation trapped by this metal bridge might be different from the arrangement seen in the LBD tight tetrameric arrangement.

Because zinc bridging could be observed for a range of LBD geometries (the T1, HH, HH D769H and HH D769E mutants) this indicates that the LBDs move enough to cross-link and that they can adopt a range of conformations during gating and might gate independently [43, 157, 402].

The investigated bridges cannot be formed in the glutamate-bound EM structure or in partial agonist-bound structures because the sites are not close enough [40, 125].

4.1.4 Domain closure upon receptor activation

It has been postulated that isolated LBD structures have different domain closures (measured by the distances ξ1 and ξ2) compared to the corresponding (i.e. same ligand bound to the LBD) full-length structures because they lack the connection to the ATD and the TMD, thereby being less restricted [125]. Comparing the WT and TR domain sLBD domain closure to other sLBD structures and full-length structures showed that for most structures (except for the NOW fl and sLBD structures) the degree of domain closure is similar for sLBD and fl structures and for both, sLBD and fl structures, the extent of domain closure decreases with ligand efficacy: ZK > apo > NOW > KA > glu (Figure 3.16), indicating that at least in the case of the investigated structures, the extent of domain closure correlates with ligand efficacy. For all three solved glutamate-bound sLBD structures (WT, TR mutant and A665C/L483Y GluA2 LBD) the degree of domain closure is nearly identical which suggests that domain closure in sLBD structures is reproducible and not influenced by different crystal packing forces.

The clamshells in the kainate-bound LBDs from the HHH mutant bound to kainate are 0.6 Å less closed compared to the glutamate-bound LBDs from the tight tetrameric arrangement and ξ1 and ξ2 increase from 9.4 Å to 10.0 Å and from 7.8 Å to 8.4 Å, respectively.

It still remains an open question, what distinguishes a partial agonist from a full agonist. Two models have been used so far in order to describe the mechanism of partial agonism: the Monod-Wyman-Changeux (MWC) and the Koshland-Nemethy-Filmer (KFN) model. The MWC model assumes that partial agonists transfer inactive receptors into the active state less efficiently than full agonists, whereas the KFN model assumes that the receptor can undergo sequential and non-concerted changes of the structure with partial agonists inducing a set of different conformational states [152, 403, 404]. Future experiments will reveal the mechanism behind partial agonism but it seems that the efficacy of a ligand to activate the receptor roughly depends on its ability to stabilize the fully closed LBD clamshell [143, 147, 349, 352, 405, 406].

4.1.5 LBD tetramer movements upon receptor activation

The extracellular LBD is connected to the transmembrane segments by three linkers. As domain closure and upward movement of D2 towards D1 is thought to drive opening of the channel by pulling the pore-forming transmembrane domains apart, the linkers also move. Therefore, the linker distances within a tetramer (measured by the Cα of marker atoms) were measured for different structures, aiming to get insights into the structural consequences of LBD clamshell closure on LBD linkers. Mutations within the linker regions or swapping experiments (exchanging GluA1 linkers for δ2 linkers) emphasized the importance of the linker regions for receptor functionality and parameters such as agonist potency and receptor desensitization [359, 407-409].

The M3-S2 linker, described by the marker atom Pro632, has already been used in glutamate receptor structures to understand how LBD cleft closure is transmitted to the ion channel pore [78]. The Pro632 distances indicate that subunits have different impacts on channel gating, with the B-D dimer pair separation being much larger than the A-C dimer pair separation, suggesting that distal subunits B and D have a larger impact on channel opening (Figure 3.24). According to our measurements, the B-D pair makes the largest movements as the first two ligands bind to the LBD (sLBD, partially active, with subunits B and D modeled as glutamate-bound subunits) (Figure 3.24), consistent with the findings that subunits act independently [43, 157]. The large movements of the M3-S2 linker might be necessary to unwind the M3 helix in the course of channel opening.

Activation of the receptor seems to be accompanied with tightening of the interdimer interface (between subunits A-B and C-D) (Figure 3.21). Although the interdimer surface becomes larger, the central opening enlarges upon activation of the receptor as measured by the A-C distance of Arg660 Cα atoms and the B-D distance of Gln756 Cα atoms (Figure 3.23). As the receptor gets activated, both, the A-C Arg660 and the B-D Gln756 increase. Both marker atoms are located at the border of the upper and lower lobes and the dimer separation measured by the two marker atoms might be minimally affected by agonist-driven clamshell-closure. All linker distances measured (S1-M1, M3-S2, S2-M4 and ATD-S1 linker) revealed a higher increase in the B-D distance upon activation compared to the A-C distance (Figure 3.25).

Interestingly, our data suggest a decrease of the interdimer angle, which is distinct from the interdimer angle obtained from full-length structures with the ion channel either closed or not resolved (Figure 3.27 and Figure 4.1) [39, 40]. Similar to the relative dimer orientation, the angle between the local two-fold symmetry axes of the LBD can be determined (Figure 4.1 B) and is very different for sLBD structures and full-length structures. This angle measures how much the LBD is angled off the overall two-fold axis of symmetry. Whereas full-length structures suggest an increase in the interdimer angle upon activation, the angle of local two-fold LBD symmetry axes is 0° for structures of isolated glutamate-bound LBDs (Figure 4.1 B, right panel), suggesting that the linkers to the TMD must be under strong tension. The strikingly different angle could also arise from completely unrestricted LBDs and clearly shows a limitation of using sLBD structures.

A top view of the LBDs shows how interdimer movements lead to channel opening through enlargement of the central gating ring. A recently published cryo-EM structure of a heteromeric GluA2/A3 full-length structure in the apo state revealed a complete different dimer arrangement on level of the LBDs, characterized by a side-by-side arrangement of helices G in subunits A and C (Figure 4.1 C), whereas in homomeric structures of either full-length or sLBD structures, the helices are arranged in a head-to-head fashion (Figure 4.1 C). At least for homomeric structures, the helices G separate upon activation of the receptor (also measured by the A-C Arg660 and the B-D Q756 Cα distances), leading to opening of the central gating ring (Figure 4.1 C). Whether or not heteromeric glutamate receptors display a different LBD orientation and undergo distinct movements upon receptor activation remains elusive.

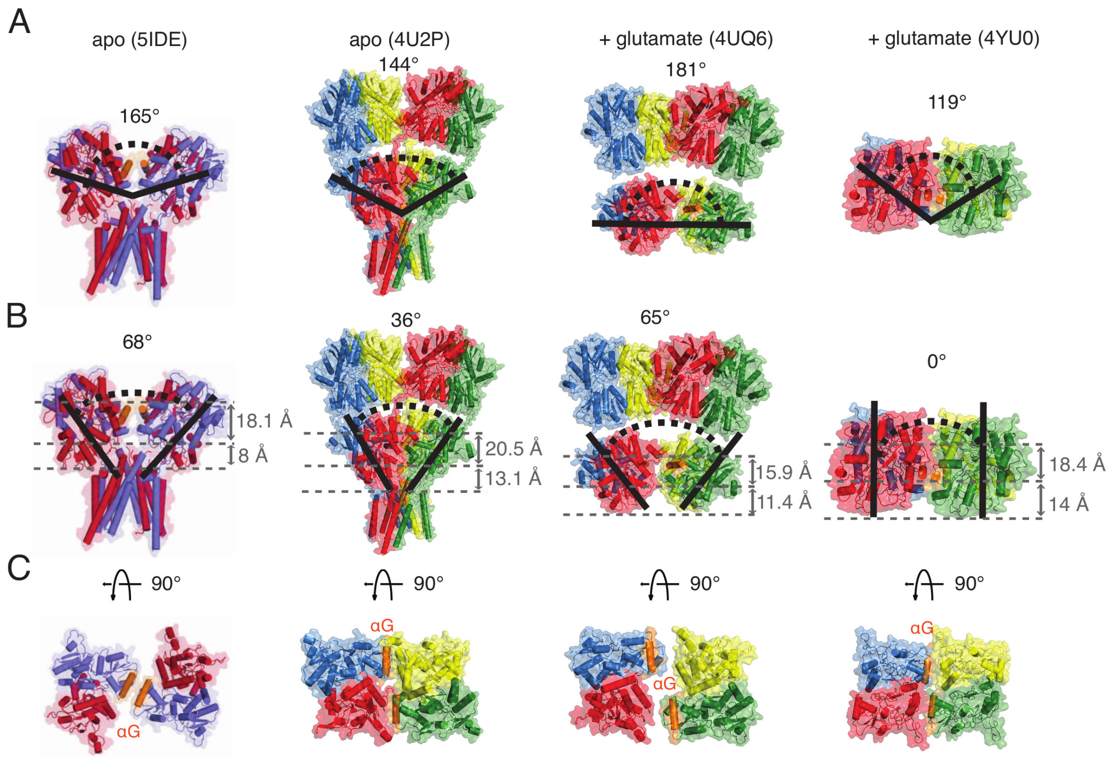

Figure 4.1: Interdomain LBD movements of glutamate receptors upon activation. (A) View of full-length GluA2 structure or isolated LBDs parallel to the membrane and perpendicular to the overall two-fold axis of molecular symmetry. The relative dimer orientation of the A-D dimer relative to the B-C dimer is indicated by a black line. The angle was determined by measuring the angle between two vectors, originating at the Ala665 Cα COM of subunits A and C to the Cα atoms of Leu748 in subunits A and C, respectively. COMs and angles were determined using Pymol. **(B)** Views of the LBD layer perpendicular to the global two-fold symmetry axes. Angles between the local two-fold rotation axes of LBD dimers A-D and B-C are shown as bold black lines. Grey dashed lines indicate the layers defined by the D1 center of mass, D2 center of mass and the center of mass (COM) defined by Pro632. Vertical arrows indicate the distance between the layers (in Å). COMs were calculated using Pymol. **(C)** Top view of the LBD layer showing the relative position of helix G (orange) in subunits A and C. Whereas helices G are orientated side-by-side in the heteromeric ligand-free GluA2/A3 cryo-EM structure, in homomeric structures, the helices are arranged head-to-head and activation leads to enlargement of the central gating ring. The angle is indicated in ° for different full-length structures and the tight tetrameric arrangement obtained from glutamate-bound sLBDs. The PDB ID's are given in parantheses. Subunits coloring (except for the GluA2/A3 heteromer): A – green, B – red, C – blue, D – yellow. Subunits GluA2 and GluA3 in the heteromeric cryo-EM structure (left panel) are colored in purple and red, respectively. First panels in (A), (B) and (C) taken from [14]

4.2 STARGAZIN CYTOPLASMATIC C-TERMINAL TAIL (STARGAZIN$^{203-323}$)

TARPs are important regulators of AMPAR function, gating and trafficking. Distinct domains of TARPs have been shown to be responsible for different regulatory aspects [226]. The C-terminal tail of stargazin, the prototypical member of TARPs, has been shown to be involved in synaptic targeting of AMPARs. The interaction of TARPs with AMPARs occurs in a phosphorylation-dependent manner.

In the framework of this thesis, we were able to establish and optimize the production of untagged complete 120 aa stargazin C-terminal tail from C-terminally tagged protein (C_GB-1). Biochemical and biophysical experiments revealed the presence of unfolded protein that was able to bind to liposomes. Phosphorylation of stargazin$^{203-323}$ interferes with lipid binding and allows for interaction with scaffolding proteins like PSD-95.

4.2.1 Stargazin$^{203-323}$ could be over-expressed and purified to obtain untagged protein

A prerequisite for the realization of biochemical, biophysical and structural experiments is the availability of sufficient protein amounts with satisfying purity. Unfortunately, the production of soluble and stable protein is still a bottleneck for structural and biochemical experiments. It has been shown that the vast majority (~75%) of biologically important proteins is characterized by low solubility and stability [410]. Accordingly, the main challenge was to obtain over-expressed, well-behaved and non-aggregated stargazin C-terminal tail.

Published data and studies on stargazin C-terminal tail or on stargazin fragments were done using either short synthetic peptides [233, 259, 411] or recombinantly over-expressed stargazin cytoplasmatic C-terminal tail fused to an expression tag as thioredoxin (Trx), His$_6$, glutathione S-transferase (GST) or the galactosidase 4 (GAL4) DNA binding domain [251, 256, 259, 262].

The low solubility of the 120 aa unfolded protein and the resulting tendency to precipitate once the tag is removed explains for the fact why untagged stargazin$^{203-323}$ has so far not been used before for biochemical, biophysical or structural experiments. Expression of a His$_6$-tagged stargazin C-terminal tail did not yield any over-expression (Figure 3.40), and fusion of stargazin$^{203-323}$ to GB-1 as solubility-enhancement tag (SET) increased the over-expression and solubility drastically, which has been reported for several proteins that were insoluble when expressed with a His-tag alone [368, 412-416]. The B1 domain of protein G used in this thesis has been widely used in order to increase protein over-expression and solubility [307, 368, 412, 417-419].

Aiming for untagged stargazin and due to the unfolded nature of stargazin$^{203\text{-}323}$ and the resulting low solubility, several protocol optimization steps were required in the framework of this project in order to obtain homogenous protein.

Because bacterial growth and therefore also protein over-expression were rather low, higher protein yields were achieved by growing the cells in more rich TB medium instead of LB medium and expression was best at 37°C. The untagged protein tended to be very sticky and precipitated at higher concentrations. A combination of ion exchange/size exclusion chromatography and denaturation of remaining impurities using urea (in case of ^{15}N-labeled protein) yielded 3.7 mg per liter of bacterial culture (Figure 3.43).

Having established an optimized strategy for purification of untagged complete stargazin C-terminal tail, the pure protein could be used for downstream applications like NMR without the need to detect stargazin$^{203\text{-}323}$ from impure sample via antibodies, which it is the case for various published studies on stargazin C-terminal tail. Out of the two major tested constructs, only the C-terminally tagged stargazin$^{203\text{-}323}$ (C_GB-1) construct was useful because the N-terminally tagged stargazin$^{203\text{-}323}$ construct (N_GB-1) was subjected to degradation, resulting in a smaller protein that could not be phosphorylated (Figure 3.41 and Figure 3.42).

4.2.2 Stargazin$^{203\text{-}323}$ is an intrinsically disordered protein (IDP)

The C-terminal domain of stargazin comprises 120 residues, which are predicted to be largely unfolded (Figure 3.40) [339, 340]. CD spectroscopic data of stargazin C-terminal tail revealed that the protein is largely unfolded (Figure 3.44). This result was also confirmed by NMR spectroscopic measurements performed in this thesis, because the NMR signals are condensed in an area between 7.9 and 8.6 p.p.m., typical for intrinsically disordered proteins (see Figure 3.57 and Figure 3.58). While the degree and domain extent of intrinsically disordered protein parts can vary extremely, it has been estimated that 68% of all proteins deposited in the PDB have unfolded parts [420]. I could also show that phosphorylation of the nine phosphorylatable Ser residues within the C-terminal tail of stargazin does neither lead to structural rearrangements of the protein nor to an increase of structural elements. Roberts and colleagues showed that stargazin C-terminal tail likely adopts a more folded conformation when interacting with lipids as shown by CD spectroscopic measurements and electron crystallographic reconstructions at ~20 Å [258]. Partial structuring of stargazin C-terminal tail upon lipid binding has not been deduced from previous studies and needs to be further investigated. Unstructured proteins are often involved in regulatory or signaling interactions with binding partners that require low affinity and high specificity [421, 422]. This holds true for stargazin C-terminal tail as well, which interacts with PDZ-containing scaffolding proteins like PSD-95, SAP-97, PSD-93, SAP-102, membrane associated guanylate kinase, WW and PDZ domain containing 2/synaptic scaffolding molecule (MAGI-2/S-SCAM) and microtubule-associated protein 1 light chain 2 (MAP1A LC2) [240, 243, 247, 259, 423]. Apart from scaffolding proteins, stargazin C-terminal tail (stargazin$^{262\text{-}282}$) has been found to interact with nPIST in order to promote AMPAR synaptic targeting [241].

The activity-regulated cytoskeleton-associated protein (Arc) has been shown to be a further stargazin interaction partner, leading to downregulation of synaptic AMPARs [424]. In case of the TARP isoform γ-8, a second interaction partner for the long C-terminal tail could be identified apart from PSD-95, the phosphatase calcineurin/PP2B, and the complex might regulate AMPAR phosphorylation and trafficking via direct association [411]. A possible role for stargazin$^{203\text{-}323}$ dephosphorylation by calcineurin/PP2B and PP1 has been proposed previously but need to be further examined, as experimental data did not show any co-immunoprecipitation of stargazin with calcineurin [251, 411].

One study postulated distinct dephosphorylations of stargazin and γ-8 as evaluated indirectly by using different phosphatase inhibitors. According to their data, γ-2 is dephosphorylated by PP1 and PP2B, while γ-8 is dephosphorylated by PP1 and PP2A [215]. It remains to be seen if there are additional scaffolding proteins or interacting partners of stargazin cytosolic C-terminal tail that might play a role in synaptic targeting of stargazin and AMPARs and how the phosphatases decrease synaptic strength.

4.2.3 Recombinantly over-expressed and purified stargazin$^{203\text{-}323}$ is monomeric in solution

MALS data obtained from stargazin$^{203\text{-}323}$ suggest that the cytoplasmatic C-terminal domain of stargazin is monomeric in solution (Figure 3.45 and Figure 3.55). There is no other biophysical or biochemical data available so far on the isolated, untagged C-terminal domain of stargazin. However, full-length stargazin has been investigated in several studies. Crystallographic electron microscopy and fluorescence resonance energy transfer (FRET) data with full-length stargazin indicated that stargazin forms a dimer in solution upon self-assembly which can disassemble upon interaction with AMPARs [228, 258, 425]. The function and reason of stargazin self-assembly, however, remains unknown.

Because no oligomerization could be observed when using the C-terminal domain of stargazin, it seems likely that other domains than the stargazin C-terminus are responsible for dimerization.

Also, several publications including a recent single particle cryo-electron microscopy study investigated the stoichiometry of the AMPAR/TARP interaction and showed that four TARP molecules can interact with the AMPAR tetramer [202], however, depending on the TARP expression level, less is possible [89]. And different studies showed that one TARP was sufficient to modulate AMPAR activity and that TARPs have a fixed stoichiometry in neuronal cells [221, 222]. Interestingly, in a different study it has been shown that the increase in kainate efficacy depends on the number of TAPR molecules associated with an AMPAR complex [220]. Notably, as AMPAR tetramers can assemble with a variety of auxiliary proteins, the number of TARPs assembling with heterotetrameric AMPARs can be less than four [87]. Remaining questions concerning the AMPA-TARP assembly will need to be answered in the future, including the question of the structural basis of different effects elicited by distinct TARP isoforms.

4.2.4 Stargazin$^{203\text{-}323}$ electrostatically binds to negatively charged liposomes

An important feature of stargazin cytoplasmatic C-terminal tail is its ability to interact with the lipid bilayer as long as it is non-phosphorylated, moving the C-terminus out of reach for interaction with PDZ domains. An electron crystallographic analysis of full-length *mm*Stargazin revealed that the C-terminus is 100 Å away from the transmembrane domain when bound to liposomes. However, the reconstruction was of low resolution and the stargazin dimers were packed antiparallel [258]. Also, artificial lengthening of the C-terminal tail of stargazin in order to mimic phosphorylation enabled it for interaction with deeper PDZ domains, like the second and third PDZ domain [257]. Therefore, lipid interaction of stargazin C-terminal tail together with its phosphorylation is a key regulator of the stargazin:PSD-95 interaction and of AMPAR synaptic targeting.

Liposome co-sedimentation assays revealed that binding of stargazin intracellular C-terminal domain is of pure electrostatic nature. We could show that stargazin C-terminal tail binds to FOLCH liposomes composed of cow brain lipids (containing negatively charged lipids like phosphatidylserine) as well as to negatively charged liposomes (Figure 3.47 and Figure 3.48). Stargazin C-terminal tail binds to anionic liposomes (PA and PIP$_2$)

with the highest intensity, followed by polar liposomes (PG and PS), whereas no binding could be observed for neutrally charged liposomes (PE and PC).

The mammalian brain is composed of 16% PS based on the total amount of phospholipids [426]. In liposome co-sedimentation assays performed with polar liposomes in this thesis, a PS concentration of 10% was used (as a 9:1 mixture of PC/PS), mimicking the native lipid bilayer composition.

In order to achieve electrostatic binding of stargazin$^{203\text{-}323}$ to negatively charged lipids, the salt concentration must be kept as low as possible. Increasing the salt concentration from 75 mM NaCl to 150 mM NaCl abolished the ability of stargazin$^{203\text{-}323}$ to interact with negatively charged liposomes (data not shown). Roberts et al. also showed that increasing the salt concentration (from 50 to 500 mM NaCl) resulted in crystals with no stargazin tail density indicating that high salt abolishes the binding of stargazin C-terminal tail to lipids [258].

In order to mimic the situation of the intracellular ion species and to unravel the dependence of the interaction on the ionic strength, KCl instead of NaCl could be used in future experiments.

The results presented in this thesis are in agreement with two previous publications. Using Trx-tagged stargazin$^{203\text{-}323}$ and a slightly different approach for liposome co-sedimentation combined with western blotting, Sumioka et al. could also find a preference of stargazin C-terminal tail for negatively charged liposomes [256]. Also for electron microscopy of full-length *mm*Stargazin$^{203\text{-}323}$, the quality of two dimensional crystallization depend on the presence of negatively charged lipids [258].

Due to the unfolded nature of the C-terminal tail of stargazin and the resulting low solubility and tendency to precipitate, a tagged version of stargazin cytoplasmatic C-terminal tail has been previously used in other studies. Detection of the tagged protein was carried out by western blotting. Such a tag must influence the availability of some parts of the tail by sequestering it. If it had no interactions, it would not function to increase solubility. Instead, in this thesis untagged protein was visualized by Coomassie-staining indicating its high purity.

The minimal necessary intensity of negative charge within the lipid bilayer to allow binding of stargazin$^{203\text{-}323}$ remains elusive and could be investigated by stepwise decreasing the anionic lipid concentration in the assay. In mammalian cells, a PIP_2 concentration of 10 µM is assumed [427]. The lipid composition itself could also affect TARP/MAGUK interaction because the lipid composition of the lipid bilayer membrane is regulated by enzymes [428]. Future experiments could elucidate the importance of the lipid composition for stargazin$^{203\text{-}323}$ binding to the membranes as the membrane composition varies for cell types.

4.2.5 Stargazin$^{203\text{-}323}$ phosphorylation is a key modulator of AMPAR mobility.

Phosphorylation is the most abundant posttranslational modification important to modulate eukaryotic signaling processes and can occur on mostly Ser, Thr and Tyr residues, hence with different ratios (in vertebrates a ratio of 90:10:0.05 for Ser:Thr:Tyr residues was determined [429]) [430].

The 120 residue long cytoplasmatic C-terminal domain of stargazin contains 19 Ser and 13 Thr residues. Out of these 32 potentially phosphorylatable residues it has been shown that 9 Ser residues within the C-terminal tail of stargazin and one Thr residue (Thr321) within the PDZ-binding motif of stargazin are phosphorylated by cyclic adenosine monophosphate (cAMP)-dependent protein kinase PKA, CaMKII, mitogen-activated protein kinase (MAPK) and PKC, respectively [215, 251, 259, 260, 262]. While phosphorylation at Thr321 disrupts interaction and clustering with PSD-95 because it interferes with PDZ binding [240, 261], phosphorylation at Ser residues within the cytoplasmatic C-terminal domain of stargazin is mandatory to allow binding to PSD-95 because phosphorylation of stargazin$^{203\text{-}323}$ leads to dissociation of the C-terminal tail from the lipid bilayer [256]. The first evidence of stargazin$^{203\text{-}323}$ phosphorylation came from the observation that diffuse stargazin bands from brain extracts shifted to lower molecular weights on western blots after λ-phosphatase treatment [251]. The co-existence of T321 which prevents stargazin C-terminal tail from binding to PSD-95 in its phosphorylated form and of the nine Ser residues within stargazin C-terminal tail that need to be phosphorylated in order to allow binding to PSD-95 illustrates how phosphorylation of stargazin intracellular C-terminal domain complexly modulates interaction with PSD-95 and thereby regulates AMPAR synaptic targeting.

The ability of stargazin intracellular C-terminal tail to get phosphorylated renders it a key modulator of AMPAR synaptic trafficking. Phosphorylation of the stargazin C-terminal tail leads to its dissociation from the lipid bilayer (Figure 3.50), thereby making it available for binding to PDS-95. The direct and tunable interaction (through phosphorylation of stargazin C-terminal tail) between stargazin and PSD-95 leads to immobilization and clustering of TARP-interacting AMPARs at the synapse, a mechanism, which has been implicated in regulation of synaptic plasticity and mechanisms of learning and memory [244, 431-433].

Whereas phosphorylation sites within stargazin$^{203-323}$ have been mapped in several publications, especially the mechanism for Ser multisite phosphorylation remains an open question. Using a combination of directly and indirectly monitored phosphorylation of stargazin cytosolic C-terminal tail upon incubation with CaMKII by means of NMR, MALDI-TOF/TOF or ESI-MS/MS and liposome co-sedimentation, respectively, we aimed to decipher the mechanism and kinetics of stargazin$^{203-323}$ phosphorylation. Time-resolved NMR spectroscopy will then reveal the kinetics and mechanism of phosphorylation (processive or distributive).

By using MALDI-TOF/TOF analysis and phosphorylation-driven dissociation of the stargazin C-terminal domain from liposomes I could show that addition of one phosphate group to the C-terminal tail decreases the ability of stargazin$^{203-323}$ to bind to lipids by more than 50% (Figure 3.50). The results indicate that the membrane-interaction of stargazin intracellular C-terminal domain is very sensitive to phosphorylation and that not all nine Ser residues need to be phosphorylated in order to drive stargazin$^{203-323}$ dissociation from lipids (Figure 3.50). Of course, since these results are partially based on mass spectrometric analyses, they might not reflect the true quantitative situation, since mass spectrometric analysis of protein phosphorylation, especially in the case of several adjacent phosphorylatable Ser residues, is not a high-resolution quantitative approach and might give averages instead of absolute numbers (also see Section 4.2.5.1)

4.2.5.1 Monitoring stargazin$^{203-323}$ phosphorylation using mass spectrometric approaches

The fastest and easiest way of evaluating stargazin$^{203-323}$ phosphorylation, which does not require isotope-labeling of the protein, is to detect protein or peptide mass shifts upon addition of phosphate groups. Phosphorylation will lead to a mass shift of 80 at each site [434].

Consequently in my experiments incubation of purified untagged stargazin C-terminal tail with activated CaMKII led to continuous increase of the protein mass, indicative of ongoing phosphorylation. On average, we saw that one Ser residue is phosphorylated after 2 minutes of incubation with CamKII and after 30 minutes 1-2 further phosphate groups are added according to mass spectrometric analyses (Figure 3.49). With the CaMKII amount used in this assay, complete phosphorylation could be observed after 16 h at 30°C. However, a few limitations of mass spectrometric phosphopeptide mapping have to be taken into consideration. First, the phosphate groups are rather labile and can be liberated upon protein fragmentation [435]. Second, the detectability of fragments is not the same for different fragments and phosphorylation complicate their detection. Therefore, mass spectrometric analysis of phosphorylation does not give any information on the stoichiometry or occupancy of the phosphorylation site. Third, and the most crucial, stargazin C-terminal tail gets phosphorylated at consecutive Ser residues (Figure 3.46) that cannot be proteolytically separated, which renders a quantitative phosphorylation analysis of these consecutive Ser residues challenging. Especially in the case of stargazin C-terminal tail with its adjacent multisite phosphorylations, exact identification of the site of modification becomes problematic.

Stable isotope labeling by amino acids in cell culture (SILAC) offers a possibility to quantitatively measure phosphorylation, however, this method is limited by the high media costs together with the necessity to establish protein production in cells [436-439].

Considering all the above-mentioned limitations, it has to be ruled out that the mass spectrometric analyses of stargazin$^{203\text{-}323}$ phosphorylation are not truly quantitative. However, they were informative in terms of testing the ability of the purified stargazin C-terminal tail to get phosphorylated by CaMKII. Notably, getting a rough idea how phosphorylation occurs on stargazin C-terminal tail together with liposome co-sedimentation helped us to understand the importance of stargazin$^{203\text{-}323}$ phosphorylation for synaptic clustering of AMPARs.

By using the complete stargazin C-terminal tail rather than short peptides for phosphorylation studies, we circumvent the possibility to lose the sequence context that might be important for protein phosphorylation and thereby reduce the danger of obtaining biased phosphorylation rates.

Also, if the kinase needs further docking sites for its specificity, these sites might get lost in peptide-based assays [440].

4.2.5.2 Monitoring phosphorylation of stargazin$^{203\text{-}323}$ indirectly using liposome co-sedimentation

As described previously, phosphorylation of stargazin cytoplasmatic C-terminal domain is an important mechanism for regulation of synaptic targeting of AMPA-TARP complexes. Having evaluated stargazin$^{203\text{-}323}$ phosphorylation with mass spectrometry, we aimed to investigate the phosphorylation-dependence of the liposome interaction. Two major conclusions could be made from liposome-binding: First, stargazin C-terminal tail electrostatically binds to anionic lipids via its basic stretch (Figure 3.46), and second, this pure electrostatic interaction depends on the environmental electrostatics (Figure 3.50).

Using a phospho-mimic mutant with all nine Ser residues mutated to Asp (S9D), it could be shown that binding to liposomes is completely abolished [256].

In this work, a more physiological approach was taken. The effect of stargazin$^{203\text{-}323}$ phosphorylation on protein-lipid interaction was investigated using activated CaMKII rather than static phospho-mimic mutants. As the interplay and fine-tuning of stargazin C-terminal tail interactions with the membrane, phosphorylation and PSD-95-interaction is unknown to date, we aimed to investigate gradual dissociation of stargazin C-terminal tail upon phosphorylation.

Whereas nearly 100% of the protein is bound to liposomes (FOLCH liposomes) in its non-phosphorylated form, fast dissociation of stargazin$^{203\text{-}323}$ from liposomes can be observed with ongoing phosphorylation. After 2 min of phosphorylation, liposome-binding is decreased by nearly 60%. According to mass spectrometric analysis, a 2 min incubation of stargazin$^{203\text{-}323}$ with CaMKII leads to phosphorylation of one Ser residue. Incorporation of one phosphate group into the C-terminal tail of stargazin and thus, partial neutralization of the basic Arg stretch (Figure 4.2 B and C) is sufficient to reduce its ability to bind to negatively charged lipids to 40%. A further decrease of liposome-binding could be observed with longer CaMKII incubation. After 16 h incubation with CaMKII, less than 10% of stargazin$^{203\text{-}323}$ bind to liposomes (Figure 3.50).

It was previously assumed that dissociation requires full phosphorylation of stargazin C-terminal tail – even though this was not measured. These results show how sensitive stargazin intracellular C-terminal tail is towards phosphorylation and how strictly stargazin-lipid interaction is regulated.

By using activated CaMKII for phosphorylation of stargazin cytoplasmatic C-terminal tail instead of a phospho-mimic mutant we were able to visualize gradual dissociation of stargazin$^{203\text{-}323}$ from lipids with ongoing phosphorylation and these results are unbiased compared to the usage of phospho-mimic mutants. Phospho-mimic mutants have been shown to not necessarily give the same effects as phosphorylated sidechains [441].

The importance of lipid binding (via stargazin Arg stretch) and Ser phosphorylation is underlined by the sequence conservation of this amino acid stretch among TARPs. Figure 4.2 C shows a sequence alignment of all TARP I class proteins and shows how conserved the phosphorylatable Ser residues and the Arg residues implicated in membrane-binding are among the TARP I class. The eight Arg residues have been shown to be sufficient to mediate lipid-interaction [256]. The conserved Arg/Ser stretch is a perfect substrate for CaMKII and PKC because both kinases preferentially phosphorylate Ser residues in basic environment [442].

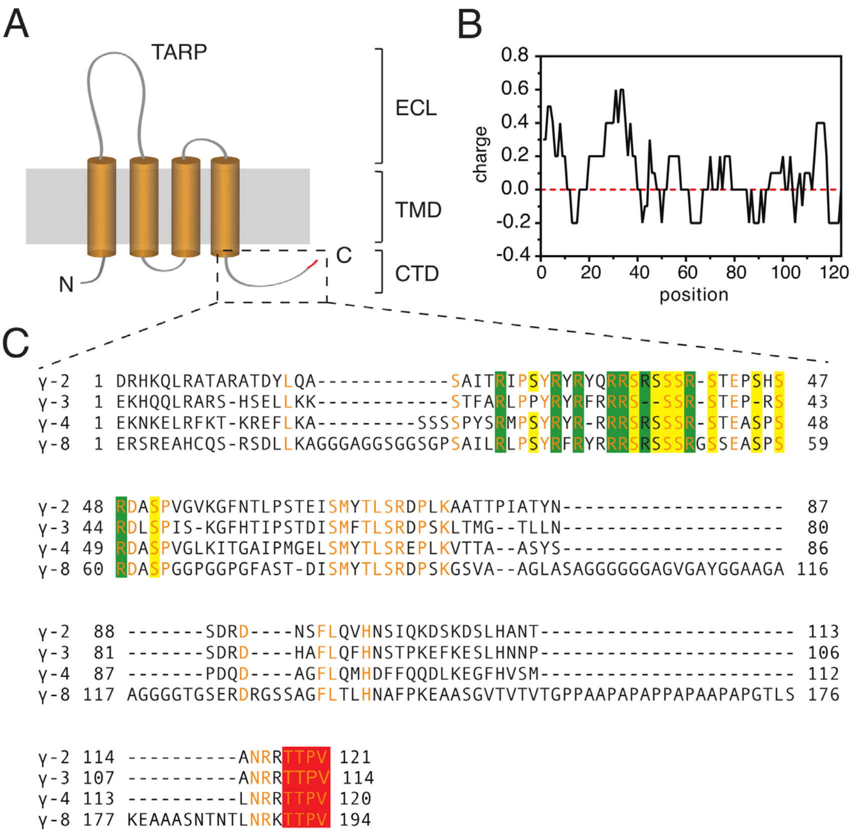

```
γ-2   1 DRHKQLRATARATDYLQA------------SAITRIPSYRYRYQRRSRSSSR-STEPSHS  47
γ-3   1 EKHQQLRARS-HSELLKK------------STFARLPPYRYRFRRRS--SSR-STEP-RS  43
γ-4   1 EKNKELRFKT-KREFLKA---------SSSSPYSRMPSYRYR-RRRSRSSSR-STEASPS  48
γ-8   1 ERSREAHCQS-RSDLLKAGGGAGGSGGSGPSAILRLPSYRFRYRRRSRSSSRGSSEASPS  59

γ-2 48 RDASPVGVKGFNTLPSTEISMYTLSRDPLKAATTPIATYN--------------------  87
γ-3 44 RDLSPIS-KGFHTIPSTDISMFTLSRDPSKLTMG--TLLN--------------------  80
γ-4 49 RDASPVGLKITGAIPMGELSMYTLSREPLKVTTA--ASYS--------------------  86
γ-8 60 RDASPGGPGGPGFAST-DISMYTLSRDPSKGSVA--AGLASAGGGGGGAGVGAYGGAAGA 116

γ-2  88 -------SDRD----NSFLQVHNSIQKDSKDSLHANT----------------------- 113
γ-3  81 -------SDRD----HAFLQFHNSTPKEFKESLHNNP----------------------- 106
γ-4  87 -------PDQD----AGFLQMHDFFQQDLKEGFHVSM----------------------- 112
γ-8 117 AGGGGTGSERDRGSSAGFLTLHNAFPKEAASGVTVTVTGPPAAPAPAPPAPAAPAPGTLS 176

γ-2 114 ----------ANRRTTPV 121
γ-3 107 ----------ANRRTTPV  114
γ-4 113 ----------LNRRTTPV 120
γ-8 177 KEAAASNTNTLNRKTTPV 194
```

Figure 4.2: The basic C-terminal tail of stargazin is able to electrostatically bind to negatively charged liposomes in a phosphorylation-dependent manner. (A) Schematic representation of the domain organization of TARPs. The transmembrane regions are depicted as orange cylinders, loops connecting the transmembrane domains are shown as grey lines. The lipid bilayer is indicated by a grey area. Intracellular TARP N- and C-termini are labeled. The PDZ binding motif (residues TTPV) within stargazin C-terminus is colored in red. Domain organization is indicated on the right as well. ECL – extracellular loop, TMD – transmembrane domain, CTD – C-terminal domain. **(B)** Calculation of protein charge for individual amino acids. The residual charge was calculated using EMBOSS:charge and the charge was plotted against the amino acid sequence of stargazin C-terminal tail purified from C-terminally tagged protein (C_GB-1). **(C)** Sequence alignment of TARP γ-2 (stargazin) (at the top) and other class I TARPs (γ-3, γ-4 and γ-8) showing the conserved phosphorylation region together with the basic stretch important for membrane-interaction. Phosphorylatable Ser residues and Arg residues important for liposome interaction are highlighted in yellow and green, respectively. Orange letters indicate fully conserved residues among class I TARPs. The PDZ binding motif (residues TTPV) is conserved in all four TARP isoforms. The sequence alignment was performed using ClustalW [301-303].

Phosphorylation-dependent competitive protein-protein and protein-membrane interaction has been described for myristoylated alanine-rich C kinase substrate (MACK) proteins. Similar to stargazin C-terminal tail, MACK is a substrate for PKC and binds to membranes in its non-phosphorylated state via a highly basic domain. MACK phosphorylation leads to its dissociation from the membrane as the positive charge is neutralized by the phosphate groups and the myristate alone by which it is also anchored to the membrane is not sufficient for stable membrane binding [427, 443], showing that phosphorylation is used in other cases as well to modulate the lipid interaction of a protein and to allow the protein to fulfill its function, in our case, the anchoring of AMPAR-TARP complexes at the PSD.

Based on the results obtained in this thesis and combined with previous knowledge, a mechanism for TARP-mediated regulation of AMPAR synaptic targeting by modulating its number at the PSD can be proposed (Figure 4.3). Phosphorylation of stargazin$^{203\text{-}323}$ is a key step in regulating AMPAR immobilization and clustering at the PSD and therefore is a crucial step for synaptic strengthening also implicated in LTP. Synaptic trafficking of AMPARs and increasing the number of AMPARs at the PSD are believed to be an important postsynaptic mechanism of LTP [33, 444-446]. Using a combination of mass spectrometry and protein-lipid interaction assay, it could be shown that the stargazin-membrane interaction seems to be very sensitive to phosphorylation. Based on the data obtained in this work, one can conclude that phosphorylation of a few Ser residues is already sufficient to promote lipid dissociation of stargazin C-terminal tail. Stargazin does not need to be fully phosphorylated in order to dissociate from the lipid bilayer. The density of phosphorylation may allow the C-terminal domain of stargazin to act as a molecular regulator and enable it for a graded response to different kinase and phosphatase levels. Hafner et al. showed that artificially lengthening stargazin cytoplasmatic tail enables it to interact with not only the first two PDZ domains but also with the third PDZ domain of PSD-95, with highest affinity for the second PDZ domain [257]. And so, dependent on the extent of phosphorylation, stargazin C-terminal domain might interact with different PDZ domains with different distances from the membrane.

Observation of phosphorylation-dependent liposome-dissociation and phosphorylation-driven PSD-95 interaction using NMR will give atomic resolution of the time course of phosphorylation and consequences of each phosphorylated Ser residue and will be a major goal for future experiments. In the framework of this thesis, isolated PDZ domains from human PSD-95 have also been purified. However, binding studies between stargazin$^{203\text{-}323}$ (C_GB-1) and PDZ domains could not be performed because of the missing free C-terminus that is required for PDZ interaction [261]. As the protein was C-terminally tagged, after cleavage, the PDZ binding motif of stargazin C-terminal tail is masked by residual amino acids of the cleavage site. The N-terminally tagged stargazin$^{203\text{-}323}$ construct (N_GB-1) did not yield sufficient protein amounts to perform binding studies and more important, was subject to degradation.

One study tried to unravel the connection between membrane-binding of stargazin C-terminal tail, its phosphorylation (using the phospho-mimic mutant S9D) and its binding to PSD-95 by covalently fusing stargazin$^{203\text{-}323}$ to liposomes and performing sucrose gradients centrifugation [256]. They could show that binding of stargazin C-terminal tail to PSD-95 is inhibited when stargazin$^{203\text{-}323}$ binds to lipids and that stargazin$^{203\text{-}323}$ phosphorylation (S9D mutant) is required to allow binding to PSD-95 [256]. By using a phospho-mimic mutant that is supposed to mimic the fully phosphorylated C-terminal tail of stargazin, again, they only get a static view of the dependence of stargazin$^{203\text{-}323}$ phosphorylation on lipid binding and PSD-95 binding. Using this phospho-mimic mutant, it is not possible to mimic physiological conditions and graded phosphorylation. NMR experiments can help us in the future to monitor this dependence of PSD-95 binding on stargazin-membrane interaction and phosphorylation in real time, continuously and resolved on atomic level.

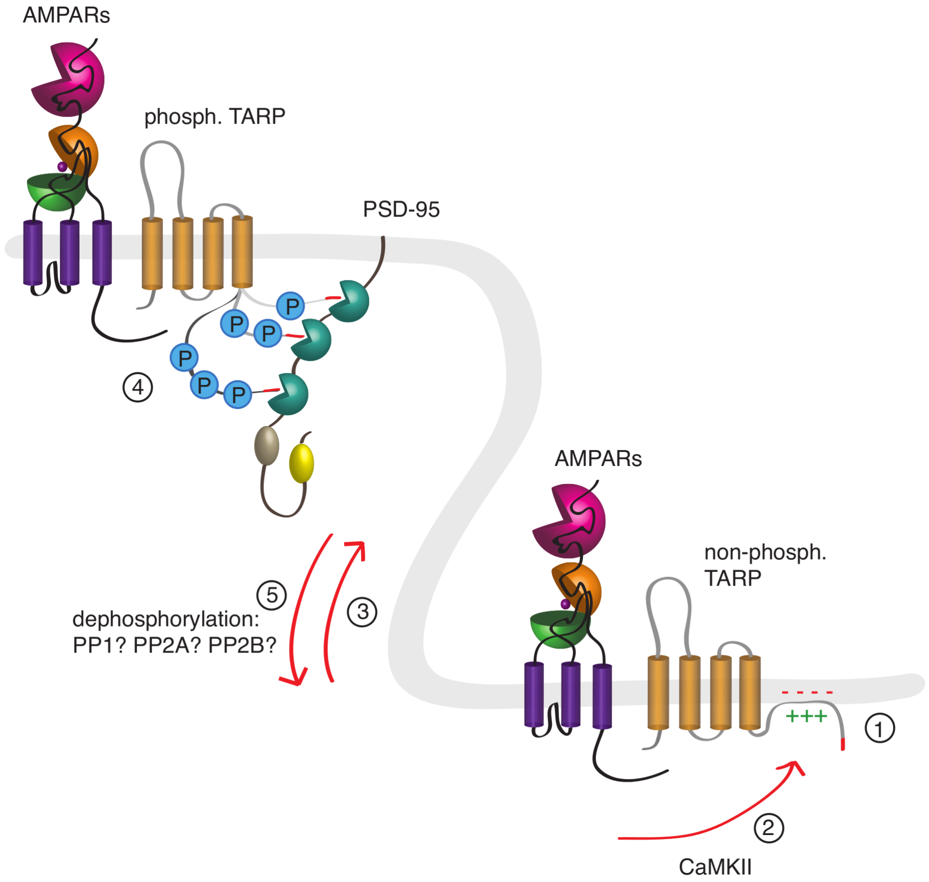

Figure 4.3: Stargazin mediates synaptic targeting of AMPARs to the PSD via its phosphorylation-dependent interaction with PSD-95. (1) Non-phosphorylated stargazin C-terminal tail electrostatically interacts with anionic lipids from the bilayer with the very C-terminus extending into the cytoplasm [257]. **(2)** Activation of NMDARs leads to Ca^{2+} influx and activation of Ca^{2+}/CaM dependent kinase CaMKII, for which stargazin C-terminal domain is a substrate. Phosphorylation of stargazin C-terminal tail neutralizes the positive charge of the protein, leading to dissociation of stargazin$^{203\text{-}323}$ from the lipid bilayer. Unbinding of stargazin's Arg-rich stretch from the membrane increases the "effective" length of stargazin C-terminal tail, enabling it to interact with PSD-95. According to liposome co-sedimentation assays, phosphorylation of a few (if not one) Ser residues is sufficient to promote stargazin$^{203\text{-}323}$ dissociation from lipids. **(3+4)** Mobile AMPAR/TARP complexes diffuse in the PSD and are anchored at the PSD via direct TARP/PSD-95 interaction. In agreement with [257], proceeding phosphorylation may enable stargazin$^{203\text{-}323}$ to interact with deeper PDZ domains. Multiple phosphorylations may enable stargazin C-terminal tail to interact with the farthest PDZ domain, whereas single phosphorylation may lead to interaction of stargazin C-terminal tail with the first PDZ domain. Stargazin is regulated bidirectionally through phosphorylation and dephosphorylation **(5)**.

Lipid binding of stargazin C-terminal tail does seem to be a critical modulator of synaptic strength by regulating AMPAR/TARP clustering at the PSD in a phosphorylation-dependent manner. Graded phosphorylation of stargazin$^{203-323}$ might also gradually regulate interaction with the PSD-95 PDZ domains, as the PDZ domains of the palmitoylated PSD-95 [246, 447, 448] are supposed to be oriented perpendicular to the membrane [55, 449, 450]. Opposite to previous mentioned data, also a C-shaped circular conformation of PSD-95 has been proposed [451, 452]. In order to reach the PDZ domains, stargazin C-terminal tail obligatorily has to dissociate from the membrane to reach deep into the PSD. The intracellular C-terminal domain of stargazin has been shown to bind to the first and/or to the second PDZ domain of PSD-95 [246, 432] with multiple stargazin C-termini being able to bind to different PDZ domains [453-456]. Another study revealed that non-phosphorylated stargazin C-terminal tail preferably binds to the first PDZ domain, whereas the phosphomimic mutant preferably binds to the third PDZ domain (as measured by fluorescence polarization assay) [257]. According to their results, lipid dissociation of stargazin C-terminal tail allows for tighter binding of PDZ domains that reach deeper into the cytoplasm, thereby leading to immobilization of AMPA/TARP complexes at the PSD. If this is the case, different degrees of stargazing phosphorylation could lead to graded synaptic anchoring of AMPARs due to the interaction with different PDZ domains with varying affinities (also see Figure 4.3).

Investigating other scaffolding proteins than PSD-95 is also of high interest. PSD-95 mutant mice lacking any PSD-95 still have intact synaptic AMPARs suggesting that clustering of AMPARs at the postsynapse can be regulated by other scaffolding proteins such as SAP102, which is functionally similar to PSD-95 [457].

Besides phosphorylation and dephosphorylation of stargazin C-terminal Ser residue [215], there are additional regulatory mechanisms to modulate the interaction between TARPs and PSD-95 and thereby regulate AMPAR anchoring at the PSD. First, it has been shown that the C-terminal domain of stargazin but not γ-8 can be proteolytically cleaved by the Ca^{2+}-dependent protease calpain and therefore offers a possibility to permanently disrupt stargazin-PSD-95 interaction. Second, the cysteine residue within stargazin C-terminal domain (Cys302) can be nitrosylated leading to an increased binding of stargazin to AMPARs and an increased AMPAR surface delivery caused by the cross-talk with the nitric oxid signaling [458]. Third, PSD-95 palmitoylation is important for its function as it anchors the scaffolding protein at the membrane and inhibition of PSD-95 palmitoylation in neurons was associated with a loss of synaptic AMPARs [459]. The modulation of PSD-95 palmitoylation therefore also represents a mechanism to regulate synaptic strength [246]. And as mentioned in Section 1.2.4.4, phosphorylation of stargazin C-terminal residue Thr321 within the PDZ binding motif disrupts the binding of stargazin$^{203-323}$ to PSD-95 [259, 260] representing a further mechanism to regulate the TARP-PSD-95 interaction.

4.2.5.3 Monitoring phosphorylation of stargazin$^{203-323}$ directly using NMR spectroscopy

Because mass spectrometric analysis of protein phosphorylation is not quantitative, NMR spectroscopic measurements of protein phosphorylation were carried out to get a precise, atomic detail view on stargazin$^{203-323}$ phosphorylation.

Recording 2D NMR spectra requires production of ^{15}N-labeled stargazin$^{203-323}$ protein, which proved to be challenging in terms of purity of the final protein. However, using a combination of charge-based purification and denaturation of impurities, pure recombinantly over-expressed protein could be obtained (Figure 3.53) that contained a mixture of differently ^{15}N-labeled stargazin C-terminal tail, because the medium was switched to M9 containing $^{15}NH_4Cl$ for expression only (Figure 3.54 B). For the determination of phosphorylation kinetics the actual effective NMR concentration can be calculated and taken into account [460]. MALS and liposome co-sedimentation assay showed that the protein biochemically and biophysically behaves similarly to ^{14}N-labeled protein (Figure 3.55). It retains its ability to bind to liposomes and this binding can be inhibited by phosphorylation of stargazin cytoplasmatic C-terminal tail (Figure 3.56).

We were able to record the first 2D ^{1}H-^{15}N NMR spectrum of stargazin C-terminal tail (Figure 3.58) and were able to overcome problems such as low protein solubility, protein precipitation and aggregation of the untagged protein.

In contrast, purified stargazin C-terminal tail from N-terminally tagged protein construct (N_GB-1) yielded protein that could not be phosphorylated (Figure 3.52 and Figure 3.57). Furthermore, it was presumably subjected to C-terminal degradation, indicating how instable the C-terminal tail of stargazin is (Figure 3.52).

The NMR spectrum of stargazin$^{203-323}$ purified from C-terminally tagged protein in Figure 3.58 shows that with the CaMKII concentration used throughout all assays, phosphorylation seems to be nearly complete after 45 minutes at 20°C. The number of signals arising from stargazin C-terminal intracellular domain also suggests that the C-terminal tail is intact and that no degradation has occurred.

This is different from the results obtained from mass spectrometry that suggested complete phosphorylation after 16 h. As mass spectrometry is not truly quantitative and only gives average mass shifts, it is not as accurate as NMR spectrometric-based analysis of phosphorylation. Using a much lower CaMKII amount in future experiments will reveal the time-course of multiple phosphorylations and together with amino acid assignment, the precise mechanism for phosphorylation of each Ser residue together with its kinetics can be deciphered.

Assignment of single residue phosphorylation events could not be performed at this stage, as amino acid assignment requires protein triple labeling (^{1}H, ^{13}C and ^{15}N).

Because NMR spectroscopy is a method with atomic resolution, adjacent phosphorylation sites (that are present in stargazin C-terminal tail, see Figure 3.46) can be determined and distinguished, being a great advantage over mass spectrometric determination of phosphorylation sites. NMR is furthermore nondisruptive, enabling for time-resolved approaches.

Real-time measurement of stargazin$^{203\text{-}323}$ phosphorylation will reveal the mechanism of multisite phosphorylation of stargazin C-terminal tail and show if graded phosphorylation of stargazin$^{203\text{-}323}$ evokes a switch-like ultrasensitive response as observed for MAPK or Cdk1 or if phosphorylation follows Michealis-Menten kinetics with a hyperbolic stimulus response [461-463]. Whether or not phosphorylation on stargazin C-terminal tail occurs randomly or in a defined order and whether or not each phosphorylation site is phosphorylated independently of the other, will be revealed by NMR spectroscopic measurements.

5 OUTLOOK

The structure of isolated LBDs presented in this thesis represents a tetrameric LBD arrangement with all four ligand-binding domains bound to glutamate. The electrophysiological recordings as well as the computational modeling suggests that the LBD tight tetrameric arrangement seen in the GluA2 WT and TR LBD structures is attained during activation of the receptor, however, it does not represent a fully active state.

Capturing the receptor in all functional states will be important to completely understand the gating mechanisms of glutamate receptors, the complex LBD movements ligand-binding will cause and how the receptor enters into the desensitized state with a closed ion channel but with the ligand bound. The homologous shaker K+ channel has been captured in an open channel conformation and transplantation of shaker transmembrane domain portions could help to capture an open ion channel pore of an AMPA receptor [464, 465].

A desensitized structure has been reported in recent crystal and cryo-EM structures and the key features of this desensitized structure is a separation of the LBDs from two-fold symmetry to four-fold symmetry, thereby matching the symmetry of the ion channel domain. In this structure, however, the transmembrane domain is not resolved and functional data to provide evidence for physiological relevance of their arrangement is missing [40]. The observed movements of the ATDs upon receptor desensitization are controversial and have to be evaluated in future experiments. In kainate receptors, desensitization has been shown to involve a 120° rotation of two LBD subunits.

The majority of the structural data on AMPA receptors has been obtained from homomeric receptors, however, in a recent study, Herguedas et al. reported the structure of a GluA2/A3 heteromer obtained by cryo-EM, showing distinct features compared to homomeric structures: a vertical compression of the extracellular domains by 21° compared to the GluA2 homomer and a new ATD arrangement, suggesting allosteric coupling between the ATD and the LBD as seen for NMDARs [19]. It remains to be shown, if further heteromeric structures will reveal a similar architecture of glutamate receptor heteromers.

Another important future research area is to structurally understand how receptor activation by lower glutamate concentrations leads to subconductance states [155].

As TARPs are the key modulator of AMPAR function, it is crucial to understand the mechanisms by which they exert their regulating properties.

Getting a high-resolution structure of an active receptor-TARP assembly will give insights into the binding mode of auxiliary proteins like stargazin which have been suggested to bind to the lower lobe of the LBD via their first extracellular loop [226].
Different functions of TARPs have already been ascribed to distinct domains of stargazin and so it is now well established that stargazin C-terminal tail is important for synaptic targeting of AMPARs as well as synaptic clustering of the receptors through their interaction with scaffolding proteins like PSD-95.

Understanding how phosphorylation of stargazin C-terminal tail affects the lipid and PSD-95 interaction in space and time will unravel the complex mechanisms by which synaptic plasticity is regulated. Future experiments will show how many TARP phosphorylation sites are required to upregulate synaptic AMPAR activity. This could be realized by using a combination of electrophysiology and high-resolution in-cell NMR with cells expressing both stargazin and AMPARs and artificially added CaMKII.

This study has shown that it is possible to prepare untagged and unfolded stargazin C-terminal tail by means of recombinant protein over-expression. Using recombinantly over-expressed CaMKII, purified stargazin C-terminal tail could be quantitatively phosphorylated as already described earlier.
However, the reason for the co-existence of multiple Ser phosphorylation sites within the disordered C-terminal tail is unclear. Future experiments using NMR spectroscopy to monitor stargazin$^{203\text{-}323}$ in real-time will unravel the kinetics and extent of stargazin$^{203\text{-}323}$ phosphorylation and show if the phosphorylatable Ser residues are all equal or if we can distinguish between slow, intermediate and fast phosphorylation sites. If the phosphorylation sites are not equal, it will be important to decipher the functional significance.

Also the interplay and time-course of phosphorylation and dephosphorylation is not clear yet. By using inhibitors for the different phosphatases it has been proposed that PP1 and PP2B might act as phosphatases on stargazin$^{203\text{-}323}$. A direct action of either phosphatase needs to be evaluated in future experiments. Also a site preference for phosphatases could be unraveled in time-resolved NMR experiments.
Once the complete stargazin C-terminal domain is assigned from NMR correlation spectra, the interplay between lipid-interaction of stargazin C-terminal tail, phosphorylation by CaMKII and PSD-95 or nPIST interaction could be investigated using real-time NMR. The scaffolding protein nPIST has been shown to bind to the C-tail of stargazin without requiring a free C-terminus, which would enable us to perform these

experiments with stargazin$^{203\text{-}323}$ purified from C-terminally tagged protein (C_GB-1) [241]. Using high-resolution NMR spectroscopy and using the C-terminal domain of stargazin together with liposomes and a scaffolding protein like nPIST could reveal the dependence of these interactions on stargazin phosphorylation.

APPENDIX

A LIST OF ABBREVIATIONS

Å	Angstrom (1 Å= 0.1 nm)
aa	amino acid
ABP	AMPA receptor binding protein
ACBD	*trans*-1-aminocyclobutane-1,3-dicarboxylic acid
ACPC	1-aminocyclopropane-1-carboxylic acid
Amp	ampicillin
AMPA	α-amino-3-hydroxy-5-methyl-4-isoxazole propionic acid
AMPAR	AMPA receptor
Arc	activity-regulated cytoskeleton-associated protein
ATD	amino-terminal domain
ATP	adenosine triphosphate
AU	arbitrary units
a.u.	asymmetric unit
BESSY	Berliner Elektronenspeicherring für Synchrotronstrahlung
bp	base pair
Cα	C alpha atom
CA	closed angle
CaM	calmodulin
Cam	chloramphenicol
CaMK II	$Ca^{2+/}$calmodulin-dependent protein kinase II
cAMP	cyclic adenosine monophosphate
CBVS	calcium bond-valence sum
CCP4	Collaborative Computational Project Number 4
CD	circular dichroism
cDNA	complementary deoxyribonucleic acid
CGC	cerebellar granule cell
CGN	cerebellar granule neuron
CKAMP44	cystine-knot AMPAR modulating protein 44
CLR	Cys-loop receptor
CNIH	cornichon homologs

COM	center of mass
COOT	crystallographic object-oriented toolkit
C-terminus	carboxy terminus
CTD	C-terminal domain
CTZ	cyclothiazide
CUB	complement C1r/C1s, Uegf, Bmp1
CuPhen	copper phenanthroline
CV	column volume
Da	dalton (= g/mol)
DLG	disc-large homolog
DNA	deoxyribonucleic acid
dNTP	deoxynucleotide triphosphate
DNQX	6,7-dinitroquinoxaline-2,3(1H,4H)dione
DOPA	1,2-dioleyl-*sn*-glycero-3-phosphate
DOPC	18:1 (Δ9-Cis) PC, 1,2-dioleoyl-*sn*-glycero-phosphocholine
DOPE	18:1 (Δ9-Cis) PE, 1,2-dioleyl-*sn*-glyero-3-phosphoethanolamine
DOPG	18:1 (Δ9-Cis) PG, 1,2-dioleoyl-*sn*-glycero-(1'-rac-glycerol)
DOPS	18:1 1,2-dioleyl-*sn*-glycero-3-phospho-L-serine
DTT	D,L-dithiothreitol
ECL	extracellular loop
EDTA	ethylenediaminetetraacetic acid
EM	electron microscopy
mEPSC	minitature excitatory postsynaptic current
ER	endoplasmatic reticulum
ESI	electrospray ionization
et al.	et alii (masc.), et aliae (fem.), et alia (neutr.)
EtOH	ethanol
fl	full-length
FMP	Leibnitz-Institut für Molekulare Pharmakologie Berlin-Buch
fP	final protein
FPLC	fast protein liquid chromatography
FRET	fluorescence resonance energy transfer
FT	flow through
FW	(S)-(-)-5-fluorowillardiine
GAL4	galactosidase 4

GB-1	B1-domain of *Streptococcal* protein G
GFP	green fluorescent protein
GK	guanylate kinase
Glu	glutamate
GluR	glutamate receptor
GRIP	glutamate receptor interacting protein
GSG1L	germ cell-specific gene 1-like protein
GST	glutathione S-transferase
HEK	human embryonic kidney
HEPES	4-(2-hydroxyethyl)-1-piperazineethanesulfonic acid
HMQC	heteronuclear multiple quantum correlation
HMW	high molecular weight
HW	hydrogen-willardiine
I	induced
IDP	intrinsically disordered protein
Ig	immunoglobulin-like domain
iGluR	ionotropic glutamate receptor
IMAC	immobilized metal affinity chromatography
iP	injected protein
IPTG	isopropyl-β-D-1-thiogalactopyranoside
5-IW	(S)-(-)-5-iodowillardiine
K	Kalvin
KA	kainate
Kan	kanamycin
KAR	kainate receptor
kb	kilobase
kDa	kilodalton
KFN	Koshland-Nemethy-Filmer
LAOBP	lysine, arginine, ornithine-binding protein
LB	Luria Miller
LBD	ligand-binding domain
LC	liquid chromatography
LIC	ligation-independent cloning
LMV	large multilammelar vesicle
LMW	low molecular weight

LTD	long-term depression
LTP	long-term potentiation
MACK	myristoylated alanine-rich C kinase substrate
MAGI-2	membrane-associated guanylate kinase, WW and PDZ domain containing 2
MAGUK	membrane-associated guanylate kinase
MALDI-TOF	matrix assisted laser desorption ionization-time of flight
MALS	multi-angle laser scattering
MAP1A	microtubule-associated protein 1
MAPK	mitogen-activated protein kinase
MARCK	myristoylated alanine-rich C kinase substrate
MDC	Max-Delbrück Zentrum für Molekulare Medizin
Met	methionine
β-MetOH	β-mercaptoethanol/ 2-sulfanylethanol
mGluR	metabotropic glutamate receptor
MLV	multilammelar vesicle
MPQX	[[3,4-Dihydro-7-(4-morpholinyl)-2,3-dioxo-6-(trifluoromethyl)-1(2H)-quinoxalinyl]methyl]phosphonic acid
MR	molecular replacement
mRNA	messenger ribonucleic acid
MS	mass spectrometry
MUPP1	multi-PDZ domain protein 1
MW	molecular weight
MWC	Monod-Wyman-Changeux
MWCO	molecular weight cut off
n.d.	not determined
Ni	nickel
NI	non-induced
NMDA	N-methyl-D-aspartate
NMR	nuclear magnetic resonance
NOW	(S)-5-nitrowillardiine
nPIST	neuronal isoform of protein-interacting specifically with TC10
nt	nucleotide
NTA	nitrilotriacetic acid
N-terminus	amino-terminus

OA	open angle
OD_{600}	optical density (at 600 nm)
OMP	outer membrane protein
o/n	overnight
P	pellet
PA	phosphatidic acid
PAGE	polyacrylamide gel electrophoresis
PC	phosphatidylcholine
PCR	polymerase chain reaction
PDB	protein data bank
PDB ID	protein data bank identifier
PDZ	postsynaptic density-95 (PSD-95)/disc large/zona occludens-2
PE	phosphatidylethanolamine
PEG	polyethylene glycol
PG	phosphatidylglycerol
pH	pondus Hydrogenii
Phenix	Python-based hierarchical environment for Integrated xtallography
PICK1	protein interaction with C-kinase
$PI(4,5)P_2$	phosphatidylinositol 4,5-biphosphate, 1-stearoyl-2-arachidonoyl-*sn*-glycero-3-phospho-(1’-myo-inositol-4’,5’-bisphosphate)
PIST	protein-interacting specifically with TC10
PKA	protein kinase A
PKC	protein kinase C
p.p.m.	parts per million
PS	phosphatidylserine
PSD	postsynaptic densitiy
PSD-95	postsynaptic density-95
PSP	PreScission protease
R_G	radius of gyration
RALS	right-angle light scattering
rcf	relative centrifugal force
RF	restriction-free
RGD	Rayleigh-Gans-Debye
RI	refractive index
rmsd	root mean squared deviation

RNA	ribonucleic acid
rpm	rounds per minute
SAP	synapse-associated protein
SDS	sodium dodecylsulfate
SDS-PAGE	SDS-polyacrylamide gel electrophoresis
SEC	size-exclusion chromatography
SET	solubility enhancement tag
SH3	Src homology 3
SILAC	stable isotope labeling by amino acids in cell culture
sLBD	soluble (isolated) ligand-binding domain
SLS	static light scattering
SN	supernatant
S-SCAM	synaptic scaffolding molecule
STG	stargazin
SynDIG1	synapse differentially induced gene 1
TARP	transmembrane AMPA receptor regulatory protein
TB	Terrific Broth
TEMED	N,N,N’,N’-tetraethylenediamine
Tet	tetracycline
TEV	tobacco etch virus
TMD	transmembrane domain
TRIS	tris-(hydroxymethyl)-aminomethane
Trx	thioredoxin
U	units
UV	ultraviolet
W	wash
WT	wild-type
XDS	X-ray detection software

B AMINO ACID ABBREVIATIONS

For amino acids, the one and the three letter code was used according to the IUPAC-IUB Joint Commission on Biochemical Nomenclature [466]: A, Ala – alanine; C, Cys – cysteine; D, Asp – aspartate; E, Glu – glutamate; F, Phe – phenylalanine; G, Gly – glycine; H, His – histidine: I, Ile – isoleucine; K, Lys – lysine; L, Leu – leucine; M, Met – methionine; N, Asn – asparagine; P, Pro – proline; Q, Gln – glutamine; R, Arg – arginine; S, Ser – serine; T, Thr – threonine; V, Val – valine; W, Trp – tryptophane; Y, Tyr – tyrosine; X – any amino acid

BIBLIOGRAPHY

1. Elegheert, J., et al., Structural basis for integration of GluD receptors within synaptic organizer complexes. Science, 2016. 353(6296): p. 295-9.
2. Collingridge, G.L., et al., A nomenclature for ligand-gated ion channels. Neuropharmacology, 2009. 56(1): p. 2-5.
3. Mayer, M.L., G.L. Westbrook, and P.B. Guthrie, Voltage-dependent block by Mg2+ of NMDA responses in spinal cord neurones. Nature, 1984. 309(5965): p. 261-3.
4. Nowak, L., et al., Magnesium gates glutamate-activated channels in mouse central neurones. Nature, 1984. 307(5950): p. 462-5.
5. Johnson, J.W. and P. Ascher, Glycine potentiates the NMDA response in cultured mouse brain neurons. Nature, 1987. 325(6104): p. 529-31.
6. Hollmann, M., et al., Cloning by functional expression of a member of the glutamate receptor family. Nature, 1989. 342(6250): p. 643-8.
7. Pasternack, A., et al., Alpha-amino-3-hydroxy-5-methyl-4-isoxazolepropionic acid (AMPA) receptor channels lacking the N-terminal domain. J Biol Chem, 2002. 277(51): p. 49662-7.
8. Horning, M.S. and M.L. Mayer, Regulation of AMPA receptor gating by ligand binding core dimers. Neuron, 2004. 41(3): p. 379-88.
9. Plested, A.J. and M.L. Mayer, Structure and mechanism of kainate receptor modulation by anions. Neuron, 2007. 53(6): p. 829-41.
10. Garcia-Nafria, J., et al., The dynamic AMPA receptor extracellular region: A platform for synaptic protein interactions. J Physiol, 2016.
11. Sia, G.M., et al., Interaction of the N-terminal domain of the AMPA receptor GluR4 subunit with the neuronal pentraxin NP1 mediates GluR4 synaptic recruitment. Neuron, 2007. 55(1): p. 87-102.
12. Leuschner, W.D. and W. Hoch, Subtype-specific assembly of alpha-amino-3-hydroxy-5-methyl-4-isoxazole propionic acid receptor subunits is mediated by their n-terminal domains. J Biol Chem, 1999. 274(24): p. 16907-16.
13. Hansen, K.B., H. Furukawa, and S.F. Traynelis, Control of assembly and function of glutamate receptors by the amino-terminal domain. Mol Pharmacol, 2010. 78(4): p. 535-49.
14. Herguedas, B., J. Krieger, and I.H. Greger, Receptor heteromeric assembly-how it works and why it matters: the case of ionotropic glutamate receptors. Prog Mol Biol Transl Sci, 2013. 117: p. 361-86.
15. Kumar, J. and M.L. Mayer, Functional insights from glutamate receptor ion channel structures. Annu Rev Physiol, 2013. 75: p. 313-37.
16. Kuusinen, A., et al., Oligomerization and ligand-binding properties of the ectodomain of the alpha-amino-3-hydroxy-5-methyl-4-isoxazole propionic acid receptor subunit GluRD. J Biol Chem, 1999. 274(41): p. 28937-43.
17. Zhu, S. and P. Paoletti, Allosteric modulators of NMDA receptors: multiple sites and mechanisms. Curr Opin Pharmacol, 2015. 20: p. 14-23.
18. Rossmann, M., et al., Subunit-selective N-terminal domain associations organize the formation of AMPA receptor heteromers. EMBO J, 2011. 30(5): p. 959-71.
19. Herguedas, B., et al., Structure and organization of heteromeric AMPA-type glutamate receptors. Science, 2016. 352(6285): p. aad3873.
20. Yuan, H., et al., Control of NMDA receptor function by the NR2 subunit amino-terminal domain. J Neurosci, 2009. 29(39): p. 12045-58.
21. Gielen, M., et al., Mechanism of differential control of NMDA receptor activity by NR2 subunits. Nature, 2009. 459(7247): p. 703-7.

22. Balannik, V., et al., Molecular mechanism of AMPA receptor noncompetitive antagonism. Neuron, 2005. 48(2): p. 279-88.
23. Ogden, K.K. and S.F. Traynelis, Contribution of the M1 transmembrane helix and pre-M1 region to positive allosteric modulation and gating of N-methyl-D-aspartate receptors. Mol Pharmacol, 2013. 83(5): p. 1045-56.
24. Salussolia, C.L., et al., A eukaryotic specific transmembrane segment is required for tetramerization in AMPA receptors. J Neurosci, 2013. 33(23): p. 9840-5.
25. Bowie, D. and M.L. Mayer, Inward rectification of both AMPA and kainate subtype glutamate receptors generated by polyamine-mediated ion channel block. Neuron, 1995. 15(2): p. 453-62.
26. Koh, D.S., N. Burnashev, and P. Jonas, Block of native Ca(2+)-permeable AMPA receptors in rat brain by intracellular polyamines generates double rectification. J Physiol, 1995. 486 (Pt 2): p. 305-12.
27. Williams, K., Modulation and block of ion channels: a new biology of polyamines. Cell Signal, 1997. 9(1): p. 1-13.
28. Traynelis, S.F., et al., Glutamate receptor ion channels: structure, regulation, and function. Pharmacol Rev, 2010. 62(3): p. 405-96.
29. Anggono, V. and R.L. Huganir, Regulation of AMPA receptor trafficking and synaptic plasticity. Curr Opin Neurobiol, 2012. 22(3): p. 461-9.
30. Greger, I.H., E.B. Ziff, and A.C. Penn, Molecular determinants of AMPA receptor subunit assembly. Trends Neurosci, 2007. 30(8): p. 407-16.
31. Sheng, M. and C. Sala, PDZ domains and the organization of supramolecular complexes. Annu Rev Neurosci, 2001. 24: p. 1-29.
32. Malinow, R. and R.C. Malenka, AMPA receptor trafficking and synaptic plasticity. Annu Rev Neurosci, 2002. 25: p. 103-26.
33. Bredt, D.S. and R.A. Nicoll, AMPA receptor trafficking at excitatory synapses. Neuron, 2003. 40(2): p. 361-79.
34. Puddifoot, C.A., et al., Pharmacological characterization of recombinant NR1/NR2A NMDA receptors with truncated and deleted carboxy termini expressed in Xenopus laevis oocytes. Br J Pharmacol, 2009. 156(3): p. 509-18.
35. Salussolia, C.L., et al., Interaction of the M4 segment with other transmembrane segments is required for surface expression of mammalian alpha-amino-3-hydroxy-5-methyl-4-isoxazolepropionic acid (AMPA) receptors. J Biol Chem, 2011. 286(46): p. 40205-18.
36. Granger, A.J., et al., LTP requires a reserve pool of glutamate receptors independent of subunit type. Nature, 2013. 493(7433): p. 495-500.
37. Boehm, J. and R. Malinow, AMPA receptor phosphorylation during synaptic plasticity. Biochem Soc Trans, 2005. 33(Pt 6): p. 1354-6.
38. Lee, H.K., Synaptic plasticity and phosphorylation. Pharmacol Ther, 2006. 112(3): p. 810-32.
39. Karakas, E. and H. Furukawa, Crystal structure of a heterotetrameric NMDA receptor ion channel. Science, 2014. 344(6187): p. 992-7.
40. Meyerson, J.R., et al., Structural mechanism of glutamate receptor activation and desensitization. Nature, 2014. 514(7522): p. 328-34.
41. Sobolevsky, A.I., M.P. Rosconi, and E. Gouaux, X-ray structure, symmetry and mechanism of an AMPA-subtype glutamate receptor. Nature, 2009. 462(7274): p. 745-56.
42. Lee, C.H., et al., NMDA receptor structures reveal subunit arrangement and pore architecture. Nature, 2014. 511(7508): p. 191-7.
43. Rosenmund, C., Y. Stern-Bach, and C.F. Stevens, The tetrameric structure of a glutamate receptor channel. Science, 1998. 280(5369): p. 1596-9.
44. Lu, W., et al., Subunit composition of synaptic AMPA receptors revealed by a single-cell genetic approach. Neuron, 2009. 62(2): p. 254-68.

45. Isaac, J.T., M.C. Ashby, and C.J. McBain, The role of the GluR2 subunit in AMPA receptor function and synaptic plasticity. Neuron, 2007. 54(6): p. 859-71.
46. Christensen, J.K., et al., A mosaic of functional kainate receptors in hippocampal interneurons. J Neurosci, 2004. 24(41): p. 8986-93.
47. Mulle, C., et al., Subunit composition of kainate receptors in hippocampal interneurons. Neuron, 2000. 28(2): p. 475-84.
48. Saab, A.S., et al., Bergmann glial AMPA receptors are required for fine motor coordination. Science, 2012. 337(6095): p. 749-53.
49. Werner, P., et al., Cloning of a putative high-affinity kainate receptor expressed predominantly in hippocampal CA3 cells. Nature, 1991. 351(6329): p. 742-4.
50. Herb, A., et al., The KA-2 subunit of excitatory amino acid receptors shows widespread expression in brain and forms ion channels with distantly related subunits. Neuron, 1992. 8(4): p. 775-85.
51. Moykkynen, T., et al., The N-terminal domain modulates alpha-amino-3-hydroxy-5-methyl-4-isoxazolepropionic acid (AMPA) receptor desensitization. J Biol Chem, 2014. 289(19): p. 13197-205.
52. Petralia, R.S., Y.X. Wang, and R.J. Wenthold, Histological and ultrastructural localization of the kainate receptor subunits, KA2 and GluR6/7, in the rat nervous system using selective antipeptide antibodies. J Comp Neurol, 1994. 349(1): p. 85-110.
53. Matsubara, A., et al., Organization of AMPA receptor subunits at a glutamate synapse: a quantitative immunogold analysis of hair cell synapses in the rat organ of Corti. J Neurosci, 1996. 16(14): p. 4457-67.
54. Petralia, R.S., et al., Ontogeny of postsynaptic density proteins at glutamatergic synapses. Mol Cell Neurosci, 2005. 29(3): p. 436-52.
55. Chen, X., et al., Organization of the core structure of the postsynaptic density. Proc Natl Acad Sci U S A, 2008. 105(11): p. 4453-8.
56. Mollerud, S., et al., Lessons from crystal structures of kainate receptors. Neuropharmacology, 2016.
57. Mayer, M.L., et al., Agonist- and voltage-gated calcium entry in cultured mouse spinal cord neurons under voltage clamp measured using arsenazo III. J Neurosci, 1987. 7(10): p. 3230-44.
58. Granger, A.J. and R.A. Nicoll, Expression mechanisms underlying long-term potentiation: a postsynaptic view, 10 years on. Philos Trans R Soc Lond B Biol Sci, 2014. 369(1633): p. 20130136.
59. Shepherd, J.D. and R.L. Huganir, The cell biology of synaptic plasticity: AMPA receptor trafficking. Annu Rev Cell Dev Biol, 2007. 23: p. 613-43.
60. Bliss, T.V. and G.L. Collingridge, A synaptic model of memory: long-term potentiation in the hippocampus. Nature, 1993. 361(6407): p. 31-9.
61. Peery, H.E., et al., Anti-NMDA receptor encephalitis. The disorder, the diagnosis and the immunobiology. Autoimmun Rev, 2012. 11(12): p. 863-72.
62. Bowie, D., Ionotropic glutamate receptors & CNS disorders. CNS Neurol Disord Drug Targets, 2008. 7(2): p. 129-43.
63. Pickard, B.S., et al., Cytogenetic and genetic evidence supports a role for the kainate-type glutamate receptor gene, GRIK4, in schizophrenia and bipolar disorder. Mol Psychiatry, 2006. 11(9): p. 847-57.
64. Li, J.M., et al., Aberrant glutamate receptor 5 expression in temporal lobe epilepsy lesions. Brain Res, 2010. 1311: p. 166-74.
65. Ibrahim, H.M., et al., Ionotropic glutamate receptor binding and subunit mRNA expression in thalamic nuclei in schizophrenia. Am J Psychiatry, 2000. 157(11): p. 1811-23.

66. Das, A., et al., Hippocampal tissue of patients with refractory temporal lobe epilepsy is associated with astrocyte activation, inflammation, and altered expression of channels and receptors. Neuroscience, 2012. 220: p. 237-46.
67. Barbon, A. and S. Barlati, Glutamate receptor RNA editing in health and disease. Biochemistry (Mosc), 2011. 76(8): p. 882-9.
68. Lynd-Balta, E., W.H. Pilcher, and S.A. Joseph, AMPA receptor alterations precede mossy fiber sprouting in young children with temporal lobe epilepsy. Neuroscience, 2004. 126(1): p. 105-14.
69. Jonas, P., The Time Course of Signaling at Central Glutamatergic Synapses. News Physiol Sci, 2000. 15: p. 83-89.
70. Sommer, B., et al., Flip and flop: a cell-specific functional switch in glutamate-operated channels of the CNS. Science, 1990. 249(4976): p. 1580-5.
71. Partin, K.M., D. Bowie, and M.L. Mayer, Structural determinants of allosteric regulation in alternatively spliced AMPA receptors. Neuron, 1995. 14(4): p. 833-43.
72. Partin, K.M., M.W. Fleck, and M.L. Mayer, AMPA receptor flip/flop mutants affecting deactivation, desensitization, and modulation by cyclothiazide, aniracetam, and thiocyanate. J Neurosci, 1996. 16(21): p. 6634-47.
73. Partin, K.M., D.K. Patneau, and M.L. Mayer, Cyclothiazide differentially modulates desensitization of alpha-amino-3-hydroxy-5-methyl-4-isoxazolepropionic acid receptor splice variants. Mol Pharmacol, 1994. 46(1): p. 129-38.
74. Mosbacher, J., et al., A molecular determinant for submillisecond desensitization in glutamate receptors. Science, 1994. 266(5187): p. 1059-62.
75. Johansen, T.H., A. Chaudhary, and T.A. Verdoorn, Interactions among GYKI-52466, cyclothiazide, and aniracetam at recombinant AMPA and kainate receptors. Mol Pharmacol, 1995. 48(5): p. 946-55.
76. Sekiguchi, M., et al., A desensitization-selective potentiator of AMPA-type glutamate receptors. Br J Pharmacol, 2002. 136(7): p. 1033-41.
77. Hennegriff, M., et al., Stable expression of recombinant AMPA receptor subunits: binding affinities and effects of allosteric modulators. J Neurochem, 1997. 68(6): p. 2424-34.
78. Armstrong, N. and E. Gouaux, Mechanisms for activation and antagonism of an AMPA-sensitive glutamate receptor: crystal structures of the GluR2 ligand binding core. Neuron, 2000. 28(1): p. 165-81.
79. Hollmann, M., M. Hartley, and S. Heinemann, Ca2+ permeability of KA-AMPA--gated glutamate receptor channels depends on subunit composition. Science, 1991. 252(5007): p. 851-3.
80. Sommer, B., et al., RNA editing in brain controls a determinant of ion flow in glutamate-gated channels. Cell, 1991. 67(1): p. 11-9.
81. Monyer, H., et al., Developmental and regional expression in the rat brain and functional properties of four NMDA receptors. Neuron, 1994. 12(3): p. 529-40.
82. Barria, A., V. Derkach, and T. Soderling, Identification of the Ca2+/calmodulin-dependent protein kinase II regulatory phosphorylation site in the alpha-amino-3-hydroxyl-5-methyl-4-isoxazole-propionate-type glutamate receptor. J Biol Chem, 1997. 272(52): p. 32727-30.
83. Mammen, A.L., et al., Phosphorylation of the alpha-amino-3-hydroxy-5-methylisoxazole4-propionic acid receptor GluR1 subunit by calcium/calmodulin-dependent kinase II. J Biol Chem, 1997. 272(51): p. 32528-33.
84. Benke, T.A., et al., Modulation of AMPA receptor unitary conductance by synaptic activity. Nature, 1998. 393(6687): p. 793-7.
85. Hosokawa, T., et al., Stoichiometry and phosphoisotypes of hippocampal AMPA-type glutamate receptor phosphorylation. Neuron, 2015. 85(1): p. 60-7.
86. Ziff, E.B., TARPs and the AMPA receptor trafficking paradox. Neuron, 2007. 53(5): p. 627-33.

87. Schwenk, J., et al., High-resolution proteomics unravel architecture and molecular diversity of native AMPA receptor complexes. Neuron, 2012. 74(4): p. 621-33.
88. Jackson, A.C. and R.A. Nicoll, The expanding social network of ionotropic glutamate receptors: TARPs and other transmembrane auxiliary subunits. Neuron, 2011. 70(2): p. 178-99.
89. Milstein, A.D., et al., TARP subtypes differentially and dose-dependently control synaptic AMPA receptor gating. Neuron, 2007. 55(6): p. 905-18.
90. Nicoll, R.A., S. Tomita, and D.S. Bredt, Auxiliary subunits assist AMPA-type glutamate receptors. Science, 2006. 311(5765): p. 1253-6.
91. Schwenk, J., et al., Functional proteomics identify cornichon proteins as auxiliary subunits of AMPA receptors. Science, 2009. 323(5919): p. 1313-9.
92. von Engelhardt, J., et al., CKAMP44: a brain-specific protein attenuating short-term synaptic plasticity in the dentate gyrus. Science, 2010. 327(5972): p. 1518-22.
93. Shanks, N.F., et al., Differences in AMPA and Kainate Receptor Interactomes Facilitate Identification of AMPA Receptor Auxiliary Subunit GSG1L. Cell Rep, 2012. 1(6): p. 590-8.
94. Diaz, E., et al., Molecular analysis of gene expression in the developing pontocerebellar projection system. Neuron, 2002. 36(3): p. 417-34.
95. O'Hara, P.J., et al., The ligand-binding domain in metabotropic glutamate receptors is related to bacterial periplasmic binding proteins. Neuron, 1993. 11(1): p. 41-52.
96. Wo, Z.G. and R.E. Oswald, Unraveling the modular design of glutamate-gated ion channels. Trends Neurosci, 1995. 18(4): p. 161-8.
97. Oh, B.H., et al., Three-dimensional structures of the periplasmic lysine/arginine/ornithine-binding protein with and without a ligand. J Biol Chem, 1993. 268(15): p. 11348-55.
98. Paas, Y., The macro- and microarchitectures of the ligand-binding domain of glutamate receptors. Trends Neurosci, 1998. 21(3): p. 117-25.
99. Wood, M.W., H.M. VanDongen, and A.M. VanDongen, Structural conservation of ion conduction pathways in K channels and glutamate receptors. Proc Natl Acad Sci U S A, 1995. 92(11): p. 4882-6.
100. Kuner, T., P.H. Seeburg, and H.R. Guy, A common architecture for K+ channels and ionotropic glutamate receptors? Trends Neurosci, 2003. 26(1): p. 27-32.
101. Nakanishi, N., N.A. Shneider, and R. Axel, A family of glutamate receptor genes: evidence for the formation of heteromultimeric receptors with distinct channel properties. Neuron, 1990. 5(5): p. 569-81.
102. Stern-Bach, Y., et al., Agonist selectivity of glutamate receptors is specified by two domains structurally related to bacterial amino acid-binding proteins. Neuron, 1994. 13(6): p. 1345-57.
103. Kuryatov, A., et al., Mutational analysis of the glycine-binding site of the NMDA receptor: structural similarity with bacterial amino acid-binding proteins. Neuron, 1994. 12(6): p. 1291-300.
104. Kuusinen, A., M. Arvola, and K. Keinanen, Molecular dissection of the agonist binding site of an AMPA receptor. EMBO J, 1995. 14(24): p. 6327-32.
105. Arvola, M. and K. Keinanen, Characterization of the ligand-binding domains of glutamate receptor (GluR)-B and GluR-D subunits expressed in Escherichia coli as periplasmic proteins. J Biol Chem, 1996. 271(26): p. 15527-32.
106. Chen, G.Q. and E. Gouaux, Overexpression of a glutamate receptor (GluR2) ligand binding domain in Escherichia coli: application of a novel protein folding screen. Proc Natl Acad Sci U S A, 1997. 94(25): p. 13431-6.
107. Chen, G.Q., et al., Probing the ligand binding domain of the GluR2 receptor by proteolysis and deletion mutagenesis defines domain boundaries and yields a crystallizable construct. Protein Sci, 1998. 7(12): p. 2623-30.

108. Armstrong, N., et al., Structure of a glutamate-receptor ligand-binding core in complex with kainate. Nature, 1998. 395(6705): p. 913-7.
109. Naur, P., et al., Crystal structure of the kainate receptor GluR5 ligand-binding core in complex with (S)-glutamate. FEBS Lett, 2005. 579(5): p. 1154-60.
110. Mayer, M.L., Crystal structures of the GluR5 and GluR6 ligand binding cores: molecular mechanisms underlying kainate receptor selectivity. Neuron, 2005. 45(4): p. 539-52.
111. Mayer, M.L., Glutamate receptors at atomic resolution. Nature, 2006. 440: p. 456-462.
112. Stawski, P., H. Janovjak, and D. Trauner, Pharmacology of ionotropic glutamate receptors: A structural perspective. Bioorg Med Chem, 2010. 18(22): p. 7759-72.
113. Pohlsgaard, J., et al., Lessons from more than 80 structures of the GluA2 ligand-binding domain in complex with agonists, antagonists and allosteric modulators. Neuropharmacology, 2011. 60(1): p. 135-50.
114. Plested, A.J. and M.L. Mayer, AMPA receptor ligand binding domain mobility revealed by functional cross linking. J Neurosci, 2009. 29(38): p. 11912-23.
115. Armstrong, N., et al., Measurement of conformational changes accompanying desensitization in an ionotropic glutamate receptor. Cell, 2006. 127(1): p. 85-97.
116. Lau, A.Y., et al., A conformational intermediate in glutamate receptor activation. Neuron, 2013. 79(3): p. 492-503.
117. Safferling, M., et al., First images of a glutamate receptor ion channel: oligomeric state and molecular dimensions of GluRB homomers. Biochemistry, 2001. 40(46): p. 13948-53.
118. Tichelaar, W., et al., The Three-dimensional Structure of an Ionotropic Glutamate Receptor Reveals a Dimer-of-dimers Assembly. J Mol Biol, 2004. 344(2): p. 435-42.
119. Nakagawa, T., et al., Structure and different conformational states of native AMPA receptor complexes. Nature, 2005. 433(7025): p. 545-9.
120. Midgett, C.R. and D.R. Madden, The quaternary structure of a calcium-permeable AMPA receptor: conservation of shape and symmetry across functionally distinct subunit assemblies. J Mol Biol, 2008. 382(3): p. 578-84.
121. Nakagawa, T., et al., Three-dimensional structure of an AMPA receptor without associated stargazin/TARP proteins. Biol Chem, 2006. 387(2): p. 179-87.
122. Midgett, C.R., A. Gill, and D.R. Madden, Domain architecture of a calcium-permeable AMPA receptor in a ligand-free conformation. Front Mol Neurosci, 2012. 4: p. 56.
123. Chen, L., K.L. Durr, and E. Gouaux, X-ray structures of AMPA receptor-cone snail toxin complexes illuminate activation mechanism. Science, 2014. 345(6200): p. 1021-6.
124. Yelshanskaya, M.V., M. Li, and A.I. Sobolevsky, Structure of an agonist-bound ionotropic glutamate receptor. Science, 2014. 345(6200): p. 1070-4.
125. Durr, K.L., et al., Structure and dynamics of AMPA receptor GluA2 in resting, pre-open, and desensitized states. Cell, 2014. 158(4): p. 778-92.
126. Schauder, D.M., et al., Glutamate receptor desensitization is mediated by changes in quaternary structure of the ligand binding domain. Proc Natl Acad Sci U S A, 2013. 110(15): p. 5921-6.
127. Jin, R., et al., Mechanism of activation and selectivity in a ligand-gated ion channel: structural and functional studies of GluR2 and quisqualate. Biochemistry, 2002. 41(52): p. 15635-43.
128. Zhu, S., et al., Mechanism of NMDA Receptor Inhibition and Activation. Cell, 2016. 165(3): p. 704-14.
129. Tajima, N., et al., Activation of NMDA receptors and the mechanism of inhibition by ifenprodil. Nature, 2016. 534(7605): p. 63-8.

130. Gielen, M., et al., Structural rearrangements of NR1/NR2A NMDA receptors during allosteric inhibition. Neuron, 2008. 57(1): p. 80-93.
131. Zheng, F., et al., Allosteric interaction between the amino terminal domain and the ligand binding domain of NR2A. Nat Neurosci, 2001. 4(9): p. 894-901.
132. Zhu, S., et al., Allosteric signaling and dynamics of the clamshell-like NMDA receptor GluN1 N-terminal domain. Nat Struct Mol Biol, 2013. 20(4): p. 477-85.
133. Dzubay, J.A. and C.E. Jahr, Kinetics of NMDA channel opening. J Neurosci, 1996. 16(13): p. 4129-34.
134. Attwell, D. and A. Gibb, Neuroenergetics and the kinetic design of excitatory synapses. Nat Rev Neurosci, 2005. 6(11): p. 841-9.
135. Popescu, G. and A. Auerbach, Modal gating of NMDA receptors and the shape of their synaptic response. Nat Neurosci, 2003. 6(5): p. 476-83.
136. Antoine Robert, J.R.H., How AMPA receptor desensitization depends on receptor occupancy. The Journal of Neuroscience, 2003. 23(3): p. 847-858.
137. Vance, K.M., K.B. Hansen, and S.F. Traynelis, Modal gating of GluN1/GluN2D NMDA receptors. Neuropharmacology, 2013. 71: p. 184-90.
138. Fenwick, M.K. and R.E. Oswald, On the mechanisms of alpha-amino-3-hydroxy-5-methylisoxazole-4-propionic acid (AMPA) receptor binding to glutamate and kainate. J Biol Chem, 2010. 285(16): p. 12334-43.
139. Holley, S.M., et al., The loss of an electrostatic contact unique to AMPA receptor ligand binding domain 2 slows channel activation. Biochemistry, 2012. 51(19): p. 4015-27.
140. Ahmed, A.H., et al., Dynamics of cleft closure of the GluA2 ligand-binding domain in the presence of full and partial agonists revealed by hydrogen-deuterium exchange. J Biol Chem, 2013. 288(38): p. 27658-66.
141. Weston, M.C., et al., Interdomain interactions in AMPA and kainate receptors regulate affinity for glutamate. J Neurosci, 2006. 26(29): p. 7650-8.
142. Hayward, S. and H.J. Berendsen, Systematic analysis of domain motions in proteins from conformational change: new results on citrate synthase and T4 lysozyme. Proteins, 1998. 30(2): p. 144-54.
143. Lau, A.Y. and B. Roux, The hidden energetics of ligand binding and activation in a glutamate receptor. Nat Struct Mol Biol, 2011. 18(3): p. 283-7.
144. Madden, D.R., The structure and function of glutamate receptor ion channels. Nat Rev Neurosci, 2002. 3(2): p. 91-101.
145. Poon, K., et al., Mechanisms of modal activation of GluA3 receptors. Mol Pharmacol, 2011. 80(1): p. 49-59.
146. Maltsev, A.S., et al., Mechanism of partial agonism at the GluR2 AMPA receptor: Measurements of lobe orientation in solution. Biochemistry, 2008. 47(40): p. 10600-10.
147. Ahmed, A.H., et al., Mechanism of AMPA receptor activation by partial agonists: disulfide trapping of closed lobe conformations. J Biol Chem, 2011. 286(40): p. 35257-66.
148. Inanobe, A., H. Furukawa, and E. Gouaux, Mechanism of partial agonist action at the NR1 subunit of NMDA receptors. Neuron, 2005. 47(1): p. 71-84.
149. Hansen, K.B., et al., Structural determinants of agonist efficacy at the glutamate binding site of N-methyl-D-aspartate receptors. Mol Pharmacol, 2013. 84(1): p. 114-27.
150. Andersen, P.H., et al., Stable expression of homomeric AMPA-selective glutamate receptors in BHK cells. Eur J Pharmacol, 1996. 311(1): p. 95-100.
151. Brauner-Osborne, H., et al., Ligands for glutamate receptors: design and therapeutic prospects. J Med Chem, 2000. 43(14): p. 2609-45.

152. Jin, R., et al., Structural basis for partial agonist action at ionotropic glutamate receptors. Nat Neurosci, 2003. 6(8): p. 803-10.
153. Unno, M., et al., Binding and selectivity of the marine toxin neodysiherbaine A and its synthetic analogues to GluK1 and GluK2 kainate receptors. J Mol Biol, 2011. 413(3): p. 667-83.
154. Frydenvang, K., et al., Full domain closure of the ligand-binding core of the ionotropic glutamate receptor iGluR5 induced by the high affinity agonist dysiherbaine and the functional antagonist 8,9-dideoxyneodysiherbaine. J Biol Chem, 2009. 284(21): p. 14219-29.
155. Smith, T.C. and J.R. Howe, Concentration-dependent substate behavior of native AMPA receptors. Nat Neurosci, 2000. 3(10): p. 992-7.
156. Poon, K., L.M. Nowak, and R.E. Oswald, Characterizing single-channel behavior of GluA3 receptors. Biophys J, 2010. 99(5): p. 1437-46.
157. Prieto, M.L. and L.P. Wollmuth, Gating modes in AMPA receptors. J Neurosci, 2010. 30(12): p. 4449-59.
158. Kleckner, N.W. and R. Dingledine, Requirement for glycine in activation of NMDA-receptors expressed in Xenopus oocytes. Science, 1988. 241(4867): p. 835-7.
159. Plested, A.J., Structural mechanisms of activation and desensitization in neurotransmitter-gated ion channels. Nat Struct Mol Biol, 2016. 23(6): p. 494-502.
160. Kussius, C.L. and G.K. Popescu, Kinetic basis of partial agonism at NMDA receptors. Nat Neurosci, 2009. 12(9): p. 1114-20.
161. Popescu, G., et al., Reaction mechanism determines NMDA receptor response to repetitive stimulation. Nature, 2004. 430(7001): p. 790-3.
162. Priestley, T., et al., Pharmacological properties of recombinant human N-methyl-D-aspartate receptors comprising NR1a/NR2A and NR1a/NR2B subunit assemblies expressed in permanently transfected mouse fibroblast cells. Mol Pharmacol, 1995. 48(5): p. 841-8.
163. Sheinin, A., S. Shavit, and M. Benveniste, Subunit specificity and mechanism of action of NMDA partial agonist D-cycloserine. Neuropharmacology, 2001. 41(2): p. 151-8.
164. Sommer, B., et al., A glutamate receptor channel with high affinity for domoate and kainate. EMBO J, 1992. 11(4): p. 1651-6.
165. Carbone, A.L. and A.J. Plested, Coupled control of desensitization and gating by the ligand binding domain of glutamate receptors. Neuron, 2012. 74(5): p. 845-57.
166. Otis, T., S. Zhang, and L.O. Trussell, Direct measurement of AMPA receptor desensitization induced by glutamatergic synaptic transmission. J Neurosci, 1996. 16(23): p. 7496-504.
167. Chaudhry, C., et al., Stability of ligand-binding domain dimer assembly controls kainate receptor desensitization. EMBO J, 2009. 28(10): p. 1518-30.
168. Monyer, H., et al., Heteromeric NMDA receptors: molecular and functional distinction of subtypes. Science, 1992. 256(5060): p. 1217-21.
169. Vicini, S., et al., Functional and pharmacological differences between recombinant N-methyl-D-aspartate receptors. J Neurophysiol, 1998. 79(2): p. 555-66.
170. Christie, L.A., et al., AMPA receptor desensitization mutation results in severe developmental phenotypes and early postnatal lethality. Proc Natl Acad Sci U S A, 2010. 107(20): p. 9412-7.
171. Zhao, H., et al., Analysis of high-affinity assembly for AMPA receptor amino-terminal domains. J Gen Physiol, 2012. 139(5): p. 371-88.
172. Kumar, J., P. Schuck, and M.L. Mayer, Structure and assembly mechanism for heteromeric kainate receptors. Neuron, 2011. 71(2): p. 319-31.
173. Jin, R., et al., Crystal structure and association behaviour of the GluR2 amino-terminal domain. EMBO J, 2009. 28(12): p. 1812-23.

174. Plested, A.J., et al., Molecular basis of kainate receptor modulation by sodium. Neuron, 2008. 58(5): p. 720-35.
175. Bowie, D., Ion-dependent gating of kainate receptors. J Physiol, 2010. 588(Pt 1): p. 67-81.
176. Bowie, D., External anions and cations distinguish between AMPA and kainate receptor gating mechanisms. J Physiol, 2002. 539(Pt 3): p. 725-33.
177. Bowie, D. and G.D. Lange, Functional stoichiometry of glutamate receptor desensitization. J Neurosci, 2002. 22(9): p. 3392-403.
178. Dingledine, R., et al., The glutamate receptor ion channels. Pharmacol Rev, 1999. 51(1): p. 7-61.
179. Sun, Y., et al., Mechanism of glutamate receptor desensitization. Nature, 2002. 417(6886): p. 245-53.
180. Weston, M.C., et al., Conformational restriction blocks glutamate receptor desensitization. Nat Struct Mol Biol, 2006. 13(12): p. 1120-7.
181. Talisuna, A.O., et al., Intensity of malaria transmission, antimalarial-drug use and resistance in Uganda: what is the relationship between these three factors? Trans R Soc Trop Med Hyg, 2002. 96(3): p. 310-7.
182. Jin, R., et al., Mechanism of positive allosteric modulators acting on AMPA receptors. J Neurosci, 2005. 25(39): p. 9027-36.
183. Nayeem, N., O. Mayans, and T. Green, Conformational flexibility of the ligand-binding domain dimer in kainate receptor gating and desensitization. J Neurosci, 2011. 31(8): p. 2916-24.
184. Nayeem, N., O. Mayans, and T. Green, Correlating efficacy and desensitization with GluK2 ligand-binding domain movements. Open Biol, 2013. 3(5): p. 130051.
185. Gallivan, J.P. and D.A. Dougherty, Cation-pi interactions in structural biology. Proc Natl Acad Sci U S A, 1999. 96(17): p. 9459-64.
186. Patneau, D.K. and M.L. Mayer, Kinetic analysis of interactions between kainate and AMPA: evidence for activation of a single receptor in mouse hippocampal neurons. Neuron, 1991. 6(5): p. 785-98.
187. Gonzalez, J., et al., Role of dimer interface in activation and desensitization in AMPA receptors. Proc Natl Acad Sci U S A, 2010. 107(21): p. 9891-6.
188. Colquhoun, D., P. Jonas, and B. Sakmann, Action of brief pulses of glutamate on AMPA/kainate receptors in patches from different neurones of rat hippocampal slices. J Physiol, 1992. 458: p. 261-87.
189. Wyllie, D.J., S.F. Traynelis, and S.G. Cull-Candy, Evidence for more than one type of non-NMDA receptor in outside-out patches from cerebellar granule cells of the rat. J Physiol, 1993. 463: p. 193-226.
190. Castillo, P.E., R.C. Malenka, and R.A. Nicoll, Kainate receptors mediate a slow postsynaptic current in hippocampal CA3 neurons. Nature, 1997. 388(6638): p. 182-6.
191. Swanson, G.T., S.K. Kamboj, and S.G. Cull-Candy, Single-channel properties of recombinant AMPA receptors depend on RNA editing, splice variation, and subunit composition. J Neurosci, 1997. 17(1): p. 58-69.
192. Swanson, G.T. and S.F. Heinemann, Heterogeneity of homomeric GluR5 kainate receptor desensitization expressed in HEK293 cells. J Physiol, 1998. 513 (Pt 3): p. 639-46.
193. Letts, V.A., Stargazer--a mouse to seize! Epilepsy Curr, 2005. 5(5): p. 161-5.
194. Letts, V.A., et al., The mouse stargazer gene encodes a neuronal Ca2+-channel gamma subunit. Nat Genet, 1998. 19(4): p. 340-7.
195. Letts, V.A., et al., Genetic and physical maps of the stargazer locus on mouse chromosome 15. Genomics, 1997. 43(1): p. 62-8.
196. Tomita, S., Regulation of ionotropic glutamate receptors by their auxiliary subunits. Physiology (Bethesda), 2010. 25(1): p. 41-9.

197. Tomita, S., et al., Functional studies and distribution define a family of transmembrane AMPA receptor regulatory proteins. J Cell Biol, 2003. 161(4): p. 805-16.
198. Fukata, Y., et al., Molecular constituents of neuronal AMPA receptors. J Cell Biol, 2005. 169(3): p. 399-404.
199. Tomita, S., et al., Dynamic interaction of stargazin-like TARPs with cycling AMPA receptors at synapses. Science, 2004. 303(5663): p. 1508-11.
200. Suzuki, H., et al., Crystal structure of a claudin provides insight into the architecture of tight junctions. Science, 2014. 344(6181): p. 304-7.
201. Saitoh, Y., et al., Tight junctions. Structural insight into tight junction disassembly by Clostridium perfringens enterotoxin. Science, 2015. 347(6223): p. 775-8.
202. Zhao, Y., et al., Architecture of fully occupied GluA2 AMPA receptor-TARP complex elucidated by cryo-EM. Nature, 2016.
203. Twomey, E.C., et al., Elucidation of AMPA receptor–stargazin complexes by cryo–electron microscopy. Science, 2016. 353(6294): p. 83-86.
204. Kato, A.S., et al., TARPs differentially decorate AMPA receptors to specify neuropharmacology. Trends Neurosci, 2010. 33(5): p. 241-8.
205. Payne, H.L., The role of transmembrane AMPA receptor regulatory proteins (TARPs) in neurotransmission and receptor trafficking (Review). Mol Membr Biol, 2008. 25(4): p. 353-62.
206. Fukaya, M., et al., Spatial diversity in gene expression for VDCCgamma subunit family in developing and adult mouse brains. Neurosci Res, 2005. 53(4): p. 376-83.
207. Menuz, K., et al., Critical role for TARPs in early development despite broad functional redundancy. Neuropharmacology, 2009. 56(1): p. 22-9.
208. Studniarczyk, D., et al., TARP gamma-7 selectively enhances synaptic expression of calcium-permeable AMPARs. Nat Neurosci, 2013. 16(9): p. 1266-74.
209. Lein, E.S., et al., Genome-wide atlas of gene expression in the adult mouse brain. Nature, 2007. 445(7124): p. 168-76.
210. Klugbauer, N., et al., A family of gamma-like calcium channel subunits. FEBS Lett, 2000. 470(2): p. 189-97.
211. Sharp, A.H., et al., Biochemical and anatomical evidence for specialized voltage-dependent calcium channel gamma isoform expression in the epileptic and ataxic mouse, stargazer. Neuroscience, 2001. 105(3): p. 599-617.
212. Chu, P.J., H.M. Robertson, and P.M. Best, Calcium channel gamma subunits provide insights into the evolution of this gene family. Gene, 2001. 280(1-2): p. 37-48.
213. Moss, F.J., et al., The novel product of a five-exon stargazin-related gene abolishes Ca(V)2.2 calcium channel expression. EMBO J, 2002. 21(7): p. 1514-23.
214. Kato, A.S., et al., New transmembrane AMPA receptor regulatory protein isoform, gamma-7, differentially regulates AMPA receptors. J Neurosci, 2007. 27(18): p. 4969-77.
215. Inamura, M., et al., Differential localization and regulation of stargazin-like protein, gamma-8 and stargazin in the plasma membrane of hippocampal and cortical neurons. Neurosci Res, 2006. 55(1): p. 45-53.
216. Fukaya, M., et al., Abundant distribution of TARP gamma-8 in synaptic and extrasynaptic surface of hippocampal neurons and its major role in AMPA receptor expression on spines and dendrites. Eur J Neurosci, 2006. 24(8): p. 2177-90.
217. Rouach, N., et al., TARP gamma-8 controls hippocampal AMPA receptor number, distribution and synaptic plasticity. Nat Neurosci, 2005. 8(11): p. 1525-33.
218. Vandenberghe, W., R.A. Nicoll, and D.S. Bredt, Stargazin is an AMPA receptor auxiliary subunit. Proc Natl Acad Sci U S A, 2005. 102(2): p. 485-90.
219. Shanks, N.F., et al., Contribution of the global subunit structure and stargazin on the maturation of AMPA receptors. J Neurosci, 2010. 30(7): p. 2728-40.

220. Shi, Y., et al., The stoichiometry of AMPA receptors and TARPs varies by neuronal cell type. Neuron, 2009. 62(5): p. 633-40.

221. Hastie, P., et al., AMPA receptor/TARP stoichiometry visualized by single-molecule subunit counting. Proc Natl Acad Sci U S A, 2013. 110(13): p. 5163-8.

222. Kim, K.S., D. Yan, and S. Tomita, Assembly and stoichiometry of the AMPA receptor and transmembrane AMPA receptor regulatory protein complex. J Neurosci, 2010. 30(3): p. 1064-72.

223. Morimoto-Tomita, M., et al., Autoinactivation of neuronal AMPA receptors via glutamate-regulated TARP interaction. Neuron, 2009. 61(1): p. 101-12.

224. Bedoukian, M.A., et al., The stargazin C terminus encodes an intrinsic and transferable membrane sorting signal. J Biol Chem, 2008. 283(3): p. 1597-600.

225. Priel, A., et al., Stargazin reduces desensitization and slows deactivation of the AMPA-type glutamate receptors. J Neurosci, 2005. 25(10): p. 2682-6.

226. Tomita, S., et al., Stargazin modulates AMPA receptor gating and trafficking by distinct domains. Nature, 2005. 435(7045): p. 1052-8.

227. Turetsky, D., E. Garringer, and D.K. Patneau, Stargazin modulates native AMPA receptor functional properties by two distinct mechanisms. J Neurosci, 2005. 25(32): p. 7438-48.

228. Bedoukian, M.A., A.M. Weeks, and K.M. Partin, Different domains of the AMPA receptor direct stargazin-mediated trafficking and stargazin-mediated modulation of kinetics. J Biol Chem, 2006. 281(33): p. 23908-21.

229. Kato, A.S., et al., AMPA receptor subunit-specific regulation by a distinct family of type II TARPs. Neuron, 2008. 59(6): p. 986-96.

230. Soto, D., et al., Selective regulation of long-form calcium-permeable AMPA receptors by an atypical TARP, gamma-5. Nat Neurosci, 2009. 12(3): p. 277-85.

231. Soto, D., et al., Stargazin attenuates intracellular polyamine block of calcium-permeable AMPA receptors. Nat Neurosci, 2007. 10(10): p. 1260-7.

232. Korber, C., et al., Stargazin interaction with alpha-amino-3-hydroxy-5-methyl-4-isoxazole propionate (AMPA) receptors is critically dependent on the amino acid at the narrow constriction of the ion channel. J Biol Chem, 2007. 282(26): p. 18758-66.

233. Cais, O., et al., Mapping the interaction sites between AMPA receptors and TARPs reveals a role for the receptor N-terminal domain in channel gating. Cell Rep, 2014. 9(2): p. 728-40.

234. Tomita, S., et al., Stargazin interacts functionally with the AMPA receptor glutamate-binding module. Neuropharmacology, 2007. 52(1): p. 87-91.

235. Sager, C., et al., C-terminal domains of transmembrane alpha-amino-3-hydroxy-5-methyl-4-isoxazole propionate (AMPA) receptor regulatory proteins not only facilitate trafficking but are major modulators of AMPA receptor function. J Biol Chem, 2009. 284(47): p. 32413-24.

236. Milstein, A.D. and R.A. Nicoll, TARP modulation of synaptic AMPA receptor trafficking and gating depends on multiple intracellular domains. Proc Natl Acad Sci U S A, 2009. 106(27): p. 11348-51.

237. Dawe, G.B., et al., Distinct Structural Pathways Coordinate the Activation of AMPA Receptor-Auxiliary Subunit Complexes. Neuron, 2016. 89(6): p. 1264-76.

238. Vandenberghe, W., R.A. Nicoll, and D.S. Bredt, Interaction with the unfolded protein response reveals a role for stargazin in biosynthetic AMPA receptor transport. J Neurosci, 2005. 25(5): p. 1095-102.

239. Hall, R.A., et al., Surface expression of the AMPA receptor subunits GluR1, GluR2, and GluR4 in stably transfected baby hamster kidney cells. J Neurochem, 1997. 68(2): p. 625-30.

240. Chen, L., et al., Stargazin regulates synaptic targeting of AMPA receptors by two distinct mechanisms. Nature, 2000. 408(6815): p. 936-43.

241. Cuadra, A.E., et al., AMPA receptor synaptic targeting regulated by stargazin interactions with the Golgi-resident PDZ protein nPIST. J Neurosci, 2004. 24(34): p. 7491-502.
242. Ives, J.H., et al., Microtubule-associated protein light chain 2 is a stargazin-AMPA receptor complex-interacting protein in vivo. J Biol Chem, 2004. 279(30): p. 31002-9.
243. Bats, C., L. Groc, and D. Choquet, The interaction between Stargazin and PSD-95 regulates AMPA receptor surface trafficking. Neuron, 2007. 53(5): p. 719-34.
244. Opazo, P., M. Sainlos, and D. Choquet, Regulation of AMPA receptor surface diffusion by PSD-95 slots. Curr Opin Neurobiol, 2012. 22(3): p. 453-60.
245. Beique, J.C., et al., Synapse-specific regulation of AMPA receptor function by PSD-95. Proc Natl Acad Sci U S A, 2006. 103(51): p. 19535-40.
246. Schnell, E., et al., Direct interactions between PSD-95 and stargazin control synaptic AMPA receptor number. Proc Natl Acad Sci U S A, 2002. 99(21): p. 13902-7.
247. Deng, F., et al., Stargazin and other transmembrane AMPA receptor regulating proteins interact with synaptic scaffolding protein MAGI-2 in brain. J Neurosci, 2006. 26(30): p. 7875-84.
248. Dakoji, S., et al., Interaction of transmembrane AMPA receptor regulatory proteins with multiple membrane associated guanylate kinases. Neuropharmacology, 2003. 45(6): p. 849-56.
249. Levchenko-Lambert, Y., D.M. Turetsky, and D.K. Patneau, Not all desensitizations are created equal: physiological evidence that AMPA receptor desensitization differs for kainate and glutamate. J Neurosci, 2011. 31(25): p. 9359-67.
250. Tsui, J. and R.C. Malenka, Substrate localization creates specificity in calcium/calmodulin-dependent protein kinase II signaling at synapses. J Biol Chem, 2006. 281(19): p. 13794-804.
251. Tomita, S., et al., Bidirectional synaptic plasticity regulated by phosphorylation of stargazin-like TARPs. Neuron, 2005. 45(2): p. 269-77.
252. Lisman, J., Long-term potentiation: outstanding questions and attempted synthesis. Philos Trans R Soc Lond B Biol Sci, 2003. 358(1432): p. 829-42.
253. Collingridge, G.L., J.T. Isaac, and Y.T. Wang, Receptor trafficking and synaptic plasticity. Nat Rev Neurosci, 2004. 5(12): p. 952-62.
254. Malenka, R.C. and M.F. Bear, LTP and LTD: an embarrassment of riches. Neuron, 2004. 44(1): p. 5-21.
255. Malenka, R.C. and R.A. Nicoll, Long-term potentiation--a decade of progress? Science, 1999. 285(5435): p. 1870-4.
256. Sumioka, A., D. Yan, and S. Tomita, TARP phosphorylation regulates synaptic AMPA receptors through lipid bilayers. Neuron, 2010. 66(5): p. 755-67.
257. Hafner, A.S., et al., Lengthening of the Stargazin Cytoplasmic Tail Increases Synaptic Transmission by Promoting Interaction to Deeper Domains of PSD-95. Neuron, 2015. 86(2): p. 475-89.
258. Roberts, M.F., D.W. Taylor, and V.M. Unger, Two modes of interaction between the membrane-embedded TARP stargazin's C-terminal domain and the bilayer visualized by electron crystallography. J Struct Biol, 2011. 174(3): p. 542-51.
259. Chetkovich, D.M., et al., Phosphorylation of the postsynaptic density-95 (PSD-95)/discs large/zona occludens-1 binding site of stargazin regulates binding to PSD-95 and synaptic targeting of AMPA receptors. J Neurosci, 2002. 22(14): p. 5791-6.
260. Choi, J., et al., Phosphorylation of stargazin by protein kinase A regulates its interaction with PSD-95. J Biol Chem, 2002. 277(14): p. 12359-63.
261. Doyle, D.A., et al., Crystal structures of a complexed and peptide-free membrane protein-binding domain: molecular basis of peptide recognition by PDZ. Cell, 1996. 85(7): p. 1067-76.

262. Stein, E.L. and D.M. Chetkovich, Regulation of stargazin synaptic trafficking by C-terminal PDZ ligand phosphorylation in bidirectional synaptic plasticity. J Neurochem, 2010. 113(1): p. 42-53.
263. Kessels, H.W., et al., Roles of stargazin and phosphorylation in the control of AMPA receptor subcellular distribution. Nat Neurosci, 2009. 12(7): p. 888-96.
264. Merrill, M.A., et al., Activity-driven postsynaptic translocation of CaMKII. Trends Pharmacol Sci, 2005. 26(12): p. 645-53.
265. Derkach, V.A., et al., Regulatory mechanisms of AMPA receptors in synaptic plasticity. Nat Rev Neurosci, 2007. 8(2): p. 101-13.
266. Hayashi, Y., et al., Driving AMPA receptors into synapses by LTP and CaMKII: requirement for GluR1 and PDZ domain interaction. Science, 2000. 287(5461): p. 2262-7.
267. Straub, C. and S. Tomita, The regulation of glutamate receptor trafficking and function by TARPs and other transmembrane auxiliary subunits. Curr Opin Neurobiol, 2012. 22(3): p. 488-95.
268. Knight, H.M., et al., Homozygosity mapping in a family presenting with schizophrenia, epilepsy and hearing impairment. Eur J Hum Genet, 2008. 16(6): p. 750-8.
269. Everett, K.V., et al., Linkage and association analysis of CACNG3 in childhood absence epilepsy. Eur J Hum Genet, 2007. 15(4): p. 463-72.
270. Liu, Y.L., et al., RASD2, MYH9, and CACNG2 genes at chromosome 22q12 associated with the subgroup of schizophrenia with non-deficit in sustained attention and executive function. Biol Psychiatry, 2008. 64(9): p. 789-96.
271. Beneyto, M. and J.H. Meador-Woodruff, Lamina-specific abnormalities of AMPA receptor trafficking and signaling molecule transcripts in the prefrontal cortex in schizophrenia. Synapse, 2006. 60(8): p. 585-98.
272. Silberberg, G., et al., Stargazin involvement with bipolar disorder and response to lithium treatment. Pharmacogenet Genomics, 2008. 18(5): p. 403-12.
273. Roth, S., et al., cornichon and the EGF receptor signaling process are necessary for both anterior-posterior and dorsal-ventral pattern formation in Drosophila. Cell, 1995. 81(6): p. 967-78.
274. Shi, Y., et al., Functional comparison of the effects of TARPs and cornichons on AMPA receptor trafficking and gating. Proc Natl Acad Sci U S A, 2010. 107(37): p. 16315-9.
275. Tigaret, C. and D. Choquet, Neuroscience. More AMPAR garnish. Science, 2009. 323(5919): p. 1295-6.
276. Jackson, A.C. and R.A. Nicoll, Neuroscience: AMPA receptors get 'pickled'. Nature, 2009. 458(7238): p. 585-6.
277. Brockie, P.J. and A.V. Maricq, In a pickle: is cornichon just relish or part of the main dish? Neuron, 2010. 68(6): p. 1017-9.
278. Vitt, U.A., S.Y. Hsu, and A.J. Hsueh, Evolution and classification of cystine knot-containing hormones and related extracellular signaling molecules. Mol Endocrinol, 2001. 15(5): p. 681-94.
279. Norton, R.S. and P.K. Pallaghy, The cystine knot structure of ion channel toxins and related polypeptides. Toxicon, 1998. 36(11): p. 1573-83.
280. Guzman, S.J. and P. Jonas, Beyond TARPs: the growing list of auxiliary AMPAR subunits. Neuron, 2010. 66(1): p. 8-10.
281. Farrant, M. and S.G. Cull-Candy, Neuroscience. AMPA receptors--another twist? Science, 2010. 327(5972): p. 1463-5.
282. Kalashnikova, E., et al., SynDIG1: an activity-regulated, AMPA- receptor-interacting transmembrane protein that regulates excitatory synapse development. Neuron, 2010. 65(1): p. 80-93.

283. Diaz, E., Regulation of AMPA receptors by transmembrane accessory proteins. Eur J Neurosci, 2010. 32(2): p. 261-8.
284. Diaz, E., SynDIG1 regulation of synaptic AMPA receptor targeting. Commun Integr Biol, 2010. 3(4): p. 347-9.
285. Ng, D., et al., Neto1 is a novel CUB-domain NMDA receptor-interacting protein required for synaptic plasticity and learning. PLoS Biol, 2009. 7(2): p. e41.
286. Stohr, H., et al., A novel gene encoding a putative transmembrane protein with two extracellular CUB domains and a low-density lipoprotein class A module: isolation of alternatively spliced isoforms in retina and brain. Gene, 2002. 286(2): p. 223-31.
287. Michishita, M., et al., A novel gene, Btcl1, encoding CUB and LDLa domains is expressed in restricted areas of mouse brain. Biochem Biophys Res Commun, 2003. 306(3): p. 680-6.
288. Zhang, W., et al., A transmembrane accessory subunit that modulates kainate-type glutamate receptors. Neuron, 2009. 61(3): p. 385-96.
289. Potterton, L., et al., Developments in the CCP4 molecular-graphics project. Acta Crystallogr D Biol Crystallogr, 2004. 60(Pt 12 Pt 1): p. 2288-94.
290. Emsley, P., et al., Features and development of Coot. Acta Crystallogr D Biol Crystallogr, 2010. 66(Pt 4): p. 486-501.
291. Sheffield, J.B., An Introduction to ImageJ; a Useful Tool for Biological Image Processing and Analysis

Microsc Microanal 2008. 14(Suppl 2)(Suppl 2): p. 898-899.
292. Leslie, A.G., The integration of macromolecular diffraction data. Acta Crystallogr D Biol Crystallogr, 2006. 62(Pt 1): p. 48-57.
293. McCoy, A.J., et al., Phaser crystallographic software. J Appl Crystallogr, 2007. 40(Pt 4): p. 658-674.
294. Adams, P.D., et al., PHENIX: a comprehensive Python-based system for macromolecular structure solution. Acta Crystallogr D Biol Crystallogr, 2010. 66(Pt 2): p. 213-21.
295. Kabsch, W., Xds. Acta Crystallogr D Biol Crystallogr, 2010. 66(Pt 2): p. 125-32.
296. Michael R. Green, J.S., Molecular Cloning - A laboratory manual

Cold Spring Harbor Laboratory Press, 2012: p. 1-34

297. Higuchi, R., B. Krummel, and R.K. Saiki, A general method of in vitro preparation and specific mutagenesis of DNA fragments: study of protein and DNA interactions. Nucleic Acids Res, 1988. 16(15): p. 7351-67.
298. van den Ent, F. and J. Lowe, RF cloning: a restriction-free method for inserting target genes into plasmids. J Biochem Biophys Methods, 2006. 67(1): p. 67-74.
299. Erdmann, A., Edmann, U., Martens, A., Müller, O., and Paul., A. , Neurobiology. Westermann Druck GmbH, 2005: p. 26 ff.
300. Thompson, J.D., D.G. Higgins, and T.J. Gibson, CLUSTAL W: improving the sensitivity of progressive multiple sequence alignment through sequence weighting, position-specific gap penalties and weight matrix choice. Nucleic Acids Res, 1994. 22(22): p. 4673-80.
301. McWilliam, H., et al., Analysis Tool Web Services from the EMBL-EBI. Nucleic Acids Res, 2013. 41(Web Server issue): p. W597-600.
302. Li, W., et al., The EMBL-EBI bioinformatics web and programmatic tools framework. Nucleic Acids Res, 2015. 43(W1): p. W580-4.
303. Sievers, F., et al., Fast, scalable generation of high-quality protein multiple sequence alignments using Clustal Omega. Mol Syst Biol, 2011. 7: p. 539.
304. Drozdetskiy, A., et al., JPred4: a protein secondary structure prediction server. Nucleic Acids Res, 2015. 43(W1): p. W389-94.
305. Secher, D.S. and D.C. Burke, A monoclonal antibody for large-scale purification of human leukocyte interferon. Nature, 1980. 285(5765): p. 446-50.

306. Olsen, J.V., S.E. Ong, and M. Mann, Trypsin cleaves exclusively C-terminal to arginine and lysine residues. Mol Cell Proteomics, 2004. 3(6): p. 608-14.
307. Cheng, Y. and D.J. Patel, An efficient system for small protein expression and refolding. Biochem Biophys Res Commun, 2004. 317(2): p. 401-5.
308. Bao, W.J., et al., Highly efficient expression and purification system of small-size protein domains in Escherichia coli for biochemical characterization. Protein Expr Purif, 2006. 47(2): p. 599-606.
309. Gronenborn, A.M., et al., A novel, highly stable fold of the immunoglobulin binding domain of streptococcal protein G. Science, 1991. 253(5020): p. 657-61.
310. Yeliseev, A., L. Zoubak, and K. Gawrisch, Use of dual affinity tags for expression and purification of functional peripheral cannabinoid receptor. Protein Expr Purif, 2007. 53(1): p. 153-63.
311. Pace, C.N., G.R. Grimsley, and J.M. Scholtz, Protein ionizable groups: pK values and their contribution to protein stability and solubility. J Biol Chem, 2009. 284(20): p. 13285-9.
312. Thurlkill, R.L., et al., pK values of the ionizable groups of proteins. Protein Sci, 2006. 15(5): p. 1214-8.
313. Wilkins, M.R., et al., Protein identification and analysis tools in the ExPASy server. Methods Mol Biol, 1999. 112: p. 531-52.
314. Pace, C.N., et al., How to measure and predict the molar absorption coefficient of a protein. Protein Sci, 1995. 4(11): p. 2411-23.
315. Laemmli, U.K., Cleavage of structural proteins during the assembly of the head of bacteriophage T4. Nature, 1970. 227(5259): p. 680-5.
316. Moos, M., Jr., N.Y. Nguyen, and T.Y. Liu, Reproducible high yield sequencing of proteins electrophoretically separated and transferred to an inert support. J Biol Chem, 1988. 263(13): p. 6005-8.
317. Fairbanks, G., T.L. Steck, and D.F. Wallach, Electrophoretic analysis of the major polypeptides of the human erythrocyte membrane. Biochemistry, 1971. 10(13): p. 2606-17.
318. Wyatt, P.J., Light scattering and the absolute characterization of macromolecules. Analytica Chimica Acta, 1993. 272: p. 1-40.
319. Zimm, B.H., The dependence of the scattering of light on angle and concentration in linear polymer solutions. J Phys Colloid Chem, 1948. 52(1): p. 260-7.
320. Kelly, S.M., T.J. Jess, and N.C. Price, How to study proteins by circular dichroism. Biochim Biophys Acta, 2005. 1751(2): p. 119-39.
321. Bulheller, B.M., A. Rodger, and J.D. Hirst, Circular and linear dichroism of proteins. Phys Chem Chem Phys, 2007. 9(17): p. 2020-35.
322. Schmid, F.X., Spectral methods of characterizing protein conformation and conformational changes. Protein structure. A practical approach, 1989: p. 252-285.
323. Whitmore, L. and B.A. Wallace, Protein secondary structure analyses from circular dichroism spectroscopy: methods and reference databases. Biopolymers, 2008. 89(5): p. 392-400.
324. Whitmore, L. and B.A. Wallace, DICHROWEB, an online server for protein secondary structure analyses from circular dichroism spectroscopic data. Nucleic Acids Res, 2004. 32(Web Server issue): p. W668-73.
325. Laouini, A., et al., Preparation of liposomes: a novel application of microengineered membranes--from laboratory scale to large scale. Colloids Surf B Biointerfaces, 2013. 112: p. 272-8.
326. Szoka, F., Jr. and D. Papahadjopoulos, Comparative properties and methods of preparation of lipid vesicles (liposomes). Annu Rev Biophys Bioeng, 1980. 9: p. 467-508.
327. Marsh, D., Thermodynamics of phospholipid self-assembly. Biophys J, 2012. 102(5): p. 1079-87.

328. Takeuchi-Suzuki, E., et al., High-level expression using baculovirus, purification, and characterization of a monomeric form of type II calmodulin-dependent protein kinase. Protein Expr Purif, 1992. 3(2): p. 160-4.
329. White, R.R., et al., Definition of optimal substrate recognition motifs of Ca2+-calmodulin-dependent protein kinases IV and II reveals shared and distinctive features. J Biol Chem, 1998. 273(6): p. 3166-72.
330. Yang, E. and H. Schulman, Structural examination of autoregulation of multifunctional calcium/calmodulin-dependent protein kinase II. J Biol Chem, 1999. 274(37): p. 26199-208.
331. Hanson, P.I., et al., Expression of a multifunctional Ca2+/calmodulin-dependent protein kinase and mutational analysis of its autoregulation. Neuron, 1989. 3(1): p. 59-70.
332. Dessau, M.A. and Y. Modis, Protein crystallization for X-ray crystallography. J Vis Exp, 2011(47).
333. Brunger, A.T., Free R value: cross-validation in crystallography. Methods Enzymol, 1997. 277: p. 366-96.
334. Davis, I.W., et al., MOLPROBITY: structure validation and all-atom contact analysis for nucleic acids and their complexes. Nucleic Acids Res, 2004. 32(Web Server issue): p. W615-9.
335. Davis, I.W., et al., MolProbity: all-atom contacts and structure validation for proteins and nucleic acids. Nucleic Acids Res, 2007. 35(Web Server issue): p. W375-83.
336. Vaguine, A.A., J. Richelle, and S.J. Wodak, SFCHECK: a unified set of procedures for evaluating the quality of macromolecular structure-factor data and their agreement with the atomic model. Acta Crystallogr D Biol Crystallogr, 1999. 55(Pt 1): p. 191-205.
337. Krissinel, E. and K. Henrick, Inference of macromolecular assemblies from crystalline state. J Mol Biol, 2007. 372(3): p. 774-97.
338. Lovell, S.C., et al., Structure validation by Calpha geometry: phi,psi and Cbeta deviation. Proteins, 2003. 50(3): p. 437-50.
339. Dosztanyi, Z., et al., IUPred: web server for the prediction of intrinsically unstructured regions of proteins based on estimated energy content. Bioinformatics, 2005. 21(16): p. 3433-4.
340. Dosztanyi, Z., et al., The pairwise energy content estimated from amino acid composition discriminates between folded and intrinsically unstructured proteins. J Mol Biol, 2005. 347(4): p. 827-39.
341. Paoletti, P., P. Ascher, and J. Neyton, High-affinity zinc inhibition of NMDA NR1-NR2A receptors. J Neurosci, 1997. 17(15): p. 5711-25.
342. Baranovic, J., et al., Dynamics of the Ligand Binding Domain Layer during AMPA Receptor Activation. Biophys J, 2016. 110(4): p. 896-911.
343. Krivov, G.G., M.V. Shapovalov, and R.L. Dunbrack, Jr., Improved prediction of protein side-chain conformations with SCWRL4. Proteins, 2009. 77(4): p. 778-95.
344. Brooks, B.R., et al., CHARMM: the biomolecular simulation program. J Comput Chem, 2009. 30(10): p. 1545-614.
345. Muller, P., S. Kopke, and G.M. Sheldrick, Is the bond-valence method able to identify metal atoms in protein structures? Acta Crystallogr D Biol Crystallogr, 2003. 59(Pt 1): p. 32-7.
346. Prinz, W.A., et al., The role of the thioredoxin and glutaredoxin pathways in reducing protein disulfide bonds in the Escherichia coli cytoplasm. J Biol Chem, 1997. 272(25): p. 15661-7.
347. Dougherty, D.A., Cation-pi interactions involving aromatic amino acids. J Nutr, 2007. 137(6 Suppl 1): p. 1504S-1508S; discussion 1516S-1517S.
348. Matthews, B.W., Solvent content of protein crystals. J Mol Biol, 1968. 33(2): p. 491-7.

349. Zhang, W., et al., Structural and single-channel results indicate that the rates of ligand binding domain closing and opening directly impact AMPA receptor gating. J Neurosci, 2008. 28(4): p. 932-43.
350. Armstrong, N., M. Mayer, and E. Gouaux, Tuning activation of the AMPA-sensitive GluR2 ion channel by genetic adjustment of agonist-induced conformational changes. Proc Natl Acad Sci U S A, 2003. 100(10): p. 5736-41.
351. Furukawa, H. and E. Gouaux, Mechanisms of activation, inhibition and specificity: crystal structures of the NMDA receptor NR1 ligand-binding core. EMBO J, 2003. 22(12): p. 2873-85.
352. Landes, C.F., et al., Structural landscape of isolated agonist-binding domains from single AMPA receptors. Nat Chem Biol, 2011. 7(3): p. 168-73.
353. Postila, P.A., M. Ylilauri, and O.T. Pentikainen, Full and partial agonism of ionotropic glutamate receptors indicated by molecular dynamics simulations. J Chem Inf Model, 2011. 51(5): p. 1037-47.
354. Ramaswamy, S., et al., Role of conformational dynamics in alpha-amino-3-hydroxy-5-methylisoxazole-4-propionic acid (AMPA) receptor partial agonism. J Biol Chem, 2012. 287(52): p. 43557-64.
355. Yao, Y., et al., Conformational analysis of NMDA receptor GluN1, GluN2, and GluN3 ligand-binding domains reveals subtype-specific characteristics. Structure, 2013. 21(10): p. 1788-99.
356. Miu, P., et al., Novel AMPA receptor potentiators LY392098 and LY404187: effects on recombinant human AMPA receptors in vitro. Neuropharmacology, 2001. 40(8): p. 976-83.
357. Green, T. and N. Nayeem, The multifaceted subunit interfaces of ionotropic glutamate receptors. J Physiol, 2015. 593(1): p. 73-81.
358. Yelshanskaya, M.V., et al., Probing Intersubunit Interfaces in AMPA-subtype Ionotropic Glutamate Receptors. Sci Rep, 2016. 6: p. 19082.
359. Stern-Bach, Y., et al., A point mutation in the glutamate binding site blocks desensitization of AMPA receptors. Neuron, 1998. 21(4): p. 907-18.
360. Klippenstein, V., et al., Photoinactivation of glutamate receptors by genetically encoded unnatural amino acids. J Neurosci, 2014. 34(3): p. 980-91.
361. Zheng, H., et al., Validation of metal-binding sites in macromolecular structures with the CheckMyMetal web server. Nat Protoc, 2014. 9(1): p. 156-70.
362. Laitaoja, M., J. Valjakka, and J. Janis, Zinc coordination spheres in protein structures. Inorg Chem, 2013. 52(19): p. 10983-91.
363. Marjorie M. Harding*, M.W.N.a.M.D.W., Metals in protein structures: a review of their principal features. Crystallography Reviews, 2010. 16(4): p. 247-302.
364. Dokmanic, I., M. Sikic, and S. Tomic, Metals in proteins: correlation between the metal-ion type, coordination number and the amino-acid residues involved in the coordination. Acta Crystallogr D Biol Crystallogr, 2008. 64(Pt 3): p. 257-63.
365. Elling, C.E. and T.W. Schwartz, Connectivity and orientation of the seven helical bundle in the tachykinin NK-1 receptor probed by zinc site engineering. EMBO J, 1996. 15(22): p. 6213-9.
366. Krintel, C., et al., Thermodynamics and structural analysis of positive allosteric modulation of the ionotropic glutamate receptor GluA2. Biochem J, 2012. 441(1): p. 173-8.
367. Partin, K.M., D.K. Patneau and M.L. Mayer, Cyclothiazide differentially modulates desensitization of alpha-amino-3-hydroxy-5-methyl-4-isoxazolepropionic acid receptor splice variants. Mol. Pharmacol., 1996. 46: p. 129-138.
368. Huth, J.R., et al., Design of an expression system for detecting folded protein domains and mapping macromolecular interactions by NMR. Protein Sci, 1997. 6(11): p. 2359-64.

369. Alexander, P., et al., Thermodynamic analysis of the folding of the streptococcal protein G IgG-binding domains B1 and B2: why small proteins tend to have high denaturation temperatures. Biochemistry, 1992. 31(14): p. 3597-603.
370. Alexander, P., J. Orban, and P. Bryan, Kinetic analysis of folding and unfolding the 56 amino acid IgG-binding domain of streptococcal protein G. Biochemistry, 1992. 31(32): p. 7243-8.
371. Tomlinson, J.H., et al., Structural origins of pH-dependent chemical shifts in the B1 domain of protein G. Proteins, 2010. 78(14): p. 3000-16.
372. Gallagher, T., et al., Two crystal structures of the B1 immunoglobulin-binding domain of streptococcal protein G and comparison with NMR. Biochemistry, 1994. 33(15): p. 4721-9.
373. Lian, L.Y., et al., Sequential 1H NMR assignments and secondary structure of an IgG-binding domain from protein G. Biochemistry, 1991. 30(22): p. 5335-40.
374. Hung, A.Y. and M. Sheng, PDZ domains: structural modules for protein complex assembly. J Biol Chem, 2002. 277(8): p. 5699-702.
375. Lee, H.J. and J.J. Zheng, PDZ domains and their binding partners: structure, specificity, and modification. Cell Commun Signal, 2010. 8: p. 8.
376. Chi, C.N., et al., Ligand binding by PDZ domains. Biofactors, 2012. 38(5): p. 338-48.
377. Opazo, P., et al., CaMKII triggers the diffusional trapping of surface AMPARs through phosphorylation of stargazin. Neuron, 2010. 67(2): p. 239-52.
378. Folch, J., M. Lees, and G.H. Sloane Stanley, A simple method for the isolation and purification of total lipides from animal tissues. J Biol Chem, 1957. 226(1): p. 497-509.
379. Louros, S.R., et al., A role for stargazin in experience-dependent plasticity. Cell Rep, 2014. 7(5): p. 1614-25.
380. Watkins, J.C. and R.H. Evans, Excitatory amino acid transmitters. Annu Rev Pharmacol Toxicol, 1981. 21: p. 165-204.
381. Lesley, S.A. and I.A. Wilson, Protein production and crystallization at the joint center for structural genomics. J Struct Funct Genomics, 2005. 6(2-3): p. 71-9.
382. Chayen, N.E., Turning protein crystallisation from an art into a science. Curr Opin Struct Biol, 2004. 14(5): p. 577-83.
383. Page, R. and R.C. Stevens, Crystallization data mining in structural genomics: using positive and negative results to optimize protein crystallization screens. Methods, 2004. 34(3): p. 373-89.
384. Derewenda, Z.S. and P.G. Vekilov, Entropy and surface engineering in protein crystallization. Acta Crystallogr D Biol Crystallogr, 2006. 62(Pt 1): p. 116-24.
385. Hald, H., et al., Distinct structural features of cyclothiazide are responsible for effects on peak current amplitude and desensitization kinetics at iGluR2. J Mol Biol, 2009. 391(5): p. 906-17.
386. Kumar, J., et al., The N-terminal domain of GluR6-subtype glutamate receptor ion channels. Nat Struct Mol Biol, 2009. 16(6): p. 631-8.
387. Henrick, K. and J.M. Thornton, PQS: a protein quaternary structure file server. Trends Biochem Sci, 1998. 23(9): p. 358-61.
388. Luo, J., et al., A structural dissection of large protein-protein crystal packing contacts. Sci Rep, 2015. 5: p. 14214.
389. Bernauer, J., et al., DiMoVo: a Voronoi tessellation-based method for discriminating crystallographic and biological protein-protein interactions. Bioinformatics, 2008. 24(5): p. 652-8.
390. Ponstingl, H., K. Henrick, and J.M. Thornton, Discriminating between homodimeric and monomeric proteins in the crystalline state. Proteins, 2000. 41(1): p. 47-57.
391. Zhu, H., et al., NOXclass: prediction of protein-protein interaction types. BMC Bioinformatics, 2006. 7: p. 27.

392. Shaanan, B., Structure of human oxyhaemoglobin at 2.1 A resolution. J Mol Biol, 1983. 171(1): p. 31-59.
393. Paoli, M., et al., Crystal structure of T state haemoglobin with oxygen bound at all four haems. J Mol Biol, 1996. 256(4): p. 775-92.
394. Fermi, G., et al., The crystal structure of human deoxyhaemoglobin at 1.74 A resolution. J Mol Biol, 1984. 175(2): p. 159-74.
395. Welsh, L.C., M.F. Symmons, and D.A. Marvin, The molecular structure and structural transition of the alpha-helical capsid in filamentous bacteriophage Pf1. Acta Crystallogr D Biol Crystallogr, 2000. 56(Pt 2): p. 137-50.
396. Janin, J. and F. Rodier, Protein-protein interaction at crystal contacts. Proteins, 1995. 23(4): p. 580-7.
397. Chaudhry, C., et al., Energetics of glutamate receptor ligand binding domain dimer assembly are modulated by allosteric ions. Proc Natl Acad Sci U S A, 2009. 106(30): p. 12329-34.
398. Mayer, M.L., Emerging models of glutamate receptor ion channel structure and function. Structure, 2011. 19(10): p. 1370-80.
399. Furukawa, H., et al., Subunit arrangement and function in NMDA receptors. Nature, 2005. 438(7065): p. 185-92.
400. Markau, K., J. Schneider, and H. Sund, Studies of glutamate dehydrogenase. The mechanism of the association-dissociation equilibrium of beef-liver glutamate dehydrogenase. Eur J Biochem, 1971. 24(2): p. 393-400.
401. Jin, R. and E. Gouaux, Probing the function, conformational plasticity, and dimer-dimer contacts of the GluR2 ligand-binding core: studies of 5-substituted willardiines and GluR2 S1S2 in the crystal. Biochemistry, 2003. 42(18): p. 5201-13.
402. Lau, A.Y. and B. Roux, Structural biology: One domain, multiple conformations. Nat Chem Biol, 2011. 7(3): p. 130-1.
403. Monod, J., J. Wyman, and J.P. Changeux, On the Nature of Allosteric Transitions: A Plausible Model. J Mol Biol, 1965. 12: p. 88-118.
404. Koshland, D.E., Jr., G. Nemethy, and D. Filmer, Comparison of experimental binding data and theoretical models in proteins containing subunits. Biochemistry, 1966. 5(1): p. 365-85.
405. Maclean, D.M., et al., Cations but not anions regulate the responsiveness of kainate receptors. J Neurosci, 2011. 31(6): p. 2136-44.
406. Robert, A., et al., AMPA receptor binding cleft mutations that alter affinity, efficacy, and recovery from desensitization. J Neurosci, 2005. 25(15): p. 3752-62.
407. Schmid, S.M., et al., A domain linking the AMPA receptor agonist binding site to the ion pore controls gating and causes lurcher properties when mutated. J Neurosci, 2007. 27(45): p. 12230-41.
408. Talukder, I., P. Borker, and L.P. Wollmuth, Specific sites within the ligand-binding domain and ion channel linkers modulate NMDA receptor gating. J Neurosci, 2010. 30(35): p. 11792-804.
409. Yelshansky, M.V., et al., Block of AMPA receptor desensitization by a point mutation outside the ligand-binding domain. J Neurosci, 2004. 24(20): p. 4728-36.
410. Christendat, D., et al., Structural proteomics of an archaeon. Nat Struct Biol, 2000. 7(10): p. 903-9.
411. Itakura, M., et al., Direct association of the unique C-terminal tail of transmembrane AMPA receptor regulatory protein gamma-8 with calcineurin. FEBS J, 2014. 281(5): p. 1366-78.
412. Zhou, P. and G. Wagner, Overcoming the solubility limit with solubility-enhancement tags: successful applications in biomolecular NMR studies. J Biomol NMR, 2010. 46(1): p. 23-31.
413. Deshmukh, M.V., et al., mRNA decapping is promoted by an RNA-binding channel in Dcp2. Mol Cell, 2008. 29(3): p. 324-36.

414. Safadi, S.S. and G.S. Shaw, A disease state mutation unfolds the parkin ubiquitin-like domain. Biochemistry, 2007. 46(49): p. 14162-9.
415. Catic, A., et al., Sequence and structure evolved separately in a ribosomal ubiquitin variant. EMBO J, 2007. 26(14): p. 3474-83.
416. Kang, J., et al., Identification of residues participating in the interaction between an intraluminal loop of inositol 1,4,5-trisphosphate receptor and a conserved N-terminal region of chromogranin B. Biochim Biophys Acta, 2007. 1774(4): p. 502-9.
417. Selenko, P., et al., In situ observation of protein phosphorylation by high-resolution NMR spectroscopy. Nat Struct Mol Biol, 2008. 15(3): p. 321-9.
418. Schwenk, J., et al., NMR analysis of KChIP4a reveals structural basis for control of surface expression of Kv4 channel complexes. J Biol Chem, 2008. 283(27): p. 18937-46.
419. Zhou, L., et al., Effects of full-length borealin on the composition and protein-protein interaction activity of a binary chromosomal passenger complex. Biochemistry, 2009. 48(6): p. 1156-61.
420. Obradovic, Z., et al., Predicting intrinsic disorder from amino acid sequence. Proteins, 2003. 53 Suppl 6: p. 566-72.
421. Oldfield, C.J., et al., Flexible nets: disorder and induced fit in the associations of p53 and 14-3-3 with their partners. BMC Genomics, 2008. 9 Suppl 1: p. S1.
422. Uversky, V.N., C.J. Oldfield, and A.K. Dunker, Showing your ID: intrinsic disorder as an ID for recognition, regulation and cell signaling. J Mol Recognit, 2005. 18(5): p. 343-84.
423. Elias, G.M., et al., Synapse-specific and developmentally regulated targeting of AMPA receptors by a family of MAGUK scaffolding proteins. Neuron, 2006. 52(2): p. 307-20.
424. Zhang, W., et al., Structural basis of arc binding to synaptic proteins: implications for cognitive disease. Neuron, 2015. 86(2): p. 490-500.
425. Price, M.G., et al., The alpha-amino-3-hydroxyl-5-methyl-4-isoxazolepropionate receptor trafficking regulator "stargazin" is related to the claudin family of proteins by Its ability to mediate cell-cell adhesion. J Biol Chem, 2005. 280(20): p. 19711-20.
426. Dawson, R.M., A hydrolytic procedure for the identification and estimation of individual phospholipids in biological samples. Biochem J, 1960. 75: p. 45-53.
427. McLaughlin, S., et al., PIP(2) and proteins: interactions, organization, and information flow. Annu Rev Biophys Biomol Struct, 2002. 31: p. 151-75.
428. Di Paolo, G. and P. De Camilli, Phosphoinositides in cell regulation and membrane dynamics. Nature, 2006. 443(7112): p. 651-7.
429. Marks, F.K., Ursula, Cellular Signal Processing: An Introduction to the Molecular Mechanisms of Signal Transduction. Garland Science, 2012: p. 1-656.
430. Khoury, G.A., R.C. Baliban, and C.A. Floudas, Proteome-wide post-translational modification statistics: frequency analysis and curation of the swiss-prot database. Sci Rep, 2011. 1.
431. Soderling, T.R., CaM-kinases: modulators of synaptic plasticity. Curr Opin Neurobiol, 2000. 10(3): p. 375-80.
432. Xu, W., et al., Molecular dissociation of the role of PSD-95 in regulating synaptic strength and LTD. Neuron, 2008. 57(2): p. 248-62.
433. Luscher, C., et al., Synaptic plasticity and dynamic modulation of the postsynaptic membrane. Nat Neurosci, 2000. 3(6): p. 545-50.
434. MacLean, D., et al., PhosCalc: a tool for evaluating the sites of peptide phosphorylation from mass spectrometer data. BMC Res Notes, 2008. 1: p. 30.
435. Dephoure, N., et al., Mapping and analysis of phosphorylation sites: a quick guide for cell biologists. Mol Biol Cell, 2013. 24(5): p. 535-42.
436. Harsha, H.C., H. Molina, and A. Pandey, Quantitative proteomics using stable isotope labeling with amino acids in cell culture. Nat Protoc, 2008. 3(3): p. 505-16.

437. Ong, S.E., L.J. Foster, and M. Mann, Mass spectrometric-based approaches in quantitative proteomics. Methods, 2003. 29(2): p. 124-30.
438. Zhang, G. and T.A. Neubert, Use of stable isotope labeling by amino acids in cell culture (SILAC) for phosphotyrosine protein identification and quantitation. Methods Mol Biol, 2009. 527: p. 79-92, xi.
439. Zanivan, S., et al., In vivo SILAC-based proteomics reveals phosphoproteome changes during mouse skin carcinogenesis. Cell Rep, 2013. 3(2): p. 552-66.
440. Molden, R.C., et al., Stable isotope labeling of phosphoproteins for large-scale phosphorylation rate determination. Mol Cell Proteomics, 2014. 13(4): p. 1106-18.
441. Anthis, N.J., et al., Beta integrin tyrosine phosphorylation is a conserved mechanism for regulating talin-induced integrin activation. J Biol Chem, 2009. 284(52): p. 36700-10.
442. Browning, M.D., R. Huganir, and P. Greengard, Protein phosphorylation and neuronal function. J Neurochem, 1985. 45(1): p. 11-23.
443. Arbuzova, A., A.A. Schmitz, and G. Vergeres, Cross-talk unfolded: MARCKS proteins. Biochem J, 2002. 362(Pt 1): p. 1-12.
444. Gomes, A.R., et al., Regulation of AMPA receptor activity, synaptic targeting and recycling: role in synaptic plasticity. Neurochem Res, 2003. 28(10): p. 1459-73.
445. Malenka, R.C., Synaptic plasticity and AMPA receptor trafficking. Ann N Y Acad Sci, 2003. 1003: p. 1-11.
446. Sheng, M. and S. Hyoung Lee, AMPA receptor trafficking and synaptic plasticity: major unanswered questions. Neurosci Res, 2003. 46(2): p. 127-34.
447. El-Husseini, A.E., et al., Dual palmitoylation of PSD-95 mediates its vesiculotubular sorting, postsynaptic targeting, and ion channel clustering. J Cell Biol, 2000. 148(1): p. 159-72.
448. Craven, S.E., A.E. El-Husseini, and D.S. Bredt, Synaptic targeting of the postsynaptic density protein PSD-95 mediated by lipid and protein motifs. Neuron, 1999. 22(3): p. 497-509.
449. Chen, X., et al., PSD-95 is required to sustain the molecular organization of the postsynaptic density. J Neurosci, 2011. 31(17): p. 6329-38.
450. Feng, W. and M. Zhang, Organization and dynamics of PDZ-domain-related supramodules in the postsynaptic density. Nat Rev Neurosci, 2009. 10(2): p. 87-99.
451. Fomina, S., et al., Self-directed assembly and clustering of the cytoplasmic domains of inwardly rectifying Kir2.1 potassium channels on association with PSD-95. Biochim Biophys Acta, 2011. 1808(10): p. 2374-89.
452. Nakagawa, T., et al., Quaternary structure, protein dynamics, and synaptic function of SAP97 controlled by L27 domain interactions. Neuron, 2004. 44(3): p. 453-67.
453. Sainlos, M., et al., Biomimetic divalent ligands for the acute disruption of synaptic AMPAR stabilization. Nat Chem Biol, 2011. 7(2): p. 81-91.
454. Wang, W., et al., Creating conformational entropy by increasing interdomain mobility in ligand binding regulation: a revisit to N-terminal tandem PDZ domains of PSD-95. J Am Chem Soc, 2009. 131(2): p. 787-96.
455. McCann, J.J., et al., Domain orientation in the N-Terminal PDZ tandem from PSD-95 is maintained in the full-length protein. Structure, 2011. 19(6): p. 810-20.
456. Long, J.F., et al., Supramodular structure and synergistic target binding of the N-terminal tandem PDZ domains of PSD-95. J Mol Biol, 2003. 327(1): p. 203-14.
457. Migaud, M., et al., Enhanced long-term potentiation and impaired learning in mice with mutant postsynaptic density-95 protein. Nature, 1998. 396(6710): p. 433-9.
458. Selvakumar, B., R.L. Huganir, and S.H. Snyder, S-nitrosylation of stargazin regulates surface expression of AMPA-glutamate neurotransmitter receptors. Proc Natl Acad Sci U S A, 2009. 106(38): p. 16440-5.
459. El-Husseini Ael, D., et al., Synaptic strength regulated by palmitate cycling on PSD-95. Cell, 2002. 108(6): p. 849-63.

460. Theillet, F.X., et al., Structural disorder of monomeric alpha-synuclein persists in mammalian cells. Nature, 2016. 530(7588): p. 45-50.
461. Ferrell, J.E., Jr., Tripping the switch fantastic: how a protein kinase cascade can convert graded inputs into switch-like outputs. Trends Biochem Sci, 1996. 21(12): p. 460-6.
462. Trunnell, N.B., et al., Ultrasensitivity in the Regulation of Cdc25C by Cdk1. Mol Cell, 2011. 41(3): p. 263-74.
463. Harvey, S.L., et al., A phosphatase threshold sets the level of Cdk1 activity in early mitosis in budding yeast. Mol Biol Cell, 2011. 22(19): p. 3595-608.
464. Long, S.B., E.B. Campbell, and R. Mackinnon, Crystal structure of a mammalian voltage-dependent Shaker family K+ channel. Science, 2005. 309(5736): p. 897-903.
465. Long, S.B., E.B. Campbell, and R. Mackinnon, Voltage sensor of Kv1.2: structural basis of electromechanical coupling. Science, 2005. 309(5736): p. 903-8.
466. IUPAC-IUB Joint Commission on Biochemical Nomenclature (JCBN). Nomenclature and symbolism for amino acids and peptides. Recommendations 1983. Eur J Biochem, 1984. 138(1): p. 9-37.

DECLARATION

This thesis presents my original research work. I hereby declare that wherever contributions of others are involved, every effort is made to indicate this clearly, with due reference to the literature, and acknowledgement of collaborative work and discussions. This thesis has not been submitted to any other faculty or university and I am aware of the doctoral regulations from the Department of Biology, Chemistry, and Pharmacy of the Freie Universität Berlin.
The work was done under the supervision and guidance of Dr. Andrew Plested, at the Leibnitz-Institut für Molekulare Pharmakologie (FMP), Berlin.

Berlin, August 2016

Miriam Chebli